Ab Initio Molecular Dynamics Simulation of Proton Transfer in Narrow Ionomer Pores

Dissertation

zur Erlangung des akademischen Grades eines
Doktors der Naturwissenschaften
-Dr.rer.nat.-

vorgelegt von

Mehmet Ali ILHAN

geboren in *Çal, Türkei*

Fakultät für Chemie
der Universität Duisburg-Essen

Mai 2014

Die vorliegende Arbeit wurde im Zeitraum von November 2008 bis Mai 2014 im Arbeitskreis von Prof. Dr. Eckhard Spohr am Institut für Theoretische Chemie der Universität Duisburg-Essen durchgeführt.

Tag der Disputation: 12.11.2014

1. Gutachter: Prof. Dr. Eckhard Spohr

2. Gutachter: Prof. Dr. Georg Jansen

Vorsitzender: Prof. Dr. Mathias Ulbricht

Abstract

In polymer electrolyte membrane fuel cells the narrowness of the ionomer pore may be considered as the rate determining factor for proton transfer. This proton conduction has been studied theoretically in various models of such narrow pores with low hydration levels by using *ab initio* molecular dynamics (MD) simulation.

The diffusion of a proton is possible, or at least strongly enhanced by the so called Grotthuss-mechanism, which has as a prerequisite the existence of hydrogen-bonded water molecules around the proton complex. Therefore, the objective of this study was to investigate the dynamics of the hydrogen bonds in order to obtain life times, fluctuations, and average numbers of hydrogen bonds in narrow pores, consisting here of hydrophilic sulfonate groups and the hydrophobic backbone of the ionomer. The effect of the water content on the chemical equilibria within these narrow pores is demonstrated by establishing the probabilities of observing different states of the proton complex. Dissociation occurs when the number of water molecules per hydrophilic sulfonate group, λ, is around 3.

Dependencies of the concentration of hydronium and Zundel states of proton complexes on the water content are shown.

The onset of the proton mobility in the narrow ionomer pore is demonstrated by comparing the diffusion coefficients at various levels of water contents. Possible factors related to the pore structure, which hinder the proton mobility, such as hydrophilic traps, are discussed. The most favorable spacing between hydrophilic groups is suggested.

The spectral densities of the translational motion of atoms in the ionomer pore, which shed light on the dynamical and structural properties of the molecular system, are represented, suggesting, that some of the bands in the spectral densities are associated with the different proton complexes.

Zusammenfassung

Die Porengröße eines Ionomers in Polymerelektrolytbrennstoffzellen determiniert maßgeblich dessen Protonenleitfähigkeit. Unter Anwendung von *ab initio* Molekulardynamik (MD) wurde der Transfer von Protonen bereits in unterschiedlichen theoretischen Studien anhand verschiedener Modelle enger Poren mit niedrigem Hydratationsniveau simuliert.

Die Diffusion der Protonen wird wesentlich durch den so genannten Grotthuss-Mechanismus angetrieben, dessen Voraussetzung die Vernetzung des Protonenkomplexes über Wasserstoffbrückenbindungen mit Wassermolekülen ist. Ziel war es daher hier, die Dynamik, Quantität, Fluktuation sowie Persistenz von Wasserstoffbrückenbindungen in engen Poren zu ermitteln und zu untersuchen. Gegenstand sind Ionomer-Poren bestehend aus hydrophilen Sulfonatgruppen und dem hydrophoben Rückgrat des Ionomers. Die Auswirkung des Wassergehalts auf das chemische Gleichgewicht innerhalb der Ionomer-Poren wird anhand der Wahrscheinlichkeit für das Auftreten verschiedener Zustände des Protonenkomplexes aufgezeigt. Dabei erfolgt die Dissoziation von Protonen, wenn die Anzahl der Wassermoleküle pro hydrophiler Sulfonatgruppe, λ, ungefähr den Wert 3 erreicht. Die Abhängigkeit der Konzentration an Hydronium- und Zundel- Zuständen der Protonenkomplexe vom Wassergehalt wird dargelegt und diskutiert.

Außerdem wird das Einsetzen des Protonentransports innerhalb der engen Ionomer-Pore durch den Vergleich der Diffusionskoeffizienten bei unterschiedlichem Wassergehalt demonstriert. Faktoren, wie "hydrophile Fallen", die bezüglich der Poren-Beschaffenheit die Protonenmobilität einschränken könnten, werden dargelegt und erörtert. Zudem werden die günstigsten Abstände der hydrophilen Gruppen zueinander vorgeschlagen.

Das hier aufgezeigte Dichtespektrum der Ionomer-Poren, welches Aufschluss über die dynamischen und strukturellen Eigenschaften des molekularen Systems gibt, verdeutlicht, dass einige der Banden des Spektrums mit den verschiedenen Protonenkomplexen assoziert sind.

To my family ...

Contents

List of Figures

List of Tables

Glossary

AFC	Alkaline fuel cell
AIMD	*Ab initio* molecular dynamics
BOMD	Born-Oppenheimer molecular dynamics
CPMD	Car-Parinello molecular dynamics
DACF	Dipole auto-correlation function
DFT	Density functional theory
DMFC	Direct methanol fuel cell
FC	Fuel cell
FTIR	Fourier transform infrared spectroscopy
HB	Hydrogen bonds
IR	infra-red
MC	Monte-Carlo
MCFC	Molten carbonate fuel cell
MD	Molecular dynamics
MEA	Membrane electrode assembly
MSD	Mean square displacement
NMR	Nuclear magnetic resonance
PAFC	Phosphoric acid fuel cell
PEMFC	Polymer electrolyte membrane fuel cell
RDF	Radial distribution function
SAXS	Small angle x-ray spectroscopy
SOFC	Solid oxide fuel cell
VACF	Velocity auto-correlation function

Chapter 1

Introduction

INTRODUCTION

One of the most important aims of science is to understand, explain, and control matter, which is understood to be governed by, and reducible to, physical laws. It is postulated in classical physics, which deals with particles and fields, that no particle can exist in nature without an action with respect to some reference frame.

At the energy and time scales relevant to chemistry, the relevant particles are the atoms and molecules. Statistical physics (or mechanics) teaches us how to relate the physical properties of these particles with the macroscopic variables observed in the laboratory, e.g. the thermodynamical properties such as temperature.

In physics, the state of a classical system is described by the Lagrangian, which is a function of the kinetic and potential energy. In order to obtain the Lagrangian for a system of particles correctly, all physical quantities (electric charge, mass ..) and interactions between particles must be known. However, considering all particles in a finite quantity of matter, say a mole, is not computationally tractable. Hence, one needs to simplify the Lagrangian and to resort to statistical methods.

Herein lies the difficulty and the art of computational experiments.

Correct description of the physical quantities is achieved by quantum mechanics, which governs the behavior, again at the energies and time scales of chemistry, of particles lighter than the proton, i.e. essentially the electrons. However including electrons in the Lagrangian increases the complexity of the problems. Applying the Born-Oppenheimer approximations, these particles can be removed from the system, their contributions being summarized and expressed in the interactions, mentioned above, between the particles of interest.

Ab initio molecular dynamics (AIMD), based on the Born-Oppenheimer approximations, is a scientific computational tool which allows for a systematic solution to the Lagrangian under the conditions described above. A detailed description of these methods will be given in Chapter 3.

Drastic changes can take place in the structure, dynamics, and thermodynamics of a fluid when it is confined to spaces of molecular dimensions. Water confined in nanometer-scale channels and pores of inorganic open framework materials is known to display unusual properties, which are of great scientific interest. The dynamical properties thus change in confining media, especially if this confinement consists of a combination of hydrophilic and hydrophobic molecules. The acidity of the medium has also some effect on these structural and dynamical properties.

Pores of ionomers demonstrate the above mentioned properties by simultaneously having hydrophobic and hydrophilic confinement with high acidity level. The dynamics of protons inside the pores, such as their mobility, shows a dependency on the water content. Also, the structure of pores, including their radius, spacing and the number of hydrophilic and hydrophobic groups affect the chemical equilibria and, hence, kinetics of medium. These effects are more pronounced especially for narrow pores with low water contents.

Waters molecules are taken up during swelling of an ionomer, because of its hydrophilicity. They, then, constitute water channels and become connected with increasing water level. One of the most important features of many ionomers, such as Nafion® , is their high proton conductivity, which is realized by proton transfers through these water channels. The structure of these water-filled pores is not homogeneous inside the ionomer and depends on water content. When the water content is low, pores become narrow, and proton conductivity decreases. Therefore, these narrow pores with low water content are the rate determining factor for proton mobility. Investigating structural properties of narrow pores for various water content is of upmost important in order to understand the required conditions for the onset of proton mobility in ionomer.

The structure of ionomers can be studied by experimental methods, such as X-ray and neutron scattering, which provide many features and properties of ionomers with high water content. However, the determination of the structure of the narrow pores at low hydration level is difficult to observe with experiments. The main difficulty arises from the fact that differentiating the narrow pores from hydrophobic polymer matrix becomes almost impossible at low water content. Hence, an atomic level of understanding is provided by molecular dynamics simulations.

The aim of this work is to get an understanding, at the level discussed above, of the main aspects of proton conductivity in the narrow pores of an ionomer network at low hydration level. Among the various approaches that can be envisaged for this purpose, we selected, for reasons to be detailed below, *ab initio* molecular dynamics. Stringent modeling assumptions are necessary in order to make the problem computationally tractable.

In the following chapter (Chap. 2), the basic working principle of a polymer electrolyte membrane fuel cell (PEMFC) is explained. Secondly, some structural and dynamical properties of ionomers are discussed briefly in order to get insight into the importance of narrow pores on proton mobility.

In Chapter 3, the computational methods used in the simulations, *ab initio* molecular dynamics, are summarized. In Chapter 4, pore models and simulations details are shown. Additionally models and strategies used for preparation of these simulations are explained.

Results of the computational experiments, which are deduced by analyzing the trajectories with various statistical samplings and correlations are represented in the following chapters. All these results are related to structural and dynamical properties of the system, which are governing the mobility of the protons. The structure of the narrow pores is discussed in Chapter 5. The analysis of the hydrogen bond dynamics, which is indispensable for the understanding of any transport phenomena within an aqueous system is shown in Chapter 6.

The possible proton states and the chemical equilibria within a highly acidic medium, which is enclosed by the hydrophilic and the hydrophobic molecules of the ionomer are elucidated in Chapter 7. Then the transport coefficients of the protons and their dependency on the water content are shown.

Finally, the spectral densities of the translational motion are shown in Chapter 8. The thesis is then concluded by summarizing and discussing some of the important results in Chapter 9.

Chapter 2

Background

In this chapter, we explain, firstly, the basic working principle of a polymer electrolyte membrane fuel cell (PEMFC) (Sec. 2.1). Secondly, some structural and dynamical properties of the ion-conducting membrane, the ionomer, are discussed briefly in order to get insight into the importance of narrow pores on proton mobility in Section 2.2.

2.1 Polymer Electrolyte Membrane Fuel Cell

The fuel cell is one of the most promising energy sources as an alternative to fossil-based energy ones. Its basic principle, based on reversing the process of electrolysis, is to convert the chemical energy of a fuel to electrical energy. The principle of the fuel cell was firstly described by Grove in 1839 when he produced electricity from hydrogen and oxygen using sulfuric acid (H_2SO_4) as an electrolyte [68].

The type of electrolyte used in fuel cells determines the main features of a fuel cell: the kind of fuel and catalysts, chemical reactions and operating temperature. Hence, fuel cells are usually classified according to their electrolyte. Some frequently used electrolytes (corresponding fuel cells) are polymer electrolyte membrane (PEMFC), alkali (AFC), molten carbonate (MCFC), phosphoric acid (PAFC), and solid oxide (SOFC). Because of its low working temperature and its adequate capacity of power production, PEMFC is especially suitable for mobile transport purposes. Some stationary applications of PEMFC are also available. Hydrogen is commonly used as fuel in PEMFC. But other fuels, such as methanol, are also employed by other kinds of fuel cells [154, 213].

In the Gemini space program, a stack of PEMFCs, developed by General Electric, was utilized [63]. Because of increasing oil price, limitation of oil reserves, development of high proton-conductive and stable membranes such as Nafion® by Du Pont, has enhanced the research on PEMFC.

2.1.1 Basic Working Principle of PEMFC

A polymer electrolyte membrane fuel cell is composed of anode, cathode, and in-between an electrolyte membrane, which is enclosed from two sides by gas diffusion layer and catalyst layer (see Fig. 2.1). Anode and cathode are connected by a (metal) conductor.

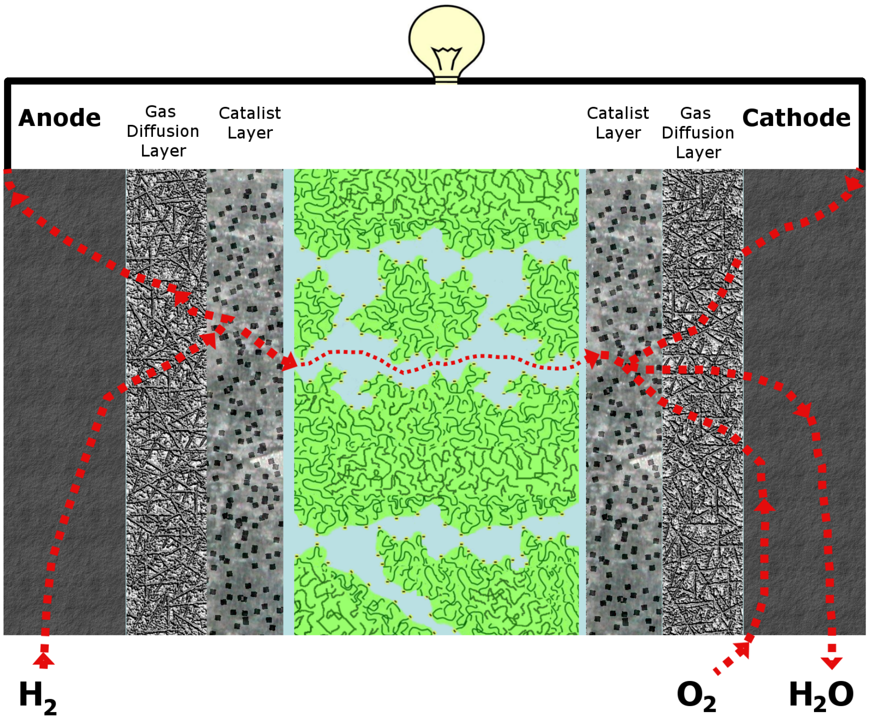

Figure 2.1: Schematic design of a PEM fuel cell

The principle of proton exchange membrane fuel cell (PEMFC) can be summarized in the following way; A hydrogen molecule, which is fed into PEMFC from anode side, is oxidized within the anode catalyst layer

$$H_2 \rightarrow 2H^+ + 2e^- \tag{2.1}$$

Two hydrogen ions and two electrons are produced. Hydrogen ions uptaken by water in the membrane are transported within the water channels through the membrane from anode to cathode. Electrons are conducted via an external metal between anode and cathode. At the cathode, oxygen (from air), hydrogen ions and electrons are combined together by reduction of oxygen. The reaction,

$$O_2 + 4H^+ + 4e^- \rightarrow 2H_2O \tag{2.2}$$

results in production of water and heat. As a result of overall, the electrical energy is produced.

Although the reactions can be written in simple forms, they include complex interactions depending on structures and properties of catalysts and electrolytes. Hence, ongoing investigations about the performance of PEMFC are related with these two main components, namely, catalyst and electrolyte.

Both chemical reactions at anode and cathode are facilitated by the catalysts. They may consist of different kinds or/and structure of atoms or alloys, such as platinum-based catalysts. Development of efficient and inexpensive catalysts is the target of much research [91, 39, 51, 37, 184].

Another complex phenomenon affecting the performance of PEMFC, which is related with the target of this study, is the transport of protons through water channels of the polymer electrolyte membrane. Proton conduction depends upon structure, morphology of the membrane, and humidity level [40, 1, 130].

2.2 Perfluorosulfonate Ionomers

Perfluorinated membranes are used in PEMFC mainly due to their high proton conductivity and mechanical stability at the working temperature of PEMFC. They are also applied in a wide range of chemical processes such as separation of liquids and gas, water electrolysis, electro-organic synthesis, catalysis, electrochemical synthesis, nanoparticle synthesis, and protective clothing [63, 28]. Perfluorosulfonate ionomers are generally co-polymers composed of a fluorinated carbon backbone with randomly distributed perfluorovinyl ether side chains terminated with sulfonic acid moieties [146]. Backbones are responsible for semi-crystallinity, whereas the hydrophilic sulfonate ending group of side chains give their amorphous character to the ionomers [79, 212, 104, 112].

Especially because of their usage as an electrolyte membrane in fuel cells, PEM is an attractive research topic for experimental and computational chemistry. It serves as proton exchange membrane, which permits transfer of protons from cathode to anode while behaving as an insulator for electrons.

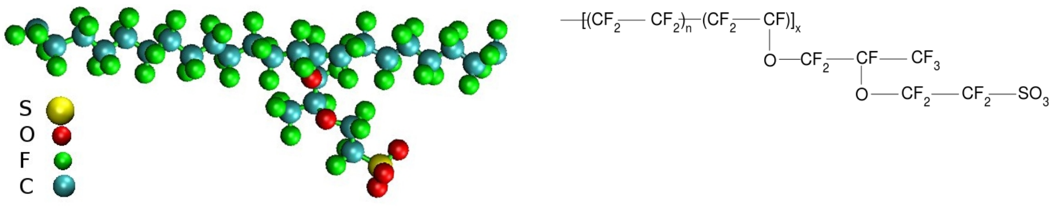

Figure 2.2: Part of a Nafion® chain: Ball-stick representation (left) and the corresponding chemical formula.

The properties of perfluorosulfonate ionomers that increase the performance of PEMFC are high proton conductivity, high electron resistivity, low water transport through diffusion and electro-osmosis, and good mechanical stability in both the dry and hydrated states. All these properties, up to some extent, depend on the morphology of ionomers. Because of its stability, power density, and lifetime, Nafion® , which is produced by Du Pont, is the most frequently used electrolyte membrane, as a benchmark in PEMFC. The chemical formula and part of Nafion® are shown in Figure 2.2.

2.2.1 Morphology of Ionomers

The exact morphology of Nafion® is still debated, and a detailed review of theories can be found in the literature [138, 108, 10, 109, 136, 88, 146, 128]. It is generally accepted that the hydrophilic and hydrophobic portions of the polymer phase-separate, and that these two phases rearrange as the membrane hydrates [93].

However different models have been proposed in order to explain the shape of the structures formed by the two phases [57, 49, 36, 53, 122, 169]. The earliest and longest-lasting model for Nafion® microstructures is that proposed by Gierke et al. in the early 1980's [57]. It was based on small-angle X-ray diffraction (SAXS) work on Nafion® at different hydration levels. According to this model, ionic clusters, which are approximately spherical in shape with a reverse micellar structure, are connected via narrow channels (approximately 1 nm in width) as shown in Figure 2.3. The selective-permeability of hydrated Nafion® is supposed to be a consequence of the presence of narrow channels. Furthermore, these narrow channels have been proposed to form interconnected pathways between the ionic aggregates that constitute the percolation network through which proton conduction takes place [41, 146].

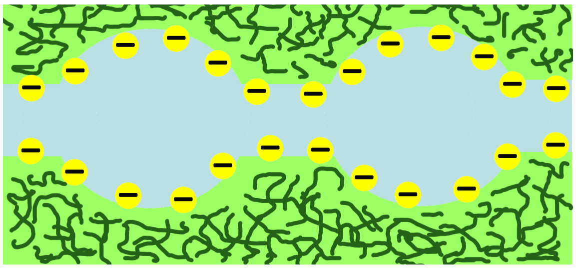

Figure 2.3: Schematic view of network cluster model: Water clusters (light blue) are connected via a narrow pore. Sulfonate groups are shown by yellow filled circles with (-), backbones of the membrane are shown in dark green.

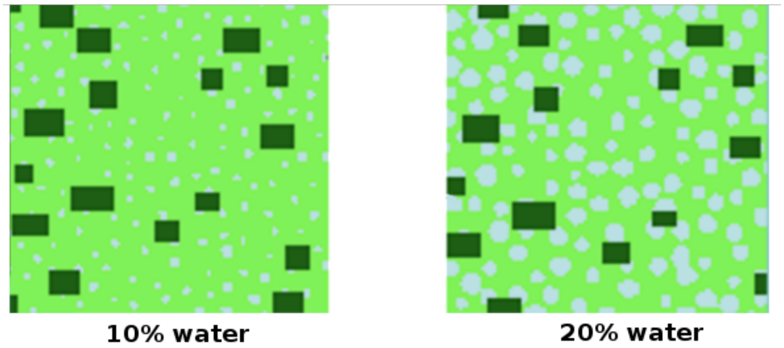

Figure 2.4: The cross sectional view of the parallel water channel model at two different hydration levels. The average diameter of the cylinders increases as hydration level increases. Dark and light green colored regions represent the crystalline and semi-crystalline regions of the membrane, respectively. Water channels are colored by light blue (reproduced from [169]).

Another model, proposed by Schmidt-Rohr et al.[169], is the parallel water channel model. According to this model, the hydrophilic side chains facilitate the formation of a water channel and the hydrophobic backbone of the polymer constructs the cylindrical wall. The crystalline and semi-crystalline regions of the structures formed by hydrophobic backbone are distinguished as well as various possible parallel water channels. For example, the average diameter of the water channels was calculated (i.e. 2.4 nm at a water content of 20 vol.%) within this model [146]. This average depends on hydration level, and increases for high water content (see Fig. 2.4).

The differences between these models become more apparent for high water content. At low water content, the existence of the narrow pores or narrow parallel channels is accepted in Grierke's and Schmidt-Rohr's models , respectively.

2.2.2 Hydration level

Significant differences are observed for the structural and dynamical properties of the membrane when the hydration level changes. For example, the structure of the water channels, their size and radius, and the spacing between hydrophilic groups are affected by changing the hydration level. These structural changes and the reorganization of the membrane due to the hydration are directly related to the proton conductivity, which increases proportionally with water content (see Fig. 2.5).

The possible evolution of the ionomer from the dry condition to a fully hydrated state (solution) has been described in the literature [52, 24, 107, 35]. Depending on the model and methodology used, there were some minor differences in describing the swelling of the membrane, for

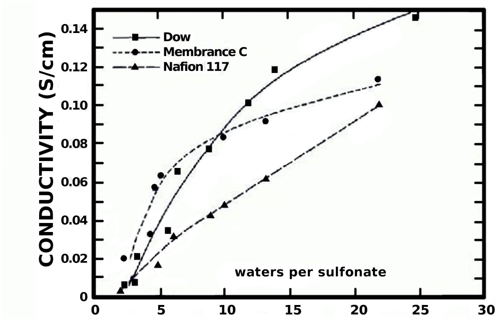

Figure 2.5: Proton conductivity dependency of the ionomers on the water content (λ) (reproduced from [62]).

example, the hydration level of the percolation threshold. However, the main aspects of the swelling process of the membrane, in general, may be explained as follows: At very low water content, $\lambda < 3$, which is defined as the number of water molecules per sulfonate group, only isolated small water clusters are observed around hydrophilic groups of the membrane. Protons are bonded to sulfonate groups or shared between water and sulfonate groups [42]. Nafion® behaves like an insulator, and proton conduction is not observed.

At low water content, λ between 3 and 5, the water molecules are still influenced by the sulfonate groups on the inner surface of the channels and cluster to form solvation shells [34]. The protons are dissociated and observed as hydronium ions. However, the sulfonate groups interact strongly with the hydronium ions and sulfonate traps may exist in a form such that a single hydronium ion is surrounded by multiple sulfonate anions [33, 83]. Hence, sulfonate trapping is expected to greatly hinder the mobility of the dissociated protons. As λ increases from 3 to 5, the water clusters become increasingly bigger and the channels become broader [112, 213]. This small amount of increase in the water content also decreases the effect of sulfonate groups on hydronium and allows the onset of the proton mobility.

At moderate water content, λ between 5 and 7, a morphological transition occurs in the Nafion® membrane. The water clusters and channels are further expanded and become partially interconnected. Therefore, continuous pathways become available for proton conduction. Hence, the proton conductivity increase dramatically [213]. The effect of sulfonate groups on hydronium is reduced and the sulfonate spacing increases, which results in vanishing of the sulfonate traps. A possible effect of sulfonate groups spacing on the proton conductivity is shown in Fig. 2.6. This also leads to the possible formation of proton complexes in form of Eigen or Zundel cations, in which protons are shared between water molecules (see Fig. 2.10).

Finally, for λ from 7 to a water-saturated hydration level, the average distance between sulfonate groups becomes larger due to Nafion® swelling, and a well-developed percolated network is formed. The proton conductivity shows an apparently monotonic increase and finally approaches a value comparable in magnitude to that of bulk water [213].

2.3 Proton Transfer in Ionomers

The proton conduction in ionomers occurs as a result of proton transfer through the water channels inside the membrane. The transport of an excess proton relies on a combination of vehicular and structural transports

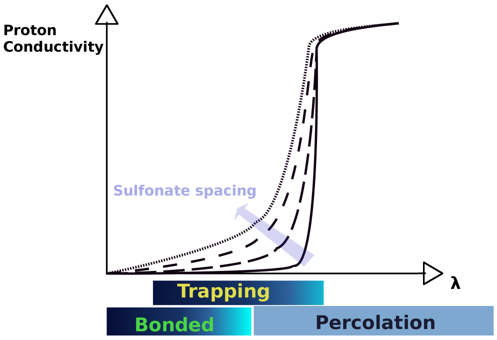

Figure 2.6: Possible dependency of the proton conductivity on hydration level for various average sulfonate spacings: Increasing sulfonate groups spacing (shown by the direction of the arrow) has an effect on the onset of proton mobility at low water content. The conductivity increases rapidly at high hydration level. At low water content, protons are bonded to sulfonate groups or hydrated protons are trapped by sulfonate groups. Larger sulfonate spacing even at low hydration level gives rise to increased proton conductivity.

[40].

2.3.1 Vehicular transport

The vehicular mechanism is the classical diffusion of the hydronium, H_3O^+, whose contribution to the overall proton conductivity is attributed to be dominant at low humidity level in the ionomer.

The proton conductance of the ionomer with low water content deviates from that of bulk water. This is mainly caused by the narrow channels, which are more probable to exist at low water content. The effect of the confinement on water is increased by closer spacings of the hydrophilic groups. However, the strength of the confinement is reduced at high water content, which leads to the water channels becoming larger. Therefore, the proton mobility in the ionomer at high humidity level approaches to the one in bulk aqueous solution.

The proton mobility in water is approximately five times higher than the mobility of light cations (e.g. Na^+) [105]. The difference can not be explained only by the vehicular mechanism. Hence, it requires the contribution of another type of mechanism, which is the structural transport [204, 1, 130, 29, 45, 108].

2.3.2 Structural transport

Structural transport of an excess proton involves the Grotthuss mechanism, which is based on the transfer of an excess proton from the hosting water molecule to the neighboring water molecule (see Fig. 2.7).

$$H_3O^+ + H_2O \leftrightharpoons (H_2O \cdots H \cdots H_2O)^+ \leftrightharpoons H_2O + H_3O^+$$

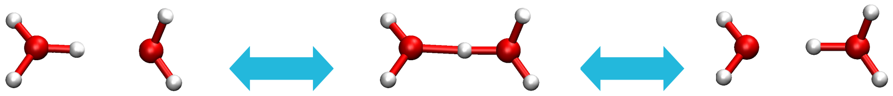

Figure 2.7: Proton transfer between hydronium and water molecules

In such a process, the mechanism governing the transport of the proton depends on the nature of the hydrated proton, the number and the fluctuations of the hydrogen bonds with neighboring molecules. In bulk water, hydrated protons can be observed as hydronium (H_3O^+), Zundel ($(H_5O_2)^+$) and Eigen ($(H_9O_4)^+$) complexes (see Fig. 2.8). In a Zundel cation, a proton is shared between two water molecules. In an Eigen complex, the excess proton is hosted by a water molecule, which has three neighboring water molecules, each of which has a strong hydrogen bond to the central water molecule. Results of MD simulations and infrared spectroscopy have shown the existence and stability of these different excess proton states [105, 134, 99, 196, 78, 7, 19].

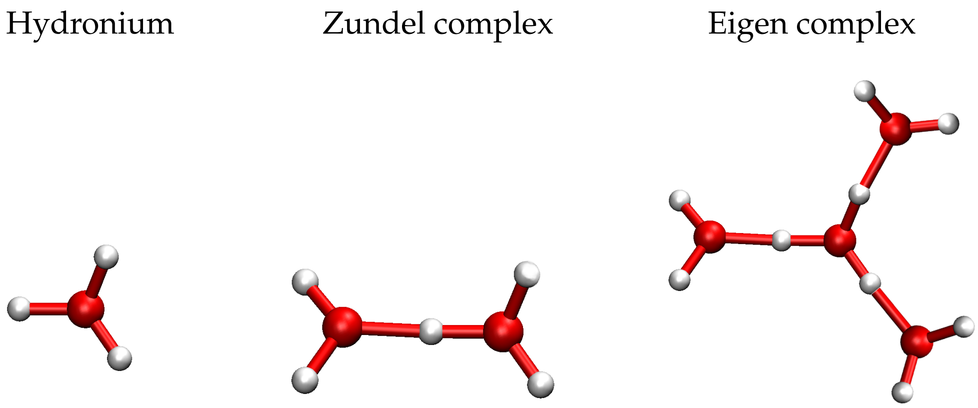

Figure 2.8: Some of the possible hydrated proton complexes: Hydronium, Zundel, and Eigen ions

Interconversions among these different hydrated proton complexes enhance the diffusion of the proton. Since this kind of reaction involves different structures of hydrated protons, it is named as structural transport. The size and shape of the solvation shell of hydrated proton complexes is strictly related to the structure of the proton complex. Any changes in the structure of the proton complex affect its solvation shell and vice versa. For example, if a Zundel ion separates and becomes a water and hydronium, then the water molecule, which was a part of Zundel ion now belongs to the solvation shell of the hydronium. It is well established that the high mobility of H^+ in water is due to structural changes, promoted by protons moving along the hydrogen bonds [190, 16, 129, 22, 21, 130]

Since this type of mechanism is based on the interaction of hydrated protons with surrounding molecules via hydrogen bonds, the structural diffusion in the ionomer pores (the contribution of the Grotthuss mechanism to the proton mobility) is much more affected by the structure of the pores and water content. This effect is more pronounced at low water content than at high water content. The low number of available water molecules and the narrow pore structure leads to the inclusion of the hydrophilic groups of the ionomers in the solvation shell of a hydrated proton complex. Therefore the hydrogen bond networks in the ionomers become more stable than the ones within bulk water [45, 25]. This limits the contribution of the structural diffusion to the proton mobility. Hence, the vehicular mechanism can be dominant at low humidity, whereas the Grotthuss mechanism dominates at high humidity, where bulk-like water clusters are more probable.

2.4 Narrow Pores of Ionomers

The morphology of ionomers at very low hydration level is different from that when it is fully hydrated. It is more probable to observe narrow-necked channels at low water content [163, 210]. Hence, the proton conductivity at low hydration level depends on the structure of narrow pores. An efficient operating PEM cell under low humidity conditions, based mainly on narrow pores, exhibits several advantages, including improvement of the electrocatalytic reactions, prevention of CO poisoning of the catalysts, and simplified water management [42, 77].

Pore diameter is proportional to water content: According to the models explaining the morphology of the membrane and the water channels, inclusion of the narrow pores is required for complete description of the proton diffusion through the ionomer [57, 169]. For example, in the network cluster model at low water content, the size of the clusters becomes smaller and its diameter decreases approximately to 2 nm. The estimated diameter of the narrow pore connecting two clusters also becomes smaller than 1 nm at low water content. A similar trend has been proposed also within the context of other morphological models, such as parallel water channels model.

Variation of the diffusion coefficient as a function of the distance from the center of the pore has been reported and it was shown that the mobility of the proton reaches the maximum value at the pore center [153]. This is also related to the influence of sulfonate groups, which decreases towards the center of the pore.

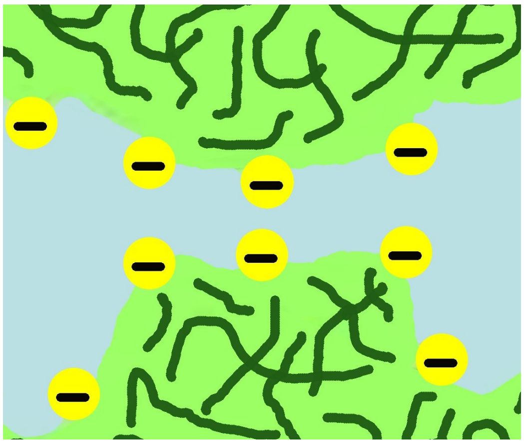

Figure 2.9: A possible narrow water channel inside ionomers: sulfonate groups are represented as yellow circles.

Narrow pores promote sulfonate traps: The sulfonate groups become closer at lower water content. This compact structure may even hinder the dissociation of the protons from sulfonate groups. Therefore, partial dissociation is observed at water content lower than 3 [185, 206]. Dissociated protons are strongly affected by short sulfonate spacing. Additionally, due to having not enough water molecules to delocalize the protons, they are forced to stay in the solvation shell belonging to multiple sulfonate groups. As a result of this compactness, close-lying sulfonate groups may behave as a trap for hydrated protons. The formation of cage-like structures similar to clathrates has also been proposed in NMR studies [136, 127]. A computational study on the mixture of water and triflate ions ($CF_3SO_3^-$) has shown that the formation of stable triflate ion-hydronium ion complexes causes low diffusion [182]. With increasing hydration, water molecules break the stability of triflate ion-hydronium ion complexes leading to enhanced diffusion and larger sulfonate spacing [182].

Narrow pores favor ice-like water structure: Strong and stable hydrogen bonds are expected as a result of close-lying sulfonate groups and a small number of water molecules. It has been proposed that even if the mobility is associated with a fluid, the derived motional activation energies are similar to those of ice [127]. This indicates a well ordered supercooled fluid consisting of hydrogen bonded water structures [127]. The energetic penalty associated with proton transfer depends on the surrounding hydrogen bond network, the state of the dissociated proton(s), and the separation between sulfonate groups [26]. A schematic diagram is presented in Fig. 2.10.

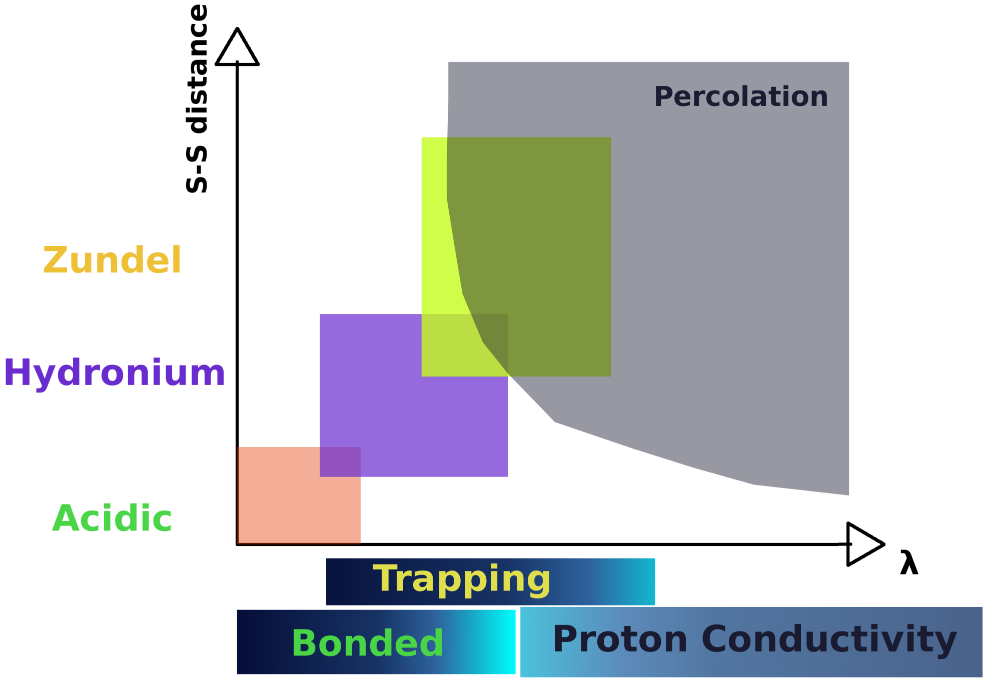

Figure 2.10: Water content is related to sulfonate spacing. The dissociation of the protons and probable state of hydrated protons depend also on both water content and sulfonate spacing. At shorter sulfonate spacing and low water content, undissociated protons are probable. As the water content increases, hydronium and Zundel cations are favored. However, multiple sulfonate groups trap the hydrated protons. At larger sulfonate spacing, Zundel cations can be trapped by multiple sulfonate groups.

Narrow pores limit the proton complex structure: Hydrated protons may have various forms in bulk-like water clusters due to the large number of available water molecules around hydrated protons. In narrow pores, however, the number of available water molecules for different forms of proton complexes is limited. For example, for an Eigen complex formation, a hydronium and three water molecules are required such that these water molecules should neither be a part of another proton complex nor be in the solvation shell of other proton complexes. Additionally, the water molecules belonging to the solvation shell of sulfonate groups can not contribute to the formation of a stable Eigen complex. From a structural point of view, the limitation stems from that the required volume for an Eigen complex can not be afforded within narrow pores.

High ratio of surface area to volume favors an irregular shape of pore structure [136, 127, 44]. However, the exact characterization of the structure of the narrow pores at the level of molecular resolution and their roles in proton mobility have not been obtained via spectroscopical techniques due to the complexity of the membrane. Indeed, the structure of the narrow pores is sensitive not only to the water content but also to many other properties, such as the length of the sidechain, the number of the sidechains on the backbone, and the functional groups of the membrane [107, 140, 170, 85, 151, 54, 52, 139, 162, 27, 3, 2, 147, 56, 148, 150, 83, 107].

Furthermore, even the preparation of the membrane affects its proton conductivity, which is related to the pore structure [136]. The high complexity and the large number of dependencies of the ionomers brings about the difficulty to investigate the narrow pore structure in advance. Therefore, molecular dynamics simulations becomes indispensable for investigating narrow pores.

2.5 Computational research on ionomers

Various computational methods are applied to investigate structural and dynamical properties of ionomers of PEMFC. The simulation methods differ in their purposes, accuracy, system size, and time scales.

Classical MD simulations with empirical potentials have been employed, for example, to study morphological changes of ionomers with water content [171, 33, 34], water cluster formation [203, 32], and for evaluation of structural models of ionomers [38, 101, 169, 128]. It has been shown, for example, that the formation of narrow necked water channels is possible and that in the vicinity of the percolation threshold proton transfer occurs most likely through these narrow pores [203]. Most of the classical MD simulations of PEM have utilized the classical hydronium cation models (or light cations Na^+ or K^+), in which proton hopping by the Grotthuss mechanism was not allowed.

Simulations, which are based on empirical valence bond (EVB) interaction potentials [98, 176, 28, 175, 158, 157], reactive force fields [197, 81] and stochastic hopping algorithms [173, 172] are not hindered by this limitation and can include transport of protons via the Grotthuss mechanism. The transition state for proton transfer obtained usually from *ab initio* calculations is used to define the reaction pathways. However, the main disadvantage is that these methods only allow predefined reaction pathways. Therefore, the contribution of unpredicted chemical reactions to dynamical and structural properties can not be taken into account. Furthermore, these methods can not provide reliable answers at very low water content, where protons interact strongly [86].

Computational studies based on First Principle methods do not suffer from these difficulties and can provide reliable answers even at low water content, since any molecular structure is allowed and the Grotthuss mechanism is inherently included. One needs to take into account, however, that the number of atoms is limited due to the computational expense. Therefore, this approach requires modeling of pores. In the following chapter, *ab initio* molecular dynamics is elaborated.

It has been employed, for example, to find out the optimized structure of hydrophilic side chain models (i.e. CF_3SO_3H+$(H_2O)_\lambda$) with respect to changing hydration level [147, 149, 148, 150, 206]. It has been found that protons start dissociating from the sulfonic acid group when the number of water molecules per sulfonate group is three.

Various models based on sulfonate groups were investigated by *ab initio* density functional theory. For example, in order to address the questions regarding the optimum sulfur-sulfur distance for the proton dissociation step, a periodic surface layer of CF_3-SO_3H and CF_3-O-CF_2-CF_2-SO_3H entities has been used [166, 141, 165]. This distance was found to be between 6 and 7 Å and depends somewhat on the length of the chain.

Another example for an ionomer pore model, which has been investigated by *ab initio* methods, is based on a sulfonated carbon nanotube containing small amounts of water [70, 71]. It was observed that fluorination of the nanotube (hydrophobicity) affects the fraction of the observed proton complexes. As stated before, *ab initio* MD studies have predicted the formation of stable triflate ion-hydronium ion complexes and shown that such formation causes low diffusion and possibly hinders the onset of the proton transfer at low water content [182].

Chapter 3

Methodology

Various experimental techniques are applied to investigate the structure and the proton transfer in polymer electrolyte membrane, among them small-angle X-ray scattering (SAXS), nuclear magnetic resonance, neutron scattering, infrared spectroscopy etc. Despite of the fact that many of these techniques can provide information for a wide range of length and time scales down to molecular resolution, an atomistic level description of the system, which is necessary for proton transfer in narrow pores of ionomers, is missing.

At the atomic scale, molecular dynamics (MD) is an indispensable tool to provide microscopic information. MD is one of the most widely used techniques to sample the phase space of a system of particles and provides necessary information about structural and dynamic processes. In general, molecular dynamics describes the time-dependent behavior of a system of particles. The coordinates of individual atoms are determined according to the equations of motion, which are the governed by their interactions.

The traditional way of using molecular dynamics is the "classical MD" approach which makes use of pre-defined interaction potentials. These interactions are represented by analytical functional forms. This simplification makes the classical MD an appropriate tool to study systems containing up to millions of atoms for thousands of nanoseconds of simulation time (depending on the computational resources). Compared to *ab initio* MD, the number of atoms and the simulation time achievable by classical MD simulations are both larger and longer than those achievable by *ab initio* MD, using the same computational resources. Therefore, within PEMFC research, the classical MD is usually preferred for investigating the morphology of ionomers [101, 128].

However, the inherent nature of the proton transfer (Grotthuss mechanism), where the bonds are broken and re-formed, limits the classical molecular dynamics approaches. A number of reactive force field schemes, where some sort of prior knowledge about the process being studied is required, have proven to be successful for describing aqueous proton transfer processes [171]. Coarse-graining methods, where a group of molecules is treated as a single particle, can be applied together with smoothed reactive force fields. This combination prolongs the length and time scale of the simulations related to proton transfer in PEMFC [97].

Another way to overcome the limitation of the classical approach is to use *ab initio* molecular dynamics (AIMD), in which the electronic structure of the system is calculated. No prior knowledge about chemical reactions in the system is required. There are various ways to solve the electronic structure problem in the context of MD simulations. The most popular among them are the Born-Oppenheimer MD and the Car-Parrinello MD. The CPMD and CP2K program packages are used for Car-Parrinello and Born-Oppenheimer molecular dynamics, respectively [30, 121, 120].

In the following, the theoretical methods relevant for the MD simulations discussed in this work are briefly explained. Basics and techniques of molecular dynamics are well documented in many textbooks and lecture notes [4, 132, 133, 31, 194, 195, 188, 161, 59].

3.1 Classical Molecular Dynamics

In this work, classical MD is applied to obtain an equilibrated pore structure. Starting from an almost equilibrated system, which has approximately a proper density, reduces the computational cost of AIMD. Therefore classical MD is used to prepare the initial configurations used as input for the AIMD simulations (see Chap. 4). The Gromacs program package [80] is employed together with force field parameters for ionomer, hydronium and water are used and adapted from [176]. These are shown in the appendix (A).

In classical MD, interactions of particles are described approximately by a set of simplified potentials. In such potentials, a bond between two atoms of a molecule can be represented by a classical harmonic oscillator. The potential related to the stretching of the bond between the *i*th and *j*th atoms depends on the force constant, k, the optimal bond length, r_0, and the distance of these atoms, r_{ij}. It is shown in Equation 3.1.

$$U_{ij}(t) = \frac{1}{2}k(r_{ij}(t) - r_0)^2 \tag{3.1}$$

A complete set of the parameters of simplified functions is called a "force field". It includes both bonded and unbonded interactions. Bonded parameters, which belong to intramolecular interactions, cover the stretching, bending and torsional degrees of freedom of molecules. Non-bonded interactions, due to van der Waals interactions (dispersion attraction and short range Pauli repulsion), are often described through the Lennard-

Jones potential functions [176].

$$U = U_{stretching} + U_{bending} + U_{torsion} + U_{non-bonded} \tag{3.2}$$

A cutoff distance is usually required for the calculation of non-bonded interactions. Depending on the chosen force field, some of these parameters may be omitted. For example, charges of some type of atoms are set to zero, so that these atoms are treated as neutral.

The equations of motion are then solved by using classical physics via the potentials described in the force field. The force, which is proportional to the acceleration acting on the atom i, equals to the negative gradient of the sum of the interaction potentials.

$$M_i \ddot{r}_i(t) = -\frac{\partial}{\partial r_i} U(t) \tag{3.3}$$

Velocities and coordinates of atoms are calculated at each time step using Newton's equations of motion (Eq. 3.3), in which one of the most commonly used method, the Velocity Verlet algorithm is employed [202].

The number of particles in the simulation box is restricted in MD simulations. Periodic boundary conditions make the boundary effects small and allow simulation of a system which is essentially infinite [160, 159]. This allows the linking of MD simulations to macroscopic quantities.

Some of the macroscopic quantities can be controlled during the simulation, such as the temperature and the pressure. The temperature, which is related to the average of the instantaneous kinetic energy of the atoms, can be managed to have a certain value by using a thermostat. The pressure can be modified by using a barostat [13, 145, 5]. A thermostat leads a system of particles to have an approximate distribution of velocities at the target temperature. A barostat enables the system to have a desired pressure. Both the thermostat and the barostat are used to generate an equilibrated system for the pore models, which are explained in Sections 4.2.1 and 4.3.1.

Positions of atoms can also be restrained by defining an extra potential for some chosen coordinates of the atoms. Equation 3.4 shows this kind of extra potential applied on the coordinates of the atom i, with initial coordinates $r_i(0)$

$$\tilde{U}_i(t) = \frac{1}{2}\tilde{k}(r_i(t) - r_i(0))^2 \tag{3.4}$$

Position restraints are used within this study in order to keep the pore structure cylindrical (see Section 4.2.1).

3.2 *ab initio* Molecular Dynamics

"*ab initio*" is a latin phrase meaning "from the beginning", or "from the first principle". It refers to computational chemistry methods which make use of fundamental laws of physics and do not require other assumptions about the system of particles in order to calculate the interaction between atoms. *ab initio* methods can provide highly accurate results for determining the interactions between particles as well as unbiased dynamics of particles. This allows the study of chemical reactions and determination of molecular structures. This is achieved by solving the Schrödinger equation (Eq. 3.5), for which an exact analytical solution is not possible for more than two particles, but approximate numerical solutions exist.

$$\mathcal{H}\tilde{\Psi} = E\tilde{\Psi}. \tag{3.5}$$

Here $\mathcal{H}$ is the Hamilton operator acting on the total wave function, $\tilde{\Psi}$, which contains all the information about the system of electrons and ions. The total energy, E, is the eigenvalue of the total wavefunction. The Hamiltonian, $\mathcal{H}$, is the sum of the kinetic energy of electrons and ions and the sum of the potential energy of all possible interactions: electron-nuclear attraction (V_{eN}), electron-electron repulsion (V_{ee}), and nuclear-nuclear repulsion (V_{NN}) (Eq. 3.6).

$$\mathcal{H} = T_{\mathrm{e}} + T_{\mathrm{N}} + V_{\mathrm{eN}} + V_{\mathrm{ee}} + V_{\mathrm{NN}} \tag{3.6}$$

3.2.1 Born-Oppenheimer Approximation

The first basic approximation required for solving the Schrödinger equation is the Born-Oppenheimer approximation. The mass difference between an electron and a nucleus affects their dynamics, such that the nuclei moves very slowly with respect to electrons. This difference allows to consider the dynamics of slow nuclei and fast electrons separately. The limiting case is to consider the electrons moving in the field of fixed nuclei (adiabatic or clamped-nuclei approximation). This leads to the Born-Oppenheimer approximation, which allows separation of the total wavefunction $\tilde{\Psi}(\mathrm{r}, \mathrm{R})$ into nuclear (slow) $\chi(\mathrm{R})$ and electronic (fast) $\Psi(\mathrm{r}; \mathrm{R})$ parts.

As a result of the Born-Oppenheimer approximation, the dependency due to the coordinates of all nuclei (denoted collectively as R) is included only parametrically in the electronic Schrödinger equation (Eq. 3.7).

$$\mathcal{H}_{\mathrm{elec}}(r; \mathrm{R})\Psi(r; \mathrm{R}) = E(\mathrm{R})\,\Psi(r; \mathrm{R}) \tag{3.7}$$

The molecular wave function, $\Psi(r; \mathrm{R})$ depends explicitly on the $3n$ coordinates of all n electrons (denoted collectively as r). The total energy, E(R) depends parametrically only on the nuclear positions. In the Hamiltonian $\mathcal{H}$ (Eq. 3.8), the term due to nuclei-nuclei repulsion, V_{NN} becomes a constant, and is included as a shift in the total energy. Therefore, the electronic Hamiltonian, $\mathcal{H}(r; R)$, consists of the following contributions: kinetic energy of electrons, electron-nuclear attraction, electron-electron repulsion, and nuclear-nuclear repulsion.

$$\mathcal{H}_{\mathrm{elec}} = T_{\mathrm{e}} + V_{\mathrm{eN}} + V_{\mathrm{ee}} \tag{3.8}$$

The explicit form of electronic Hamiltonian in atomic units is expressed as

$$\mathcal{H}_{\mathrm{elec}}(r; \mathrm{R}) = -\frac{1}{2}\sum_{i} \nabla_i^2 - \sum_{i,I} \frac{\mathrm{Z}_I}{|r_i - \mathrm{R}_I|} + \sum_{i<j} \frac{1}{|r_i - r_j|} \tag{3.9}$$

where $\nabla_i^2 = \frac{\partial^2}{\partial x_i^2} + \frac{\partial^2}{\partial y_i^2} + \frac{\partial^2}{\partial z_i^2}$, is the Laplacian, Z_I are the charges of the nuclei, and r_i and R_I are the coordinates of electrons and nuclei, respectively. The wavefunction of the electrons is then calculated using this electronic Hamiltonian.

Even though the Born-Oppenheimer approximation reduces the complexity of the problem to the electronic Hamiltonian (Eq. 3.8), its solution is not straightforward. Approximate solutions are provided by various schemes such as Hartree-Fock (HF), configuration interaction (CI), coupled cluster (CC), and density functional theory (DFT). These schemes are applied in order to find the converged wavefunction, which is an approximate eigenfunction of the Hamiltonian.

As the potential surface depends on the choice of an appropriate force field in classical MD, it appears in *ab initio* MD as choosing an approximation method for solving the Schrödinger equation. Hence selecting a proper approximation method is the critical decision making step, which is related with the purpose of simulations.

As far as the number of atoms, the type of molecules, and possible chemical reactions in a model of ionomer pores are concerned, DFT turns out to be the best candidate for MD simulations with respect to available computer resources. Before explaining DFT, some additional requirements and approximations common to most of these schemes are briefly introduced in the following.

For simplicity, the spin of electrons is omitted in the above description of the wave function. However, including the spin of the electrons is indeed necessary in order to describe correctly the antisymmetric wave function, which should obey the Pauli exclusion principle. The energy is lowered due to the antisymmetrization requirement. This energy difference is called the "exchange energy".

For example, by implying the independent electron approximation, the total wave function can be written in the form of an antisymmetrized product of single-electron wave functions as

$$\Psi(r_1, s_1; r_2, s_2; ...) = \frac{1}{\sqrt{N!}} \hat{A}[\psi_1(r_1, s_1)\psi_2(r_2, s_2) \ldots \psi_n(r_n, s_n)] \tag{3.10}$$

where Â is the antisymmetrization operator [50]. The antisymmetrization of the above (de-)composition leads to the Slater determinant, which is a generalized form of the equation (Eq. 3.10) and consists of a linear combination of all possible permutations of products of orthonormal single-electron wave functions $\psi_i(r, s)$ [6]. A single Slater determinant fulfills the requirement of the antisymmetrization, but the instantaneous electron-electron correlations are not included by using only one determinant. This missing correlations have an effect on the total energy, this difference is referred to as the "correlation energy".

In order to increase the computational efficiency, a single-electron wave function is approximated by a set of computationally-efficient basis functions, which is referred to as "basis set". Basis sets are named according to the type of the basis functions, such as Gaussian-type and Slater-type. The basis sets can be composed of the minimum number of basis functions required to represent all of the electrons (minimal basis sets), or more than one basis function can be used for one "orbital" (double-zeta, triple-zeta, and etc.). In addition to localized, atom-centered basis sets, a finite number of plane waves, limited by a cutoff energy, can also be used to represent single-electron wave functions.

An additional technique for decreasing the computational cost is using pseudo potentials. Since chemical properties of a molecule depend mainly on the valence electrons, an effective potential can be used to describe the core electrons. This reduces the number of electrons in the calculation. Usually only valence electrons are included for the calculation. This is especially useful for plane-wave basis sets, since oscillations in the wavefunctions due to the core electrons require a very high energy cutoff. Therefore plane waves are often used in combination with pseudo-potentials.

Lastly, i.e in HF, the optimum of these single-electron wave functions (molecular orbitals) is calculated by variationally minimizing the total energy. When this iterative minimization calculation procedure reaches the desired accuracy, the resulting wave functions are converged and consistent with their own electric field.

3.2.2 Density Functional Theory

An efficient scheme providing an approximate solution to the electronic Hamiltonian is the density functional theory (DFT), which makes use of a physical observable, the electron density rather than the many-electron wave function in order to find the ground state energy [171]. Using the electron density as a fundamental quantity reduces the number of dependencies dramatically to only 3 spatial variables. Therefore, it is one of the most commonly used and efficient methods for the investigation of molecular systems consisting of large or many molecules. It was originally intended for band structure calculations of crystalline solids and also proven to be successful for describing proton transfer in various media [189, 190, 191, 178, 135, 134, 192, 77].

In DFT, the total energy, E, of a many-electron system in the presence of an external potential, $\mathrm{V}(r; \mathrm{R})$ (for given nuclear coordinates, R), is expressed as a functional of the total electron density, $\rho(r)$. The total energy functional can be defined as

$$E[\rho(r)] = T[\rho] + U[\rho] + E_{xc}[\rho] \tag{3.11}$$

where $T[\rho]$ is the kinetic energy term, $U[\rho]$ is the electrostatic potential (Coulomb) term, and a many-body term, $E_{xc}[\rho]$, which is due to the exchange and correlation of electrons.

The variational principle is applied in order to find the minimum of the total energy functional, at which its partial derivative with respect to the electron density is zero (Eq. 3.13). The variation in electron density is subject to the constraint

$$\int d^3r\, \delta\rho(r) = 0 \tag{3.12}$$

since the number of electrons is constant. The minimum value of the total energy functional corresponds to the ground state energy, E_0, which is, hence, uniquely determined by the ground state electron density, $\rho_0(r)$ [82].

$$E_0 = E[\rho_0(r)] \leq E[\rho(r)]; \quad \left.\frac{\delta E[\rho(r)]}{\delta\rho(r)}\right|_{\rho_0} = 0 \tag{3.13}$$

The challenge in DFT is the design of accurate functionals, and, specifically, the difficulties arise from determining $T[\rho(r)]$ and $E_{xc}[\rho(r)]$ [171]. The reformulation of DFT by Kohn and Sham provides an efficient way for overcoming some of these difficulties [102]. The electron density, $\rho(r)$, is considered as a sum of non-interacting electron densities.

$$\rho(r) = \sum_k |\phi_k(r)|^2 \tag{3.14}$$

where ϕ_k is the Kohn-Sham orbital. Indeed the energy functional of the molecular system is precisely the same as that of a non-interacting electron system in which the electron moves in an effective external potential [50].

$$V_{\text{eff}}(r) = V(r) + \int \frac{\rho(r')}{|r - r'|} dr' + V_{xc}(r) \tag{3.15}$$

where the exchange-correlation potential, $V_{xc}(r)$, is defined by

$$V_{xc}(r) = \frac{\delta E_{xc}[\rho(r)]}{\delta \rho(r)} \quad . \tag{3.16}$$

Therefore, the kinetic energy can be evaluated exactly through the self-consistent set of Kohn-Sham equations (see Eqs. 3.14 and 3.17).

$$\left(-\frac{1}{2}\nabla^2 + V_{\text{eff}}(r)\right)\phi_k(r) = \epsilon_k \phi_k(r) \tag{3.17}$$

where the eigenvalue, ϵ_k, is the solution of the KS equation. Therefore, by using the kinetic energy, the total energy is expressed as

$$E = \sum_k \epsilon_k - \frac{1}{2}\int \frac{\rho(r)\rho(r')}{|r - r'|}\, dr\, dr' \; - \int V_{xc}(r)\,\rho(r)\, dr \; + \; E_{xc}[\rho(r)] \tag{3.18}$$

The Kohn-Sham equations resemble the Hartree equations, only that, in the later, the correlation energy, E_c ($=E_{xc} - E_x$), is not involved. Therefore, the practical treatment is interpreted as a variant of HF theory. The complexity of the electronic Hamiltonian, consisting of many electrons, is reduced to the determination of the unknown exchange-correlation energy, $E_{xc}[\rho(r)]$ [50].

Local density approximation (LDA): The simplest approximation for the exchange-correlation energy, $E_{xc}[\rho(r)]$, is based on the exchange-correlation energy per particle of a uniform interacting electron gas of density, $\epsilon_{xc}[\rho(r)]$.

$$E_{xc}^{\mathrm{LDA}}[\rho(r)] = \int \epsilon_{xc}[\rho(r)]\rho(r)dr \tag{3.19}$$

where $\epsilon_{xc}[\rho(r)]$ is known from many-body theory [208, 18]. As a result of LDA (Eq. 3.19), the exchange-correlation energy, E_{xc}, and, hence, the effective potential, V_{eff}, depends only on the electron density, $\rho(r)$, which leads to the approximation called local.

For metallic and strongly delocalized systems with approximately constant electron densities, the Kohn-Sham orbitals in the LDA approximation are surprisingly close to HF orbitals, although the nonlocal nature of the exchange terms is neglected in the LDA [171]. The reason is that the homogeneous electron gas is a better description for a system with slowly varying electron densities than for one with strongly varying electron densities.

Furthermore, including spin states of the electrons leads to the local spin density approximation (LSDA), which is an expanded version of LDA. The exchange-correlation energy here is described as

$$E_{xc}^{\mathrm{LSDA}}[\rho_{\uparrow}(r), \rho_{\downarrow}(r)] = \int \epsilon_{xc}[\rho_{\uparrow}(r), \rho_{\downarrow}(r)]\ (\rho_{\uparrow}(r) + \rho_{\downarrow}(r))\ dr \tag{3.20}$$

where $\rho_{\uparrow}(r)$ and $\rho_{\downarrow}(r)$ represent the electron density for spin-up and spin-down, respectively. LSDA allows magnetic properties to be included in the simulations.

Generalized gradient approximation (GGA): A significant improvement in the accuracy of DFT is provided by including the gradient of the electron density in the exchange and correlation energy. The generalized gradient approximation, which is, thus, also termed gradient-corrected, is based on partial inclusion of the nonlocal nature of the exchange terms. Therefore, not only the electron densities but also their gradients are taken into account in the description of the exchange-correlation energy, which is shown in Equation 3.21 by including the electron spin densities and their gradients.

$$E_{xc}^{GGA}[\rho_\uparrow(r), \rho_\downarrow(r)] = \int f(\rho_\uparrow(r), \rho_\downarrow(r), |\nabla\rho_\uparrow(r)|, |\nabla\rho_\downarrow(r)|)dr \qquad (3.21)$$

Functionals are usually labeled by the initials of the authors and, additionally, the publication year of the article, in which the functionals were introduced. Popular exchange-correlation GGA functionals, which are also used in this work, include BLYP, PBE, and HCTH [11, 114, 155, 74]. The exchange and correlation contributions can be combined together from different type of functionals. For example, in BLYP, the gradient-corrected correlation functional LYP [114] are used in combination with the Becke exchange functional [11].

Unfortunately, a functional which is successful for describing some dynamical properties of a system may underestimate (or overestimate) the binding energies, or some other quantities. Therefore, comparing the results of simulations based on different functionals is not straightforward. There is no systematic way of selecting the "best" functional but comparing them in a try-and-error procedure or by making use of previous studies.

The functionals used in this work are selected to be among the most commonly used ones, which are appropriate for studying a molecular system including water and ionomers [90, 177, 183, 67, 193].

An even more pragmatic type of approximation is the introduction of hybrid functionals, such as, B3LYP and X3LYP. They include the Hartree-Fock or full exact exchange via a fixed mixing parameter in addition to the standard GGA terms. They are useful to find the optimized structure of small molecular system [196, 85, 19]. Furthermore, meta-GGAs, functionals including higher-order density gradients or the local kinetic energy density, have also been suggested [156, 181, 180]. Unfortunately, these implementations are still computationally too expensive to be applied for molecular dynamics.

3.2.3 Equations of motion in *ab initio* molecular dynamics

The trajectory of the ions i.e., the time series of the nuclear coordinates ($R_I(t)$), is the solution of the equations of motion. Depending on how the equations of motion are solved, the AIMD simulations can be classified into two categories: Born-Oppenheimer molecular dynamics (BO-MD) and extended Lagrangian molecular dynamics.

BO-MD requires a fully converged electronic structure for each time step of the trajectory. The self consistent convergence procedure for the electronic structure, based on Kohn-Sham DFT, is explained in Section 3.2.2. Whereas the extended-Lagrangian-based molecular dynamics, for example, the Car-Parrinello (CP) MD, does not require the full convergence of the electronic structure at each time step. Once the wave function is converged, then it is treated together with the nuclei as a dynamic variable of the extended Lagrangian, which requires an appropriate adjustment of a fictitious mass and thus the time scales for the electronic system. Both the electronic and nuclear systems can be propagated satisfactorily with Lagrangian equations of motion, without the extra work of converging the wavefunction at each step [168].

3.2.3.a Born-Oppenheimer Molecular Dynamics

As a result of the Born-Oppenheimer approximation, the dependency of the electronic structure on the nuclear coordinates is reduced only to a parametric dependency, in which the potential due to the nuclei can be treated as an external potential. Thus, the electronic structure calculation turns to a static problem with the given set of "fixed" nuclear coordinates. In the BO-MD, the electronic and nuclear structures are incorporated into the BO Lagrangian.

$$\mathcal{L}_{\mathrm{BO}} = \frac{1}{2}\sum_{I}^{\text{nuclei}} M_I \dot{\mathbf{R}}_I^2 - \min_{\{\phi_i\}} E_{\mathrm{KS}}\left[\{\phi_i\}, \{\mathbf{R}_I\}\right] \tag{3.22}$$

where the Kohn-Sham energy functional, E_{KS}, is restricted to the orthogonality of the KS orbitals, ($\delta_{ij} = \langle\phi_i|\phi_j\rangle$). The converged electronic structure energy is used as a potential, whose variation with respect to the nuclear coordinates equals to the force on the nuclei (see Eq. 3.23). The classical equations of motion for ions, deduced from BO Lagrangian, is expressed as:

$$M_I \ddot{\mathbf{R}}_I = -\nabla_I \left(\min_{\{\phi_i\}} E_{\mathrm{KS}}\left[\{\phi_i\}, \{\mathbf{R}_I\}\right] \right) \tag{3.23}$$

where the minimization is constrained to the orthogonal sets of KS orbitals, $\{\phi_i\}$. The nuclei are propagated by using this equations of motion to the new coordinates at the next MD time step. The new nuclear coordinates are then used again to calculate the converged electronic structure and the procedure is repeated.

3.2.3.b Car-Parrinello Molecular Dynamics

Car-Parrinello molecular dynamics (CP-MD) is based on the revolutionary idea of R. Car and M. Parrinello about keeping the electrons (wavefunction) in the ground state by fictitious dynamics [17]. The computational cost, which is required for the wave function optimization at each time step in BO-MD, is reduced in the CP-MD due to this fictitious dynamics, which makes use of the adiabatic separation between the nuclear (slow) and electronic (fast) dynamics [183, 161, 142, 113, 17].

The extended Lagrangian, which governs the fictitious dynamics, proposed by Car and Parrinello, is shown below.

$$\mathcal{L}_{\mathrm{CP}} = \frac{1}{2}\sum_{I}^{\text{nuclei}} M_I \dot{\mathbf{R}}_I^2 + \frac{1}{2}\mu \sum_{i}^{\text{orbitals}} \langle \dot{\phi}_i | \dot{\phi}_i \rangle - E_{\mathrm{KS}}\left[\{\phi_i\}, \{\mathbf{R}_I\}\right] \tag{3.24}$$

where $E\left[\{\phi_i\}, \{\mathbf{R}_I\}\right]$ is the Kohn-Sham energy density functional and μ is the fictitious mass, a parameter assigned to the orbital degrees of freedom. The fictitious dynamics relies on the use of this parameter, μ, which must ensure that there is very little energy transfer between nuclei and electrons, which is required to ensure the adiabaticity.

The equations of motion, calculated by applying the Euler-Lagrange equations on the Lagrangian (Eq. 3.24), can be expressed for the nuclear system as

$$M_I \ddot{\mathbf{R}}_I = -\nabla_I \, E_{\mathrm{KS}} \left[\{\phi_i\}, \{\mathbf{R}_I\} \right] \tag{3.25}$$

and for the electronic system as

$$\mu \ddot{\phi}_i = -\frac{\partial E_{\mathrm{KS}} \left[\{\phi_i\}, \{\mathbf{R}_I\} \right]}{\partial \phi_i^*} + \sum_j \Lambda_{ij} \phi_j \tag{3.26}$$

where Λ_{ij} are the Lagrange multipliers which impose the orthogonality of the Kohn-Sham orbitals.

These electronic orbitals should adiabatically follow the motion of the ions, performing only small oscillations about the electronic ground state [171]. The adiabatic separation between the electronic and nuclear subsystems depends on the fictitious mass [132, 133]. Depending on the MD simulation, an appropriate range of the fictitious mass is between 400 and 800 a.u. in order to ensure the adiabaticity.

Once the electronic structure has been converged, both the electronic and nuclear subsystems can propagate concurrently in the CP-MD simulation, as long as the coupling between them is small [188]. The electrons do not deviate much from the ground state and stay close to the Born-Oppenheimer surface. Therefore the trajectory extracted from a CP-MD simulation is comparable to a trajectory from a BO-MD simulation.

Dispersion correction The long-range van der Waals interactions resulting from dynamical correlations between fluctuating charge distributions can not be predicted correctly by the functionals in DFT. To account for these long-range interactions, pragmatic methods have been proposed [64, 65, 61, 186]. For example, in the Grimme approach, the conventional

Kohn-Sham energy is corrected by adding a semi-empirical dispersion potential. These corrections might give rise to influences on the structural and dynamical properties of the molecular system. These differences depend on the functionals. For example, including vdW interactions in the PBE functional has little influence on both structural and dynamical properties of water [119, 95]. On the other hand, dispersion corrections with the BYLP functional have been shown to lead to a highly mobile water structure in better agreement with experimental data than the one predicted by the bare BLYP functional [119, 95].

Chapter 4

Models and Simulations

As stated in Section 2.5, *ab initio* molecular dynamics (AIMD) is appropriate for investigating proton transfer e.g. in the narrow ionomer pores of interest here. Because, within AIMD, the Grotthuss mechanism is involved without pre-defined molecular structures and reaction path ways. However, it requires modeling of narrow pores in order to have a feasible simulation. Such kind of molecular system should include as small as possible a number of atoms and thus simulation cells for the reason of computational efficiency. The computational models should include properties of the narrow pores appropriate to the suggested models based on experimental and computational research (see Sec. 2.2.1 and Sec. 2.4).

The essential features of the narrow ionomer pore models for AIMD The protons, which are the charge carriers, are transferred, when the fuel cell is operated as a power generator, through the water channels of the ionomer (Sec. 2.1). The proton conductivity depends on the structure of these channels, which globally depends on the water content of the ionomer: the pores are known to become narrow with decreasing water content (Sec. 2.2). The interactions between the sulfonate groups and the water molecules become relatively more important at low hydration levels, since a smaller number of water molecules is included and the spacing between sulfonate groups is shorter than the one at high hydration levels (Sec. 2.4). The characteristics of such narrow pores in an ionomer should thus be amenable for a modeling effort reflecting its main characteristics; the spacing between the sulfonate groups and the hydration level (the number of water molecules per sulfonate group).

The spacing between the sulfonate groups and the length of the polymer side-chains affect the global morphology of the ionomer. However, the investigation of the proton transport including the morphological changes is presently beyond the scope of *ab initio* molecular dynamics. The large number of atoms, the resulting large simulation boxes and the long simulation times required also preclude the naive usage of this method. Therefore, simplified models of the pore are required.

Various models have been proposed for the structure of water channels inside the membrane (see Sec. 2.2). The modeling builds on the experience gained from previous investigations of the ionomer structure via experiments and computer simulations. We have mainly considered the parallel cylindrical water channel model proposed by Schmidt-Rohr and Chen. This model resembles in several aspects Gierke's model [58] at low water content, where the size of water-filled spheres (reverse micelle) decreases [109]. Such channels were also found to be stable on the time scale of classical MD simulations (10 to 100 of nanoseconds), in several such simulations [101, 128].

In this work, three different cylindrical model pores are prepared. The first one includes only simplified hydrophilic (4 $CF_3SO_3^-$) and hydrophobic (8 CF_3CF_3) groups of the perfluorosulfonate membranes (see Sec. 4.1). The cylindrical pore structure is enforced by fixing an atom of each of these molecules on a helical path of given radius and pitch. Hence, it will be called "simple helical model", or shortly "simple model". Four different such simple models with different radii and pitches are considered in order to investigate the effect of the spacing between sulfonate groups (see Fig.

4.1).

The second model includes a larger number of hydrophobic (40) and hydrophilic (8) groups, the length of the pore is thus longer than that of the simple model (see Sec. 4.2). The cylindrical pore structure is maintained by position restraints, which are more flexible than the strict position fixing in the simple model. Therefore, this model is called "flexible model". A derivative of this flexible model is also prepared by removing all position restrains. This additional model is called as "free model".

The last model contains eight Nafion® monomers, whose backbones are parallel to the channel axis and constitute the wall of the cylindrical pore. Their sidechains are pointing towards the center of the pore (see Sec. 4.3). Since this model includes more or less parallel backbones, it is called "long parallel backbone model", or simply "long model".

Since all simulations use periodic boundary conditions, all models represent infinitely long pores in a chosen (z-) direction. Therefore, a connected water channel structure is assumed. Even if the flexible, free and parallel backbone models are eligible to show disconnected water channels, the pore stability and connected water channels are maintained and tested by classical MD before *ab initio* simulations (see Sec. 4.4). The radii of the water channels change depending on the model; they are generally smaller than 1.0 nm, which is appropriate for narrow pores in an ionomer.

In the following sections, the pore models and simulation techniques will be described in full detail.

4.1 Simple Helical Pore Model

The wall of the pore consists of eight hexafluoroethane, CF_3CF_3, molecules, referred to as the hydrophobic backbone part and four triflic acid, CF_3SO_3H, entities, referred to as the hydrophilic side chain (terminated by sulfonate group). Similar examples for the simplification of Nafion® groups have been reported before in the literature, for example, [42], [152, 70].

These simplified representative molecules are placed on a single helix (see Fig. 4.1) in order to mimic a cylindrical pore. This model is inspired from the ion channels of gramicidin [167] and from the helicity in perfluorinated alkanes [92].

The characteristics of the single helix are given below in Equation 4.1, in which $\mathrm{r_h}$ is the radius, $\mathrm{box_z}$ is the pitch of helix and θ is the cylindrical angle in radian.

$$\begin{aligned} x(\theta) &= \frac{\mathrm{box_x}}{2} + \mathrm{r_h}\cos(\theta) \\ y(\theta) &= \frac{\mathrm{box_y}}{2} + \mathrm{r_h}\sin(\theta) \\ z(\theta) &= \frac{\mathrm{box_z}}{2\pi}\theta \end{aligned} \tag{4.1}$$

where $\mathrm{box_x}$ and $\mathrm{box_y}$ are the xy-coordinates of the center of the simulation box in xy-plane.

The outer carbon atom positions are located equidistantly on the helical path in such a way that each triflic acid entity, CF_3SO_3H, is followed by two hexafluoroethane entities, CF_3CF_3. This places the SO_3H groups at 90° from each other (left, right, top and bottom) along the cylindrical pore perimeter (see Fig. 4.1 for outer carbon atoms). These carbon atoms are kept immobile in order to maintain the pore geometry cylindrical during the simulations [87].

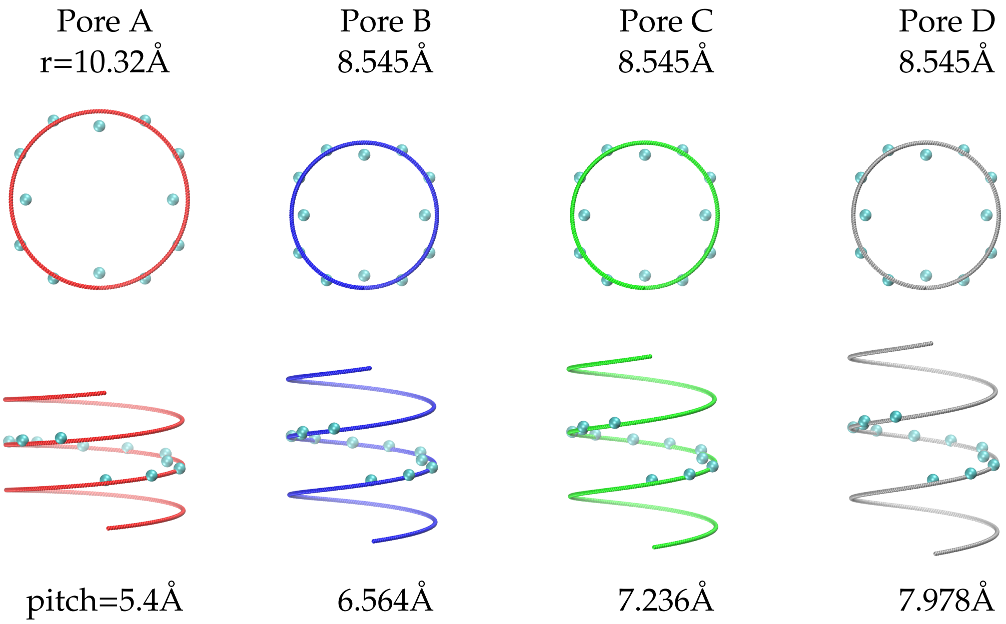

Figure 4.1: Single helix on which the molecules of the simple model are arranged. The radius, r_h, and the pitch of helix are shown for corresponding pores. Top orthographic and side views of single helix are shown by line. The outer (fixed) carbon atoms are shown by small spheres. The carbon atoms of sulfonate groups are shifted towards the center of the pore.

Since we want to compare the effect of the sulfonate group spacing, several models with different helix pitches have been prepared. For pore A (left frame in Fig. 4.2) the outer carbon atoms are thus fixed at a distance of r_h=10.32 Å from the central axis of the pore, for the narrower pores B,C, and D (right frame in Fig. 4.2) the corresponding distance, r_h is 8.49 Å. The CF_3SO_3H entities are shifted 2 Å towards the center of the pore to increase the effective exposure of the sulfonate group to the water channel, this mimics the structural environment observed in classical simulations (see Fig. 4.1).

Pore B is constructed from equilibrated runs of pore A by stepwise stretching in the *z*-direction and compressing in the *x*- and *y*-directions until the desired diameter was reached. The stretching and compressing parameters are chosen such that the surface of the cylinders are equal for pores A and B. For pores C and D, only stretching in *z* -direction is applied without compressing in radial direction. The effect of this stretching is shown in Figure 4.3. Increasing the pitch of helices to values larger than 8 Å will lead to some "holes" in the pore wall through which some water molecules may escape. An unphysical diffusion in *x*- or *y*-direction would thus be possible. This limits the choice of our geometrical model parameters.

Table 4.1: Box dimensions of simple helical ionomer pore model

name	Volume ($\AA^3$)	$box_z = d_{S-S}$ periodic	$box_x = box_y$
Pore A	2160	5.400	20.0
Pore B	1770	6.564	16.454
Pore C	1956	7.236	16.454
Pore D	2159	7.978	16.454

These pores are then filled with different numbers of water molecules to have low hydration levels λ ranging from 2.5 to 5.5 molecules per sulfonate group, these are shown in Table 4.2. The effect of increasing the water content of the ionomer, due to hydration, is an increase in its volume and thus a possible decrease in its density. Since the density of the water is smaller than that of the ionomer, in general one expects a decrease in the density due to hydration. However, at low water content, possible voids in the ionomer can be filled with the absorbed water molecules. In this case, an increasing density is expected when there is no expansion in the volume of the ionomer. Within the simple model, the cell volume of each pore model is fixed, given in Table 4.1. Therefore, increasing the water content leads to an increase in the density of the system (see Fig. 4.4).

This strategy (various hydration levels for each fixed pore structure) enables us to investigate the different states of water in possible ionomer pores with low water content (for example capillary-like water), since the behavior of water is expected to deviate from bulk in the narrow ionomer pores at low hydration level.

Another way of filling the pores with water could be to relax the volume of the cell by applying pressure, which would results in a decreasing density with increasing water content. However, this would cause a modification of pore structure, hence, a deviation from the purpose of investigating the behavior of the water in ionomer pores with different sulfonate spacings would be inevitable.

The simple helical model is also helpful for describing a material with a stable pore structure, such as nanopores embedded in an insulating material. The wall of nanopores in such a material may consist of hydrophobic groups and enriched with hydrophilic sulfonate groups. In such a pore, the simple model covers partially the possible sulfonate groups spacing and orientations.

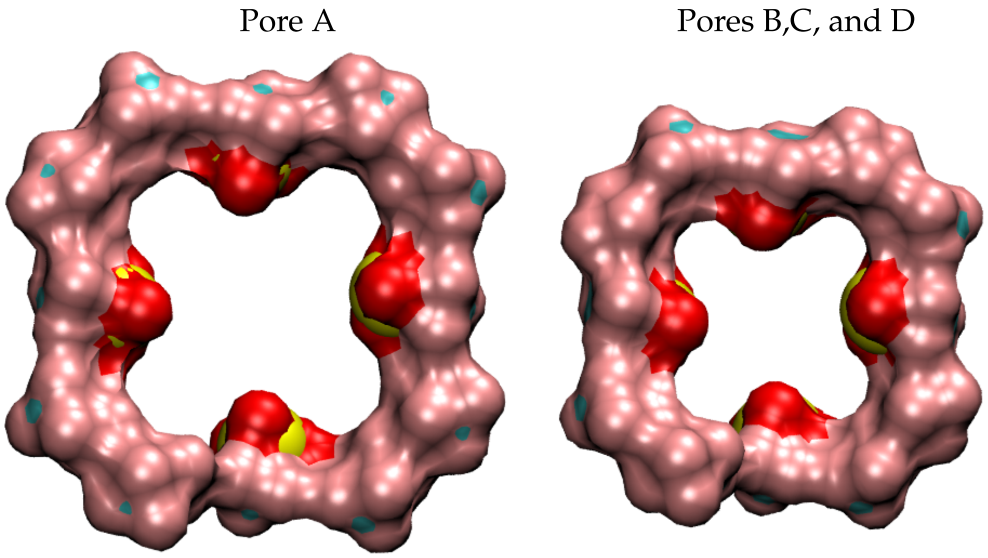

Pore A

Pores B,C, and D

Figure 4.2: Simple pore models are shown from top view. Pore A (on the left) has larger radius than the other pores, B, C, and D.

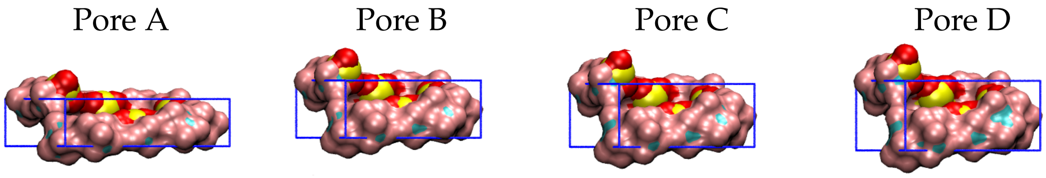

Pore A

Pore B

Pore C

Pore D

Figure 4.3: Representation of simple pore models together with simulation boxes are shown from side view. Pitch of helix, which is equal to the length of box edge in z-direction, increases from pore A to D.

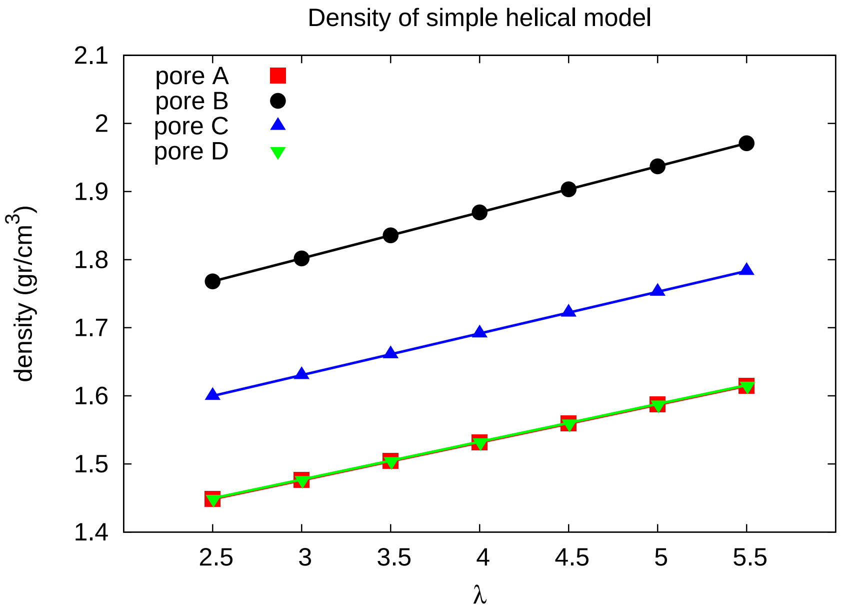

Figure 4.4: Density of simple pore models: Density highest to lowest: B,C,D, and A.

4.1.1 Setup of the Car-Parrinello MD

The prepared pore models with different hydration levels are simulated by using Car-Parrinello molecular dynamics (see Sec. 3.2.3.b). The equations of motion are integrated using the CPMD code [30] in the constant volume ensemble with a simulation time step of 4 au (corresponding to 0.0967 fs).

The electron fictitious mass is 400 au. A small fictitious electron mass in CPMD is chosen to keep the electronic structure of the system closer to the BO surface, which improves the agreement with BOMD [90]. However this small electron mass has side effects regarding the dynamical properties, which results in lower diffusion coefficients [67].

A Nosé thermostat is used for the ions with target temperature 400 K, which is above the operating temperature (350 K) of a PEM fuel cell [145]. Since CPMD simulations are known to have slower dynamics compared to the experiments, the target temperature is often set approximately 20% higher than the operating temperature [95]. This procedure is also followed here. The frequency of the Nosé thermostat is set to 3000 cm^{-1}, which corresponds to the O-H vibrational frequency. Similarly, a Nosé thermostat for electrons is applied with a frequency of 10 000 cm^{-1}. The chosen target fictitious kinetic energy depended somewhat on the number of electrons and is slightly different for each simulation, ranging from 0.011 to 0.014 au (0.30 to 0.38 eV).

At the beginning of the run the wave functions are quenched to the Born-Oppenheimer surface. The quenching procedure is repeated several times during the equilibration procedure.

For the approximation of the exchange-correlation energy, two different generalized gradient functionals, BLYP and HCTH are used. Equilibration and production time for the simulations are listed in Table 4.2.

Table 4.2: Simulation time of the simple helical ionomer pore models with the BLYP and the HCTH functionals.

functional	model name	$\lambda = \frac{n_{\text{Water}}}{n_{\text{Sulfonate}}}$	equilibration (ps)	production (ps)
BLYP	Pore A	2.5 3.0 3.5 4.0 4.5	20	72.0
	Pore B	2.5 3.0 3.5 4.0 4.5		
	Pore C	2.75 3.0 3.25		
	Pore D	3.0 3.5		
HCTH	Pore A	2.5 4.0 5.5	5.0	19 15 11
	Pore B			32 28 22
	Pore C			35 30 22
	Pore D			35 30 24

4.1.1.a Simulations with the BLYP functional

The BLYP functional [11, 114] is used with ultrasoft Vanderbilt pseudopotentials [113, 198], which has been used in many CPMD studies before, but we are aware of the fact that this approach can also have shortcomings [90, 193]. The cutoff was chosen as 25.0 Ry. Trajectories were integrated over 9.2 $\times 10^5$ steps, of which the first 2 $\times 10^5$ steps were discarded during equilibration. Hence the simulated trajectories used in the analysis below all last for approximately 70 ps [87].

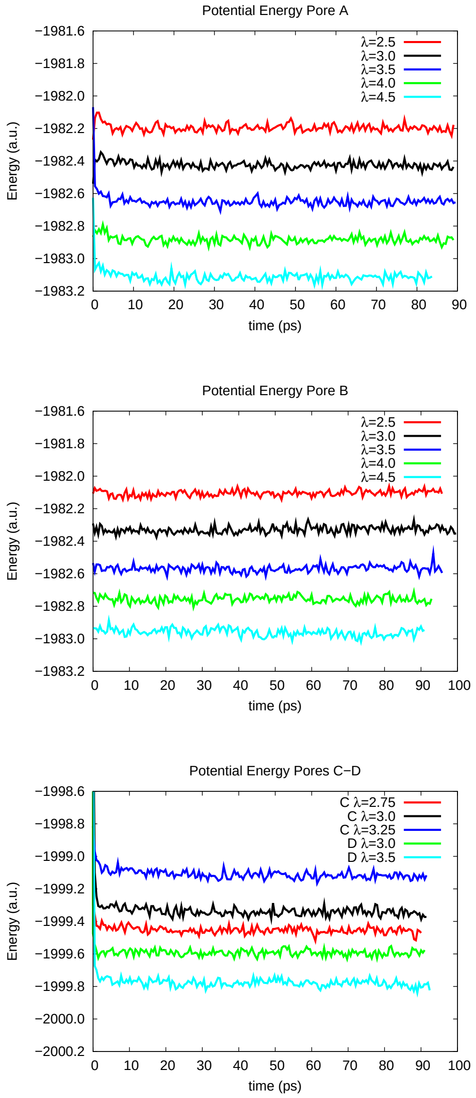

Figure 4.5: Potential energy for the simple pore models with the BLYP functional. The curves are shifted for better visibility.

4.1.1.b Simulations with the HCTH functional

The HCTH/120 exchange correlation functional [74] are used together with Trouiller-Martins norm-conserving pseudo-potentials [187]. Simulations with this functional show higher diffusion coefficients than the one with

BLYP [90, 193].

Empirical van der Waals corrections are applied. Four periodic cells in every direction are considered for dispersion corrections [64, 119, 95]

The kinetic energy cutoff for the plane-wave expansion of Kohn-Sham wave functions is chosen as 75.0 Ry, which is close to the cutoff value used in [90]. Larger basis sets were shown to improve structural and dynamical properties of liquid water within density functional approach [77, 115, 116].

The equations of motion are integrated using the CPMD code in the constant volume ensemble with a simulation time step of 4 au (corresponding to 0.0967 fs). The electron fictitious mass is 400 au. The first 5×10^4 steps of trajectories are discarded during equilibration. The simulated trajectories used in the analysis are shown in Table 4.2.

The potential energies of the simulations are shown in Figures 4.5 and 4.6. According to these potential energy curves, the equilibration parts are discarded, and all runs appear to be well equilibrated for the final production parts.

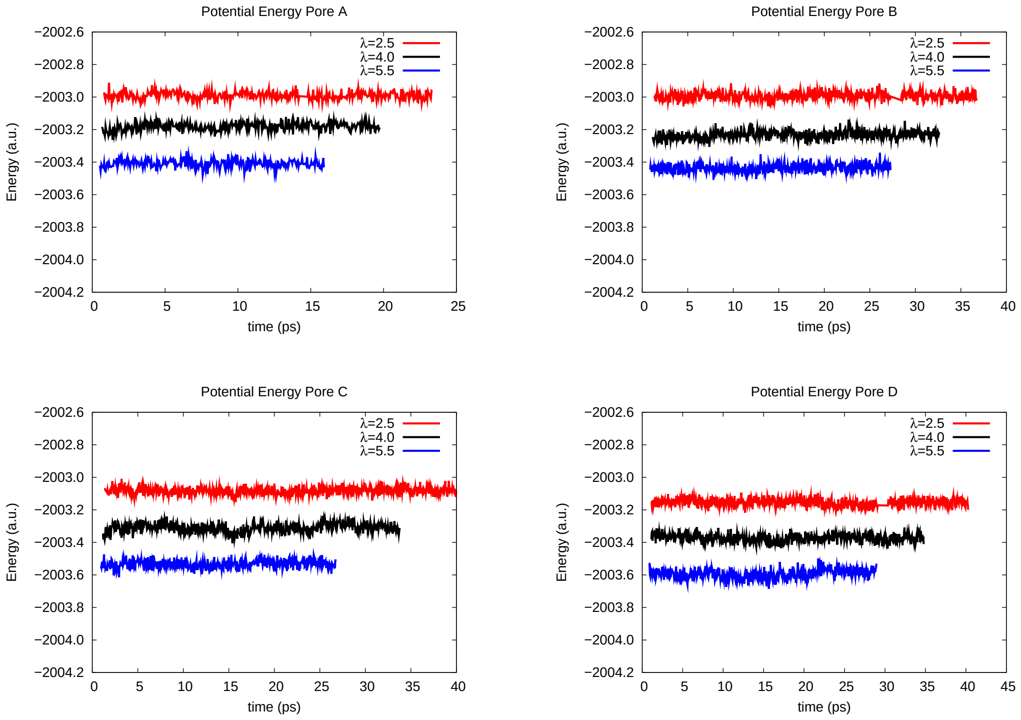

Figure 4.6: Potential energy for the simple pore models with the HCTH functional. The curves are shifted for better visibility and the potential energies belonging to the first 1 ps of simulations are not shown.

4.2 Flexible Ionomer Pore Model

An improved model that does not have all the disadvantages of the simple pore model, which suffers from having small box size and fixed geometry, is prepared. This new model includes 8 hydrophilic groups in a simulation box, whose height (box_z) is longer than the previous simple model. The number of hydrophobic groups is also increased from 8 to 40 in order to keep the water molecules inside the pore.

Increasing box dimensions and number of atoms, especially in z-direction, of simple pore models allows us to observe the diffusion of protons along the pores for longer distances than by using the simple cylindrical models. The effect of finite size of the simple helical model will also be decreased. Multiple stacking of these simple pore models is an alternative way for generating longer pores, in which the position constraints are required to maintain the pore structure. However, removing the position constraints at least partially will increase the flexibility of the side chains, which is considered to affect the proton diffusion. Since the flexibility of the side chains depends also on its length, side chains of the new model are designed to be longer than in the simple model.

Based on the above mentioned consideration, a flexible pore model, longer than the simple one, is designed by using four turns of the helix, at which the molecules are located.

A new polar helical turn, **P2**, is generated by modifying the hydrophilic groups of the simple pore model from $CF_3SO_3^-$ to $CF_3CF_2CF_2SO_3^-$ by inserting CF_2CF_2. The hydrophobic groups belonging to **P2** are also modified in

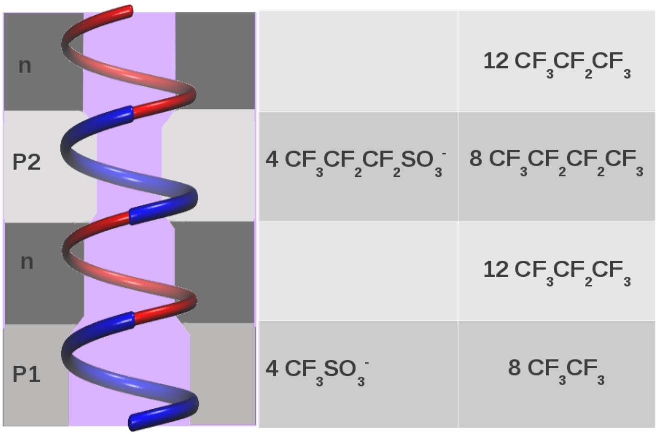

Figure 4.7: A schematic view of the flexible pore model, which is composed of two non-polar slices labeled by **n** (red colored helix parts), and two polar slices labeled by **P1** and **P2** (blue colored helix parts). The molecules of each slice are shown on the right.

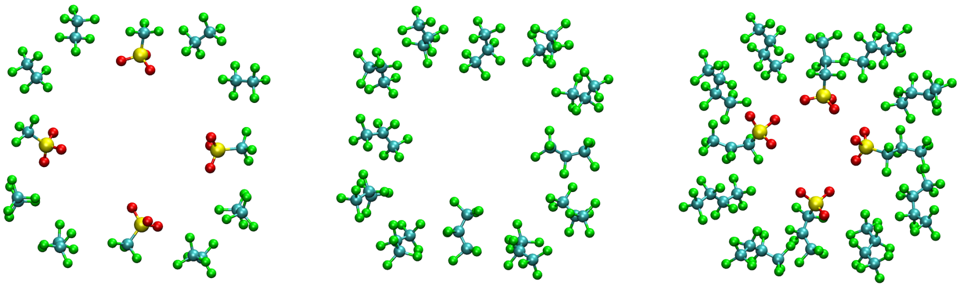
p1 n p2

Figure 4.8: Helical slices of flexible pores are generated by modifying the fixed helical model in such a way that for the non-polar slices (shown in the middle), all entities of simple geometrical model (on the left) are replaced by hydrophobic $CF_3CF_2CF_3$ molecules. For the polar slice (on the right), these entities are not replaced but changed by inserting an additional $-CF_2CF_2-$ chain.

the same way and become $CF_3CF_2CF_2CF_3$ (see Fig. 4.7 and Fig. 4.8).

A non-polar helical turn, **n**, composed of only hydrophobic groups

$CF_3CF_2CF_3$ is also generated.

A combination of these polar (**P2**) and non-polar (**n**) helical turns is used together with the simple model (**P1**). The helical slices of **P1**,**n**, **P2** and **n** are replaced on top in z-direction, respectively (see Fig. 4.7).

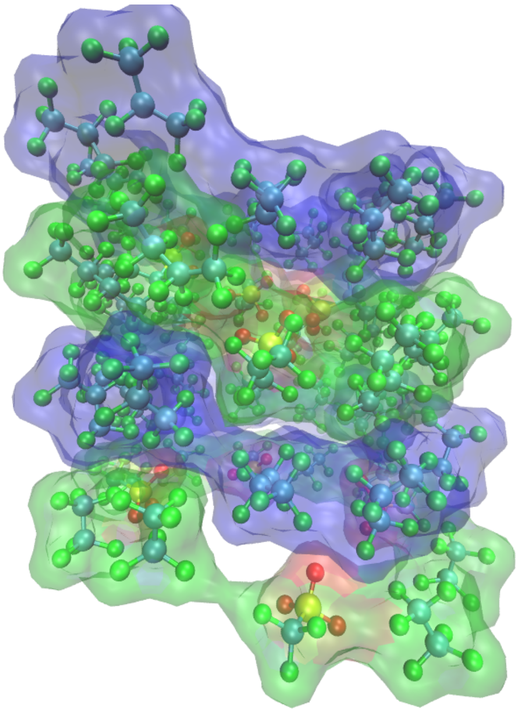

Figure 4.9: Side perspective view of the irregular pore structure: a combination of polar helical turns **P1** and **P2** (in green) and non-polar helical turns, **n** (in blue surface).

This irregular pore is again filled with a varying number of water molecules, like in the simple pore models, in order to investigate the effect of the hydration level on the proton transfer.

Again three hydration levels, i.e., number of water molecules per sulfonate group, are considered; these are 2.5, 4.0, and 5.5. Here, we have not followed the same strategy as in the simple model, where the various pores (pore A, B ..) are considered with changing hydration levels. The pore structure within this model is not kept fixed, it is aimed to find an appropriate density depending on the water content.

A relaxation of the pore structure is required for each water content. Therefore, classical molecular dynamics with NPT ensemble is applied to reach an equilibrated stable initial structure for the AIMD simulations.

4.2.1 Equilibration of the flexible pore model

During the classical molecular dynamics simulation, which has been carried out with the Gromacs package [80], the excess protons, bonded to water molecules are represented by the hydronium model given in [167]. Force field parameters for pore molecules are adapted from [28] and the SPC water model is used [12]. These force field parameters and simulation details for MD are given in appendix A.

At the beginning of the MD run, position restraints on outer carbon atoms (one carbon atom of each molecule of pore) are used to maintain the pore structure stable. During MD, these restraints are weakened and finally completely removed. This procedure of controlled relaxation results in a connected water channel and stable pore structures.

This equilibration procedure is established as following and corresponding densities depending on simulation time are shown in Figure 4.10.

- (0-11 ns) NPT dynamics with position restraints with strong force constants is applied. In each 1 ns, the positions constraints on the outer carbon atoms are redefined on their new positions of these atoms. This restarting positions is repeated 10 times until it effect on the system becomes negligible.

- (11-51 ns) A long simulation (40 ns) again within the NPT ensemble together with position restraints with the same force constants is applied. The resulting configurations are used as starting coordinates of atoms for BO-MD simulations (flexible model).
- (51-71 ns) Then the system is relaxed once more by NPT with position restraints whose force constant is weaker than the before. This caused the system to reach a more relaxed state.
- (71-121 ns) Lastly position restraints are removed from the system, and a final relaxation of the free system is reached under NPT ensemble conditions. Final configurations are used as initial structures for BO-MD simulations (free model)

During the NPT simulations without position restraints, a sudden expansion of the simulation cell would result in a loss of the connectivity of the water channel. Indeed, the position restraints decrease the effect of the barostat by creating an artificial force, which hinders the simulation box to shrink or to expand suddenly and thus maintains the pore structure. Therefore, the position restraints are firstly weakened and finally removed.

4.2.2 Setup of the Born-Oppenheimer MD

The prepared pore models with different hydration levels (λ 2.5, 4.0, and 5.5) are simulated by using Born-Oppenheimer molecular dynamics (see

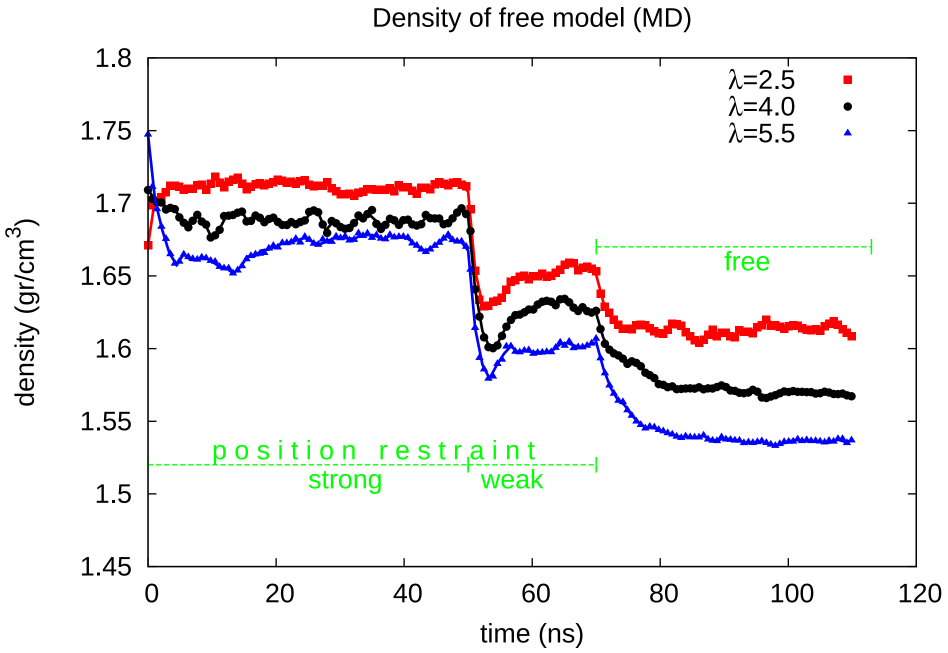

Figure 4.10: Density of the flexible model equilibration with classical MD. Position restraints are gradually weakened in order to maintain the connectivity of the water channel and finally removed (last 40 ns).

Sec. 3.2.3.a). The equations of motion are integrated using the Quickstep algorithm in the CP2K code [199, 200, 103] in the constant volume ensemble with a simulation time step 0.25 fs.

A density cutoff of 180 a.u. is used for Gaussian plane waves, using the GPW method [121]. For the approximation of the exchange-correlation energy, the generalized gradient-corrected BLYP functional is used. The DZVP-GTH (Goedecker-Teter-Hutter) pseudo-potentials are used for the core electrons[106, 60, 76]. Grimme type-3 dispersion corrections to the exchange-correlation functional are applied [65].

A Nosé-Hoover thermostat [145, 144] is used for the ions with target temperature 350 K. Equilibration and production time for the simulations are listed in Table 4.3.

Table 4.3: Simulation time of the flexible and free ionomer pore models with BOMD.

name	$\lambda = \frac{n_{Water}}{n_{Sulfonate}}$			equilibration (ps)	production (ps)		
flexible	2.5	4.0	5.5	2	13.0	12.0	11.5
free	2.5	4.0	5.5	2	8.0	11.0	9.0

Potential energies for the free and flexible models are shown in Figure 4.11. Based on the potential energies, the AIMD simulations appear to be reasonably well equilibrated after 2 ps of simulation time.

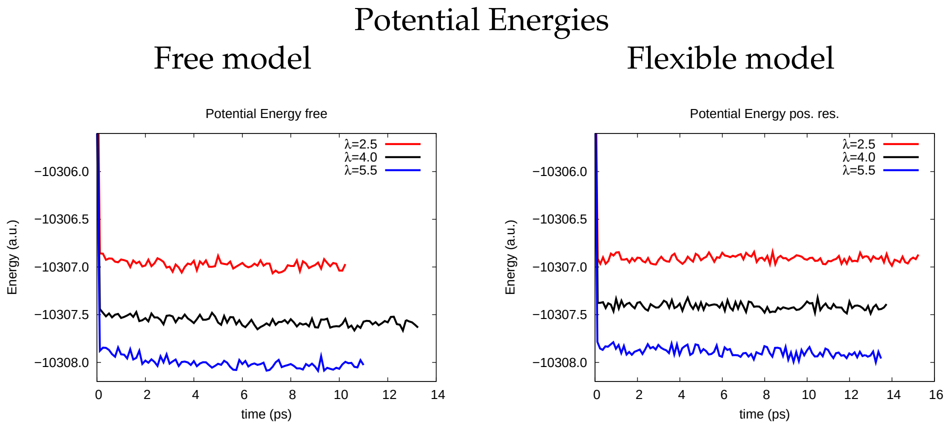

Potential Energies

Free model

Flexible model

Figure 4.11: Potential energies of the flexible model without position restraints (free model on the left) and with position restraint (on the right). The curves are shifted for better visibility.

4.3 The Parallel Nafion® Backbone Pore Model

Another pore model based on 8 Nafion® monomers is prepared such that each monomer is connected to its periodic images in the backbone and its side-chain terminated by a hydrophilic sulfonate group, pointing to the center of pore.

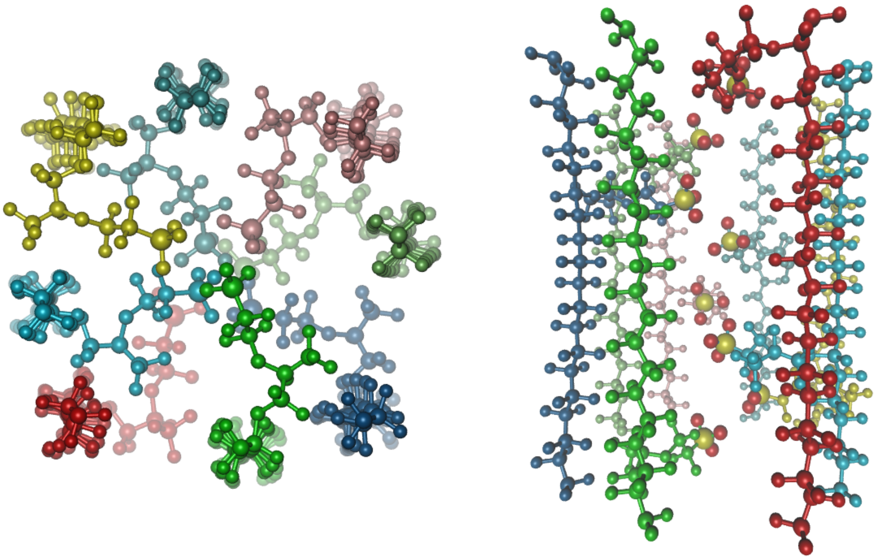

Figure 4.12: Pore model consisting of 8 Nafion® monomers. Each monomer is represented by a different color. Left: orthographic projection from top; right: side view of the simulation box.

Again after modeling the polymer pore, it is filled with various numbers of water molecules, ranging from 20 to 44 in order to investigate the effect of hydration level on proton transfer. The corresponding water content, λ, is 2.5, 4.0, and 5.5, respectively.

An equilibration procedure is also required to have a connected water channel and a stable pore structure.

4.3.1 Equilibration of the parallel backbone model

Classical molecular dynamics is also applied to equilibrate the configuration of pore and water by using a thermostat in the first stage at constant volume and in the second stage together with pressure coupling. This leads to a system that has a reasonable distribution of water molecules inside the pore and the desirable density at thermostat temperature.

During the classical molecular dynamics simulation, which has been carried out with the Gromacs package, excess protons, attached to water molecules, are represented by the hydronium model given in [167]. Force field parameters for Nafion® are taken from the article [28] and the SPC water model [12] is used.

In the constant volume simulation, at the beginning, the positions of two atoms of connected monomer chains are fixed in order to prevent sliding of chains in z direction and to confine the water molecules inside the pore center. After a few nanoseconds of simulation, more flexible position restrains are used by decreasing force constants. When all water molecules are collected inside of the pore, these restrains are completely removed.

In the second stage of classical MD, pressure coupling is applied to the system to decrease the volume of the simulation cell and to reach a density comparable to the experimental one.

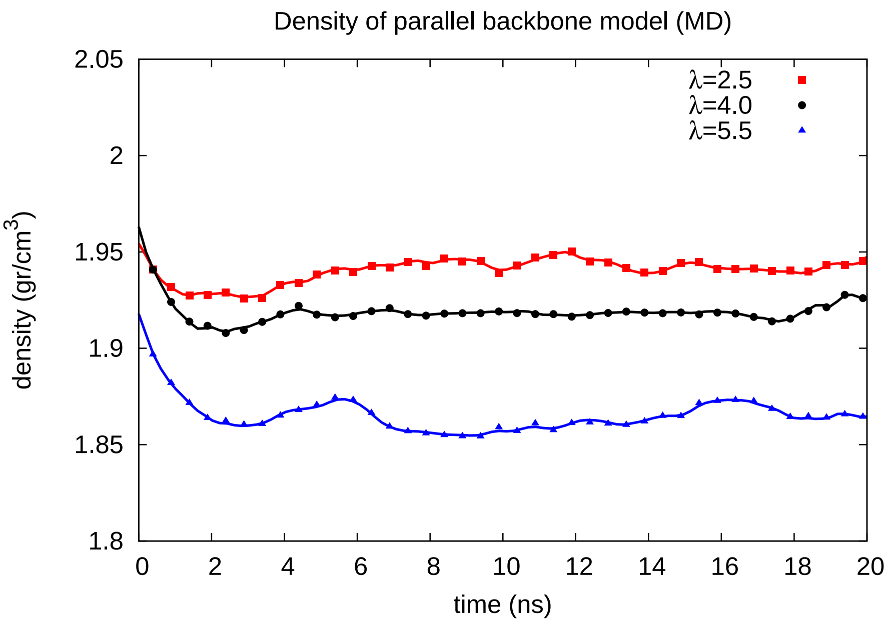

Figure 4.13: Density of the parallel backbone model during equilibration with classical MD.

4.3.2 Setup of the Born-Oppenheimer MD

The prepared pore models with different hydration levels (λ= 2.5, 4.0, and 5.5) are simulated by using Born-Oppenheimer molecular dynamics (see Sec. 3.2.3.a). The equations of motion are integrated using the Quickstep algorithm in the CP2K code [199, 200, 103] in the constant volume ensemble with a simulation time step 0.25 fs.

A density cutoff of 180 a.u. is chosen for the Gaussian plane waves, using the GPW method [121]. The generalized gradient-corrected BLYP functional is used with DZVP-GTH (Goedecker-Teter-Hutter) pseudo-potentials [106, 60, 76]. Grimme type-3 dispersion corrections are applied to the exchange-correlation functionals [65].

A Nosé-Hoover thermostat [145, 144] is used for the ions with target temperature 350 K.

Potential energies for the parallel backbone model are shown in Figure 4.14.

Potential Energy

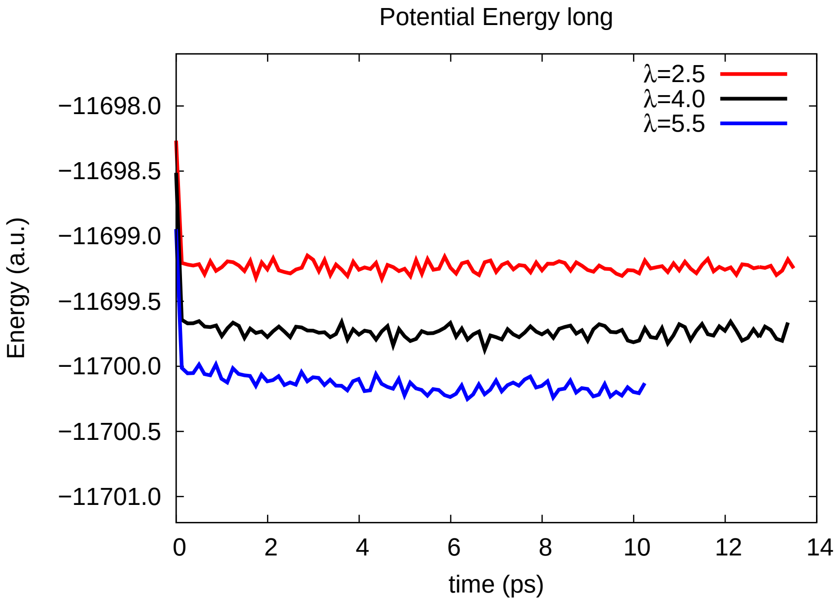

Figure 4.14: Potential energies of the parallel backbone model. The curves are shifted for better visibility.

4.4 Stability of the pore models

The simple helical model: The stability of the simple pore model is ensured during the simulation by fixing the position of a carbon atom of each hydrophilic and hydrophobic molecule. The small size of the simulation cells also does not allow any water molecules to leak through the pore wall. However, having connected water channel together with a stable pore without any restraints is not straightforward.

The flexible model: A stable pore structure and a connected water channel along only one direction is achieved by defining position restraints on the molecules which are involved in forming the pore walls. These, however, depend on the water content.

We have tested the flexible pore model with hydration levels equal and smaller than 10.0 by classical MD. It is possible to get a stable pore only by a controlled relaxation procedure (as explained in Sec. 4.2.1). In other cases, depending on the water content, it is possible that water connects in more than one direction at high hydration level, or for low hydration level, water forms a reverse micelle, in which the connectivity of water is lost.

The parallel backbone model: Formation of a stable pore within the parallel backbone model is easier than with the free model. Because of the backbone, which is composed of bonded chains of perfluorinated carbons, the conformational freedom is smaller than in the flexible model, which includes unbonded hydrophilic molecules.

In order to find a stable pore model which consists of a minimum number of Nafion® monomers with parallel backbones, classical molecular dynamics simulations with NPT ensemble are applied.

Firstly a pore only including 4 Nafion® monomers with parallel backbones was tested with hydration level λ =10; this model leads to the water phase becoming connected in more than one direction, which indicates the loss of the cylindrical structure. Therefore, the number of Nafion® monomers with parallel backbones was increased gradually to 8, for which a stable pore structure together with a connected water channel only in one chosen direction is possible.

If the length of the backbone of Nafion® is decreased, it is also possible to get a cylindrical stable pore with a smaller number of Nafion® monomers than 8. As an example, a pore consisting of 4 Nafion® monomers and 2 perfluorinated carbon chains (a Nafion® monomer without sidechain) results also in a stable cylindrical pore, where the number of CF_2 groups in the backbone is 20.

Final configurations of the MD simulations are used as initial configurations for the AIMD. The corresponding densities of the pore models are shown in Fig. 4.15.

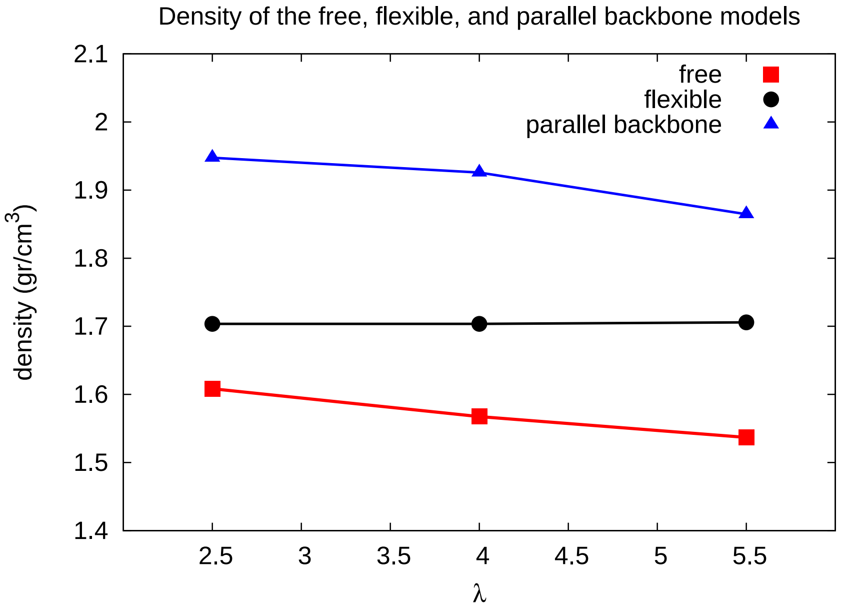

Figure 4.15: Densities of the free, flexible, and parallel backbone models

Chapter 5

Spatial Distribution of Atoms

The coordinates of the atoms are recorded in trajectory files for selected, equally spaced time steps. A statistical sampling based on these coordinates yields the properly thermodynamically averaged information about the spatial distributions of atoms. These structural properties can be compared to experimental observations, they depend, as always in numerical methods, on the quality and method of the sampling.

We consider four different correlations in order to quantify the structural information;

1. The radial distribution function of atoms (RDF), which is the correlation of the distances among pairs of atoms.

2. The cylindrical distribution of atoms around an axis, which is the correlation of the radial distances (2-D) between atoms and a chosen lab frame axis.

3. The number density projected onto a plane of the laboratory frame, which is a correlation between the (2-D) coordinates of the atoms and a fixed point of the plane

4. The 3-D distributions of neighboring atoms in a molecular frame, which is a vectorial correlation between these atoms and the selected molecular frame.

The statistical accuracy of these correlations depends on the number of atoms involved and on the number of time steps in the trajectory. Correlations related to the lab frame are only evaluated for the simple helical model, in which the wall of the pore structure is kept fixed. The simplicity of this pore structure allows to easily identify the density profile of the atoms.

The RDF is one of the most used descriptions of the microscopic structure in molecular dynamics. Hence, our analysis will mainly depend on the computed RDFs.

Since *ab initio* molecular dynamics allows molecules to form and to break their chemical bonds (i.e. there are no unchanging, fixed molecules), the statistical sampling must, in many cases, be based on a dynamical selection scheme. Therefore, identification of the selected types of atoms at each time step of the simulation is required. For this purpose, it was necessary to write a specific new analysis tool based on geometrical criteria. The overall RDFs can be used as a guideline to devise such more specific geometrical criteria. In the present case the dynamical selection is essential in order to differentiate proton complexes and other possible chemical states of the diffusing proton.

The details of the calculation will be described explicitly at the beginning of each section. The atom-atom RDFs are shown in the first section; they are classified into three categories;
1) pairs of sulfonate groups,
2) pairs of sulfonate groups and water, and
3) pairs of water molecules.
We focus mostly on the effect of water content and of the sulfonate spacing.

In the second section, the number density of atoms on the $x - y$ plane is examined to find the probable locations of proton complexes and the concomitant distribution of water molecules inside the narrow ionomer pores.

In the third section, a complementary analysis of density maps, cylindrical distributions of proton complexes, and water molecules is shown.

In the last section, the local tetrahedrality of the structure around a water molecule is investigated by comparing the 3-D number densities of water oxygen in a molecular frame.

An additional remark for differentiating the simulations of the simple pore model, the one with the HCTH functional and dispersion corrections will be called as "the simple pore model with HCTH" and it will be marked with "*" in the figures, if it is not explicitly specified. The results presented in this chapter will guide us for further analyses of the trajectories.

5.1 Radial Distribution of Atoms

The radial distribution function (RDF), $g(r)$, describes how the density of particular atoms varies as a function of the distance from specific atoms (which can be the same or different) [4]. The structure of liquids is mostly described by $g(r)$, which is related to the pair correlation of interatomic distances.

A normalized distribution of the distances between pairs $i - j$ is computed as:

$$\delta(r - r_{ij}(t)) = \begin{cases} 1 & r \leq r_{ij}(t) < r + \Delta r \\ 0 & \text{otherwise} \end{cases} \tag{5.1}$$

where Δr is the bin width, and $r_{ij}(t) = |(\vec{r}_i(t) - \vec{r}_j(t))|$ is the distance between atoms i and j. The average over time, $\langle ... \rangle$, equals to the probability of finding these particle at a distance r away from each other.

$$P_{ij}(r) = \langle \delta(r - r_{ij}(t)) \rangle_t \tag{5.2}$$

Summation over j results in $P_i(r) = \sum_j^N P_{ij}(r)$, the number of particles whose distance from the i-th atom is r. By considering not only the i-th, but all atoms, the average number of particles is:

$$P(r) = \langle P_i(r) \rangle_i = \frac{1}{N} \sum_i^N \sum_j^N \langle \delta(r - r_{ij}(t)) \rangle_t \tag{5.3}$$

This function is then spherically averaged. The resulting function $g(r)$ leads to the average relative (to the bulk value) probability to find a particle j in the distance range $(r, r + \Delta r)$ from particle i.

$$g(r) = \frac{P(r)}{4\pi r^2 \Delta r} \tag{5.4}$$

For large distances, one has:

$$\lim_{r\to\infty} g(r) = 1 \tag{5.5}$$

The integral of $g(r)$ between 0 and r_0 equals to the coordination number, $n(r_0)$, which is the average number of atoms within a spherical volume.

$$n(r_0) = \int_0^{r_0} P(r)\,dr = \int_0^{r_0} 4\pi r^2\, g(r)\,dr \tag{5.6}$$

The structure factor, usually called $S(Q)$, is related to the Fourier transform of the RDF. This provides an opportunity to compare with experimental results e.g. neutron or X-ray scattering.

The r-range up to which a g-function can be computed straightforwardly from simulations with periodic boundary conditions is limited to distances r smaller than the smallest edge of the box. This is a particular limitation for the simple helical model with its small extension in the z-direction, (see Fig. 4.1). In Pore A, for example, the closest sulfonate group is one from the periodic images, hence the distance between other sulfonate groups is larger than the box length in z-direction. Therefore, all radial distribution functions of the simple helical models are calculated by first replicating the trajectories four times in z-direction. This inclusion of periodic images affects the RDF, especially for larger distance, and causes artificial periodic peaks in the large-r region. A comparison of the RDF of the sulfur atoms, with and without including multiple boxes, is shown in Figure 5.1.

The thickness of the spherical shell, Δr, is chosen as 0.05 Å for all functions. For values smaller than 0.05 Å, $g(r)$ becomes noisy. Values larger than 0.05 Å do not provide enough sensitivity for the conclusions that we wish to draw.

5.1.1 Distribution of the sulfonate groups

The strategy for developing various models can be explained in other words as determining the effect of water content on the sulfonate groups spacing and the effect of, both, sulfonate spacing and water content on the mobility of protons. Therefore, the distribution of sulfonate groups is crucial. Even for the simple helical model, where all carbon atoms of hydrophilic groups is fixed, the sulfonate groups (-SO_3^-) may still move. This freedom is increased for the flexible model, and finally completely free sulfonate groups are modeled.

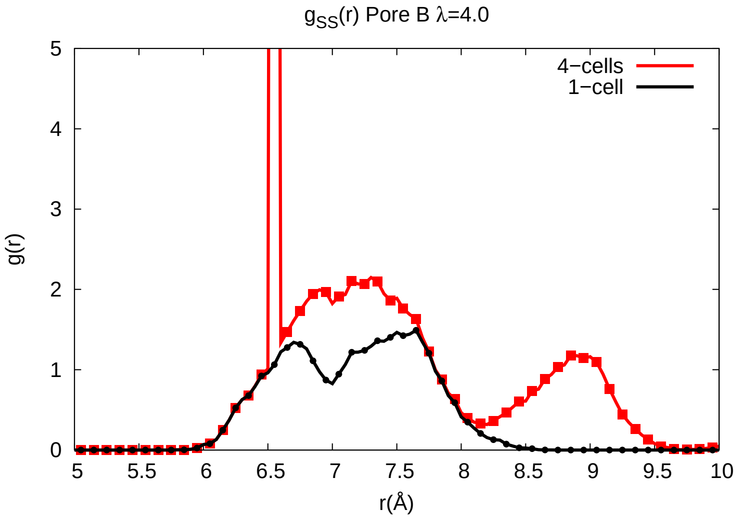

Figure 5.1: The effect of multiple simulation cells on $g(r)$ of the sulfur atoms. The highest peak reflects the periodic images of sulfur atoms in neighboring cells.

The radial distributions of the sulfur atoms are calculated for all pore models and are shown in Figs. 5.2, 5.3, and 5.4. In order to mimic the relation between hydration levels and sulfonate spacings, they are plotted with the GNUPLOT free graphics package using the pm3d map technique [209]. In these figures, the RDFs are colored according to the values of the function in order to visualize their minima and maxima.

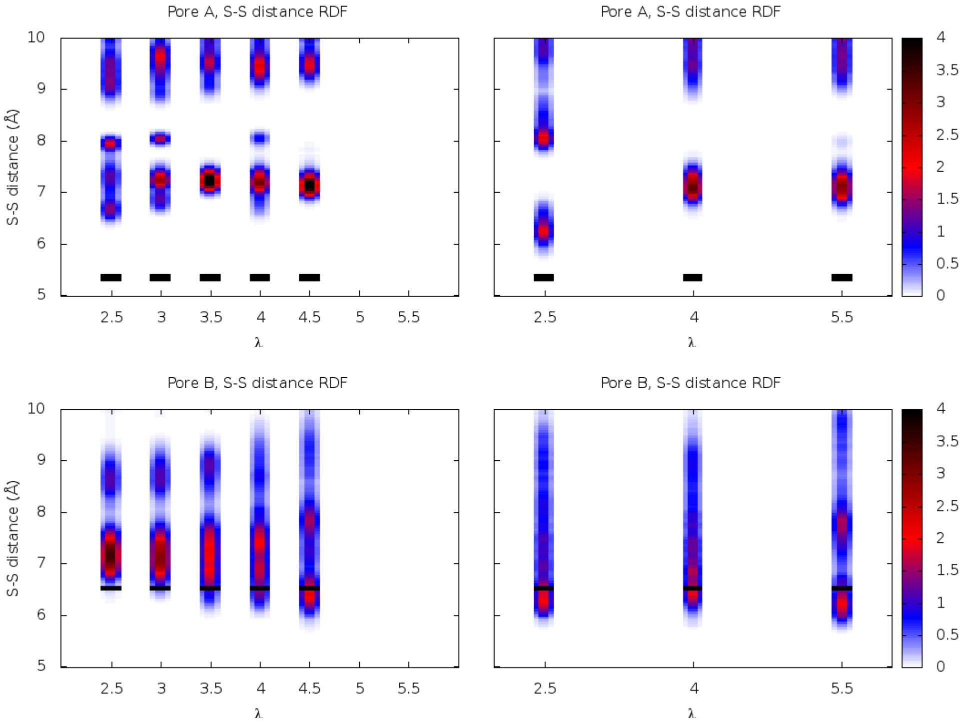

Figure 5.2: The sulfonate spacing vs. hydration level in pores A (top) and B (bottom) of the simple model: Comparison of the RDFs of the sulfur atoms for the BLYP (left) and the HCTH (right) functionals. Dashed black lines represent periodic images of the sulfur atoms.

The minimum sulfonate spacing in Pore A of the simple model is 5.4 Å, which is due to its periodic image. There is a gap between the first and the second peaks of these $g(r)$ for all water contents, which indicates that the distance between a sulfonate group and its periodic images is closer than the distance between any two sulfonate groups in the same box. This gap vanishes for all other pore models.

In pore B, as the number of water molecules per sulfonate group, λ increases, $g(r)$ becomes flatter and smoother; there is no well-defined minimum.The minimum sulfur-sulfur spacing in pore B with the BLYP functional decreases as the water content increases. For λ larger than 3, it becomes smaller than the box dimension in z-direction. For pore B with the HCTH functional, the average minimum distances for all λ values are lower than 6.56 Å. This indicates that the sulfonate groups becomes more mobile.

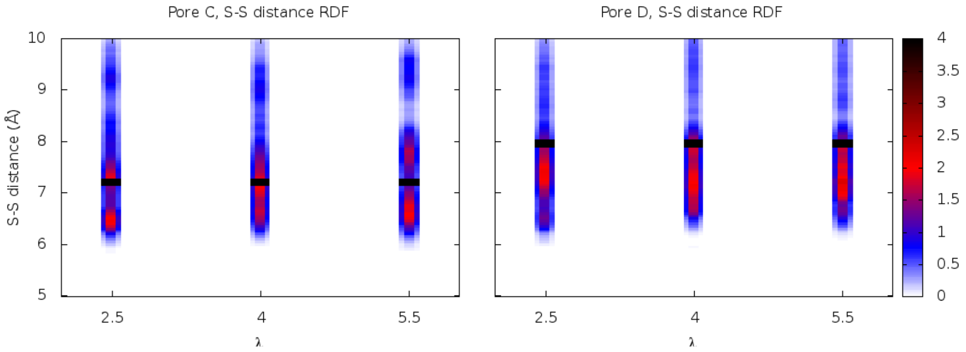

Figure 5.3: Sulfonate spacing vs. hydration level for pores C (left) and D (right) of the simple model: Dashed black lines represent periodic images of sulfur atoms

For pores C and D with the HCTH functional, the first peak of $g(r)$, located around 7 Å, is smaller than the box dimension in z-direction. Hence, the minimum sulfur-sulfur spacing is not determined by the cell periodicity. The corresponding RDFs are distributed fairly continuously and do not show gaps.

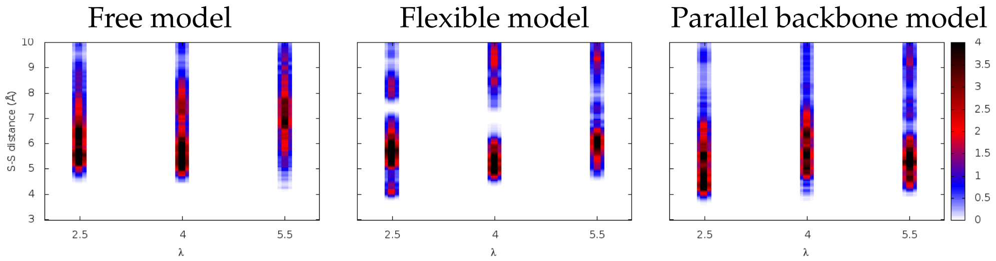

Figure 5.4: Sulfonate spacing vs. hydration level for the free model (left), the position restraint model (middle), and the parallel backbone model (right).

The sulfur-sulfur radial distribution functions of the free, flexible, and parallel backbone models show that the minimum spacing is lower than the one in the simple model, varying between 4 and 5 Å. Except for the flexible model, in which position restraints are applied to the sulfonate groups, there is no well defined minimum of the $g(r)$s. In the free model, the maximum of $g(r)$ shifts to around 7 Å for $\lambda = 5.5$. For other hydration levels (2.5 and 4.0), the most probable sulfur spacings are around 6.0 and 5.8 Å, respectively. For the flexible model at $\lambda = 5.5$, $g(r)$ is smoother and does not have a gap.

In general, we find that the sulfur-sulfur spacing depends on the flexibility of the hydrophilic groups. For fixed and position restrained hydrophilic groups, in which the motion of sulfur atoms is somehow restricted, $g(r)$ of the sulfonate groups is affected by the increasing number of water molecules. The effect of increasing hydration level for low values of λ (up to 4.5) is indirect and secondary compared to the influence of the flexibility of the hydrophilic groups. The distribution of sulfur spacings becomes smoother with increasing hydration level. The more water is included, the more dynamic the sulfonate groups. Hence we will consider now the correlations between water and sulfonate groups.

5.1.2 Correlations between sulfonate groups and water

First we need to differentiate the oxygen atoms belonging to sulfonate groups from water oxygen for the rest of the analysis, because atoms are not unequivocally assigned to molecules in AIMD simulations as they are in classical ones. The radial distribution functions of sulfur and oxygen are used in order to classify the oxygen atoms. The $g(r)$s are shown in Figure 5.5 only for a water content of $\lambda = 4.0$.

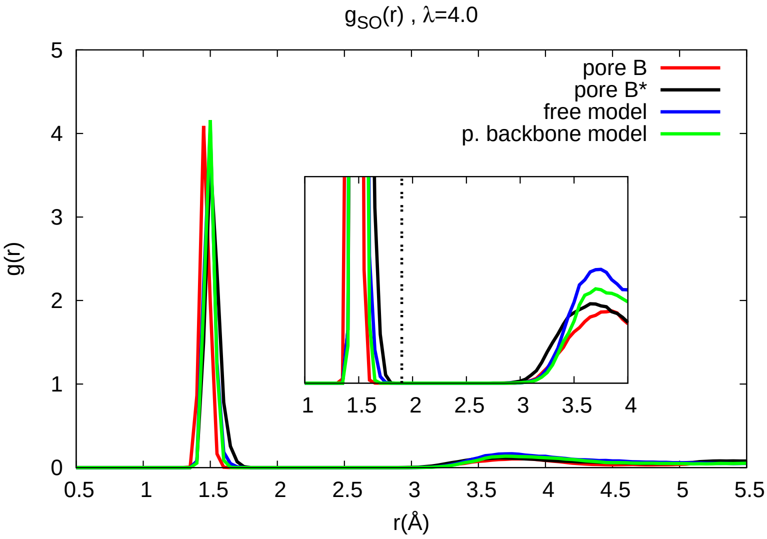

Figure 5.5: Radial distribution function of sulfur and oxygen atoms for $\lambda = 4.0$. Inset the dashed vertical line at 1.9 Å shows cutoff distance. For better visibility, the height of g(r)s are scaled. The simple pore model with the HCTH functional and the dispersion corrections is marked with "*".

The first peak is intramolecular, it shows the oxygen atoms bonded to sulfur. There is a clear minimum between 1.7 Å and 3.0 Å. It is followed by a second peak related to oxygens that do not belong to the sulfonate group.

Hence the oxygen of sulfonate groups and the other oxygen atoms can be differentiated by their distances to the sulfur atom. A cutoff distance of 1.9 Å is thus chosen in order to select the sulfonate oxygens, so that only the first peak of $g_{\mathrm{SO}}(r)$ is included. The cutoff distance is shown as a dashed horizontal line in Figure 5.5 with $g(r)$s of some of the pore models. For all other models, this cutoff distance is large enough to include only the first peak of $g(r)$ and to differentiate the oxygen atoms.

Oxygen atoms belonging to sulfonate groups are named for short $\mathrm{O_S}$; the abbreviation $\mathrm{O_W}$ is used for the water oxygens. Because of the excess protons, another subset of oxygen atoms must be defined such that if a proton is bonded to $\mathrm{O_S}$, or if an excess proton proton is bonded to $\mathrm{O_W}$ it will be called $\mathrm{O_P}$, protonated oxygen. A detailed classification of the protonated oxygen atoms is introduced in the chapter on proton dynamics (Chap. 7).

The correlation between hydrogen atoms and sulfonate groups ($\mathrm{SO_3^-}$) are characterized in terms of the sulfur-hydrogen radial distribution functions $g_{\mathrm{SH}}(r)$ and the sulfonate oxygen-hydrogen ones, $g_{\mathrm{O_SH}}(r)$. They are shown here only for the simple model with the BLYP functional in Figure 5.6. The RDFs for the other pores are shifted to appendix C.1 (Figs. C.1, C.2 for the simple model with HCTH functional, Fig. C.3 for the free and flexible models, and Fig. C.4 for the parallel backbone model).

5.1.2.a The structure of undissociated sulfonate group ($-\mathrm{SO_3H}$)

The first peaks of $g_{\mathrm{SH}}(r)$ and $g_{\mathrm{O_SH}}(r)$ are due to the intramolecular interaction between one of the oxygen atoms of the sulfonate group and the hydrogen atom. The strong correlation shows the existence of a chemical bond between sulfonate oxygen and hydrogen.

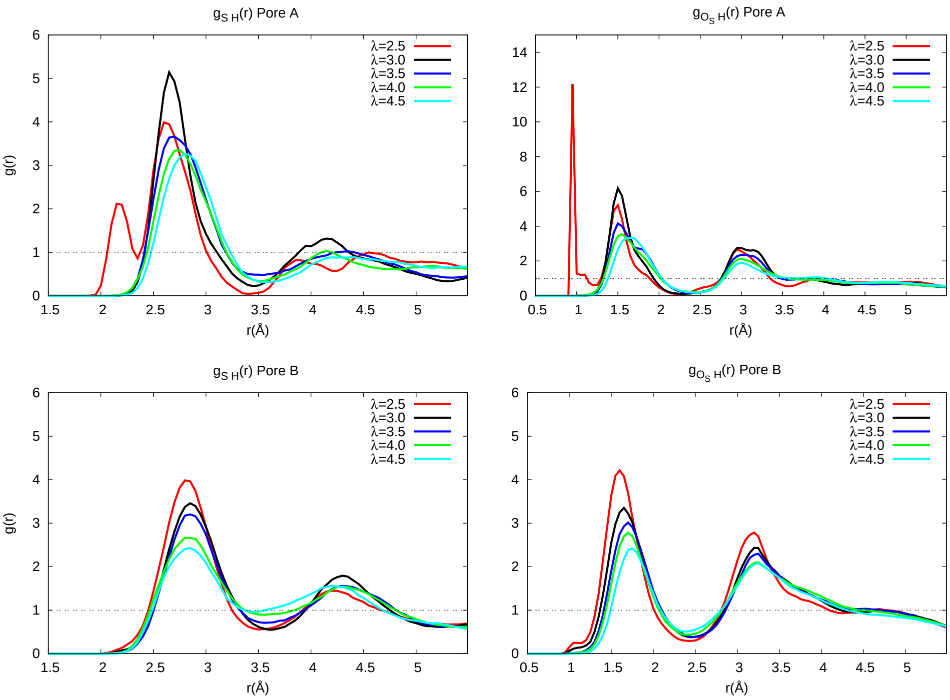

Figure 5.6: S-H (left) and O_S-H (right) RDFs belonging to pores A and B of the simple helical model with the BLYP functional.

The maxima of these "acidic proton peaks" in $g_{O_SH}(r)$ and $g_{SH}(r)$ are located approximately at 1.0 Å, and 2.2 Å, respectively. The first peaks of the sulfonate-oxygen and hydrogen RDFs are sharper and narrower than the ones belonging to sulfur and hydrogen distributions.

Since only the first peak is required for the undissociated protons, a simplified comparison of the pore models can be done by using the integral of the $g(r)$. The area under this first acidic peak of $g_{O_SH}(r)$ is related to the coordination number, $n(r)$, average number of undissociated protons around sulfonate oxygens. These are proportional to the probability of observing undissociated acidic protons (see Fig. 5.7).

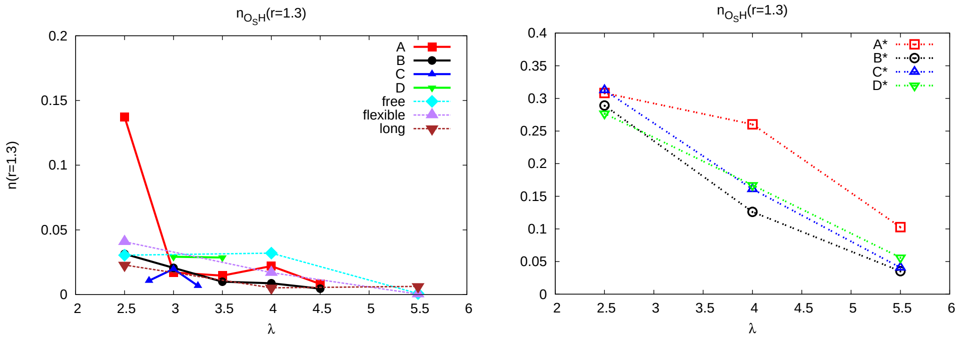

Figure 5.7: The coordination number O_S at r=1.3 Å (right) for the simple helical model with the HCTH functional and (left) for the simple pore model with the BLYP functional, the free, the flexible, and the parallel backbone (long) pore models.

Firstly, the main difference stems from the functionals used in the simulations. In the simple model with the BLYP functional, an undissociated proton is only observed at the hydration level $\lambda = 2.5$ for pore A. At hydration levels higher than 2.5 for pore A and for the other pores at all hydration levels, the amount of undissociated protons is statistically insignificant.

The acidic proton fractions in the free, flexible, and parallel backbone models (the same functional is used) show the same tendency as described above for the simple model with BLYP. The peak related with intramolecular interaction is very small and the amount of undissociated protons is statistically insignificant (see also Figs. C.3 and C.4).

On the other hand, in the simple model with the HCTH functional, the coordination number, $n(r)$, shows a significant existence of acidic protons (see also Figs. C.1 and C.2). This leads to conclude that the dissociation rate of the protons depends on the functionals employed in the simulations.

Secondly, there is a trend for all simulations that an increase in water content leads to a decrease in the coordination number, $n(r)$, hence, the fractions of the acidic protons decrease. This trend is apparent especially for the HCTH functional, since high fractions of the acidic protons are observed, here.

Linearity of the acidic proton bond : As seen in Figures C.1 and C.2, the first peak of $g_{SH}(r)$, which is due to the S-H stretching, is broader than the corresponding one in $g_{O_SH}(r)$. This indicates that the hydrogen interacts predominantly with O_S not with S. Additionally, the $g_{SH}(r)$ is affected by the stretching of the O_S-S bond and possible rotations of the sulfonate oxygens around the sulfur atoms. A triangular inequality, which indicates some deviation from linearity, is

$$r_{SH} < r_{SO_S} + r_{O_SH} \tag{5.7}$$

where r_{SH} is the distance between sulfur and the acidic proton, r_{O_SH} is the distance between the acidic proton and the sulfonate oxygen, and r_{SO_S} is the distance between sulfur and its oxygen.

Hence, the sulfur-oxygen-hydrogen angle (see Fig. 5.8), $\alpha = \widehat{SO_SH}$, is studied in order to explicitly observe the deviation from linearity. Sulfonate oxygens and hydrogens are selected with the distance criteria $r_{SO_S} \leq 1.9$ Å and $r_{O_SH} \leq 1.1$ Å. This enables us to select acidic protons bonded to the sulfonate oxygen. Another criterion, 1.1 Å $\leq r_{O_SH} \leq 1.4$ Å, is also used for selecting protons that may be shared between sulfonate and water.

The normalized cosine angle distributions, $P_{r\leq 1.1}(\cos(\alpha))$ and $P_{1.1\leq r\leq 1.4}(\cos(\alpha))$ are calculated for the water content λ=2.5 (only for this λ value, there is

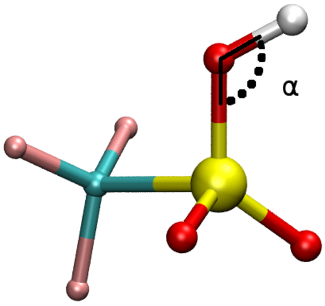

Figure 5.8: Schematic view of the S-O-H angle in CF_3SO_3H molecule

statistically enough acidic protons for both functionals). They are shown in Figure 5.9.

The maxima of the peaks of $P_{r \leq 1.1}(\cos(\alpha))$, are located around 110°. Whereas the peaks corresponding to shared protons ($1.1 \leq r \leq 1.4$) are shifted to larger values (around 120°) than the purely acidic ones. Angle distributions of shared protons are also broader than the purely acidic ones.

$P(\cos(\alpha))$ for two cut-off values 1.0 and 1.1 Å are also compared for pore A and are shown in Figure 5.9 (top left). Since the exact value of the cut-off does not change the distribution much for the other pore models, their angle distributions are calculated only for the cut-off value r =1.1 Å. In all cases, the angles related to the purely acidic protons are smaller than the ones related to the loosely-bonded protons.

Stability of acidic protons: What has been identified as "undissociated" proton in the λ = 2.5 BLYP-pore A seems, however, to be composed of two sub-ensembles, the first one with a sharp peak at 1.0 Å and the second one appears as a shoulder around 1.2 Å in Fig. 5.6. The sharp peak indicates

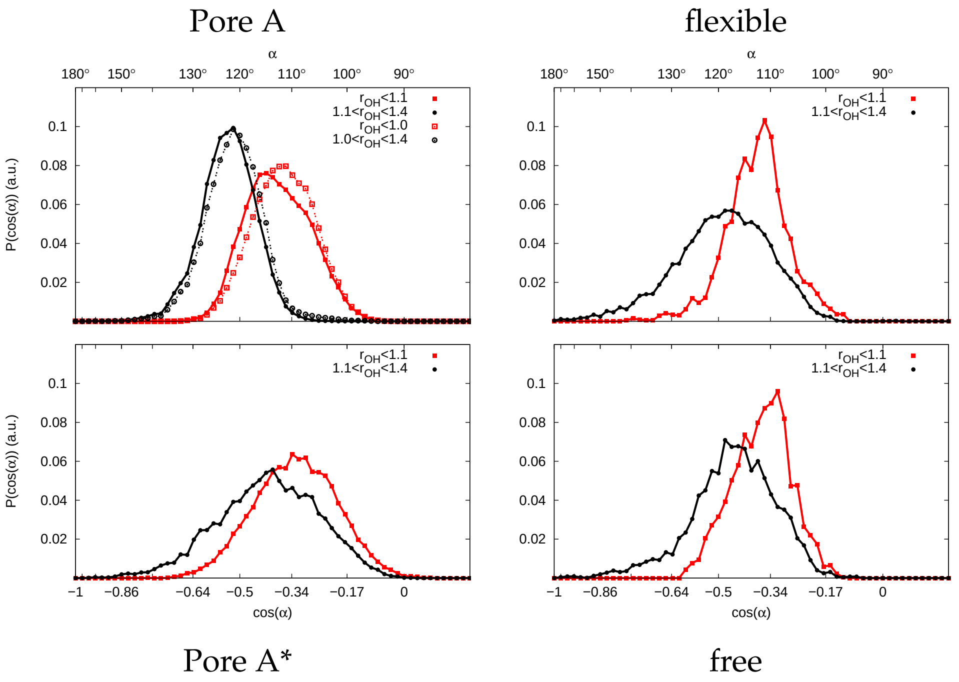

Figure 5.9: Normalized cos(α) distributions (α is the S-O-H angle) at λ=2.5 for the simple model pore A with the BLYP (top left), the HCTH (bottom left) functionals, flexible model (top right), and free model (bottom right). Two ranges for the O-H distance, defined by the cutoff values, 1.1 Å and 1.4 Å have been used, the results are shown in red and black, respectively.

a stable undissociated proton complex. The shoulder shows the breakage and formation of bonds between O and H and indicates a metastable state of the proton complex, which oscillates between undissociated proton and hydronium. This proton state is called as "pseudo-Zundel".

$$-SO_3 - H \cdots OH_2 \rightleftharpoons -SO_3^- \cdots H^+ - OH_2$$

There is not a clear minimum between the first and the second peaks of $g_{O_SH}(r)$, which indicates a possible back and forth hopping of protons between sulfonate groups and water molecules (Fig. 5.6).

The radial distribution functions gives indirect clues about possible back and forth jumps of protons between sulfonate and water. This will be investigated in detail in Chapter 7. We note, however, already here that in the simple model with the HCTH functional, the shoulder (around 1.2 Å) of the first peak of $g_{O_SH}(r)$ does not appear, because of the high fraction of acidic protons and possibly a fast oscillation between the acidic and the pseudo-acidic states. Indeed, since the peaks are broader here than in the BLYP case, they may also include the protons shared between sulfonate and water.

5.1.2.b First shell around the sulfonate groups

The second peak of $g_{O_SH}(r)$s located between 1.4 and 1.7 Å is due to the hydrogen atoms of water molecules or protonated water molecules (see Fig. 5.6). This range of distances are indeed appropriate for having a hydrogen bond.

Firstly, the positions of the maxima of the second peaks are considered. These are shown in Figure 5.10 for all pore models with the BLYP functional. The result indicates that their maxima shift to larger values with increasing water content.

On the other hand, in the pore models with the HCTH functional, identifying a clear second peak is not possible at water content level 2.5 (see appendix C.1) due to the high fraction of undissociated sulfonate groups. This can be associated to the fact that the undissociated sulfonate groups attract the oxygen of water molecules and repels the hydrogens of water molecules. Therefore, a peak located between 1.4 and 1.7 Å can

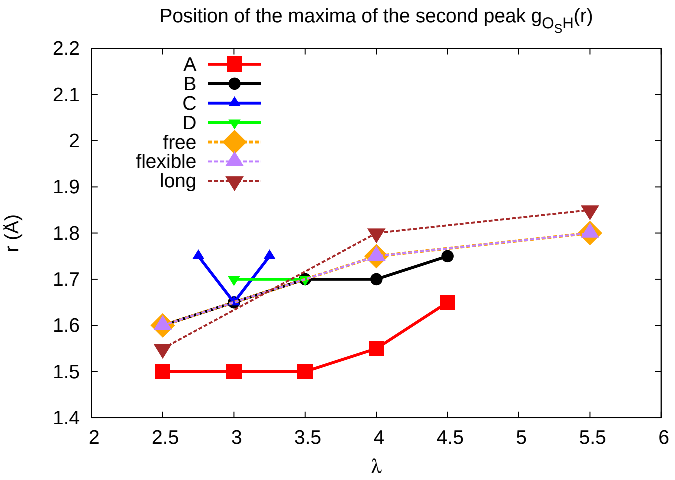

Figure 5.10: Peak position of the second maxima of g_{O_SH} for the simple pore model with the BLYP functional, the free, the flexible, and the parallel backbone (labelled as long) models.

not be observed in $g_{O_SH}(r)$ of a pore model whose sulfonate groups are undissociated.

This effect is valid even for the pore models where partial dissociation is observed, e.g. pore A at the hydration level 4.0. Therefore, a comparison of the second peak maxima is not possible for the pore models with the HCTH functional at hydration levels 4.0 and 5.5, or the amount of shift is smaller than the bin width of the RDF, which is 0.05 Å.

As far as the RDFs of sulfonate oxygen and the other oxygen are considered, the same trend, which is explained above, can also be observed. The $g_{O_SO_W}(r)$s for the simple pore model with the BLYP functional are shown in Figure 5.11. The maxima of the first peak shifts to larger values by increasing water content. This trend is more obvious for pore B than for pore A.

Furthermore, the first peak in pore A includes a shoulder, which is not seen in pore B, located at around 2.8 Å. Inclusion of a shoulder in RDFs shows that there is an additional different type of interaction and that the mobile oxygen may belong to a different molecule than water.

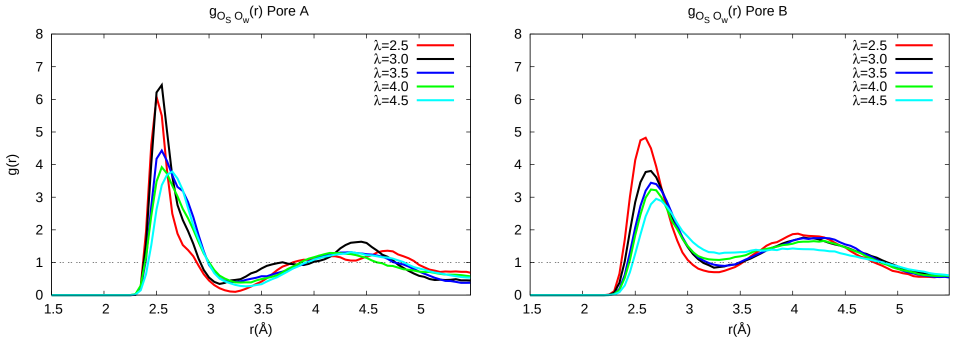

Figure 5.11: Radial distribution function, $g_{O_S O_W}$(r) for pores A (left) and B (right) for the simple model with the BLYP functional.

In order to find out the reason for the shoulder and the effect of the dissociated protons on the average distance between oxygens, the mobile oxygens are decomposed into two classes, which are protonated oxygens (hydronium) and not-protonated oxygens (water oxygens). Then, their RDFs are calculated and shown in Figure 5.12 for the simple pore model with the BYLP functional. The RDFs belonging to the other pore models can be found in appendix C.1 in Figures C.5, C.6, and C.7.

The decomposition of the RDFs proves that the shoulder, which appears in RDFs of sulfonate oxygen and the mobile oxygen for pore A (Fig. 5.11), is due to the non-protonated water oxygens. As the water content increases, the contribution due to the oxygen of the water molecules in $g_{O_S O_W}(r)$ increases too. This leads the peak of the RDFs to shift to larger values. For

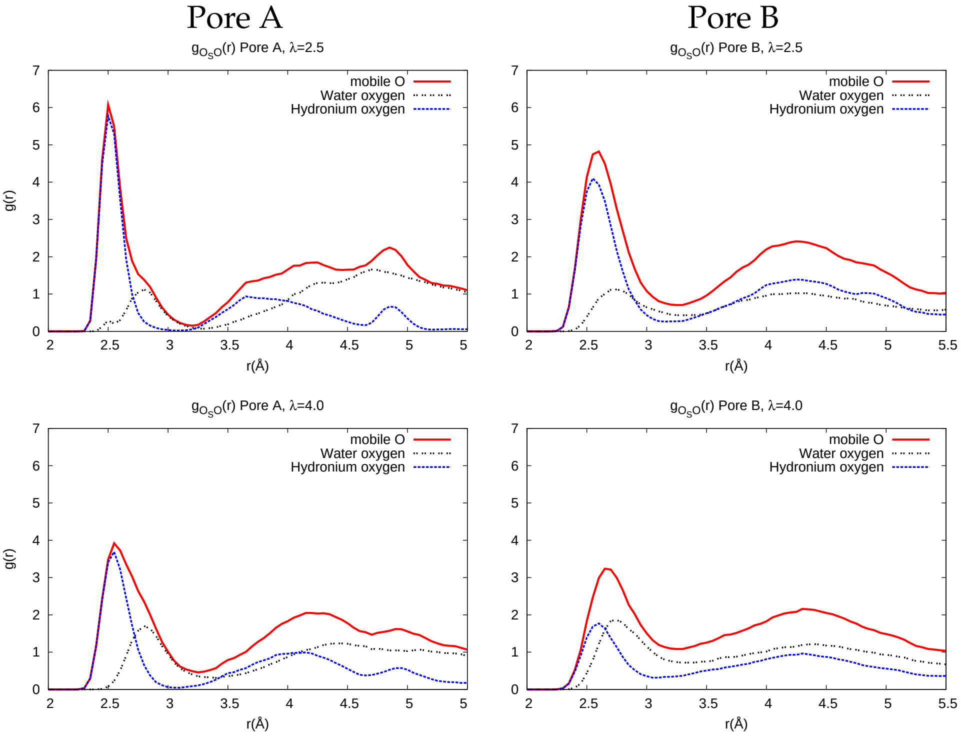

Figure 5.12: RDF of sulfonate oxygen and all mobile oxygen, composed of water and hydronium oxygen for λ=2.5 (left) and 4.0 (right) for simple helical model with the BLYP functional.

pore A at λ=4.5, the shoulder can not be distinguished anymore.

The RDFs belonging to water oxygen in pore B, even at low hydration level, do not have shoulder, since their peaks are broader than the ones in pore A. Hence, the sum of the peaks due to two decompositions becomes also smoother in pore B than that of pore A.

Furthermore, in all pore models, it is found that the average distance between hydronium oxygen and sulfonate oxygen is shorter than the one between water oxygen and sulfonate oxygen. These distances (2.5 and 2.8 Å) are related to the length of the hydrogen bond between hydronium and sulfonate oxygens and the one between water and sulfonate oxygens.

5.1.3 The structure of water in ionomer pores

Increasing the number of water molecules in ionomer pore models affects not only the structure of the sulfonate groups but also the water itself. As it was explained before in Chapter 2, the connectivity of the water channels mainly depends on the hydration level in an ionomer. The interaction between water molecules is one of the key factor determining the connectivity of the water channels.

In order to elucidate the interaction between water molecules, the RDFs of the hydrogen and mobile oxygen atoms are calculated without taking into account that the water molecules are protonated or not. These are shown for pores A and B of the simple model with the BLYP and the HCTH functionals in Figures 5.13 and 5.14, respectively. The RDFs belonging to the free and the parallel backbone (long) models are shown in Figure 5.15.

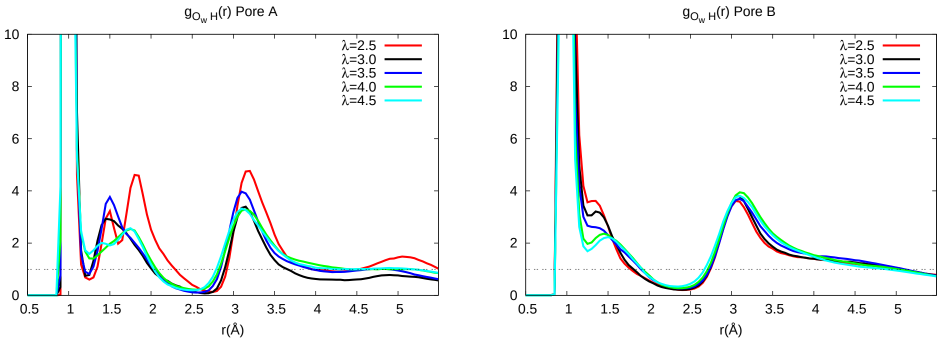

Figure 5.13: Ow-H RDFs for the fixed simple models with the BLYP functional.

In all of the RDFs, the first peak, which is located at around 1.0 Å, is due to the intramolecular interaction between the hydrogen and oxygen of a water molecule. It is followed by a broad peak, whose ranges are between the first peak and the minimum located at around 2.5 Å. This broad peak is due to the hydrogen bonded molecules, which may also include hydronium and Zundel complexes. A detailed analysis of the RDFs of the protonated water molecules will be given in Chapter 7.

In pore A of the simple model with the BLYP functional, the second peak is composed of two peaks, which are located at around 1.5 and 1.8 Å. This dual feature is not observed for pore B. A clear minimum between the first and the second peaks is observed in pore A. Whereas in pore B, the second peak appears as a shoulder for low hydration levels. A minimum between the peaks can be observed only for λ larger than 3.5.

Additionally, the maxima of the second peaks slightly shift to larger values as the water content increases. This trend is similar to the RDFs of the sulfonate oxygen and the water oxygen, which was explained above, and can be associated to the increasing contribution of not-protonated water molecules. The dissimilarities between the RDFs of pore A and B may indicate that the dynamical properties of the water in both pores may also show different behavior.

The significant differences observed between pores A and B of the simple model with the BLYP functional are not seen while comparing pores A and B model with the HCTH functional. Within these pores (HCTH), neither the dual feature of the second peak nor the trend of changing the position of the maxima with increasing water content are observed. The effect of the functionals on the water structure is also shown in a 3-dimensional analysis in Section 5.3.

In the free and parallel backbone models (see Fig. 5.15), there is an

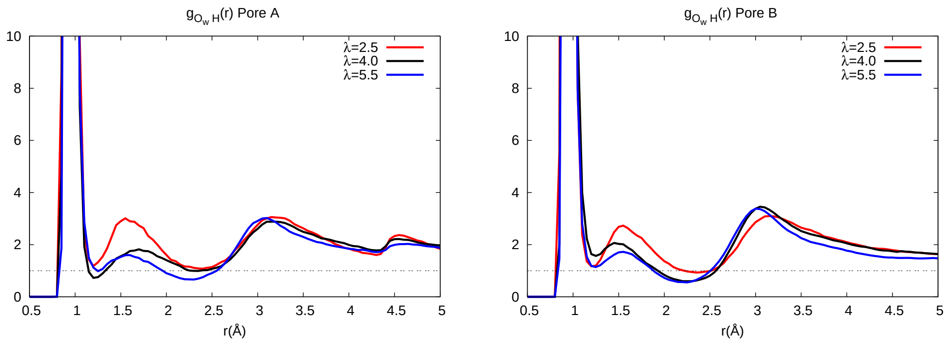

Figure 5.14: Ow-H RDFs for the fixed simple models with the HCTH functional.

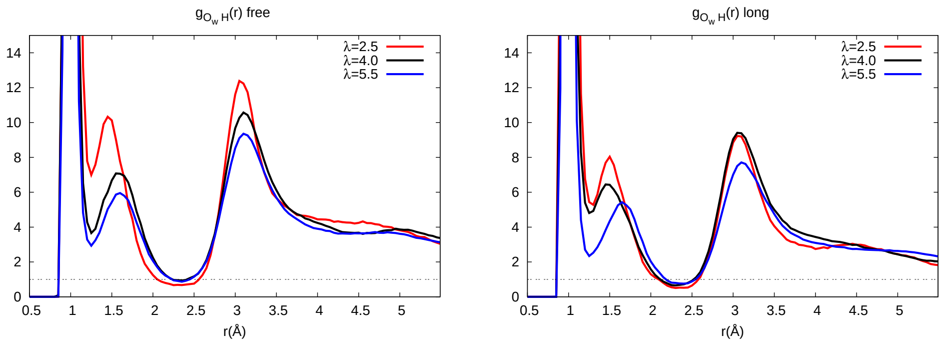

Figure 5.15: Ow-H RDFs for the free and the long models

overlap of the first and the second peaks of the RDFs. This is similar to the RDFs of the simple pore model with the BLYP functional at water contents 4.0 and 4.5. The second peak can be differentiated from the first one due to a minimum located at around 1.2 Å. Increasing water contents leads also to a slight shift in the position of the second peaks maxima towards larger values.

Lastly, the height of the minimum, located around 2.5 Å, between the second and the third peaks in the simple pore models with the BLYP functional is lower than the ones belonging to the other pore models. The RDFs between oxygen of water molecules are shown in appendix C.1.

5.2 Proton Delocalization

5.2.1 Density maps of the proton complexes

The fixed and simple geometrical pore structures allow to project the coordinates of atoms onto a plane perpendicular to the channel 'axis'. Here, it is simply the laboratory xy-plane. For this purpose, the xy-plane is divided into small grid elements and the positions of selected atoms are mapped at every time step onto this grid. The number of occurrences in each grid element are then normalized by the simulation time step and particle number, yielding the probability of observing the selected atom with the given x and y coordinates anywhere on top or below the plane.

We first calculate the oxygens of the sulfonate groups and determine their density maps; they are shown in Figs. (5.16, C.11 , 5.17 and C.12) as blue spots such that the intensity of the color is proportional to the probability. In these graphs the positions of the sulfonate oxygens change very little since they are bonded to fixed carbon atoms. They can be considered as reference points for visual recognition of the pore structure.

Next the density maps of the protonated oxygens, shown in green, are calculated and merged on top of the sulfonate oxygens plot. Protonated oxygen, O_p, refers in the acidic case to the oxygen of sulfonate group to which a proton is bonded. This undissociated proton state leads to an overlapping of the green and blue colors. In the hydronium state, O_p is the oxygen of the hydronium ion; in the pseudo-Zundel and Zundel states, an oxygen atom that has a smaller distance to the central hydrogen, is assigned as O_p.

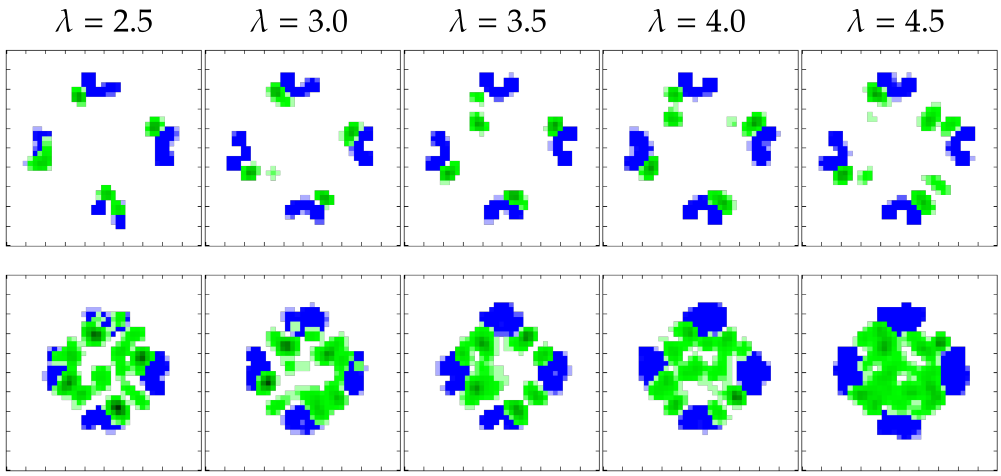

Figure 5.16: Density map of the simple model with the BLYP functional. The center of proton complex, O_P (green), and the oxygen of sulfonate groups O_S (blue) in pores A (top) and B (bottom).

In pore A of the simple model with the BLYP functional, the distribution of the center of proton complex, O_p, is located at the sulfonate groups in the case of undissociated protons. It is located around the sulfonate groups in the case of dissociated protons. In general, O_p is less distributed and mobile in pore A then the one in pore B. The distribution in pore B diffuses towards pore center as the water content increases. Its area enlarges and fills almost all of the pore area when the λ becomes 4.5.

The density map of O_p in pore models with the HCTH functional is similar to the one with the BLYP ones. The distribution of O_p is observed to cover the pore as the water content increases in pore B. In pore A, it is less distributed and more localized than the one in pore B. In pore A only for λ=5.5, the center of the proton complex can be observed close to the pore center. The less-distributed density map of O_p in pore A can be associated to the close sulfonate spacing of this pore.

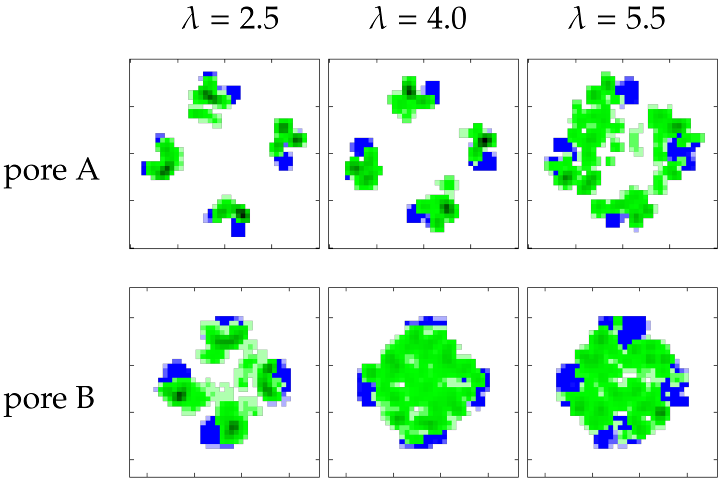

Figure 5.17: Density map of pores A and B of the simple helical model with the HCTH functional. Center of proton complex, O_P (green), and sulfonate oxygens, O_S (blue).

5.2.2 Distribution of the proton complexes around the channel axis

The distribution of the 2-dimensional distances between atoms and the central z-axis of pore has been calculated as follows. We set

$$\delta(r - r_i(t)) = \begin{cases} 1 & r \leq r_i(t) < r + \Delta r \\ 0 & \text{otherwise} \end{cases} \tag{5.8}$$

where Δr is the bin width, and $r_i(t) = \sqrt{(x_i(t) - x_c)^2 - (y_i(t) - y_c)^2}$ is the 2-D distance between the ith atom and the central axis, which is specified by the coordinates of geometrical center of the simulation box, x_c and y_c. The time average is equal to the probability of finding the particle at a distance r away from central axis.

$$P_i(r) = \langle \delta(r - r_i(t)) \rangle_t \tag{5.9}$$

Summation over i leads to $P(r) = \frac{1}{N} \sum_i^N P_i(r)$, the normalized number of particles whose 2-D distance from the central axis. Division by the volume of cylindrical shell, $l_z\ 2\pi\ r^2 \Delta r$, where l_z is the dimension of the simulation box in z-direction, results in g_{cyl}(r), the normalized number of particles per volume of cylindrical shell with thickness Δr,

$$g_{cyl}(r) = \frac{P(r)}{l_z \pi (2\, r\, \Delta r + \Delta r^2)} \tag{5.10}$$

where l_z is the box dimension in z-direction. The value of Δr is chosen as 0.1 Å.

The cylindrical distributions of protonated oxygen, g_{cyl}, of the simple model pores A and B for both functionals are calculated and shown together with the cylindrical distributions of oxygen of sulfonate in Figure

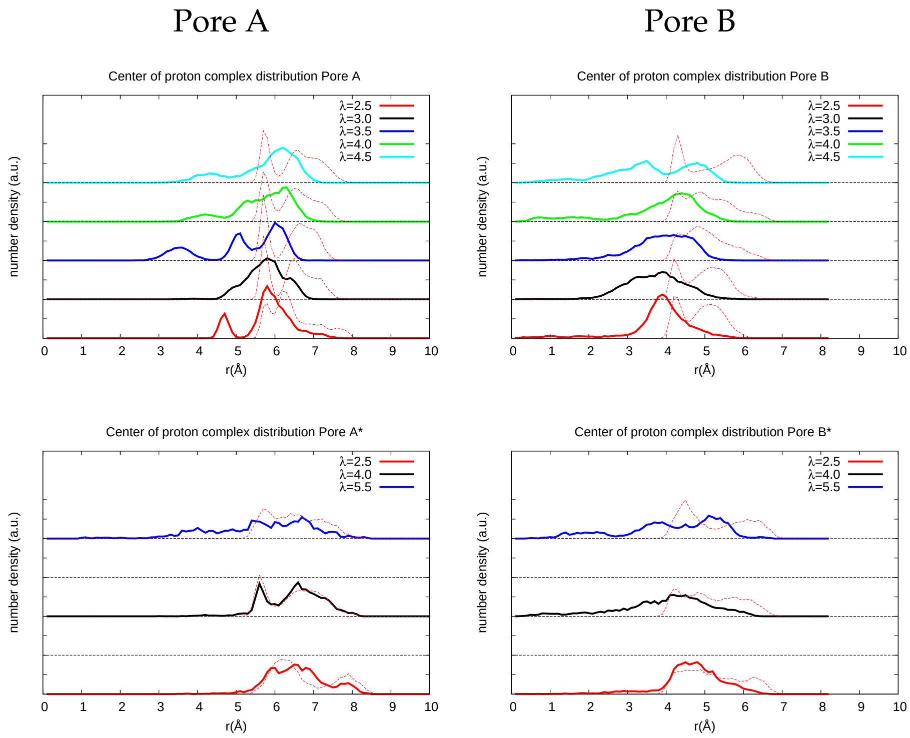

Figure 5.18: Distribution, in cylinder coordinates around the channel axis, of the proton complexes for the simple helical model with BLYP (bottom) and HCTH (bottom) functionals. For visibility, the curves are shifted and the reference axis are shown as dotted lines.

5.18. The definition of protonated oxygen, Op, includes oxygen atoms belonging to hydronium ions and the (acidic) oxygens of the sulfonate group when there is a hydrogen atom within 1.35 Å.

In the pore A for both functionals, the probability to find protons around the central axis of the channel ($r < 3$ Å) are almost zero. The only exception is the pore A with the HCTH functional at λ =5.5. The density maps of protonated oxygen also show that protons are located near the sulfonate group and free no-proton-land exists in the center of the channel, which is shown in Figures 5.16 and 5.17.

However, in the pore B, which is narrower than the pore A, this probability is higher than zero, which proves that the delocalization of protons is possible. It becomes more likely and evident for the water content higher than 4.0. As the water content increases, the protonated oxygens move away from sulfonate groups towards the center of the channel in pore B. The O_S-hydronium RDFs support also this conclusion, which are shown in Figures 5.12 and C.5.

5.3 Spatial Distribution of the Water Molecules in the Channel

5.3.1 Density maps of the oxygen atoms

The distribution of water oxygens in the simple pore models is analyzed without characterizing them as protonated or not by calculating the number density of mobile oxygens (i.e. oxygen atoms not fixed at the channel wall). The number densities of these oxygens are calculated for the last 20.0 ps of the trajectories in order to compare them with equivalent statistics. These number densities are normalized. The three dimensional (3-D) number densities are shown in Figure 5.19 for pores A and B with a hydration level of λ=2.5 and both the BYLP and HCTH functionals.

Due to the simple geometry, the 3-D number densities are mapped directly onto the xy-plane, as explained for the protonated oxygens in Section 5.2. They are shown in Figure 5.20 only for pores A and B with the BLYP and HCTH functionals.The dark red color shows the region with higher density.

At λ=2.5 pore A, it is observed that the pore is not entirely filled with water, with both functionals. Furthermore, in the simple model with the BLYP functional, an ice-like water structure is observed. As the water content is increased, e.g. to 4.0 in pore A, the darker spots become more evenly distributed. At Pore B, the ice-like water structure disappears for λ=4.0.

The figures in the bottom row of Fig. 5.20, corresponding to the density maps of water oxygens with HCTH functional, do not have dark spots,

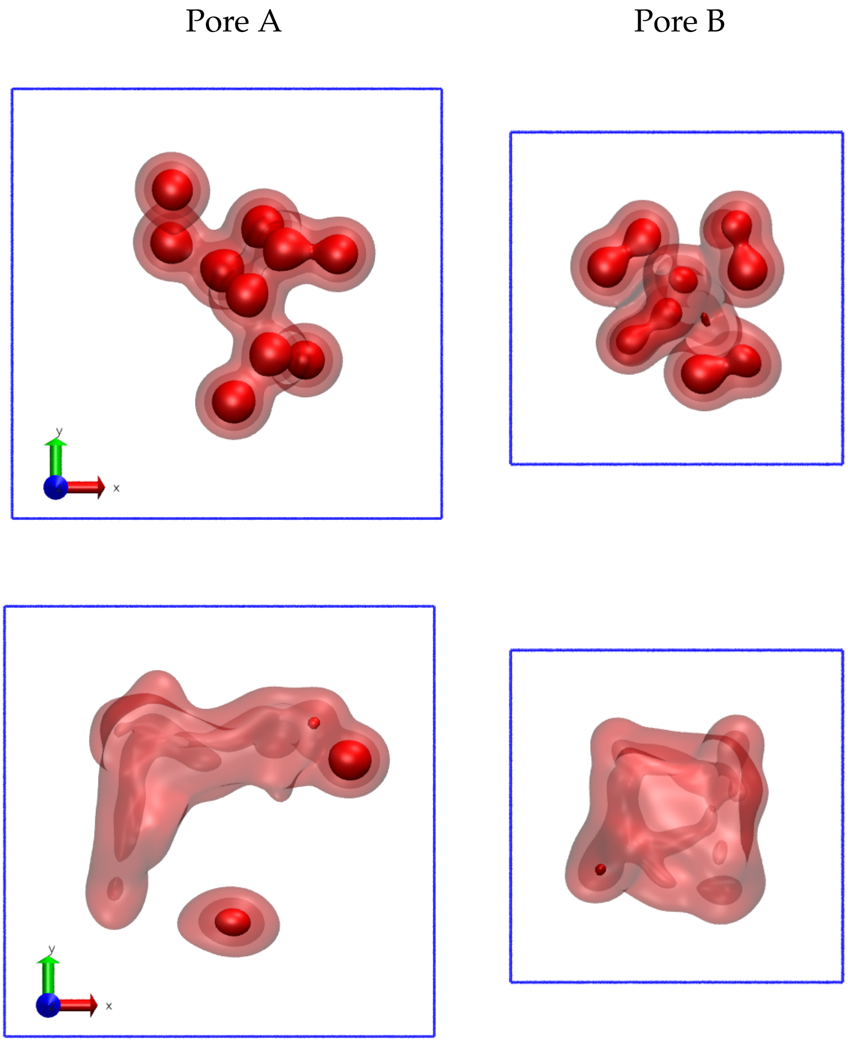

Figure 5.19: Top orthographic view of the 3-D number densities of mobile oxygen with a hydration level of λ=2.5, in the simple helical model for pores A and B with the BLYP (top) and the HCTH (bottom) functionals. Blue lines corresponds to the boundary of the simulation boxes. The graphics were prepared with vmd [84], using the tachyon ray tracing [179] feature

except for one in pore A at λ=2.5. This clearly indicates that the oxygen (of water) is more mobile here than with the BLYP functional. Since the mobility of the protons depends on the water dynamics, a higher proton mobility is expected with the HCTH functional.

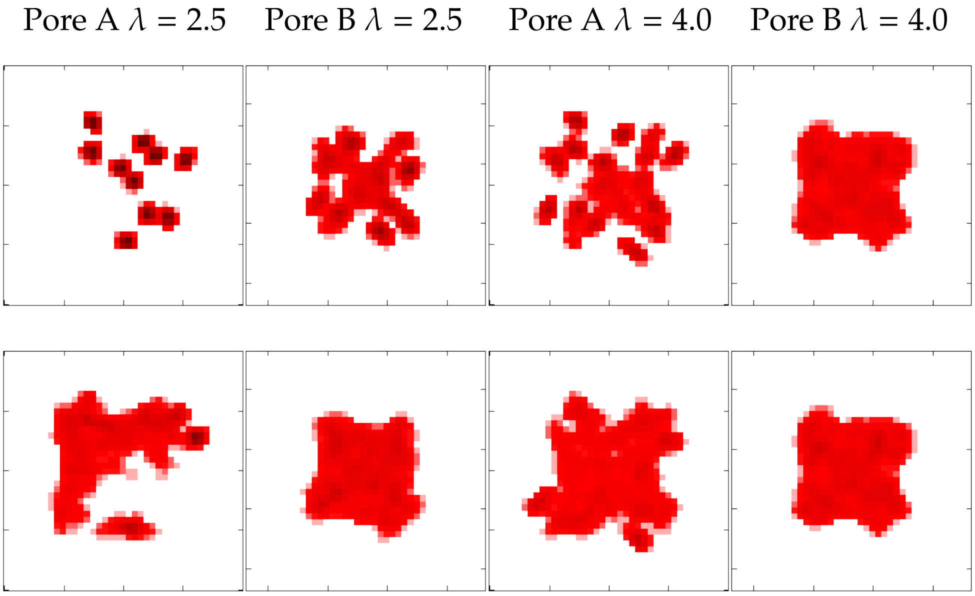

Figure 5.20: Density map of the water oxygens for the simple helical model with the BLYP (top) and HCTH (bottom) functionals. The water structure with the BLYP ones for low density and low water content becomes ice-like. Water is more evenly distributed within the HCTH simulations

5.3.2 Tetrahedrality of the water

In bulk water at room temperatures, the water molecules are thought to form a loosely tetrahedral arrangement. The tetrahedrality of the first neighbor shell of a water molecule has been investigated in many instances [125, 8, 94] from simulations. There is a consensus that while this ice-like tetrahedrality is still apparent when the averaged (over suitable times!) positions of the neighbors are used, it appears at best as extremely distorted when instantaneous positions are considered. Different models give quantitatively different results in this respect [15, 96, 117, 164].

In order to compare the effect of the BLYP and the HCTH functionals on the tetrahedral structure of water in the channel, the three dimensional number density of oxygen atoms of water molecules is calculated in the molecular frame. The axes of the molecular frame are chosen such that the atoms of the water molecule define the $x-y$ plane and the direction of $+x$-axis divides the angle between hydrogen atoms into halves (see Fig. 5.21).

The coordinates of the neighboring oxygen atoms are projected into cubic grid elements in the molecular frame. Then the number density of these atoms is calculated by averaging the number of observation for each grid element over time frames. A cutoff distance of 3.6 Å is chosen to include all possible oxygen atoms in the first spherical shell of the water oxygen, which is defined by the first minimum of the RDFs of oxygen-oxygen of water molecules (see Figs. C.8 and C.9).

Only pore B of the simple model with water content level, λ =4.0, is

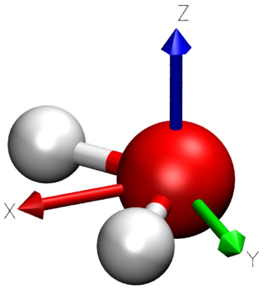

Figure 5.21: Molecular frame for a water molecule: its orientation with respect to axes.

considered for this analysis. The number density of water oxygen atoms for both functionals are shown in Figure 5.22. It indicates that the tetrahedrality is less pronounced with the HCTH functional than with BLYP. As a consequence of this, one can also argue that the strength of the hydrogen bonds between water molecules is also less pronounced with the HCTH functional than the one with the BLYP functional. Therefore, a frozen water structure is more likely to be expected from the simulations with the BLYP functional.

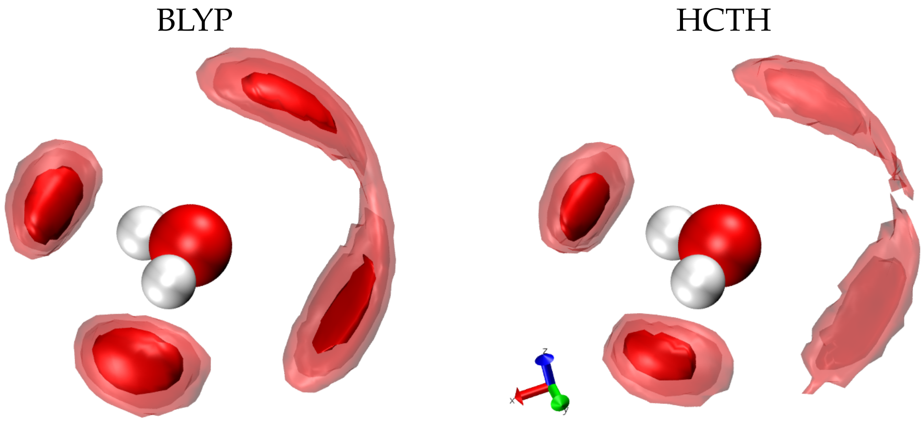

Figure 5.22: Comparison of 3-dimensional normalized number density neighboring water oxygen atoms around a water molecule within a cutoff distance of 3.6 Å. Pore B with water content, λ =4.0. Three isosurfaces are shown such that the red colored opaque surface covers the highest number density, other two half-transparent surfaces cover for lower values respectively.

5.4 Conclusions

It was found that sulfonate groups influence excess proton solvation, as well as the proton hydration structure, by stabilizing a more Zundel-like ($H_5O_2^+$) structure in their first solvation shells [45].

The AIMD trajectories showed that dissociation of the acidic proton increased with increasing density of sulfonic acid groups; however, greater densities also brought about trapping of the dissociated proton. Similar systems without fluorination of the carbon nanotube walls [70] exhibited a propensity for the formation of Zundel cations ($H_5O_2^+$), while the fluorinated systems favored hydrated structures involving hydronium ions or hydrated H_3O^+ species depending on the amount of water in the system.

The following conclusions can be drawn

- It is more probable to have undissociated sulfonate groups for low hydration level. Sulfonate spacing also affects the dissociation probability.

- Protons become more delocalized as the number of water molecules increases inside the pore with a favorable sulfonate spacing. Oxygen atoms of the sulfonate groups become more mobile when increasing the water content. For a pore structure with larger sulfonate spacing, it is possible to have more mobile sulfonate groups.

- The average distance between sulfonate oxygen and the other oxygen atoms increases with increasing water content. This is also affected by the dissociation rate. Even dissociated protons are localized between sulfonate groups (see Fig. C.11), which behaves as a dynamical trap for protonated water molecules. This trapping effects decreases as sulfonate spacing and water content increase.

- After dissociation and being free from sulfonate trapping, protons move away from the sulfonate groups towards the center of the pore. It is expected that these protons near the center of the pore show higher mobility; at least, this is valid for high water content and in pores without sulfonate trapping. It is certain that being away from sulfonate groups is a required condition for high mobility at high water content. But, is it also a sufficient condition? We will address this question in Chapter 7.
- Anisotropic distribution of water molecules inside narrow pores supports that water exhibits a different behavior than in bulk.
- The BLYP and the HCTH functionals have differences in describing the tetrahedrality of water, dissociation fractions and sulfonate trapping at same water content. This leads us to expect that faster molecular dynamics will be observed with the HCTH functional than with the BLYP one. Additionally, this effect can be seen on the hydrogen bond dynamics, which will be introduced in the next chapter, and the diffusion of atoms.

Chapter 6

Hydrogen Bond Dynamics

Hydrogen bonds are attractive interactions between an electro-negative atom and a covalently-bonded hydrogen atom. They are much weaker than covalent bonds, but often stronger than van der Waals′ interactions. Hydrogen bonds arise from the effect of partial charge distribution of polar molecules on hydrogen atoms of neighboring molecules. Hence the geometry of polar molecules as well as the distance (and orientation) of hydrogen atoms to electro-negative sites changes strength and nature of hydrogen bonds.

Hydrogen bonds play a crucial role in determining many complex chemical reactions, equilibrium structures as well as dynamical quantities of substances. For example, in biology, two strands of the DNA double helix are held together by hydrogen bonds. They are also essential to the working of the genetic code contained in DNA [47]. Water is one of the peculiar examples that shows the crucial role and effects of hydrogen bonds in its dynamical properties.

Indeed, the typical energy of hydrogen bonds ranges from 5 to 30 kJ/mol. The small energy threshold of an individual hydrogen bond enables repetitive breaking and formation of hydrogen bonds under normal conditions. However, water remains a liquid over a wide range of temperature, because it contains numerous hydrogen bonds. A water molecule in bulk tends to have about four hydrogen bonds with its neighboring water molecules. The energy required to break multiple hydrogen bonds causes water to have a high boiling point. The number of hydrogen bonds is enhanced by their cooperative features for bulk water [211].

High numbers of hydrogen bonds and their fluctuative behavior, which is enhanced by breakage and formation, affect many dynamical properties. Among them the high diffusion rate of protons in water is important for polymer electrolyte membrane fuel cells (PEMFC).

The structure and dynamics of water inside PEMFC is indeed different from the bulk, especially for low water content. In PEMFC, water interacts with hydrophilic sulfonate groups, and is surrounded by hydrophobic backbones. It includes excess protons. Mainly because of these reasons, structural and dynamical properties (such as mobility) of water are sensitive to the change of hydration level. Since these features are related to hydrogen bonds, a detailed investigation of the dynamics of hydrogen bonds is required.

Hydrogen bonds, their life times, networks of hydrogen-bonded water molecules, and their spectra together with the dangling O-H bonds in PEMFC have been analyzed by many experimental and computational groups. NMR, X-Ray, FTIR, A-FTIR and femtosecond spectroscopy have been used in experiments in order to obtain information about hydrogen bond dynamics [89, 48, 47, 73, 123]. Computationally, classical MD with different force fields and methods on larger scale, and *ab initio* MD on a smaller scale are applied to get insight into the dynamics of water in PEMFC [124, 100, 85] [131, 193, 20, 77].

For example, as far as breakage and formation of hydrogen bonds are concerned, the lifetime of hydrogen bonds and their decay rates give clues about chemical reactions including proton transport. Mobility of proton transfer is deduced through a detailed analysis of H-bonds [124, 111, 131, 193, 20].

In this chapter, the effect of water content and sulfonate groups spacing on, firstly, the hydrogen coordination number, which is the number of atoms around hydrogen atoms, will be studied. Secondly, the probability and number of hydrogen bonds with respect to angle and radial distribution functions will be addressed. Then, the number of hydrogen bonds per water molecules and the life time of hydrogen bonds and dangling O-H bonds will be discussed. This will be followed by a brief discussion on hydrogen bond dynamics.

6.1 Hydrogen Coordination Number

The number of oxygen atoms in the neighborhood of a hydrogen atom is the coordination number of this hydrogen atom. The neighborhood is defined by the distance between hydrogen and oxygen atoms, which has to be smaller than a chosen cutoff radius, r_{cutoff}, or equal to this value (see Fig. 6.1). For an oxygen atom with index j and a hydrogen atom with index i, these criterion can be represented by the unit step function $\theta(r_{cutoff} - |r_{H_iO_j}|)$, which is unity, if the value inside the bracket is not negative, otherwise it is zero. A summation of this unit step function for all oxygen atoms results in the coordination number of the hydrogen atom with index i

$$c_i(t) = \sum_{j=1}^{n_O} \theta(r_{cutoff} - |r_{H_i\,O_j}(t)|) \tag{6.1}$$

where $r_{H_i\,O_j}$ is the distance between the hydrogen atom and oxygen atoms, and n_O is the total number of oxygen atoms. The hydrogen coordination number, $c_{i,O,r_{cutoff}}$ is labeled by the hydrogen atom index (i), the oxygen atoms (i.e. " O_S" or "O_W") and the cutoff radius (r_{cutoff}). They will not be always specified in the following, unless it is necessary. Since the distance between the atoms is involved, it inherently depends on time, hence, is a dynamical quantity.

The average number of oxygen atoms around a hydrogen atom within the cutoff radius is calculated by averaging the hydrogen coordination number over time and hydrogen index, as shown in Eq. 6.2. Indeed, it equals also to the integral of the radial distribution function (RDF) of hydrogen and oxygen atoms with boundary of integral up to the cutoff radius

$$\langle \mathrm{c_i(t)} \rangle = \frac{1}{\mathrm{n_H}}\frac{1}{\tau}\sum_{\mathrm{t=0}}^{\tau}\sum_{\mathrm{i=1}}^{\mathrm{n_H}} \mathrm{c_{i,O,r_{cutoff}}(t)} \quad = 4\pi \int_0^{\mathrm{r_{cutoff}}} g_{\mathrm{HO}}(r)\rho\, dr \tag{6.2}$$

where τ is the number of time frames, and $\mathrm{n_H}$ is the total number of hydrogen atoms.

The hydrogen coordination number can then be used as a dynamical selection criteria for sampling the hydrogens. As an example, the RDF of oxygen and hydrogen atoms with coordination number $\mathrm{c_i}$=1 and $\mathrm{c_i} \geq 2$ are calculated. Their summation equals to the usual RDF of hydrogen and oxygen atoms and is shown as

$$g_{\mathrm{OH}}(r) = \quad g_{\mathrm{OH_{c_i=1}}}(r) + g_{\mathrm{OHc_i\geq 2}}(r) \tag{6.3}$$

where $g_{\mathrm{OH_{c_i=1}}}(r)$ includes only those hydrogen atoms belonging to dangling O-H bonds with $\mathrm{c_i(t)}$ equals to one. In the same way, hydrogen atoms with more than one oxygen neighbor within the cutoff radius are included in $g_{\mathrm{OH_{c_i\geq 2}}}(r)$ calculations, if $\mathrm{c_i}$ is greater than 1. The same normalization constant is used for RDFs to satisfy the equation 6.3.

The corresponding RDFs with the cutoff value of $\mathrm{r_{cutoff}}$ =2.0 Å for the simple pore model with λ =2.5 are shown together with the average hydrogen coordination number, $\langle \mathrm{c_i(t)} \rangle$, and the integral of the RDFs of oxygen and hydrogen in Figure 6.2. Within cutoff radius, an overlap of $g_{\mathrm{OH_{c_i=1}}}(r)$ and $g_{\mathrm{OH_{c_i\geq 2}}}(r)$ occurs at the first peak, which corresponds to intra-molecular interactions. The following two peaks, which appear only for $g_{\mathrm{OH_{c_i\geq 2}}}(r)$, indicate the existence of two different types of hydrogen bonded molecules, which will be discussed in Chapter 7.

For the outside of the cutoff radius, the peak belonging to $g_{\mathrm{OH}_{c_i=1}}(r)$ is located at 3.25 Å and the peak belonging to $g_{\mathrm{OH}_{c_i\geq 2}}(r)$ is located at 3.1 Å. The difference in the peak positions, which are due to the second shell of oxygens around a hydrogen, indicate that the structure of water without dangling O-H bonds is more compact than the one including a dangling O-H bond. Furthermore, the existence of the $g_{\mathrm{OH}_{c_i=1}}(r)$ between the cutoff distance and the minimum of the $g_{\mathrm{OH}}(r)$ (between 2.4 and 2.6 Å) indicates that our choice for the cutoff value is too small.

Therefore, the RDFs are calculated by using two different cutoff values, which are $\mathrm{r}_{\mathrm{cutoff}}$ =2.0 and 2.4 Å. The first peak of RDFs with $\mathrm{c}_\mathrm{i} = 1$ and $\mathrm{c}_\mathrm{i} \geq 2$ for both cutoff values is shown for the simple pore model in Figure 6.3.

The first peak of $g_{\mathrm{OH}_{c_i=1}}(r)$ is at distances shorter than 1.0 Å and is zero until cutoff radius. This represents only hydrogen atoms of dangling O-H bonds. The oscillation of dangling O-H distances in the first peak is bounded in the smaller interval between 0.95 and 1.0 Å. On the other hand, the first peak of $g_{\mathrm{OH}_{c_i\geq 2}}(r)$ is broadened and shifted to larger values. This broad peak leads also to broader spectral lines with smaller intentsities when compared to free O-H vibrational spectra. Vibrational spectra will be discussed explicitly in Chapter 8.

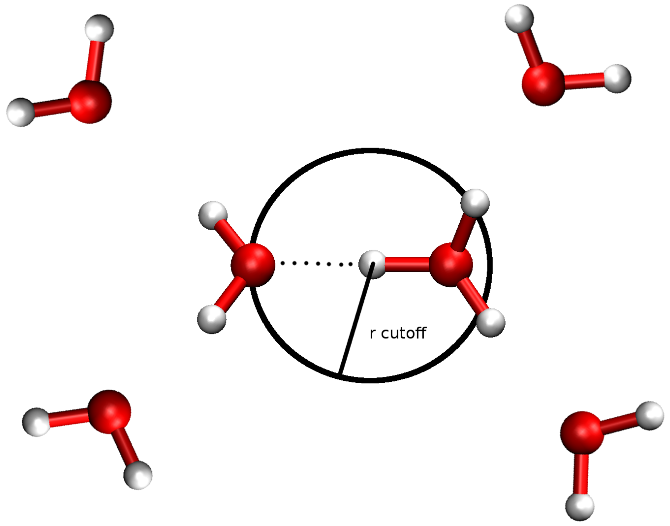

Figure 6.1: A schematic view represents the hydrogen coordination number, c_i, which is the number of oxygen atoms around the hydrogen atom with index, i. Here it is shown that the hydrogen atom located at the center of the sphere with a given cutoff radius has a coordination number of two.

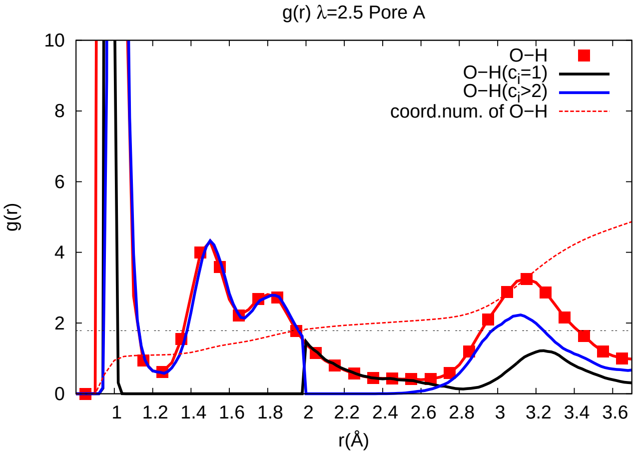

Figure 6.2: The radial distribution functions of oxygen and hydrogen atoms with c_i=1 (black) and with c_i ≥2 (blue) are shown. The sum of these two functions equals to the RDF of oxygen and all hydrogen atoms (red filled squares). The dashed horizontal black line corresponds to the average number of oxygen around hydrogen atoms. It intersects the dashed red line, which corresponds to the integral of the g_{OH} in the pore A with λ =2.5, at the cutoff value of r_{cutoff} =2.0 Å.

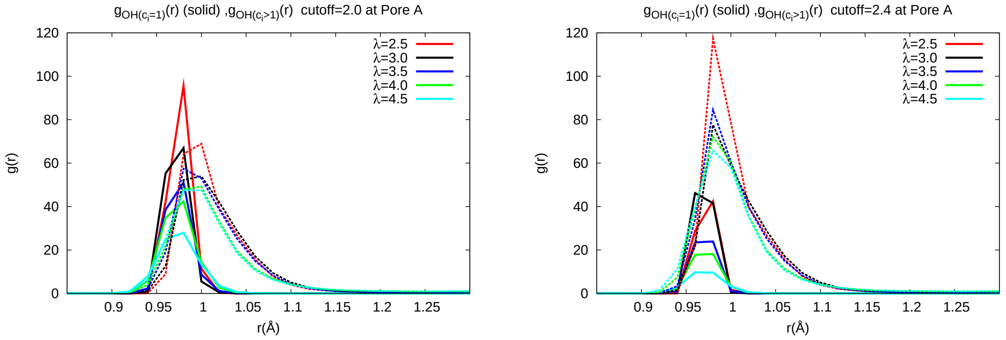

Figure 6.3: Radial distribution functions of the oxygen and the hydrogen atoms for pore A. Hydrogens with c_i=1 and c_i ≥2 are shown in solid lines and in dashed lines, respectively. Two cutoff values are chosen; r_{cutoff}= 2.0 and 2.4 Å.

6.1.1 O-H-O linearity

Another structural property related to the intermolecular interaction is the linearity of the triplets, O-H-O, which include a central hydrogen atom and two neighboring oxygen atoms. In order to investigate this property, the distribution of the angle α, which is $\mathrm{O}\cdots\widehat{\mathrm{H}\cdots}\mathrm{O}$, is calculated for the hydrogen atoms with coordination number equal to and greater than 2. If there are more than two oxygen atoms around a hydrogen within the cutoff radius, only the two closest oxygens are included in the angle distribution function. The distribution functions are normalized and hence the areas under the curves are unity.

Firstly, the effect of the cutoff radius of the hydrogen coordination number on the angle distribution is considered. The corresponding distributions are shown in Figure 6.4 for the simple pore model with the BLYP functional at the water content 3.

Increasing the cutoff radius results in a slight shift to lower values of the maximum of the angle distribution. The probability of having a smaller angle increases with a larger cutoff radius. As it is expected, with larger distances, deviations from linearity become probable. Furthermore, the effect of increasing the cutoff radius on the angle distribution can also be interpreted as an increasing contribution from weaker-hydrogen-bonded oxygens, if the strength of a hydrogen bond is assumed to decrease by enlarging the distances.

Secondly, the effect of the hydration level on the angle distribution is considered. The angle distribution functions with cutoff radius 2.4 Å are

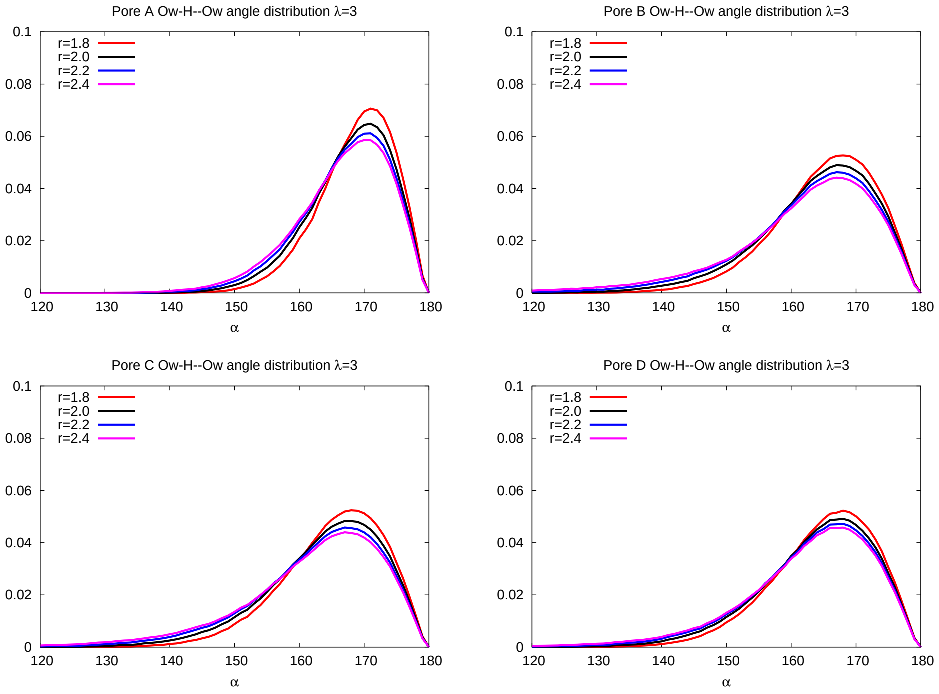

Figure 6.4: Hydrogen bond angle distribution with various cutoff radii for λ=3.

shown in Figure 6.5 for the same model at all water contents. Similar to the effect of cutoff radius, the maxima shift to lower values by increasing the water content. These effects are more pronounced for pore A than for the other pores.

The results indicate that the dynamical properties of the molecular system related to the hydrogen bonds, i.e., hydrogen bond lifetime, are expected to be affected by increasing hydration level.

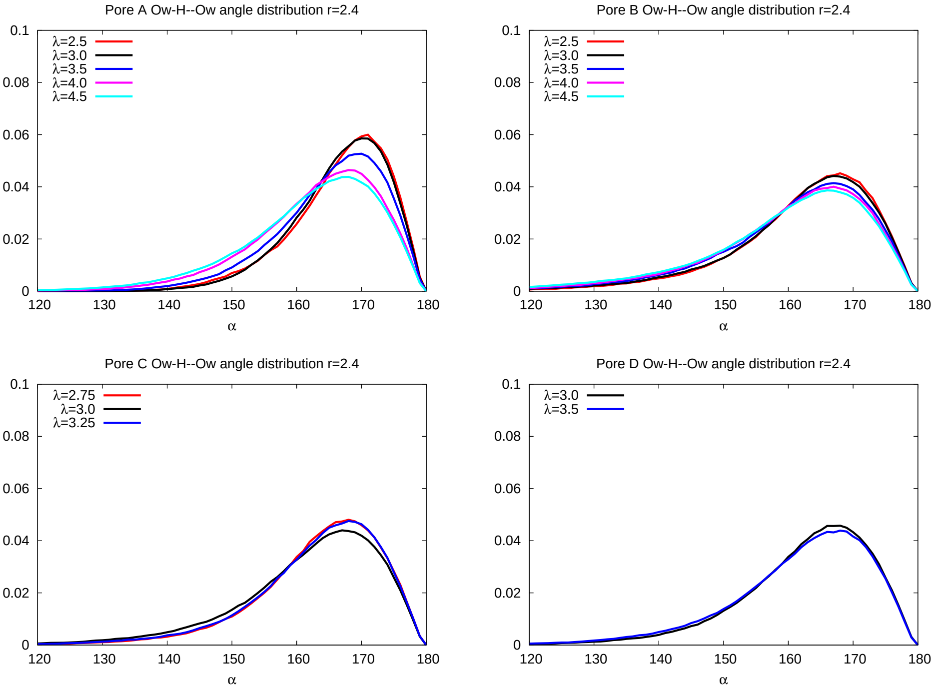

Figure 6.5: Hydrogen bond angle distribution with cutoff radius r_{cutoff}=2.4 for all water contents of the simple pore model.

6.2 Hydrogen Bonds

The hydrogen coordination number explained in the previous section can be used to describe hydrogen bonds by demanding three additional requirements. The first one is related to the orientation, which is the angle among the hydrogen atom and the oxygen atoms, $\alpha(\mathrm{H_{(i)}O_{(j)}O_{(k)}})$, which should be smaller than a chosen cutoff value. The other two requirements are the distance between the oxygen atoms and the distance between the hydrogen atom and (at least one of) the oxygen atoms. These requirements (shown in Eq. 6.4) are valid only for the hydrogen atoms with $c_i \geq 2$ and are used to define the hydrogen boolean function. If a hydrogen atom with coordination number c_i satisfies simultaneously these conditions, then the hydrogen atom with index i is engaged in a hydrogen bond.

The hydrogen bond boolean function, h_i, shows whether the hydrogen atom is engaged in a hydrogen bond or not and can be defined as

$$\begin{array}{lcl} h_{ijk} = 1 & : & \begin{cases} r_{H_{(i)}O_{(j)}} \leq 1.35\text{Å} \\ r_{O_{(j)}O_{(k)}} \leq 3.5\text{Å} \\ \alpha(H_{(i)}O_{(j)}O_{(k)}) \leq 30^\circ \end{cases} \\ h_{ijk} = 0 & : & \text{otherwise} \end{array} \tag{6.4}$$

where i,j, and k are atom indices and $j \neq k$. The hydrogen boolean function, hence, inherits all the dependency of the hydrogen coordination number.

Its average over time and hydrogen indices

$$\langle h_i(t) \rangle = \frac{1}{n_H} \frac{1}{\tau} \sum_{t=0}^{\tau} \sum_{i=1}^{n_H} h_{i,O,r_{\text{cutoff}}}(t) \tag{6.5}$$

equals to the probability of observing hydrogen engaged in hydrogen bonds with specified cutoff radius and angle.

The hydrogen bond boolean function of all oxygen atoms, $h_{i,O}$ can be decomposed into its subsets, hydrogen bonds between $O_W - O_W$, $O_W - O_S$ and $O_S - O_W$.

$$h_{i,O}(t) = h_{i,O_W-O_W}(t) + h_{i,O_W-O_S}(t) + h_{i,O_S-O_W}(t) \tag{6.6}$$

Since, for almost all pores and hydration level, there is no hydrogen bond between $O_S - O_S$ atoms, it is not included in Eq. 6.6. Furthermore, in order to calculate the probability of the hydrogens which are not involved in a hydrogen bond, the complement of $h_{i,O}$, which represents the subset of hydrogen atoms belonging to dangling O-H bonds, $h_{i,dangling}$, is also calculated by using

$$\langle h_{i,danglingO-H}(t)\rangle = 1 - \langle h_{i,O}(t)\rangle \tag{6.7}$$

The simple pore models: The resulting probabilities corresponding to the hydrogen bonds between all the oxygen atoms and the ones between the mobile oxygens are shown in Figure 6.7. For all hydration levels considered in the simulations, more than 30 percent of the hydrogen atoms

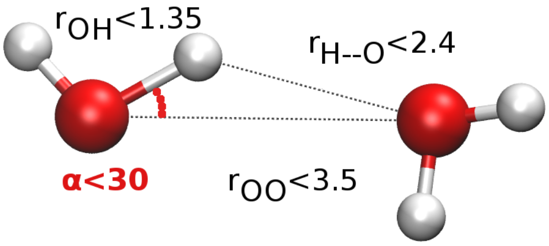

Figure 6.6: Hydrogen bond citerion

are involved in a hydrogen bond by considering all the oxygens.

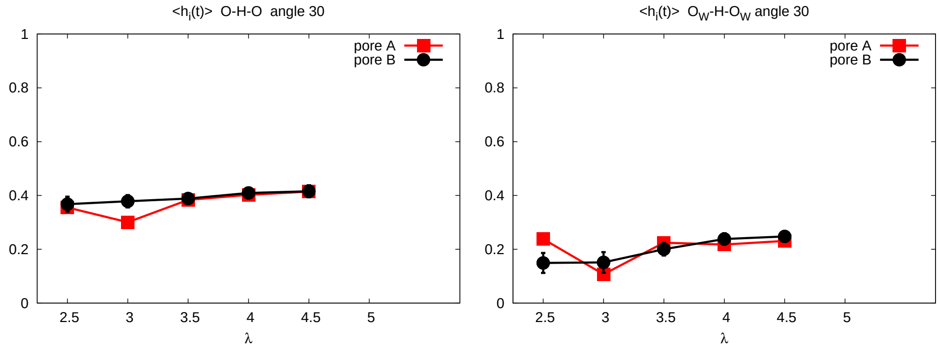

Figure 6.7: Hydrogen bond probability vs. hydration level for the simple pore model with the BLYP functional, r_{cutoff} = 2.4 and $\alpha \leq 30$.

There is a trend observed for both pores A and B, that the fraction of the hydrogen-bonded hydrogens is increasing with increasing water content. The only exception is at pore A with λ = 2.5, in which a high fraction of acidic protons is observed (See Chap. 7) and the distribution of the water molecules inside the pore is not homogeneous.

While considering the hydrogen bonds between the mobile oxygens (O_W), the trend becomes clearer for pore B. Indeed, an increase in the number of water molecules increases the number of available atoms to constitute a hydrogen bond, therefore the probability of having a hydrogen bond increases with the hydration level for all pores. Again, the λ=2.5 pore A is the exceptional case for the above mentioned reasons. However, the probability of the hydrogen bonds between sulfonate oxygens and mobile oxygen decreases with increasing hydration level for all pores (except pore A λ=2.5). This is shown in figure 6.8.

This tendency is also expected as a consequence of the fact that increasing the number of water molecules will have no effect on the number of hydrogen bonds between sulfonate groups and water molecules, once the first solvation shell of the sulfonate groups are filled. Hence, beyond the filled first shell, additional water molecules would have no possibility to have hydrogen bonds to sulfonate oxygens.

The simple pore models with the HCTH functional: The dependency of the hydrogen bonds on the hydration level at the simple pore models with the HCTH functional (see Fig. 6.9) resembles the one at pore B with the BLYP functional. The corresponding probabilities here are only slightly lower than the ones with the BLYP. There is no exceptional behavior observed for pore A at λ =2.5 and the fraction of the hydrogens involved in a hydrogen bond increases with increasing water content.

The flexible, the free and the parallel backbone pore models: The probability of observing a hydrogen bond within these pore models are larger

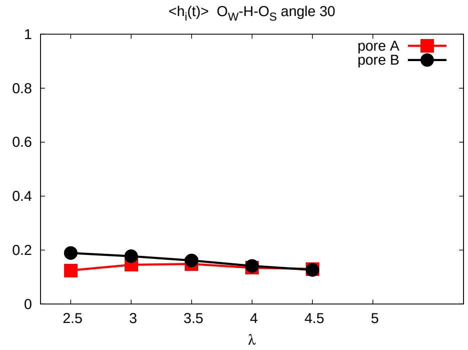

Figure 6.8: The probability of hydrogen bond between O_W and O_S vs. hydration level for the simple pore model with the BLYP functional, r_{cutoff} = 2.4 and $\alpha \leq 30$.

than the ones belonging to the simple pore models with both functionals. For all hydration levels in these simulations, more than 70 percent of the hydrogen atoms are involved in a hydrogen bond. The corresponding probabilities are shown in Figure 6.10.

The fractions of the hydrogen bonds between mobile oxygens, O_W, for these models are larger than the ones of the simple pore models. Furthermore, these differences becomes more apparent as the hydration level increases. For example, at λ=5.5, the probabilities of observing hydrogen bonds between mobile oxygens in these models are approximately 0.5. On the other hand, the ones in the simple pore models are smaller than 0.3. These results, corresponding to the fractions of hydrogen bonds either between all oxygens or between mobile oxygens can be associated with the number of water molecules in the pore models, which in the free, the flexible, and the parallel backbone models include two times more water molecules than the simple pore models at the same hydration level.

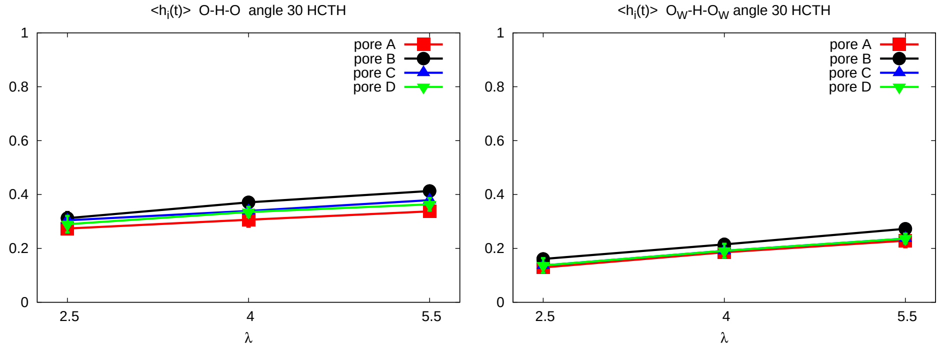

Figure 6.9: Hydrogen bond probability vs. hydration level for the simple pore model with the HCTH functional, r_{cutoff} = 2.4 and $\alpha \leq 30$.

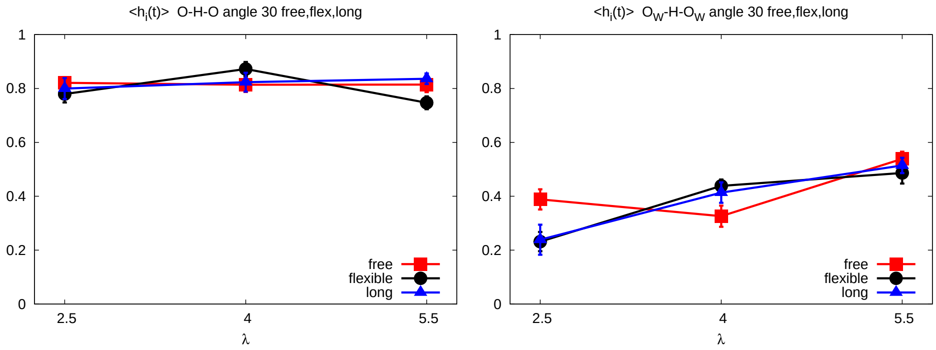

Figure 6.10: Hydrogen bond probability vs. hydration level for the free, flexible, and parallel backbone (long) models, $r_{\text{cutoff}} = 2.4$ and $\alpha \leq 30$

6.3 Hydrogen Bond Lifetime

Hydrogen bond lifetime is calculated by integrating the hydrogen bond auto-correlation function (ACF), which was proposed by Luzar [124]. We have used the continuous hydrogen bond auto-correlation function, which is defined as

$$\langle H_i(\tau)\rangle = \frac{\langle \mathrm{h}_i(t)\tilde{\mathrm{h}}_i(t+\tau)\rangle}{\langle \mathrm{h}_i(t)\mathrm{h}_i(t)\rangle} \tag{6.8}$$

where τ is the correlation time, $\mathrm{h}_i(t)$ is the hydrogen bond boolean function (see Eq. 6.4), and

$$\tilde{\mathrm{h}}_i(t+\tau) = \prod_{\tau'=0}^{\tau'=\tau} \mathrm{h}_i(t+\tau') \tag{6.9}$$

is the multiplication of the hydrogen boolean functions. The continuity of a hydrogen bond is preserved by the definition of this function (Eq. 6.9), which is sensitive to any breakage of the hydrogen bond. Its value is one for a hydrogen bond only if this hydrogen bond has no breakage at any time between t and $t+\tau$. Otherwise it becomes zero. After having calculated the hydrogen bond ACF, its exponential fit is also calculated, if the value of the ACF does not approach 0 at the end of the selected correlation time interval. In Figure 6.11, the exponential fit and ACFs are shown as an example for the hydrogen bond between $\mathrm{O_W}$ and $\mathrm{O_S}$ for the simple model.

The hydrogen bond lifetime is calculated by explicit integration of the continuous hydrogen bond auto-correlation function, H, over the interval between 0 to correlation time length, τ and for the rest (τ to ∞), the fitted exponential function is used (Eq. 6.10).

$$\tau_{\mathrm{HB}} = \int_0^\infty H(t)\, dt \tag{6.10}$$

Furthermore, the hydrogen bond lifetime dependency on the type of the oxygen atoms involved in a hydrogen bond are also considered so that three possible groups of hydrogen bonds are handled. The first one corresponds to the hydrogen bond between any two oxygen atoms, $\tau_{\mathrm{O-O}}$. The second one corresponds to the hydrogen bond only between mobile oxygens, $\tau_{\mathrm{O_W-O_W}}$. The last one is related to the hydrogen bond between mobile oxygens and sulfonate oxygens, $\tau_{\mathrm{O_W-O_S}}$. These are shown in Figures 6.12, 6.13, and 6.14 for the pore models, respectively.

While considering the hydrogen bonds between all oxygens and between the mobile oxygens, it is valid that the corresponding lifetimes, $\tau_{\mathrm{O-O}}$ and $\tau_{\mathrm{O_W-O_W}}$, for the pore A are longer than the ones for pore B, which

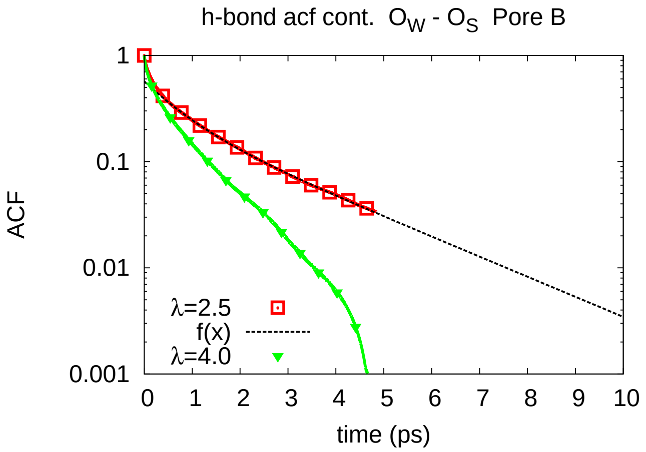

Figure 6.11: Hydrogen bond auto-correlation function for the simple pore model B λ 2.5 and 4.0 together with the exponential fit.

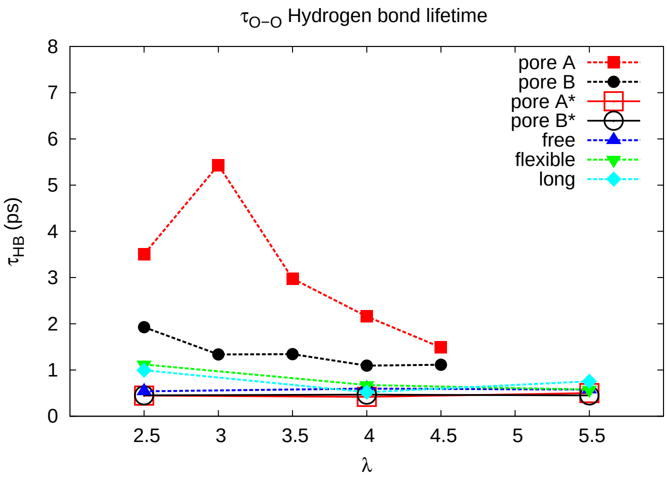

Figure 6.12: The lifetime of the hydrogen bonds. The simple pore models with the HCTH functional are marked by *.

is also longer than the ones for the other pores at the same water content,

$$\tau_A(\lambda) > \tau_B(\lambda) > \tau_{\text{others}}(\lambda) \quad \text{for} \quad O-O \quad \text{and} \quad O_W - O_W \tag{6.11}$$

Furthermore, as the water content increases, the hydrogen bond lifetime in the pores A and B decreases and converges to the value of the other pores. This also indicates that the differences in the hydrogen bond lifetime caused by the functionals observed for low water contents are expected to be less pronounced or vanishingly small for high water content.

The lifetime of the hydrogen bond between the sulfonate oxygens and the mobile oxygens, $\tau_{O_W-O_S}$, is shorter than the one between the mobile oxygens, $\tau_{O_W-O_W}$, in the pores A and B for all hydration levels.

$$\tau_{O_W-O_S} < \quad \tau_{O_W-O_W} \tag{6.12}$$

In many cases, the above relation does not hold for the other pores. A clear distinction between the lifetimes of these hydrogen bonds is not possible,

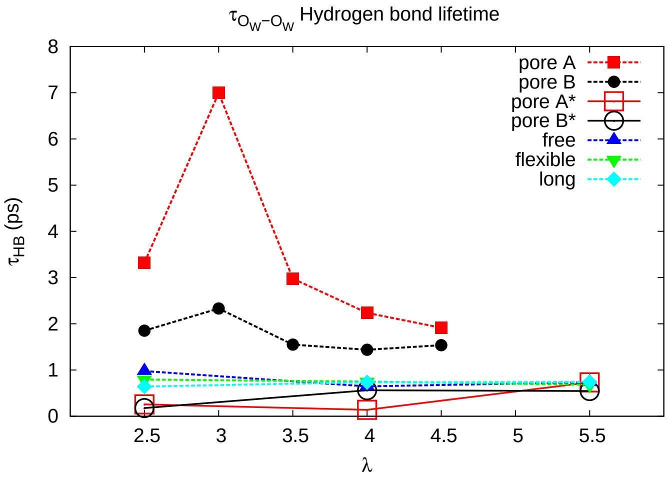

Figure 6.13: The lifetime of the hydrogen bonds between the mobile oxygens. The simple pore models with the HCTH functional are marked by *.

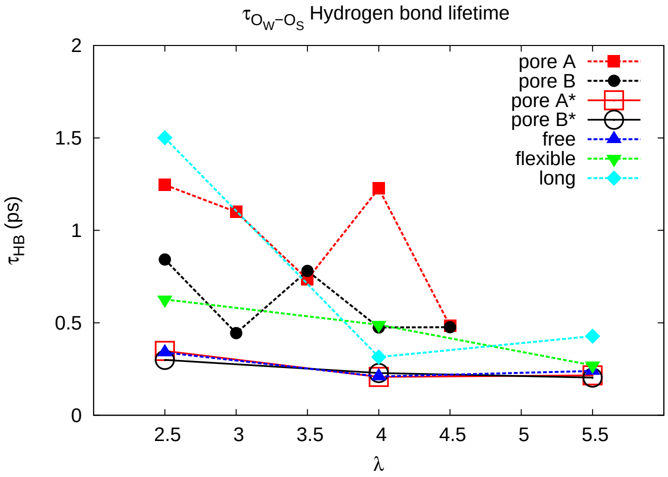

Figure 6.14: The lifetime of the hydrogen bonds between the mobile oxygen and the sulfonate oxygens. The simple pore models with the HCTH functional are marked by *.

since their differences are too small and even in some cases $\tau_{O_W-O_S}$ becomes slightly longer than $\tau_{O_W-O_W}$. However, as the water content increases, again the lifetime of the hydrogen bond between O_W and O_S becomes shorter and converges to a value slightly shorter than around 0.5 ps.

6.4 Discussion on Hydrogen Bond Dynamics

Two factors related to the dynamical properties of the proton transfer in the ionomer were investigated through hydrogen bond dynamics. The first one was associated to the hydrogen-bond-connected water structure and represented by the probability of having hydrogen bonds, since the path of proton hopping is indeed along the hydrogen bond network. In that respect, having a high probability of hydrogen bonds stimulates proton transfer. The simple pore models for low water content were shown to have a low probability of hydrogen bonds and hence the water structure in this model deviates from bulk-like water by showing a lack of well connected water. Furthermore the cooperativity of hydrogen bonds, which is observable near to bulk-like water, is prevented by the effect of close sulfonate groups especially for pore A and low water content. Therefore, this case is expected to show also low dynamics related to the proton transfer.

The other pore models (the free, the flexible, and the parallel backbone models) exhibited high probabilities of having hydrogen bonds. This stems from the fact that the number of water molecules in these models were larger than the ones in the simple pore models and the structures of the pore wall were more flexible and had longer side chains than in the simple pore models. Therefore the water as well as the hydrophilic and hydrophobic groups of the ionomer have more freedom to rearrange in order to constitute hydrogen bonds. Hence, in these models, a well connected water structure (through hydrogen bonds), which is close to bulk-like water, was observed, especially for high water content. Due to this feature, these models are expected to have a more dynamical water structure and possibly also to have high proton mobility.

The second factor is having a short lifetime of the hydrogen bonds, which should be close to the value in a bulk-like liquid water. A long lifetime of the hydrogen bonds is significant for the frozen water structure, in which the proton mobility is restricted. In this respect, except the simple model pore A with the BLYP functional, all other pore models showed the hydrogen bonds to have short lifetime. Therefore, they are expected to have a more dynamical water structure and again possibly a high proton mobility.

In order to elucidate the dependency of these conditions on the proton mobility, which is crucial for having an operating fuel cell, the dynamics of the protons and water inside the ionomer will be investigated in the following chapter.

Chapter 7

Dynamics of Proton Complexes

A proton in the liquid phase is not a free particle. It is bonded to some other atom or molecule, or is shared between molecules or atoms. Hydrated protons within our calculations are able to assume different states, since we do not use classical force fields for their description and the proton species are therefore not restricted to specific structures.

This feature of *ab initio* molecular dynamics (MD) allows us to handle the proton transfer, Grotthuss mechanism and proton equilibria. Unfortunately, the use of tools implemented to analyze classical MD trajectories was partly restricted, due to their implementation. Because of this reason, it was necessary to re-implement some of these tools such that they became applicable to the present case and able to follow the various proton species and differentiate between them.

The state of a proton depends on its neighboring atoms. Therefore, we defined geometrical criteria to classify various proton complexes in the molecular system. This classification is necessary at every step of the MD trajectories, hence, it is a dynamical procedure.

A detailed description of this dynamical selection of the proton complexes will be given in Section 7.1 together with the average fraction of these proton states. In the following section (Sec. 7.2), the radial distribution functions of possible proton complexes will be discussed, also in the context of the used geometrical criterion.

The proton mobility, which is one of the key factors related to the subject of this work, will be discussed in Section 7.3. The self diffusion of the water and the proton complexes will be shown by calculations of their mean square displacement within ionomer pores.

7.1 Proton States

The state of the protons in the system is analyzed according to "a weighted-coordination-number", k (Eq. 7.1), which is a linear function of the number of oxygen neighbors. It depends both on the number of bonded sulfonate oxygen neighbors (m) and the number of bonded mobile oxygen neighbors (n)(the oxygens that do not belong to sulfonate groups).

$$k = 4 - 3 * m + n \tag{7.1}$$

The nature of these bonds, either chemical or hydrogen bonds, are not differentiated at this level. If the distance between hydrogen and oxygen atoms is smaller than a cut-off value, r_0, they are considered as bonded atoms. By using this definition, it is possible to classify the proton complexes in our pore models such that each state corresponds to different values of k (see Table 7.1).

Table 7.1: Proton states are classified by weighted coordination number, k.

Proton States	$(CF_3SO_3^-)m - H^+ - (OH_2)_n$	m	n	$k = 4 - 3 * m + n$
Acidic	CF_3SO_3H	1	0	1
Pseudo-Zundel	$CF_3SO_3^- - H^+ - OH_2$	1	1	2
Hydronium	H_3O^+	0	1	5
Zundel	$H_5O_2^+$	0	2	6

The following proton states are defined:

(i) If a proton has only one oxygen neighbor with $r < r_0$ and this neighbor is an oxygen atom of the sulfonate group, we call this proton an ‘acid proton’; (ii) if a ‘mobile’ oxygen atom (all oxygen atoms except the sulfonate oxygen

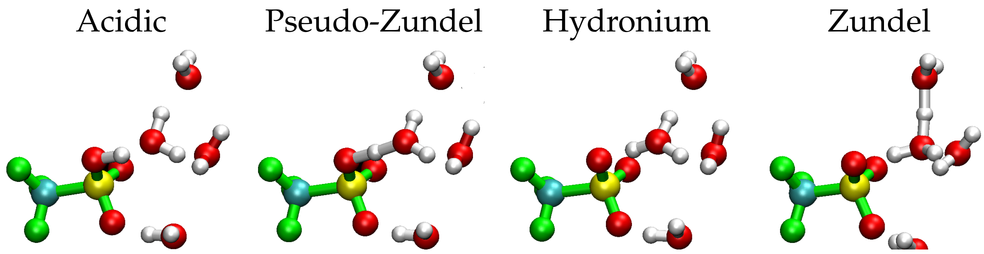

Figure 7.1: Possible proton complexes.

atoms) has three proton neighbors with r <r_0 , it is termed a 'hydronium', provided that at the same time none of the three protons has two oxygen neighbors within $r < r_0$;
(iii) if any of the protons has two oxygen neighbors within $r < r_0$ and both oxygen neighbors are 'mobile' water oxygen atoms, it is termed 'Zundel' proton;
(iv) if any of the protons has two oxygen neighbors within $r < r_0$ and one of these neighbors is a sulfonate oxygen, it is termed a 'pseudo-Zundel' proton (a proton shared between a water molecule and a sulfonate group).

We have investigated different values of r_0. With increasing r_0 the number of Zundel-style complexes increases as expected, but at the same time the number of less well-defined proton complexes (i.e. those that do not fit obviously into the classification scheme given above, or they belong to more than one class) increases as well. We thus chose $r_0 = 1.3$ Å for the following analysis. Using this value, it was possible to assign most proton complexes to one of these classes; with the exception of less than 10^{-4} of the configurations in the simple pore model.

Since the states of the protons change with time, the classification is

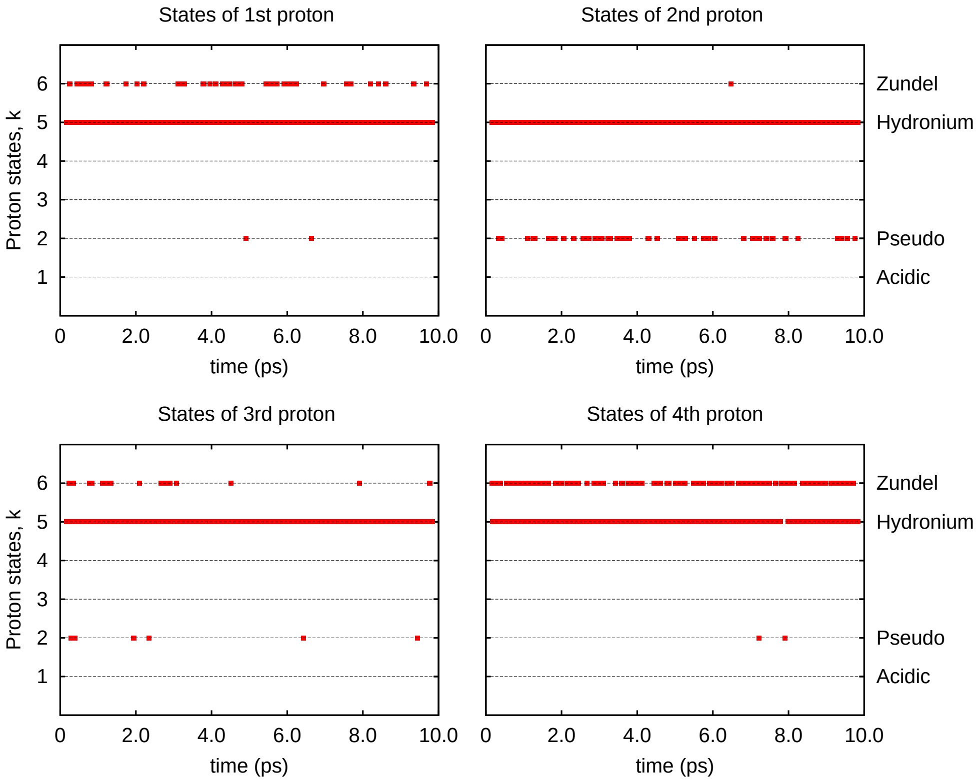

Figure 7.2: States of the protons in the simple pore model B in an arbitrary selected 10 ps time interval.

calculated for each frame of the trajectories. Hence, the weighted coordination number, k (Eq. 7.1) depends on time. In Figure 7.2, $k(t)$ is plotted for each proton species in order to show how the proton states evolves in time.

The probability of observing a specific proton state is calculated by

$$P(\tilde{k}) = \frac{1}{\mathrm{N}\,\mathrm{M}\,\tilde{k}} \sum_{i=1}^{\mathrm{N}} \sum_{j=1}^{\mathrm{M}} k_i(t_j)\, \delta_{k_i \tilde{k}} \tag{7.2}$$

where $\tilde{k}$ is the integer value corresponding to the specified proton state, N is the number of protons in the system, M is the number of trajectory frames and $\delta_{k_i\tilde{k}}$ is 1 only if $k_i = \tilde{k}$ and 0 otherwise.

$$\delta_{k\tilde{k}} = \begin{cases} 1 & k_i = \tilde{k} \\ 0 & k_i \neq \tilde{k} \end{cases} \tag{7.3}$$

As an example, the probability of the hydronium state, whose $\tilde{k}$ equals to 5, is

$$P(5) = \frac{1}{\mathrm{NM}5} \sum_{i=1}^{\mathrm{N}} \sum_{j=1}^{\mathrm{M}} k_i(t_j)\, \delta_{k_i 5}. \tag{7.4}$$

Using the values of weighted coordination numbers from Table 7.1, the probabilities of the corresponding proton states are calculated for each hydration level of the pore models and shown in Figures 7.3, 7.4, and 7.5.

The simple pore model with the BLYP functional: At the lowest water content, pore A contains a large fraction (more than 30%) of undissociated $-SO_3H$ groups, indicating that there is not enough water in the pore to completely solvate the excess protons. With increasing water content the number of undissociated $R-SO_3H$ groups rapidly approaches zero. At the same time the amount of Zundel-like configurations increases monotonously.

In pore B there are fewer undissociated $R-SO_3H$ groups than in pore A and the other pores at any λ (see Fig. 7.3). The number of Zundel-like configurations in pore B is always larger than in pore A, increasing slightly with increasing λ. In all pores the number of pseudo-Zundel ions is low for all values of λ. The results indicate that even at low water content almost complete dissociation is possible. However next to the humidity level λ, the local structure, spacing and arrangement of the $R-SO_3^-$ groups apparently also play a role.

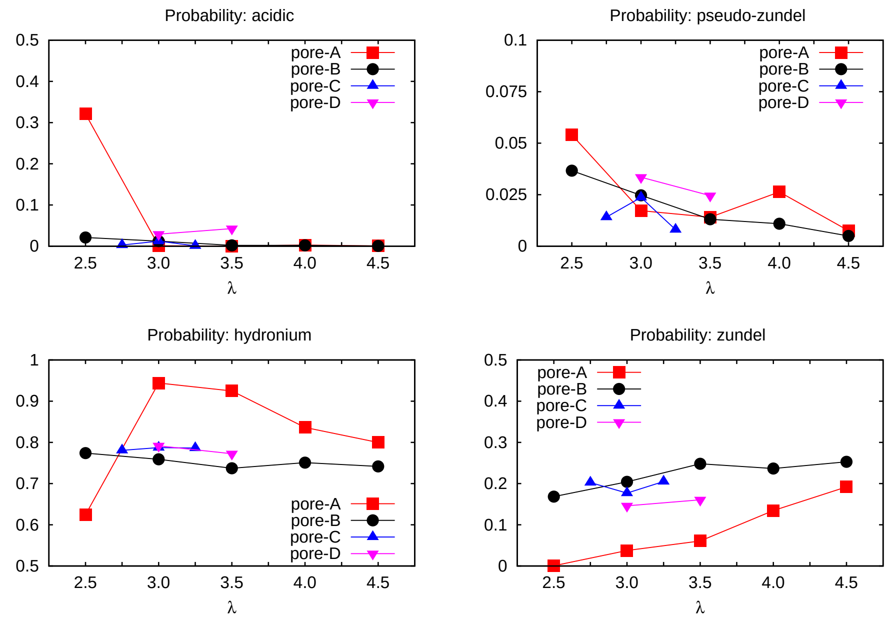

Figure 7.3: Probability of observing given proton states with respect to the water content for the simple pore model with the BLYP functional.

The simple pore model with the HCTH functional: A large fraction of acidic protons is observed at the lowest water content for all pores. It decreases with increasing water content. However, even at λ = 5.5, a considerable fraction of acidic protons is observed (approximately 20%). Both hydronium and Zundel ions fractions increase with increasing humidity. Furthermore, the fraction of hydronium is comparable to the one of acidic protons at λ = 4.0 and becomes the largest one only at λ = 5.5.

The fractions of pseudo-Zundel in pore A is slightly larger than in pores B, C, and D for all water contents. Increasing water content leads to a slight change in their fractions.

In contrast to the BLYP functional, where complete dissociation is observed already for $\lambda \geq 3.0$, here such an observation is made only when

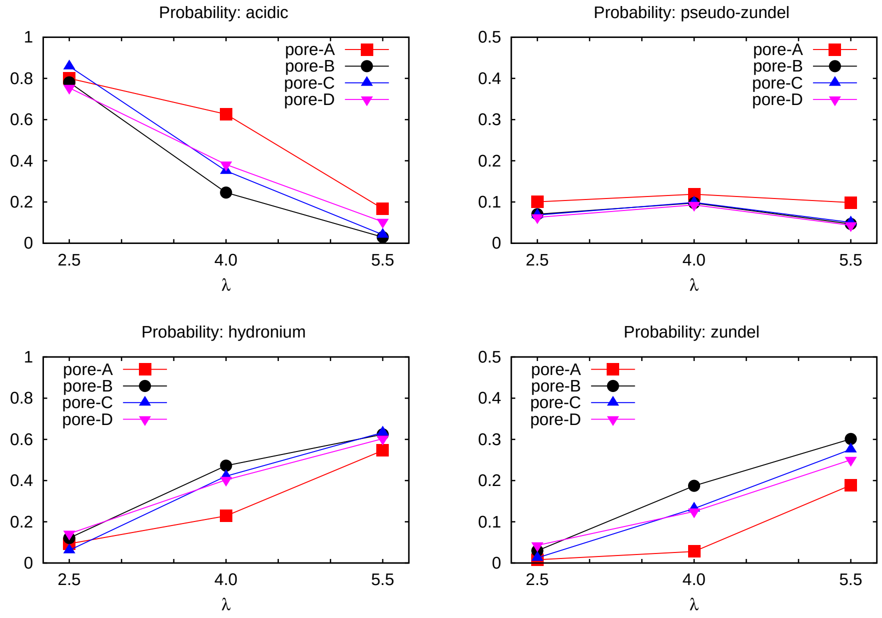

Figure 7.4: Probability of observing given proton states with respect to the water content for the simple pore model with the HCTH functional.

λ >4.0 is reached. A dependency of the fractions of the protons states on the pore structure, for example sulfonate spacing, is observed, since the fraction of acidic protons in pores differs. However, the differences in the fraction of proton states are mainly affected by the functionals. Their effects were also observed in the description of the water and sulfonate group structures (see Chap. 5 for the corresponding radial distribution functions).

The free, the flexible, and the parallel backbone models: Within these three models, changes in the fractions of the proton complexes (hydronium, Zundel, pseudo-Zundel ions) with respect to humidity level are almost the same as in the simple fixed model with the BLYP functional. The only difference is that there is not a large fraction of undissociated sulfonate groups even at very low water content. The probability of observing the acidic protons is less than 0.075% for all water contents. For these pore models at all considered water contents, the largest fraction of proton states are identified to be hydronium ions. The fraction of Zundel ions is the second largest proton state. For the parallel backbone model, its fraction increases when the water content is increased from λ =2.5 to 4.0. For the free and the flexible models, this increase is observed when λ reaches 5.5.

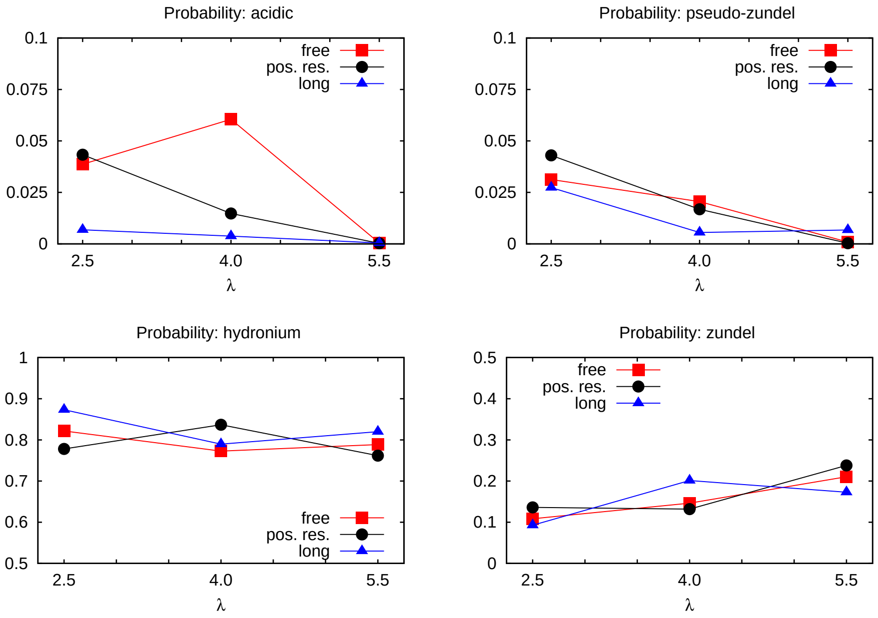

Figure 7.5: Probability of observing given proton states with respect to the water content for the free, the flexible and the parallel backbone models.

7.2 Radial Distribution of Proton Complexes

Based on the geometric criterion, explained in Section 7.1, the radial distribution functions (RDFs) of possible species of proton complexes are calculated and compared. This analysis leads to a better understanding of the structure of the proton complexes. It is, thus, restricted to the simple pore model with the BLYP functional, which is sufficient to reveal the structural differences among the proton complexes.

Two subsets of oxygen atoms are considered: oxygen of the sulfonate groups ($\mathrm{O_S}$) and the mobile oxygen atoms ($\mathrm{O_W}$), the ones which do not belong to sulfonate groups. Then, the RDFs between the hydrogen atoms of a selected proton complex and these two subsets of oxygens are calculated. These partial RDFs are indeed connected to the RDF belonging to all oxygens

$$g_{\mathrm{O-H}} = \frac{n_{\mathrm{O_S}}}{n_{\mathrm{O}}} \cdot g_{\mathrm{O_S-H}} + \frac{n_{\mathrm{O_W}}}{n_{\mathrm{O}}} \cdot g_{\mathrm{O_W-H}} \tag{7.5}$$

where H denotes the hydrogens of the considered proton complex, $n_{\mathrm{O_S}}$ is the total number of oxygens, and $n_{\mathrm{O_S}}$ and $n_{\mathrm{O_W}}$ are the number of sulfonate oxygens and mobile oxygens, respectively. So the sum of the partial RDFs equals to the one of all oxygens.

Firstly, the acidic protons, those hydrogens which are bonded only to the sulfonate oxygens are considered. The corresponding RDFs, $g_{\mathrm{OH_{acidic}}}(\mathrm{r})$, are shown in Figure 7.6. The first peak of the radial distribution function, $\mathrm{g_{O_S-H}}$, which is centered at 1.0 Å, is equal to the one of all $\mathrm{O-H}$. It has a shoulder, which indicates that the separation into acidic and pseudo-Zundel categories is imperfect. The following peak, centered at 1.4 Å,

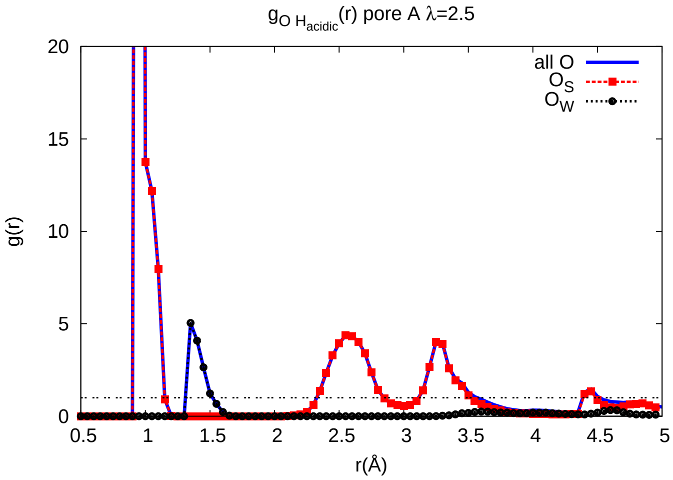

Figure 7.6: RDF of the oxygens and the acidic protons for the simple model.

belongs to the mobile oxygens (O_W), which are hydrogen bonded to the sulfonate oxygens.

The third and fourth peaks, which involve the contributions from the sulfonate oxygens, are due to the interaction of the acidic proton with two other oxygens of the sulfonate, which are not directly bonded with the acidic proton. Having no water oxygen around indicates that the acidic proton in the simple model pore A is isolated. This result supports the volumetric pictures and the density map analysis presented in Chapter 5, where the structural properties of the undissociated sulfonate groups were also discussed.

The RDFs of the pseudo-Zundel cations, in which a proton (central hydrogen) is shared by a sulfonate oxygen and a mobile oxygen, are shown in Figure 7.7 for two water contents, 2.5 and 4.0, for the simple pore model. The two peaks between 1.0 and 1.3 Å are clearly distinguishable for both values of λ. The first peak belongs to the $g_{O_W H}$ (in black color) and indicates that it is more probable to find pseudo-Zundel cations, whose central hydrogen atom is closer to the mobile oxygen than to the sulfonate oxygen. As the water content increases, this distinction becomes even more pronounced.

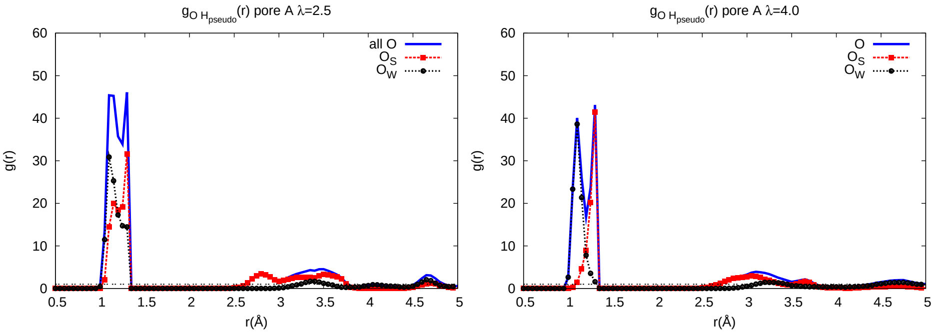

Figure 7.7: RDF of the oxygen atoms and the hydrogen of the pseudo-Zundel ions for the simple model.

This result agrees with the literature and the findings in Chapter 5, which state that the protons tend to be away from sulfonate groups as the water content increases. Although the distance criteria for the considered proton complex lowers the probability of observing pseudo-Zundel cations compared to the other proton complexes calculated here, the fraction of the pseudo-Zundel cations represents a possible transition state from an acidic case to a hydrated proton complex. Therefore, a change of its structure depending on the water content is important.

The next considered proton complex is the hydronium, whose RDFs are shown in Figure 7.8 for $\lambda = 2.5$ and 4.0 in the simple pore model. The first peak of the RDFs of hydrogens of the hydronium cations and oxygen atoms is due to the intramolecular interaction and is centered at 1.0 Å.

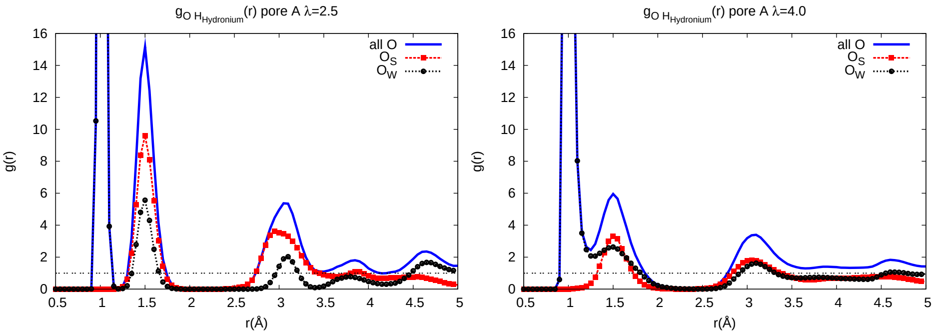

Figure 7.8: RDF of the oxygens and the hydrogen of the hydronium ions for the simple model.

This peak contains only contributions from the partial RDFs belonging to O_W. For λ = 2.5, there is a clear minimum around 1.3 Å, where the first and the second peak are separated; the corresponding RDFs are zero. This clear minimum indicates a stable hydronium structure for the lowest water content. Even though such a minimum exists in RDFs at λ = 4.0, they are not zero. Therefore, transitions from the hydronium state to other proton complexes e.g. Zundel cation or vice versa are expected.

The second peak of the RDFs, due to intermolecular interactions, corresponds to the hydrogen-bonded oxygen atoms surrounding the hydrogens of the hydronium ions. It is centered at 1.5 Å for both water contents. For λ = 4.0, this peak is broader than the one for λ = 2.5. Because of this broadness, the hydrogen bond life is expected to be shorter for λ = 4.0 compared to the one at λ =2.5 (discussed in Chapter 6).

The last proton complex, which is observed in the simple pore model, is a Zundel cation, where a proton (the central hydrogen atom) is shared between two water molecules. Since, for λ = 2.5, the fraction of the Zundel

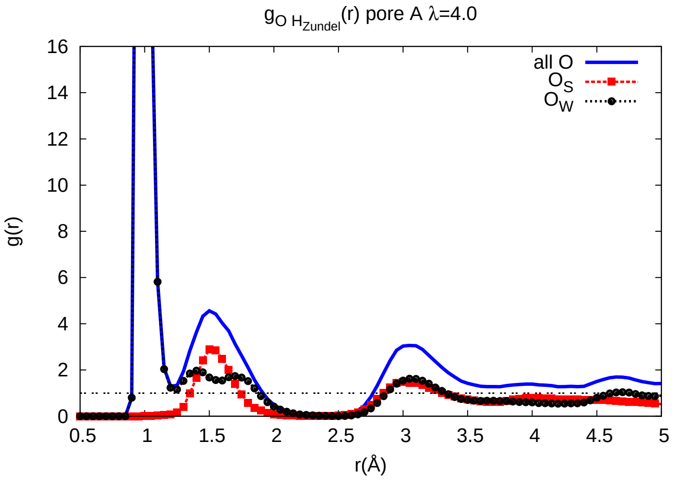

Figure 7.9: RDF of the oxygens and the hydrogen of the Zundel ions for the simple model.

cations is almost negligible, only the RDFs for $\lambda = 4.0$ are shown in Figure 7.9. The second peak at 1.5 Å of the RDFs belongs to the oxygens of the sulfonate groups and resembles the one of the hydronium at the same water content. The second peak of the $g_{\mathrm{H-O_W}}$ (black color) contains two maxima, which are centered at 1.4 and 1.7 Å, and can be traced back to the central hydrogen between the oxygens of the Zundel cations.

Due to the asymmetry of the Zundel cations, the second peak of the RDF of hydrogen and all oxygen atoms (blue colored) becomes broad. An increase in the broadness of the second peak due to increasing hydration level stems not only from the transitions between proton complexes but also from the increasing fraction of the Zundel cations with increasing water content. Furthermore, both reasons contribute to the high mobility of the protons.

In order to compare the effect of the pore structure on the structure

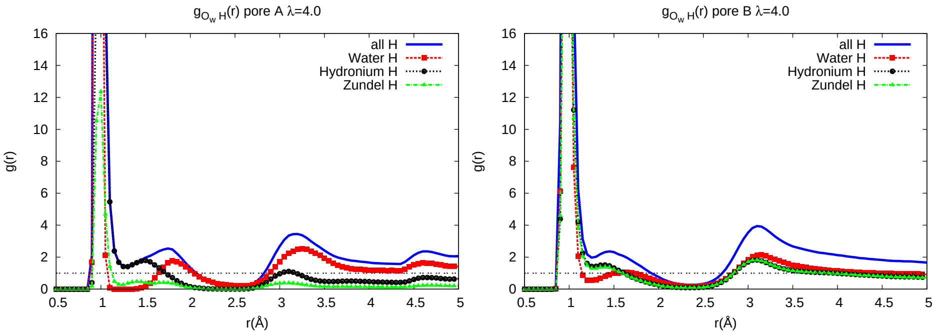

Figure 7.10: The effect of the pore structure on the RDF of the oxygens and the hydrogens of proton complexes for the simple model (pore A and B).

of the proton complexes, the RDFs between the hydrogen of the proton complexes and the mobile oxygen atoms, O_W, are shown for pores A and B at λ =4.0 in Figure 7.10. The RDFs of the acidic protons and pseudo-Zundel cations are not included in the figures due to their negligible contributions. In addition to the hydronium and the Zundel cations, the RDFs for the hydrogens of the water molecules are calculated and shown in Figure 7.10.

The second peak located at 1.75 Å belonging to all hydrogens (blue color) in pore A is shifted to a lower value, 1.5 Å in pore B. The partial RDF belonging to the water hydrogens (red color) in pore A shows a clear minimum between 1.1 and 1.5 Å. In pore B, the corresponding minimum still exists but it is not zero within this interval. Its second peak, which is broader than the one in pore A, indicates that the water molecules exhibit more dynamical features than the ones in pore A. For the hydronium and the Zundel cations, the positions of their second peaks in pore A is shifted to lower values in pore B, in which the RDFs of both proton complexes differ only slightly. Furthermore, the splitting of the second peak belonging to Zundel hydrogens, which is observed in pore A, disappears in pore B.

7.3 Proton Mobility

Proton conductivity is a very important property of a polymer electrolyte membrane. A direct measurement of proton conductivity is not possible within the simulation methods used in this work. Instead, the proton mobility, which is proportional to the conductivity, is used to access this quantity [24, 25]. It can be calculated by using Einstein's relation (see Eq. 7.6),

$$D = \mu k_B T \tag{7.6}$$

which connects the diffusion coefficient, D, and the mobility, μ. Here $k_B T$ is the product of the Boltzmann's constant and temperature. A comparison of the diffusion of protons depending on the water content and pore models should produce the same trend as a comparison of the proton conductivity, since the proton conductivity is proportional to the diffusion of protons.

There are two common methods for calculating a diffusion coefficient within molecular dynamic simulations: (i) by using mean square displacement (MSD) of atoms and (ii) by using velocity auto-correlation function (VACF). Theoretically both approaches produce results identical, but for statistical uncertainties. In the latter method (VACF), the integral of the velocity auto-correlation function is calculated by using Green-Kubo's relation, divided by d, the dimensions of the velocities [174].

$$D = \frac{1}{d} \int_0^\infty dt \, \langle \mathbf{v}_i(0).\mathbf{v}_i(t) \rangle \tag{7.7}$$

where $\mathbf{v}_i(t)$ is the velocity of the ith atom. The velocity auto-correlation, which will be explained in detail in Chapter 8, is not used here to calculate the diffusion coefficient of the proton. Since a direct implementation of the VACF of the protons is not a straightforward due to the proton hopping mechanism, we chose to use only the MSD method.

In the MSD method, the mean square displacement of atoms is calculated by using their coordinates,

$$\langle|\Delta\mathbf{r}(\tau)|^2\rangle = \frac{1}{I}\frac{1}{J}\sum_{i=1}^{I}\sum_{j=0}^{J-1}|\mathbf{r}_i(t_j+\tau)-\mathbf{r}_i(t_j)|^2 \tag{7.8}$$

where I and J correspond to the number of the atoms and the time origins, respectively. For an aqueous system, the slope of the MSD as a function of time converges to a constant value as the correlation time approaches infinity. This is expressed in Einstein's equation (Eq. 7.9), in which the diffusion coefficient is proportional to the slope of the MSD,

$$D = \frac{1}{2d}\lim_{\tau\to\infty}\frac{\langle|\Delta\mathbf{r}(\tau)|^2\rangle}{\tau} \tag{7.9}$$

where τ is the correlation time. The dimensionality factor, d, equals 3, if all components of the coordinates are used, $\mathbf{r}_i = (x_i, y_i, z_i)$. Since the construction of the pore is such that water channels are connected in the z-direction, the z-component of the diffusion coefficient contributes to the mobility of the proton in the channel. Therefore, the diffusion coefficient presented here includes only the z-component. It is expressed as

$$D_z = \frac{1}{2}\lim_{\tau\to\infty}\frac{\langle|\Delta z(\tau)|^2\rangle}{\tau} \tag{7.10}$$

where $\mathbf{r}_i$ is replaced with $(0, 0, z_i)$, and the dimensionality factor is taken as one.

In order to increase the statistical accuracy, a long simulation time is required.

In the following, first the diffusion coefficients of the water oxygen, which is calculated for all pore models, are shown. Then the diffusion coefficients of the center of the proton complexes are represented together with the dynamical selection scheme for keeping track of the center of the proton complexes.

7.3.1 Self diffusion of water

Mean square displacements of mobile oxygen atoms, which do not belong to the sulfonate group or the side chain of Nafion® (for long model) are calculated by using Equation 7.8 for all pore models and water contents.

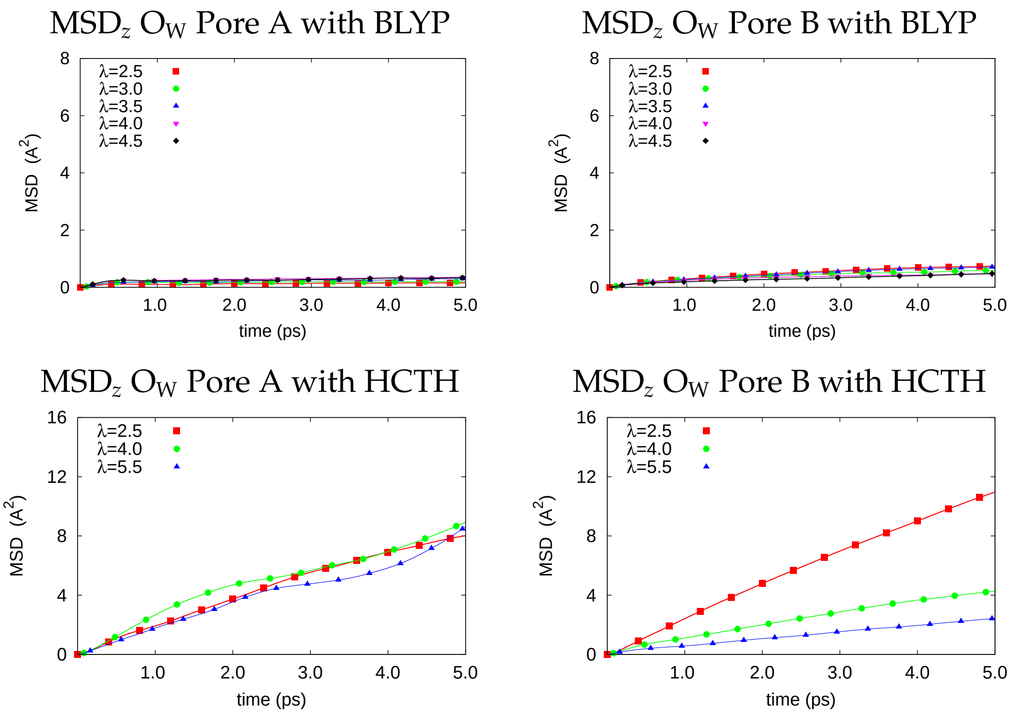

MSD$_z$ O$_W$ Pore A with BLYP

MSD$_z$ O$_W$ Pore B with BLYP

MSD$_z$ O$_W$ Pore A with HCTH

MSD$_z$ O$_W$ Pore B with HCTH

Figure 7.11: Mean square displacement (only in z-direction) of the mobile oxygen for pores A (left) and B (right) are shown at top and below, for the BLYP and the HCTH functionals, respectively.

The MSDs in the direction parallel to the pore axis are shown in Figure 7.11 for pores A and B of the simple fixed model. In order to compare the MSDs of the simulations performed with the BLYP and the HCTH functionals, the same correlation time length, 5 ps, is used. As it was already discussed in Chapter 5, it is expected that the HCTH functional leads to much faster dynamics than BLYP. Here, the difference in MSDs between both models clearly supports this expectation. In addition, it is observed that the diffusion of water is decreasing with increasing water content in the pore B with the HCTH functional.

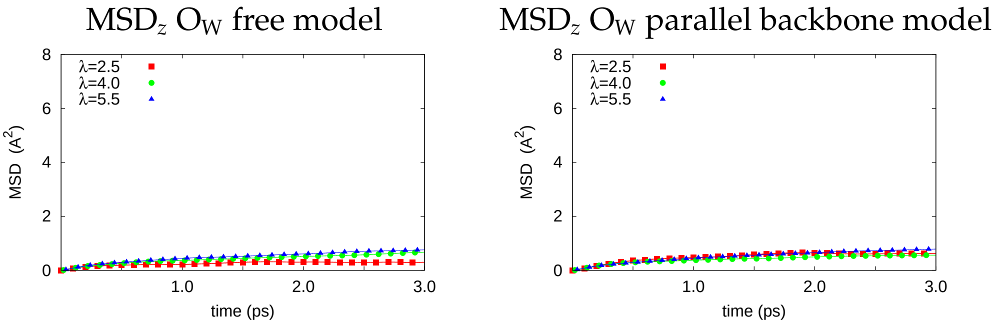
MSD_z O_W free model

MSD_z O_W parallel backbone model

Figure 7.12: Mean square displacement (only in z-direction) of the mobile oxygen for the free pore model (left) and the parallel backbone model (right).

As another example, the MSDs of water for the free and the parallel backbone models are shown in Figure 7.12. In order to analyze all MSDs of the mobile oxygens, their diffusion coefficients are calculated by using a linear fit to their MSD curves. The resulting diffusion coefficients are plotted in Figure 7.13.

The most prominent effect on the diffusion of the mobile oxygens is due to the functional used in the simulations. In the simple model with the HCTH functional, the diffusion of the mobile oxygens decreases with increasing water content. It is much higher than in the other models. These high diffusion coefficients with the HCTH functional might also be attributed to the dispersion corrections, which are employed within these simulations. However, the simulations of the other pore models (the free, the flexible, and the parallel backbone models) include also dispersion corrections, yet with the BLYP functional. The water diffusion in these pore

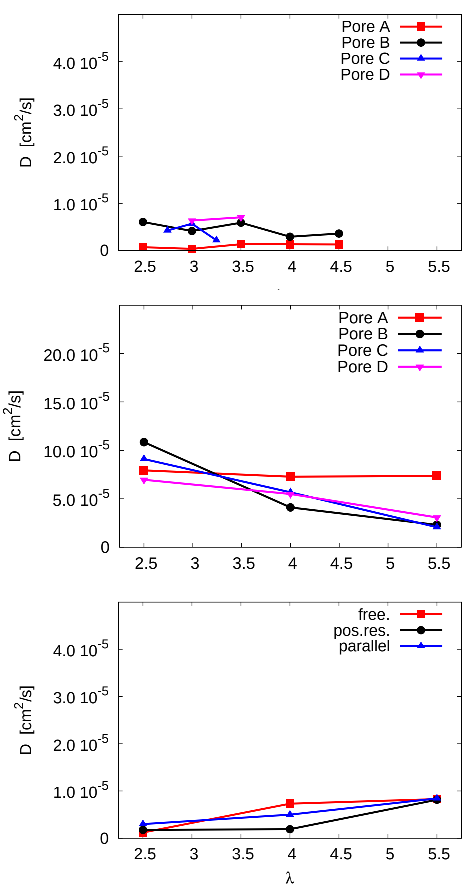

Figure 7.13: Diffusion coefficients of the mobile oxygen are shown for the fixed pore model with the BLYP functional (top) and with the HCTH functional (middle). In the bottom frame, the diffusion coefficients for the irregular free model, position restraint model, and parallel backbone model (all with BYLP functional) are presented.

models is approximately of the same order as in the simple pore model with the BLYP functional. Therefore, it is deduced that the dynamical behavior of the molecules is mainly affected by the used functional. In addition to this, it is known that the effect of the dispersion corrections on the dynamics of the system might be different and depends on the functionals [90, 119, 95].

An increasing hydration level leads to a slight increase in the diffusion of the mobile oxygen in the pore A with the BLYP functional. Whereas it leads to a decrease in the diffusion coefficients in the pore B with the BLYP and the pores B, C, and D with the HCTH functional, which have the same pore radius. Therefore, it is deduced that an increase in the hydration levels, which leads to an increase in the density, causes the diffusion coefficients of the water molecules to decrease. This effect is most pronounced in the simulations with the HCTH functional, due to a higher diffusivity of water. However, the exceptional slight increase in the diffusion coefficients with respect to the increasing density in the pore A with the BLYP functional is attributed to decreasing the strength of the sulfonate trapping with increasing the number of water molecules. The relation between diffusion coefficients and density is shown in Figure 7.14.

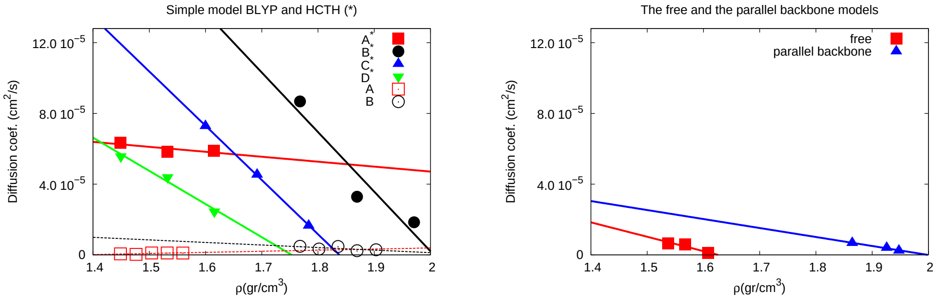

Figure 7.14: The relation between diffusion coefficients of the mobile oxygen and the pore density is shown for the simple pore model on the left frame: the data belonging to the simulations with HCTH functional is labeled with filled symbols. The data belonging to the free and the parallel backbone models is shown in the right frame, in which the density decreases with increasing hydration level. The relation in the flexible model is not included, since here the density with respect to hydration is constant.

7.3.2 Self diffusion of protons

It was stated before that keeping track of the proton requires a dynamical selection mechanism to calculate the mean square displacement of the protons. Instead of selecting a hydrogen atom as a proton, the oxygen atom, to which an excess hydrogen is bonded, is considered as the center of the proton complex. Therefore the definition used in Section 7.1 is also applied to define the protonated oxygen. If the state of the proton complex is acidic or a hydronium, the center of the proton complex is the sulfonate oxygen (to which the excess proton is bonded) or the oxygen of the hydronium, respectively. If the proton complex is at the state of a pseudo-Zundel or a Zundel cation, then the oxygen atom, which closest to the bridging hydrogen, is selected as the center of the proton complex.

The mean square displacement of the center of the proton complex contains two contributions, the classical ion diffusion and the Grotthuss hops. The displacement between two adjacent timesteps is either a classical or a Grotthuss process, and defined as

$$\Delta \mathbf{r}_{\text{total}} = \begin{cases} \mathbf{r}_a(t_{j+1}) - \mathbf{r}_a(t_j)\,; & \text{classical diffusion} \\ \mathbf{r}_b(t_{j+1}) - \mathbf{r}_a(t_j)\,; & \text{Grotthuss hop} \end{cases} \tag{7.11}$$

In a Grotthuss hop, the index of the protonated oxygen changes from a to b, where a and b are the index number of the oxygens [205, 90, 86]. The new center of the proton complex, the oxygen atom with index b, is a neighbor of the protonated oxygen with index a at time steps t_j and t_{j+1}. Additionally, the indices of the hydrogens of both oxygens (indices a and b) at time steps t_j and t_{j+1} are stored and then compared to follow the track of the protonated oxygen. This is required, if more than one proton jumps occur at one timestep. The MSDs of the center of proton complexes, $\mathrm{MSD}_{\mathrm{total}}$, can be calculated using Equation 7.11, which may include both contributions.

Furthermore, the $\mathrm{MSD}_{\mathrm{Grotthuss}}$, which includes only the Grotthuss hops, is calculated by omitting the contributions from classical ion diffusion.

$$\Delta\mathbf{r}_{\mathrm{Grotthuss}} = \begin{cases} 0\,; & \text{classical diffusion} \\ \mathbf{r}_b(t_{j+1}) - \mathbf{r}_a(t_j)\,; & \text{Grotthuss hop} \end{cases} \tag{7.12}$$

In the same manner, the $\mathrm{MSD}_{\mathrm{classical}}$, which includes only the classical ion diffusion, is calculated by replacing the contributions from Grotthuss hops with 0.

$$\Delta\mathbf{r}_{\mathrm{classical}} = \begin{cases} \mathbf{r}_a(t_{j+1}) - \mathbf{r}_a(t_j)\,; & \text{classical diffusion} \\ 0\,; & \text{Grotthuss hop} \end{cases} \tag{7.13}$$

As an example, the $\mathrm{MSD}_{\mathrm{total}}$ together with the separate contributions, $\mathrm{MSD}_{\mathrm{Grotthuss}}$ and $\mathrm{MSD}_{\mathrm{classical}}$, are shown for pore D of the simple model in Figure 7.15.

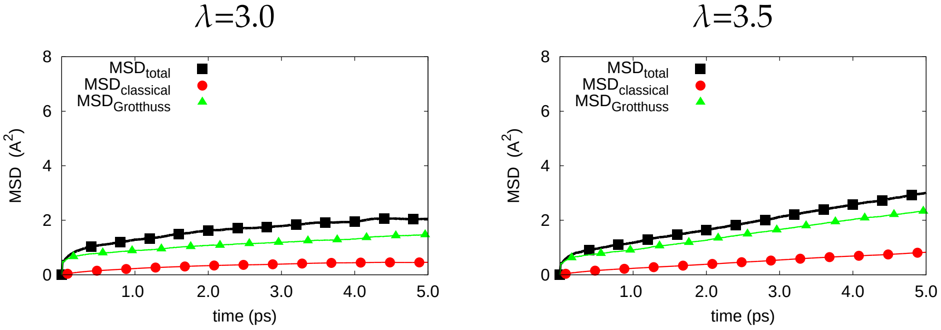

Figure 7.15: The $\mathrm{MSD}_{\mathrm{classical}}$, based on the classical ion diffusions, and the $\mathrm{MSD}_{\mathrm{Grotthuss}}$, based on the Grotthuss hops, are shown together with the $\mathrm{MSD}_{\mathrm{total}}$, which includes both of these mechanisms, pore D with water contents 3.0 (left) and 3.5 (right) for the simple model with the BLYP functional. Only the z-component of the displacements is considered.

For the other pore models, including the simple model (only pores A and B), the free model, and the parallel backbone model, only the total MSDs are represented in Figures 7.16, 7.17, and 7.18.

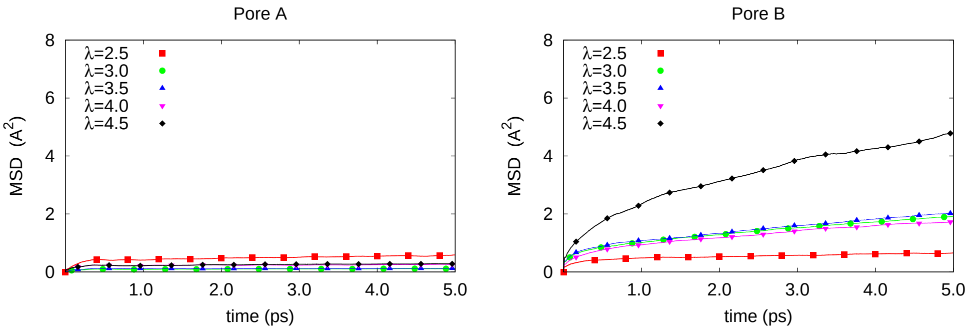

Figure 7.16: Mean square displacement (only in z-direction) of the protons in the simple model for pores A and B with BLYP functional are shown.

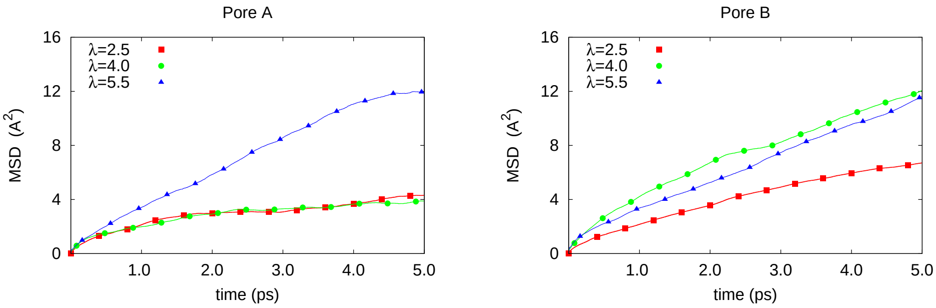

Figure 7.17: Mean square displacement (only in z-direction) of the protons in the simple model with HCTH functional for pores A and B are shown.

The diffusion coefficients of the protonated oxygens calculated by using the $\mathrm{MSD}_{\mathrm{classical}}$, based on the classical ion diffusion, the $\mathrm{MSD}_{\mathrm{Grotthuss}}$, based on the Grotthuss hops, and the $\mathrm{MSD}_{\mathrm{total}}$, including both contributions, are shown in Figure 7.19 for the z-component.

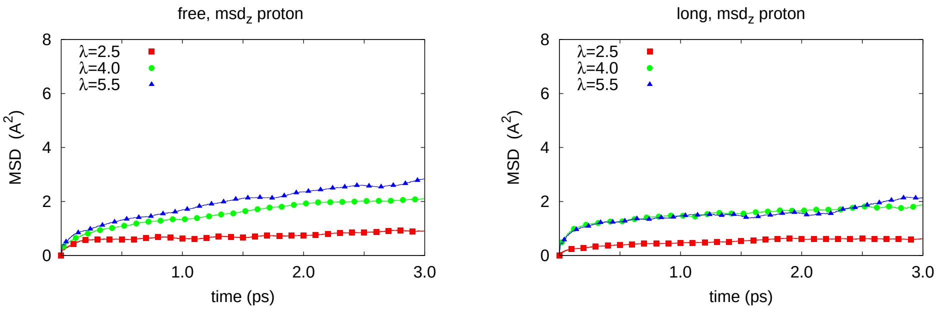

Figure 7.18: Mean square displacement (only in z-direction) of the protons in the free and the parallel backbone models are shown.

The simple pore model with the BLYP functional: The classical diffusion of the protonated oxygens resembles the diffusion of the mobile oxygens, since the protons exist mostly in the dissociated proton states. An increasing hydration level does not lead to changes in the diffusion of the protons in the pore A. However, in the pore B especially at high water content (higher than 3), changes in total diffusion of the protonated oxygens with respect to the hydration level demonstrate a tendency similar to the one which is based on the Grotthuss hops. A sudden increase in the proton diffusion is observed in the pore B at 4.5 water content.

The simple pore model with the HCTH functional: At low water content, the classical diffusion of the protonated oxygens differs from the diffusion of the mobile oxygen due to the high fraction of the acidic protons, in which the protonated oxygens are sulfonate oxygens. By increasing water content, this fraction decreases and the protons are bonded to the mobile oxygens. This causes the classical diffusion of the protons to become similar to that of the mobile oxygens. At water content 5.5, this similarity is more pronounced than at λ=4.0.

Interestingly, even at very low water content, in which a high fraction of acidic protons exist, the Grotthuss mechanism contributes to the diffusion of the protons and results in high proton mobility. This is related to the functional, which leads to a high diffusion of water molecules. A possible dynamics of the protons is explained as in the following: whenever a proton is dissociated from the sulfonate group, the high diffusivity of the water molecules promotes the proton mobility either via classical ion diffusion or Grotthuss hop mechanism. The increasing hydration level causes the classical diffusion of the water to decrease (see Fig. 7.14). Therefore, the effect of high water diffusion which promotes the Grotthuss mechanism at low water content is also decreased. However this decrease is compensated by an increase in the possible pathways for a Grotthuss hop, due to an increase in the number of hydrogen bonds, as a result of the increasing hydration level.

The free and the flexible models: The diffusion of protonated oxygens based on the total and the Grotthuss hops increases almost linearly with increasing hydration level in the free model. However, in the flexible pore model, the diffusion drops at the water content 4.0, at which the sulfur-sulfur radial distribution function resembles to the one of the pore A in the simple model with the BLYP functional (see Figures 5.2 and 5.4 in Section 5.1.1). The close sulfonate spacing at water content 4.0 hinders the diffusion of the protons in the flexible pore model, in which flexible position restraints are used during the simulations.

The parallel backbone model: The classical, the Grotthuss-based, and total diffusion coefficients of protonated oxygens increase almost linearly with increasing hydration level in the parallel backbone model.

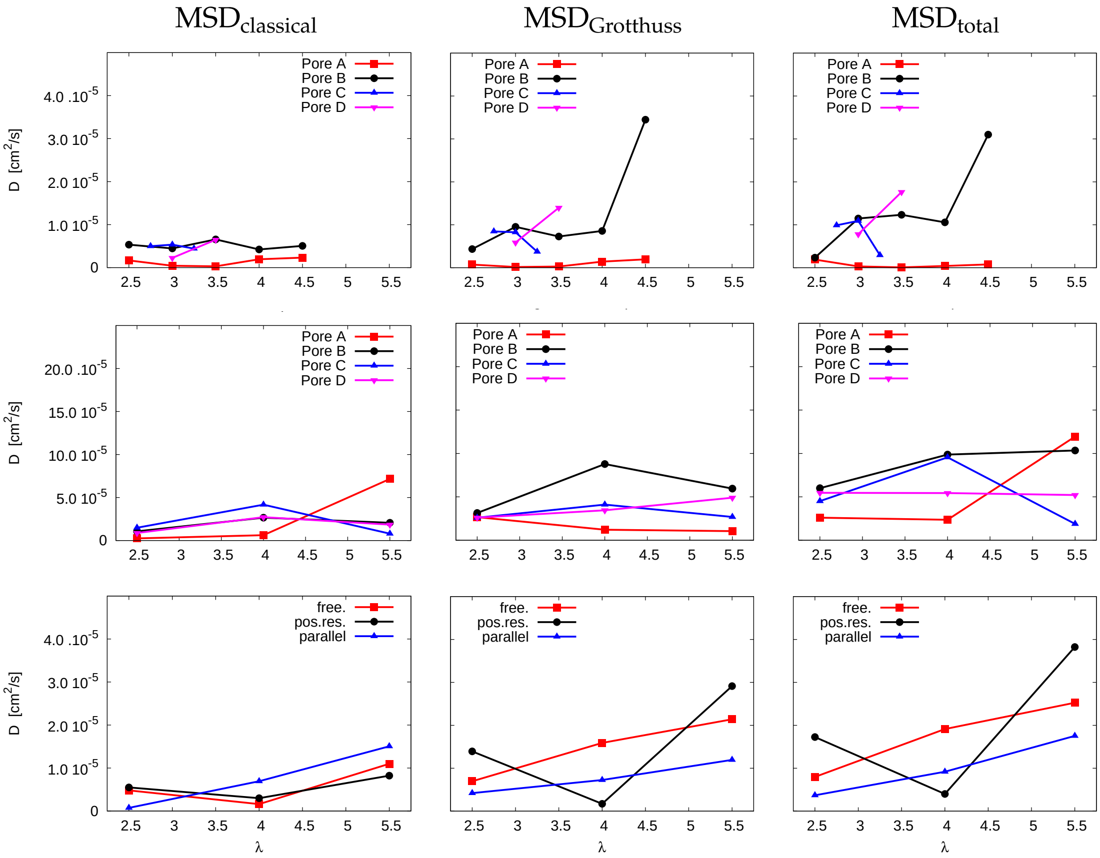

Figure 7.19: Diffusion coefficients of the protonated oxygens are shown for the fixed pore model with BLYP functional (top) and with HCTH functional (middle). In the frames at the bottom row, the diffusion coefficients for the free model, the flexible model, and the parallel backbone model, are presented. The frames in the left and the middle columns represent the MSDs based on the classical ion diffusions and the Grotthuss mechanism, respectively. The frames on the right column represent the total MSDs.

7.4 Discussion

The dependencies of both the fraction of the possible proton states and the self-diffusion of the protons on the hydration level in the simple pore models reveals that the exchange-correlation functional and additionally the dispersion corrections used in the simulations lead to different results related to the chemical equilibria of the proton complexes and the dynamics of the system. For example, the threshold for the dissociation of the protons is found at λ=3.0 for the simulations with the BLYP functional and no dispersion correction. Whereas, at the ones with the HCTH functional and dispersion corrections, the threshold for the complete dissociation is realized only at λ larger than 5.5.

As far as the mobility of the protons is concerned, the difference between these two models becomes more apparent in that the self-diffusion of the protons in the simulations with the HCTH functional with dispersion corrections is much larger than the one in the simple pore model with the BLYP functional for the same water content. Approximately the same tendency is observed for the diffusion of the water molecules (mobile oxygens). Indeed, as it was suggested in the literature, the HCTH functional leads to more dynamics than BLYP [90].

Even at very low water content in the simple pore model with the HCTH functional, a high proton mobility has been observed along with a high fraction of undissociated protons. This indicates that the proton transfer mechanism in this model is similar to surface hopping mechanisms. A proton, which is bonded to one of sulfonate oxygens, might hop to a water molecule, at which it stays for a very short time as bonded. Then it returns back to the sulfonate group and could be possibly not bound to the original sulfonate oxygen but to another oxygen of this sulfonate group. Such a kind of mechanism is enhanced by high diffusion coefficients of the water molecules in this model.

Furthermore, the short length of the simulations with the HCTH functional (approx. 20 ps) also plays a role in having different results, insofar as statistics based on these simulations are less accurate than the ones obtained with the BLYP functional. Unfortunately, again due to the short length of the simulations, a direct error calculation could not be done.

The difference between the total diffusion coefficients and the sum of the diffusion coefficients based on the Grotthuss mechanism and the classical transport is shown in Figure 7.20. This also reflects that the statistics used in the calculation of the diffusion coefficients in the pore model with the HCTH functional should be increased and hence longer simulation length is required.

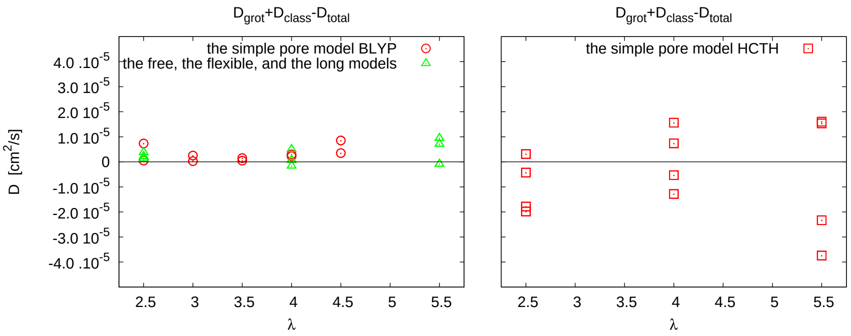

Figure 7.20: The difference between the total and the sum of the Grotthuss and the vehicular diffusion coefficients

Although many proton hops are observed, they do not contribute to the mobility of the protons overall, because, in the most cases, a proton hopping is followed by another hop in which it returns back to the original partner. This behavior of the protons during Grotthuss diffusion, which can be labeled as the back-and-forth hopping mechanism, happens between two or three water molecules, and in some cases also a sulfonate group is involved. Due to the high fraction of this back-and-forth hoping, the contribution of the Grotthuss mechanism to the mobility of the protons is limited at low water content. The main reason for this high fraction of the back-and-forth proton hops is a lack of neighboring water molecules with correct orientation, which is affected by the narrow pore structure with close sulfonate groups spacings. Therefore, the number of available water molecules to which a proton may hop, is limited.

Chapter 8

Spectral Densities of Motion

Infrared (IR) and Raman spectroscopy are powerful tools to study the dynamics, in particular of intramolecular vibrations and periodic intermolecular motions. The infrared (IR) and Raman spectra of the perfluorosulfonate ionomer were extensively studied by various techniques [44, 66, 126, 207, 118, 9, 73, 143, 46]. Usually, the effect of the hydration level on the membrane is investigated by comparing the IR spectra at various levels of relative humidity, changing from the dry case to a fully hydrated one. The changes in the IR spectra may appear as a decrease, an increase in the intensity of certain peaks, a shift of peak position to a lower or a higher frequency, or a peak may become broader or narrower. For example, the effect of the dissociation of sulfonate groups is observed as a decrease in the intensity of the S-O-H peak.

In molecular dynamics simulations, the spectral densities of motion of the atoms can be calculated as the Fourier transform of the velocity auto-correlation function. The dipole-dipole auto-correlation function can also be used to compute in a similar way the IR signal. These spectra can be compared with experimental ones [123]. Computational spectra for molecular systems, including Nafion® , triflic acid, and hydrated protons, have been reported in the literature [55, 110, 81, 196, 206, 7, 45, 19, 78]

Within this chapter, we will first briefly explain how the spectral density (SD) of motion is calculated. Then, the SD, which is based on the velocity auto-correlation of individual atoms constituting the ionomer pores, will be discussed, followed by a section, in which the effect of the coordination number of hydrogen atoms on their spectral density is investigated. Then, the SD of proton complexes, including hydronium, pseudo-Zundel-, and

Zundel-cations is shown. Lastly, the effect of hydration levels is shown by comparing the integrated SDs.

8.1 Calculating the spectral density

The spectral density of the motion is calculated by using the Fourier transform of the velocity auto-correlation function. Since dipole moments were not calculated during the simulations for the simple pore model with the BLYP functional, only the velocity auto-correlation functions are used to for the analysis.

Velocity auto-correlation function: The correlation of the velocities of an atom is expressed by the scalar product of its velocity at time t with the one at a later time $t + \tau$, where τ is the correlation time. The velocity auto-correlation function of a single atom for a single time origin, t, is then given by

$$c_{vv}(\tau) = \mathbf{v}(t + \tau) \cdot \mathbf{v}(t) \tag{8.1}$$

where $\tau = k\Delta t$ is the correlation time and Δt is the time step. This correlation function, based on a single atom and a single time origin, is usually averaged over sets of atoms and time origins. The normalized velocity auto-correlation function (VACF) is thus

$$C_{vv}(\tau) = \frac{1}{I}\frac{1}{J}\sum_{i=1}^{I}\sum_{j=1}^{J}\frac{\mathbf{v}_i(t_j + \tau) \cdot \mathbf{v}_i(t_j)}{\mathbf{v}_i(t_j) \cdot \mathbf{v}_i(t_j)} \tag{8.2}$$

where I and J correspond to the number of atoms in the set and of time origins, respectively.

Figure 8.1 shows the velocity auto-correlation function once for all atoms in the studied simple pore model (excluding the fixed carbon atoms) and once just for the H atoms within the pore.

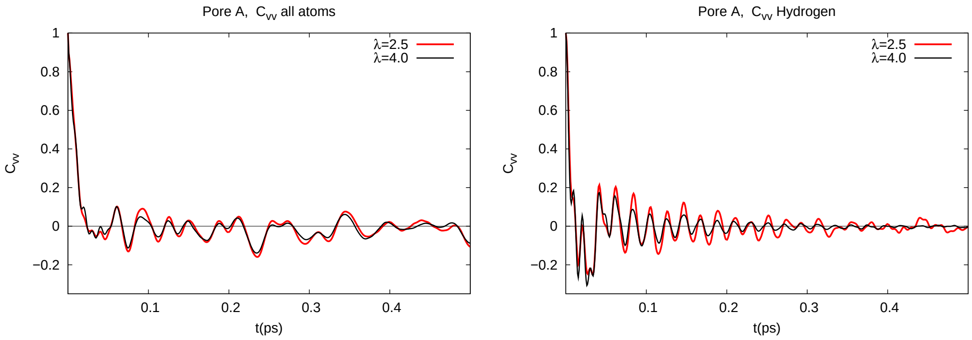

Figure 8.1: Velocity auto-correlation functions of all atoms (left) and of the H atoms (right) for the simple pore model with water contents 2.5 and 4.0 (the number of water molecules per sulfonate group).

Even though the velocities of the water molecules are included in the VACFs of all atoms, the contributions due to the water molecules have less effect than the ones due to the atoms of the ionomer (C, F, SO_3). Hence the characteristics of the VACF are mainly determined by the atoms belonging to the ionomer (C, F, SO_3). Therefore, the effect of the hydration, which is the difference between the VACFs for λ =2.5 (red) and 4.0 (black), is more pronounced in the VACFs of the hydrogen atoms (right frame in Figure 8.1) than in the one of all atoms.

Furthermore we define a conditional velocity auto-correlation function as

$$\tilde{C}_{vv}(\tau) = \frac{1}{I}\frac{1}{J}\sum_{i=1}^{I}\sum_{j=1}^{J}\frac{\tilde{\mathbf{v}}_i(t_j+\tau)\cdot\tilde{\mathbf{v}}_i(t_j)}{\mathbf{v}_i(t_j)\cdot\mathbf{v}_i(t_j)} \tag{8.3}$$

where the velocity of the atom, $\tilde{\mathbf{v}}_i(t)$, is taken to be 0, if a specified condition is not satisfied. As further discussed below,

$$\tilde{\mathbf{v}}_i(t_j) = g_i(t_j)\mathbf{v}_i(t_j) = \begin{cases} \mathbf{v}_i(t_j) & \text{if the condition is true; } g_i(t_j) = 1 \\ 0 & \text{if the condition is false; } g_i(t_j) = 0 \end{cases} \tag{8.4}$$

where $g_i(t_j)$ is a boolean function, which takes the values of either 0 or 1.

It is needed to distinguish, for example, the VACFs of the hydrogen atoms belonging to the water molecule from the ones belonging to hydronium. Due to proton hoping, a water molecule may change its state and becomes a hydronium, which is a time dependent process. Therefore the selection criterion is applied dynamically. The differences between the VACFs of hydrogen atoms belonging to water and hydronium, shown in Figure 8.2, are detectable. However, for a comprehensive understanding of these complex signals, one needs to transform them to the frequency domain.

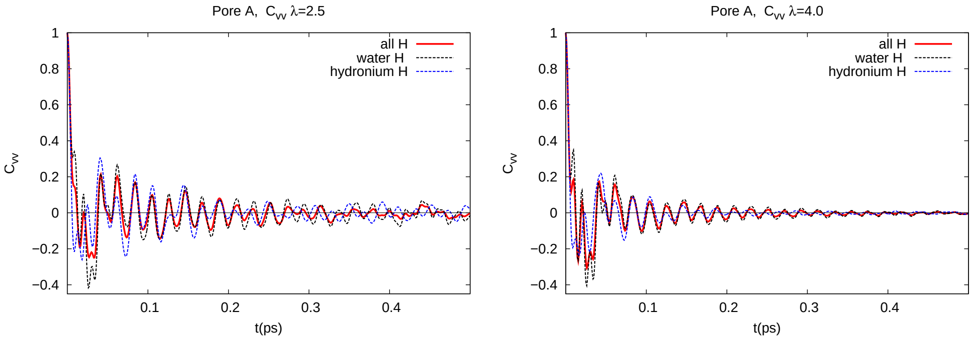

Figure 8.2: Velocity auto-correlation functions of the hydrogen atoms of water and hydronium for the simple pore model with BLYP with water contents 2.5 (left) and 4.0 (right) together with the one for all H atoms.

The Fourier transform of the velocity auto-correlation The discrete Fourier transformation is used to calculate the spectral densities of the motion. It is a transformation from the time domain to the frequency domain, and is defined as

$$I(\omega) = \sum_{k=0}^{K-1} C_{vv}(k\Delta t)\frac{1}{2}\left[e^{-i\omega k\Delta t} + e^{-i\omega(k+1)\Delta t}\right]\Delta t \tag{8.5}$$

where the frequency, ω, is usually expressed in terms of discrete values $i\Delta\omega$. The commonly used unit for frequencies is the wavenumber, cm^{-1}. Since the velocity auto-correlation is a real valued function, its Fourier transform is real as well,

$$I(\omega) = \sum_{k=0}^{K-1} C_{vv}(k\Delta t)\frac{1}{2}\left[cos(2\pi\omega k\Delta t) + cos(2\pi\omega(k+1)\Delta t)\right]\Delta t \tag{8.6}$$

and represented by the cosine function. For the calculation of the velocity auto-correlation function 1000 configurations are used which corresponds a correlation time length of approximately 1 ps (4.10^4 in atomic units). The velocity auto-correlation function is also smoothed by using a Blackman-Harris 4-term (-75 dB) window function [75] with the following parameters

$$\text{S}_{\text{BH}} = 0.40217 - 0.49703\cos(\omega) + 0.09392\cos(2\omega) - 0.00183\cos(3\omega) \tag{8.7}$$

The effect of this smoothing on the C_{vv} and its Fourier transform is shown for the hydrogen atoms in the simple pore model at the water content 4.5 in Figure 8.3. A detailed discussion of the H spectra will be given in Section 8.3. One can repeat the window function recursively. A high number of the repetitions (N=50) leads to smoother spectra compared to spectra with N=10 or to non-smoothed ones. However, the intensity difference between N=50 and N=10 is, in many cases, larger than the effect of the hydration, as seen in Figure 8.4. For this reason, a damping factor of 10 is chosen. This value ensures smooth spectra while keeping the deviations small.

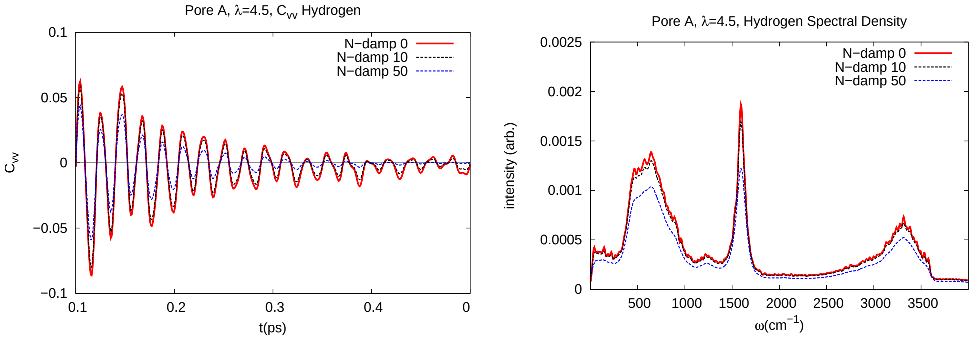

Figure 8.3: Effect of the window functions on the velocity auto-correlation functions of the H atoms (left) and its Fourier transform (right) for the simple pore model with BLYP at the water content 4.5. N-damp is the number of repetitions of the window function.

8.2 Spectral of densities of motion of the heavy atoms

The heavy atoms (C, F, S, O_S) belonging to the molecules of the ionomer models are considered first, since their spectra can be calculated by using the normal VACF. The corresponding spectra are also comparable with the experimental ones in the literature i.e. [126, 73].

The vibrational spectral densities of motion of the carbon and fluorine atoms are calculated by the procedure described above. The resulting spectra are shown here only for the water content 2.5 and 4.0 in the simple fixed pore model with the BLYP functional (see Figure 8.4). Since the interactions between the carbon and water are indirect, screened by the fluorine atoms or sulfonate groups, the effect of hydration on the carbon spectra is less pronounced than the one on the fluorine atoms.

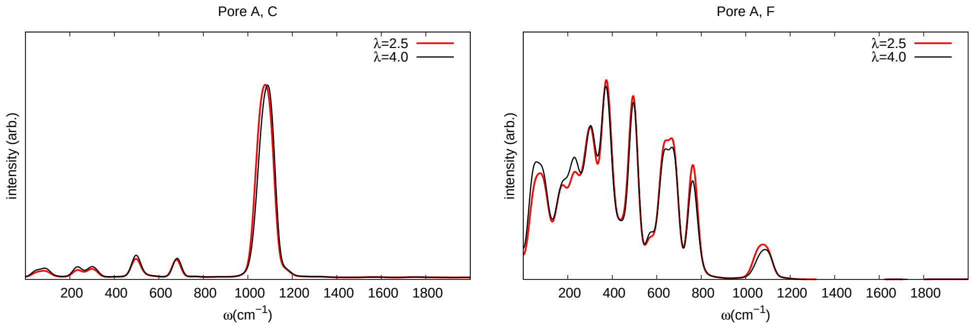

Figure 8.4: Fourier transforms of the velocity auto-correlation functions of the C atoms (left) and F atoms (right) for the simple pore model with BLYP at water contents 2.5 and 4.0.

The spectra of C and F (see Figure 8.4) are also affected due to the defined position restraints, which are used to maintain the pore structure.

Table 8.1: The peak positions, in cm^{-1}, in the spectral densities of motion belonging to C and F atoms for pore A at λ 2.5 and 4.0.

λ=2.5		λ=4.0	
C	F	C	F
84	77	86	78
	178		178
236	232	236	
299	300	301	303
	373		371
498	493	498	493
	570		570
	638		638
679	667	682	669
	762		762
1078	1076	1089	1087

Therefore, the vibrations of the atoms bonded to fixed carbon atoms are expected to deviate from the experimental IR spectra.

The spectral densities have broad peaks whose maxima are given in Table 8.1. The effect of the hydration appears as small shifts of the frequencies. It is significant that the center of the broad peak in the C spectra, located at the wavenumber 1078 cm^{-1} for λ=2.5, is shifted to 1089 cm^{-1} for λ=4.0.

If the peak positions of the C and F spectra coincide, or appear at almost identical wavenumbers, then the corresponding mode is interpreted as due to the C-F stretching or bending. A clear distinction between bending and stretching modes is only possible by a normal mode analysis, which is not within the scope of this work. For this reason, the spectra are compared with the ones found in the literature, which allows to differentiate some of these particular modes of the vibrational spectra [126, 69, 72, 23]. A representative example of this is that the peak at 667 cm^{-1} which was assigned to F-C-F bending [69]. However, it is not possible to match all calculated spectra with the peaks reported in the literatures on Nafion® , since our model is simplified (CF_3CF_3) and does not include, for example, C-O-C bending or CF_2 stretching.

Then, the spectral densities of motion for the sulfur and oxygen atoms of the sulfonate groups are considered. These are shown in Figure 8.5. The peak positions of the corresponding spectra are listed in Table 8.2.

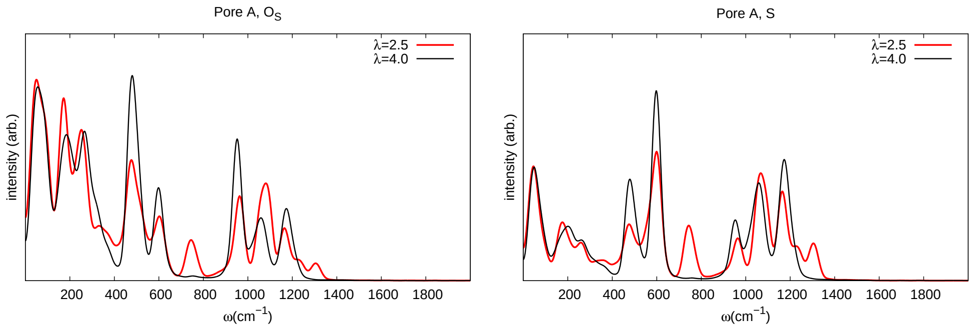

Figure 8.5: Fourier transform of the velocity auto-correlation functions of the oxygen atoms belonging to sulfonate groups (left) and the sulfur atoms (right) for the simple pore model with BLYP at water contents 2.5 and 4.0.

The effect of the hydration on the spectra of S and O_S is even more pronounced and complicated than the one on the C and F spectra, since increasing the hydration level may change the chemical state of the sulfonate groups. As it was shown in Chapter 7, an undissociated sulfonate group was observed only in pore A at water content 2.5. In the other cases, all the protons were observed as dissociated from the sulfonate groups in the simple pore model with the BLYP functional. Therefore, the calculated

S and O_S spectra should show this chemical change.

The comparison of the S and O_S spectra at water contents 2.5 and 4.0, as expected, indicates the effect of dissociation such that the peaks, due to the undissociated sulfonate groups, located at 744 and 1304 cm^{-1} and the shoulder at 1228 cm^{-1} in the O_S spectra for λ=2.5 disappear for water content 4.0. These peaks can, therefore, be attributed to undissociated sulfonate groups. The effect of dissociation has also been reported as decreasing the intensity of the sulfonate groups spectra with increasing hydration level in literature i.e. [126, 73].

The peak located at 1059 cm^{-1}, which is observed only for λ=4.0, is assigned to symmetric vibrations of SO_3^-. It is shifted for the undissociated case to 1068. The same peak was found also at 1058 and 1070 cm^{-1} for hydrated (dissociated) and protonated Nafion® in experiments [23].

Additionally, the effect of the hydration appears as shifts in the frequency of the peaks positions, between two water contents, λ 2.5 and 4.0. These shifts in S and O_S spectra are larger than the ones in the C and F spectra.

Table 8.2: The peak positions, in cm^{-1}, in the spectral densities of motion belonging to S and O_S atoms for pore A at λ 2.5 and 4.0. Very weak signals are observed and denoted by (*).

λ=2.5		λ=4.0	
S	O_S	S	O_S
48	52	49	56
	84		
176	172	201	185
259	252	260	266
356	332		
	369		
476	477	479	479
600	601	598	598
744	745	758(*)	753(*)
964	964	953	952
1068	1080	1059	1059
1165	1165	1173	1173
1228	1227		
1304	1305		

8.3 The effect of the hydrogen coordination number on its spectra

Changes in the hydration level lead to changes in the spectral densities of motion of the hydrogen atoms (see Figure 8.6). The hydration level is related to the coordination number of hydrogen, as shown in Section 6.1. To understand the effect the hydration level has on the spectral densities, the coordination number is therefore explicitly taken into consideration while calculating the spectral densities. The conditional velocity auto-correlation functions (see Eq. 8.3) are used to calculate these spectral densities.

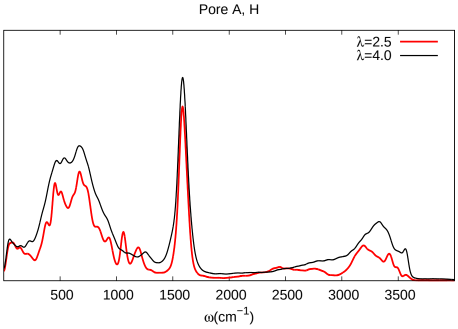

Figure 8.6: Spectral density of motion for H atoms in the simple fixed model pore A at water contents 2.5 and 4.0.

A cutoff radius is used as a selection criterium to determine the coordination number, c_i, of the hydrogen atoms. If a hydrogen has only one neighboring oxygen atom within the cutoff radius, it is labeled as $c_i = 1$. If a hydrogen has two neighboring oxygens, then the coordination number is larger than one, $c_i > 1$, which indicates that it might be engaged in a hydrogen bond.

The spectral density of the hydrogen atoms, depending on this selection criterion, is represented for the simple fixed model with two different hydration levels 2.5 and 4.0, in Figures 8.7 and 8.8. The coordination numbers have been evaluated at various cutoff radii, between 1.8 Å and 2.4 Å. For the largest cutoff value, 2.4 Å, a non-hydrogen-bonded case ($c_i = 1$) indicates the presence of a dangling O-H. This might belong to a water molecule or an undissociated sulfonate group $R - SO_3H$. For $c_i > 1$, the cutoff value of 2.4 Å selects the hydrogen atoms engaged in a very weak hydrogen bond, whereas a radius of 1.8 Å selects the ones engaged in a strong hydrogen bond. An angle criterion, which is included in the usual definition of hydrogen bonds, is not taking into account.

The spectral densities between 0 and 900 cm^{-1} in Figure 8.7 are assigned essentially to the translational and the librational motions [14]. The highest intensity of the broad bands is observed at around 450 and 490 cm^{-1} for $c_i = 1$ with λ=2.5 and λ=4.0, respectively. For $c_i > 1$, the maxima are strongly shifted to higher frequencies and observed at around 650 cm^{-1} with both water contents. This shift is valid for all cutoff values. Increasing the cutoff radius leads to a decrease in the intensity of the broad peaks of the spectra belonging to the atoms with one neighbor, $c_i = 1$, which is shown by solid lines in Figure 8.7. However, the intensities of the spectral densities of the hydrogen having more than one neighbor, $c_i > 1$, increase with the cutoff value. The same dependencies are also valid for the spectral densities at the water content 4.0.

The spectral densities between wavenumbers 1000 and 1800 cm^{-1} correspond to undissociated sulfonate group vibrations (the peak centered at 1060 cm^{-1}) and the bending of water molecules (between 1500 and 1700

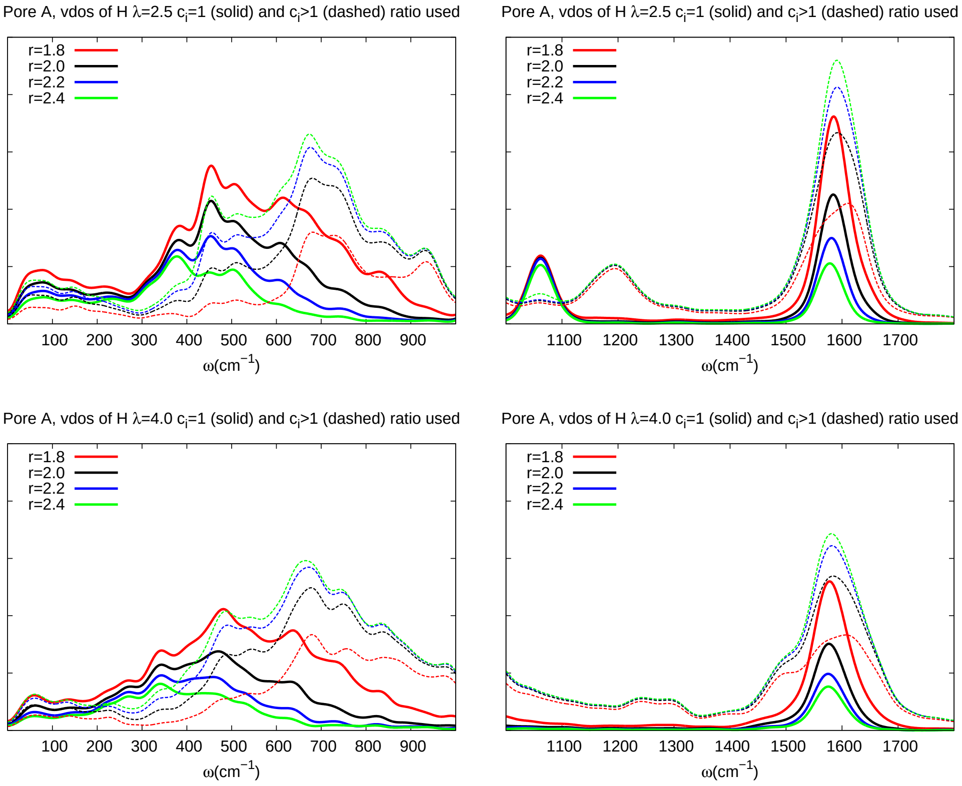

Figure 8.7: Spectral density of motion for the H atoms depending on their coordination number determined with various cutoff radii. The coordination number, c_i, corresponds to the number of oxygen atoms around a hydrogen atom within a chosen cutoff radius. Hydrogen atoms with $c_i > 1$ are possibly engaged in a hydrogen bond. The Fourier transform of the velocity autocorrelation functions is presented for the simple pore model with BLYP at the water contents 2.5 (top) and 4.0 (bottom).

cm^{-1}). Comparing the spectra at λ=2.5 and λ=4.0 indicates that the peak centered at 1060 cm^{-1} is only observed for λ=2.5 and disappears for other λ values. Since the undissociated sulfonate groups are only observed at λ 2.5 for pore A (see Sec. 7.1), this peak most likely corresponds to the stretching of the $O_S - H$ bonds in the undissociated sulfonate groups.

Considering the spectra belonging to $c_i > 1$, a broad peak centered at

1200 cm^{-1} is observed for λ=2.5 with $c_i > 1$. In contrast, two broad peaks at 1250 cm^{-1} and 1300 cm^{-1} are observed for λ=4.0. These two peaks are related to the one observed for λ=2.5 as representing a shift and split of the latter. Changing the cutoff radius has here almost no effect on the peak positions centered at 1060 and 1200 cm^{-1} for both $c_i = 1$ and $c_i > 1$. This can be attributed to a stable hydrogen bond network and also to stable O-H bonds of the undissociated sulfonate group (λ=2.5).

The peak located at 1580 cm^{-1} is related to the H-O-H bending of the water molecule. Hydrogen atoms with coordination $c_i = 1$, have a narrower band than the ones whose coordination number is larger. This is valid for both water contents. Furthermore, at λ=4.0, a splitting of the spectra of the hydrogen atoms with $c_i > 1$, which includes a shoulder around 1500 cm^{-1}, is observed. The reason of the broadening and splitting of the spectra of hydrogen atoms with $c_i > 1$ is the inclusion of hydronium or/and Zundel complexes in the spectral densities, as will be shown in Section 8.4. For both water contents, increasing the cutoff radius leads to a decrease in the intensity of the spectra with $c_i = 1$, whereas, the ones with $c_i > 1$ increases with the cutoff radius.

The spectral densities between 1800 cm^{-1} and 2900 cm^{-1} are shown in the left frame of Figure 8.8 For both water contents, only the spectra of the hydrogen atoms with coordination number greater than one are observed. They show almost no dependency on the cutoff radius, hence all spectra belonging to different cutoff radii appear as one line. This indicates that the spectra correspond to hydrogen atoms which have two neighboring oxygens within 1.8 Å. These hydrogens are possibly engaged in a strong

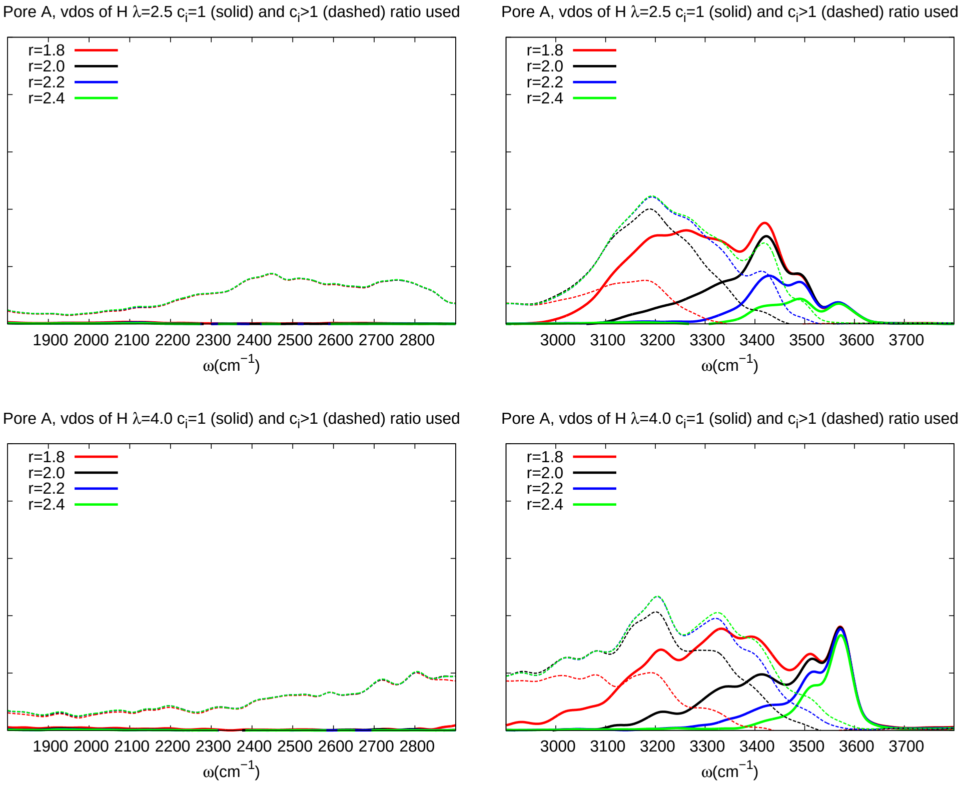

Figure 8.8: Spectral density of motion for H atoms depending on their coordination number is shown with various cutoff radius. The coordination number, c_i, corresponds to the number of oxygen atoms around hydrogen within chosen cutoff radius. $c_i > 1$ corresponds to hydrogen atom possibly engaged in a hydrogen bond. The Fourier transform of conditional velocity auto-correlation functions for the simple pore model with BLYP at water contents 2.5 (top) and 4.0 (bottom) are weighted according to the number of hydrogen atoms.

hydrogen bond and may belong to hydronium or Zundel cations. The hydronium or Zundel spectra will be shown in the next section (see Sec. 8.2).

The spectral densities between 2900 cm^{-1} and 3800 cm^{-1} include O-H stretching bands and are shown in Figure 8.8. The intensity of the spectral densities within the interval between 3000 cm^{-1} and 3580 cm^{-1} exhibits a strong dependency on the cutoff radius. Increasing the cutoff radius leads to an increase in the intensity for hydrogens with $c_i > 1$ and to a decrease in the spectra of hydrogens with $c_i = 1$ for both λ 2.5 and 4.0. These changes are due to the strength of the hydrogen bonds in which these atoms participate. However, for wavenumbers larger than 3600 cm^{-1}, only spectra belonging to the hydrogens with $c_i = 1$ are observed. These spectra correspond to the stretching of dangling O-H and their intensities do not depend on the cutoff radius.

8.4 The spectral densities of water and proton complexes

The spectral densities of the hydrogen atoms are decomposed here according to the classification described in Section 7.1, which is based on a geometrical criterion. This criterion defines hydrogen and oxygen atoms as a single proton complex if the distance between the atoms is smaller than the chosen cutoff value, 1.35 Å. The proton complexes can then be classified according to the number of hydrogen and oxygen atoms (oxygens of sulfonate, O_S, are treated different from the other oxygens, O_W). They contain acidic protons, pseudo-Zundel, hydronium, Zundel, and water. These are listed in Table 8.3.

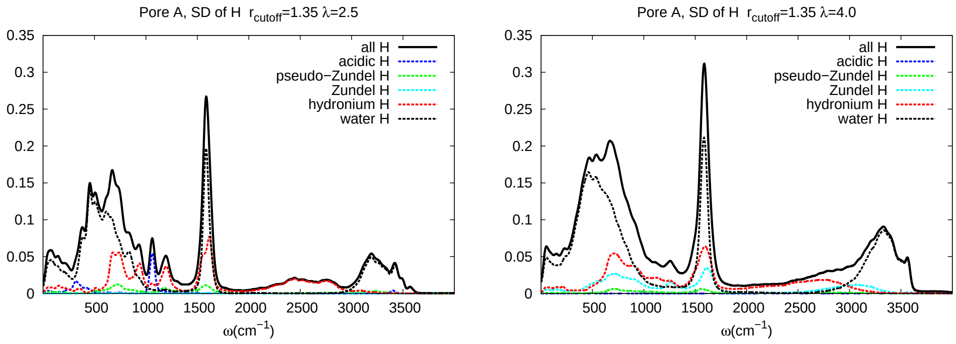

Figure 8.9: Spectral densities of H atoms for the different complexes.

The corresponding spectral densities are weighted according to the number of hydrogen atoms in the system, which are 24 and 36 for λ 2.5 and 4.0, respectively. The resulting spectral densities of the hydrogen atoms of the proton complexes and water are shown in Figure 8.9 for the simple fixed model with the BLYP functional at two water contents, 2.5

Table 8.3: The number of H, O_W, and O_S in a connected atom list used to classify the proton complexes. The cutoff radius, 1.35 Å, is chosen in order to group the atoms as connected. Then, the connected atoms are classified according to their type, which can be either H, O_W, or O_S.

Proton complex	n_H	n_{O_W}	n_{O_S}
Acidic	1		1
Pseudo-Zundel	3	1	1
Hydronium	3	1	
Zundel	5	2	
water	2	1	

(left frame) and 4.0 (right frame).

This decomposition of spectral densities allows us to distinguish the peaks and assign them to a specific proton complex. At first glance, the dominant spectra belong to the hydrogen of water, as can be expected, since the number of hydrogen atoms belonging to water is the largest. However, as also expected, in some intervals, the spectra of the hydrogen of hydronium or acidic protons are more intense than that of the water. These regions are presented in more detailed plots in Figures 8.10 and 8.11. The contribution of each proton complex to the total hydrogen spectra is explained in the following.

Between 0 and 1000 cm^{-1}: for both water content levels, 2.5 and 4.0, the main contribution belongs to water hydrogen. The acidic proton spectra for the water content 2.5 appear as a broad band, located between 300 and 450 cm^{-1}. The hydronium contribution becomes the second most important one between 600 and 1000 cm^{-1}. Furthermore, it has a peak at 940 cm^{-1}, which is larger than that of water. The contribution of the

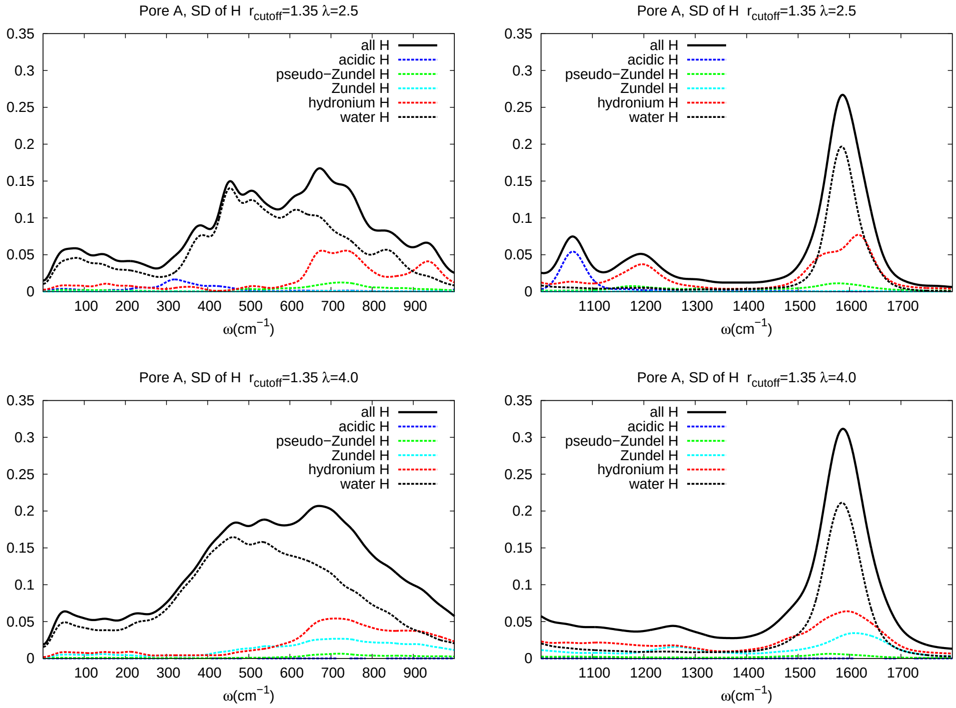

Figure 8.10: Spectral density of motion for H atoms depending on their coordination number is shown with various cutoff radius.

pseudo-Zundel ion is also seen between 600 and 1000 cm^{-1}. As the water content is increased to 4.0, the spectrum of the acidic proton disappears and the pseudo-Zundel contribution decreases strongly. The spectral densities due to Zundel cations appear between 600 and 1000 cm^{-1} at the water content 4.0 only.

Between 1000 and 1800 cm^{-1}: The water spectra no longer dominate the spectral densities between 1000 and 1450 cm^{-1} for both water contents. The spectral densities of the acidic proton, which have a peak at 1060 cm^{-1} for λ=2.5, disappear for λ=4.0. The hydronium spectral densities, which involve a clear peak at 1200 cm^{-1} for λ=2.5, become distributed and indistinguishable for λ=4.0. This indicates that a stable structure of hydronium, which exists for λ=2.5 due to sulfonate traps, looses its stability and incorporates proton hopping. The band between 1450 and 1700 cm^{-1} is related to the H-O-H bending mode, consequently the contribution of the water molecules governs the total spectrum. In this region, for λ=2.5 the hydronium spectrum is a superposition of two broad peaks, the first one centered at 1545 cm^{-1} and the second one at 1630 cm^{-1}. For λ=4.0, this dual feature is not observed. Instead, the Zundel spectrum appears as a broad peak, whose center is shifted towards higher wavenumbers.

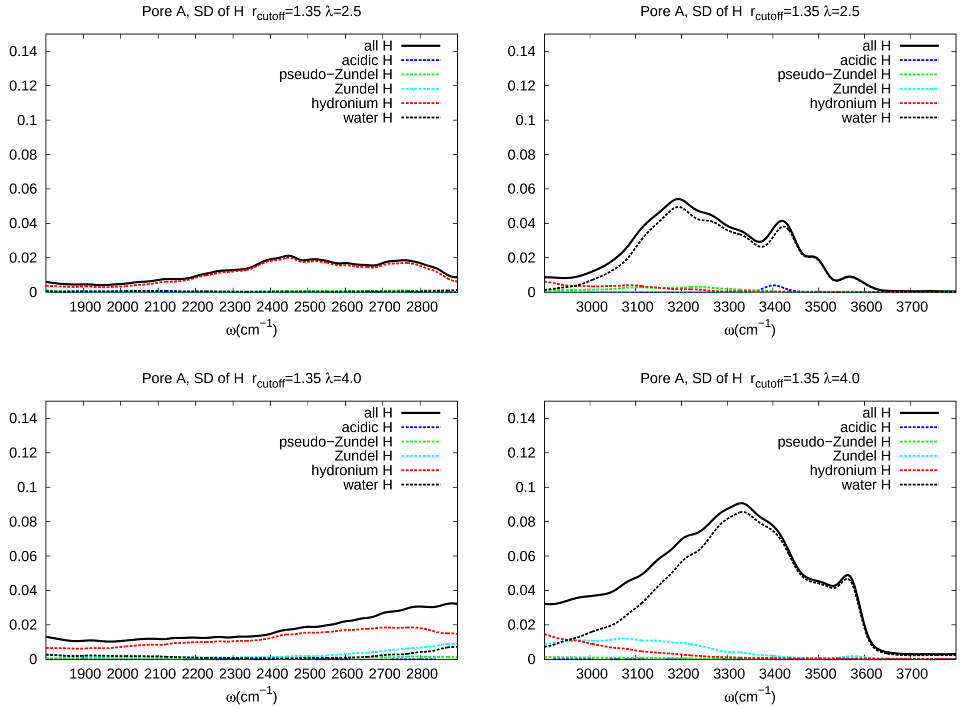

Figure 8.11: Spectral densities of motion for H atoms depending on various proton complexes between 1800 and 3800 cm^{-1}

Between 1800 and 2900 cm^{-1}: The dominating contribution to the total spectral density of the hydrogen atoms comes from hydronium for both water contents. At λ =2.5, there is almost no other contribution. At λ =4.0, very slight spectral densities of the Zundel ion and water are observed for wavenumbers larger than 2700 cm^{-1}. As it was explained in the previous section, there is no presence of the dangling O-H bonds spectra. This indicates that the hydronium cations establish hydrogen bonds with neighboring molecules.

Between 2900 and 3900 cm^{-1}: The most important contributions to the total hydrogen spectra come from the hydrogens of the water molecules, whose stretching of the O-H bonds is associated to the bands between 2950 and 3600 cm^{-1}.

The effect of the hydrogen bonds on the spectral densities can be also deduced by comparing the spectra of the water and the Zundel complex, which has a strong hydrogen bond. Its spectrum is shifted towards lower wavenumbers than the one belonging to the water, which is observed as a broad band and includes strongly and loosely hydrogen-bonded and non-hydrogen-bonded hydrogens. This mirrors the observation made in Section 8.3 for the spectra of the hydrogen which is engaged in a hydrogen bond. Indeed, a Zundel complex can be interpreted as involving a water molecule and a hydronium ion. Therefore its spectrum may include the features of both water and hydronium. Interestingly, a very small peak at 3400 cm^{-1} is observed in the spectral densities of the acidic proton for λ=2.5.

The spectral densities of motion, including the hydrogen atoms of water molecules and the hydrogen of hydronium, are represented in Figure 8.12

for the simple model pore A with all water content levels. The comparison of these spectra will be made in the following section, in which the integral of these spectra is considered.

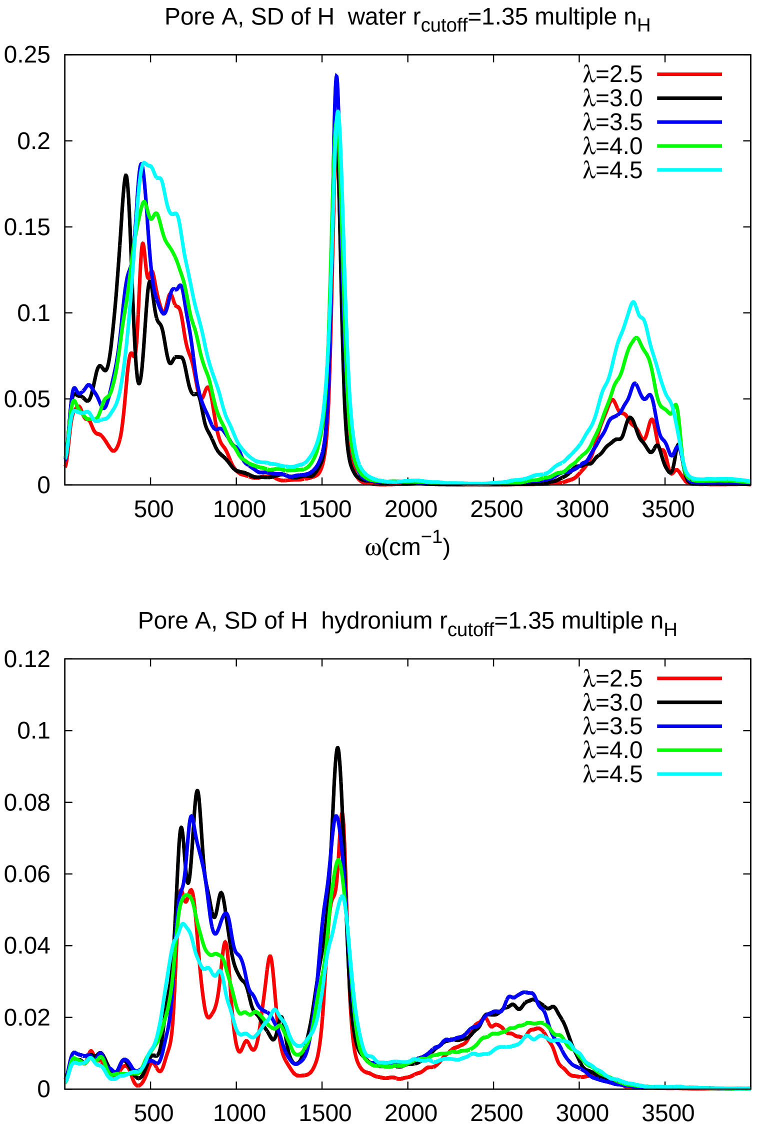

Figure 8.12: The spectral density of motion of the H atoms belonging to water molecules are shown at the top frame for all water contents. The hydronium spectra are shown in the bottom frame for all water contents.

8.5 Integrated spectral densities of hydrogen

A simplification of the analysis of the spectral densities is required in order to be able to compare the various spectra (e.g. for different water contents). A simplification is an integration of the spectral densities over specific intervals. The intervals are chosen such that possible peculiarities of the molecular system can be deduced from the total spectral densities. Therefore, the results of Sections 8.3 and 8.4, in which peaks or bands of the hydrogen spectral densities are associated with the chemical states of the hydrogen (by using either the coordination number of hydrogen or proton complex structure), are used to determine these intervals. They are described in Table 8.4.

Table 8.4: Summary of the dominating contributions to the total hydrogen spectra given with respect to possible proton complex structure and coordination number of the hydrogen. The right most column gives a brief description of the effects an increase in the hydration level has on the intensity of the spectra.

interval [cm^{-1}]	classification	coord. number	effect of increasing hydration level
1010–1110	acidic proton	$c_i = 1$	decrease due to dissociation
1150–1250	trapped hydronium	$c_i > 1$	shifts to larger ω includes trapped Zundel
1500–1800	water and hydronium	$c_i \geqq 1$	increase
1800–3000	hydronium	$c_i > 1$	increase then decrease
2600–3400	Zundel	$c_i > 1$	increase
3000–3550	H-bonded water	$c_i > 1$	increase
3550–4000	Dangling O-H	$c_i = 1$	increase

The integrated spectral densities of all hydrogen atoms together with the separate contributions from proton complexes, depending on the previously explained schemes, are shown in Figures 8.13, 8.14, and 8.15.

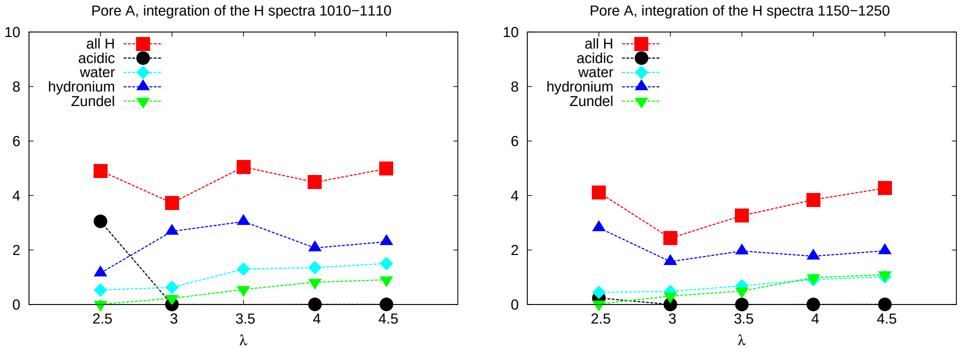

Figure 8.13: Spectral densities of motion for H atoms, in various environments, integrated over selected intervals for pore A at all λ values. The ranges of integration are 1010-1110 cm^{-1} (left panel) and 1150-1250 cm^{-1} (right panel).

The largest contribution to the integrated spectra of the hydrogen atoms is observed for the the interval between 1010 and 1110 cm^{-1} for λ=2.5 (see left frame of Figure 8.13) and associated to the acidic protons. An increase of the hydration level leads to an almost complete dissociation, thus the contribution due to acidic protons is no longer observed. Instead, the hydronium gives the largest contributions to the integrated spectra for $\lambda > 2.5$. The contributions of the hydrogen atoms belonging to Zundel cations and water molecules increase proportionally to the water content. Therefore the overall hydrogen spectra in this interval (1010-1110 cm^{-1}) demonstrate only slightly the effect of the dissociation.

The integrated hydrogen spectra in the interval between 1150-1250 cm^{-1} (see right frame of Figure 8.13), depend mainly on the hydronium contributions, which decrease at λ=3.0 and stay approximately constant for λ >3.0. The Zundel cations and water contributions increase slightly just as in the aforementioned case. Therefore the total integrated hydrogen spectrum increases slightly with increasing hydration level for λ >3.0.

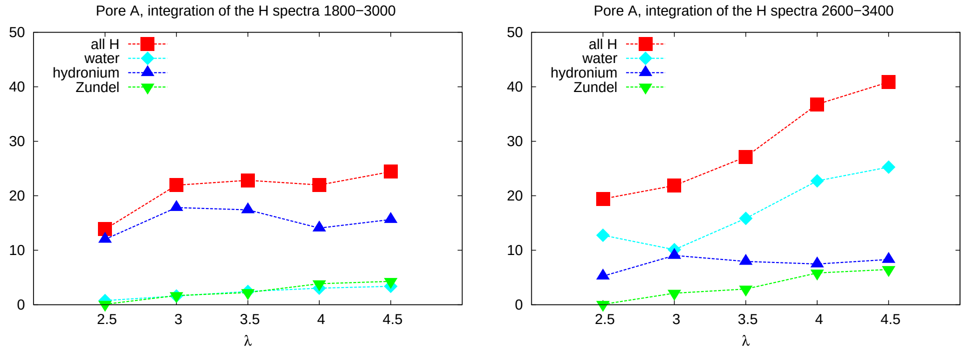

Figure 8.14: Spectral densities of motion for the H atoms, integrated over selected intervals for pore A at all λ values. The ranges of integration are 1800-3000 cm^{-1} (left panel) and 2600-3400 cm^{-1} (right panel). The contributions to the overall hydrogen spectra are labeled according to the proton complex.

The hydrogen spectra integrated over the interval 2600-3400 cm^{-1} and the interval 2600-3400 cm^{-1} are shown in the left and right frames of Figure 8.14. In both cases, the hydronium contributions are larger than those of the Zundel cations for all water content levels. The largest contribution in the former one is due to the hydronium, whereas, in the latter interval, the integrated water spectrum dominates.

In the interval 3000 to 4000 cm^{-1} the integrated hydrogen spectra are dominated by the contributions of the water. Within the interval 3000 to 3550 cm^{-1} (see the left frame of Figure 8.15), the effect of increasing hydration level leads to a slight increase in the integrated spectra of the Zundel cations, whereas there is almost no change in the hydronium ones.

Lastly, the dangling OH bonds, which correspond to a wavenumber

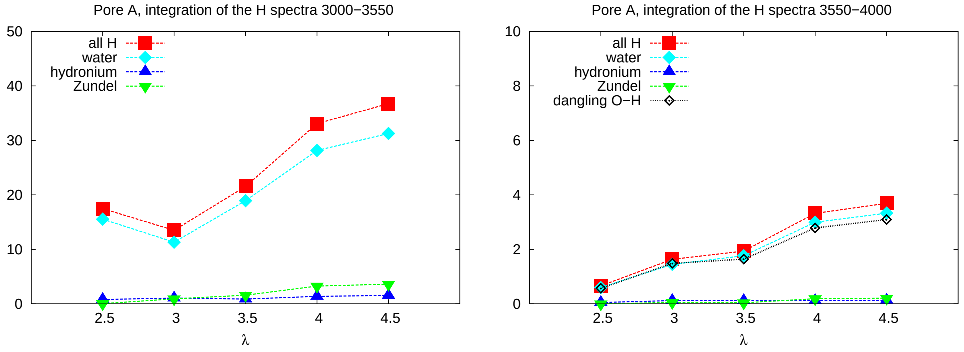

Figure 8.15: Spectral densities of motion for the H atoms, integrated over intervals for pore A at all λ values. The ranges of integration are 3000-3550 cm^{-1}and 3550-4000 cm^{-1}, shown in the left and the right frames, respectively. The contributions to the overall hydrogen spectra are labeled according to the proton complex.

larger than 3550 cm^{-1}, are also considered. The integrated hydrogen spectra in the interval between 3550 and 4000 cm^{-1} (see right frame of Figure 8.15) demonstrate that, for all water contents, the largest contribution comes from water hydrogen.

Chapter 9

Conclusion

CONCLUSION

Various pore models which are possible in an ionomer with different levels of water content λ ranging from 2.5 and 5.5 were investigated by *ab initio* MD simulations using density functional theory for the description of the electronic structure. The structures of these pore models were arranged to have a connected water channel of almost cylindrical shape (see Chap. 4). The reasons behind preparing the various pore models with low water content can be listed as the following; the first one was to determine a favorable sulfonate groups spacing, which leads to the onset of the proton mobility. The second one, which is restricted to the cylindrical pores (the simple pore model), was to find out a limit for the diameter of the narrow pore, which does not hinder the proton transfer. The last one was to investigate the effect of the flexibility and, hence, the length of the side chains on the structure of the water channel and on the proton mobility (see Chap. 4).

During this work, we have employed two different schemes for the molecular dynamics simulations, namely, Car-Parrinello and Born-Oppenheimer MD. The simple pore models were investigated by using CP-MD, the algorithm included in the CPMD program packages [30, 121, 120]. In order to compare the effect of the functionals, the simple pore models were simulated by using two different exchange-correlation functionals (the BLYP [11, 114] and the HCTH functionals [74]). These functionals were used together with ultrasoft Vanderbilt pseudo potentials [113, 198] and Trouiller-Martins norm-conserving pseudo-potentials [187], respectively. Within these simulations, dispersion corrections to the DFT calculations were not included in the ones with the BLYP functional [64, 65, 61].

Similar to the simple pore model, another pore model consisting of longer side chains was also generated. This pore model was then simulated with and without using position constraints, which were employed in order to maintain a stable pore structure (the flexible and the free pore models). Finally, a pore model consisting of 8 parallel backbones was generated (the parallel backbone model). Each backbone had a side chain terminated by a sulfonate group, similar to Nafion® . Hence, the length of the side chain is the longest among the pore models studied here. These pore models (the flexible, the free and the parallel backbone models) were studied by BO-MD using the BLYP functional with the Grimme III-type of dispersion corrections [64, 65, 61].

Based on this work, the following main conclusions can be drawn:

- The onset of the proton mobility was observed as being dependent on the water content, the pore structure, and the dynamics of the water molecules (see Chap. 7).

- The diffusion of water, which was found to be inversely proportional to the density of the molecular system, enhanced the proton mobility at low water content in ionomer pores (see Chap. 7).

- The dissociation of the protons from the sulfonate groups was observed to be dependent on the number of water molecules around the sulfonate group. The required number of water molecules per sulfonate group, in turn, was found to be affected by the pore structure and dynamics of the molecular system (see Chap. 7).

- The narrowness of the pores and the flexibility of the sidechain favored close sulfonate groups at low hydration level. Depending on the water content, close sulfonate groups may lead to the formation of ion contact pairs, which hinders the proton mobility. It was found that the effect of the sulfonate traps decreases by increasing the water content (see Chap. 5 and 7).

- Both the number of hydrogen bonds and the hydrogen bond lifetime were found to be related to the proton transfer mechanism, hence, to the proton mobility. In a molecular system, a large number of hydrogen bonds with a short lifetime favors the proton mobility (see Chap. 6).

- The characteristic dimensions of the pores observed in the ionomer with low water content prevent the formation of Eigen ions (see Chap. 5 and 7). The formation of Eigen complexes is expected to enhance the proton mobility via increasing the number of possible partners for a proton jump. As a result of such a hydrated proton structure, the proton becomes more delocalized.

- In the parallel backbone model, eight parallel backbones were required for having a connected water channel in an almost cylindrical shape, in which the water molecules stayed inside the channel and did not leak through the pore walls (see Chap. 4).

- The intensty of the spectra of the dangling O-H bonds was found to be proportional to the intensity of the spectra of the water molecules in the fixed narrow pores of ionomer (the simple pore model). Increasing water content led to increasing the intensity of the vibrational spectra around 3600 cm^{-1} (see Chap. 8).

9.1 Discussion

The proton mobility, which was characterized as the self diffusion coefficients of the center of the proton complexes, has shown a dependency on the functionals used in the DFT simulations (see Chap. 7). The HCTH functional with dispersion correction gives rise to a higher mobility than the BLYP functional. This difference is indeed consistent with the literature [90], in which aqueous proton solvation and transport were investigated by CPMD simulations using these two functionals. Similarly, different results related to the dynamics of the molecular system were found in the DFT simulations on liquid water and water-vapor interfaces as a result of the functionals [201, 95]. Furthermore, inclusion of the dispersion corrections has been shown to affect the dynamics of the molecular system and this effect depends on the functionals [119, 95]. Therefore, the difference observed in the mobility of the protons as well as that of water can be attributed to the functionals and the dispersion corrections. Beside this fact, even at very low water content in the simple pore model with the HCTH functional, a high proton mobility has been observed with a high undissociated proton fraction. This indicates that the proton transfer in this model at very low water content is stimulated by surface hopping mechanisms, which occur as a result of high diffusive water molecules (Chap.

7). In contrast to this, in the simple pore model with the BYLP functional, a sudden increase in the proton diffusion coefficients was observed only for pore B at λ = 4.5. This indicates that the onset of the proton mobility depends on the number of water molecules per sulfonate group and the pore structure. For the free and the parallel backbone model, the proton mobility was observed to have a linear dependency on the water content.

A linear dependency between the diffusion of the water molecules and the density of the molecular system was observed such that the water diffusion in a pore model decreases with increasing density (Chap. 7). This effect is related to the pore model such that each pore model yields a different amount of change in water diffusion with respect to the density. Similar to the proton diffusion, the HCTH functional with dispersion corrections was observed to have a higher diffusion of the water molecules than BLYP.

A necessary condition for the proton mobility is the dissociation of the proton from the sulfonate group. The number of water molecules per sulfonate group (λ) is the governing factor for the dissociation. Similarly, due to the effect of the functionals, different dependencies of the dissociation on the water content were observed. The fraction of the undissociated sulfonate groups was shown in Chapter 7 and it was found that this fraction decreases with increasing water content within the simple pore model with the HCTH functional. Even, at λ = 4.0, it was possible to find a considerable amount of undissociated sulfonate groups. This can be associated to the dispersion correction, which apparently leads hydrogen to make a strong bond with sulfonate oxygens. In contrast to this, partial dissociation was observed only for $\lambda < 3$ in pore A of the simple pore model with the BLYP functional. Due to the less dynamical features of the water molecules within the BLYP functional, one of the sulfonate groups in pore A stayed isolated and could not get in a contact with the water molecules. For all other pore models, the same tendency, similar to the simple model with the BYLP functional, was observed such that almost complete dissociation is possible for $\lambda \geq 3$. This finding predicted within the simulation with the BYLP functional is consistent with the literature, in which it was stated that a water content of $\lambda \geq 3$ favors proton dissociation in a model of a fluorinated carbon nanotube [70, 71]. Another previous computer simulation reported that approximately the same water content of between 3 and 4 was found to be necessary for a complete dissociation of the protons from the hydrophilic groups [148].

A crucial factor which hinders the proton mobility at low water content is the sulfonate groups spacing. For very close sulfonate groups (whose distance to each other is up to around 5 Å), the first solvation shell of the sulfonate group overlaps with the neighboring one. This compact structure may even not allow for the dissociation of the protons from the sulfonate groups, since a number of water molecules can not have the correct orientation allowing hydrogen bonds with sulfonate groups. Therefore, the sulfonate spacing in the simple pore model was arranged to have a greater distance than 5 Å. However, even at the distance 5.4 Å, sulfonate spacing might lead the protons to behave as if they were bonded. When the barrier for the dissociation was overcome by increasing the water content to 3, i.e. for the simulations with the BLYP functional, the dissociated protons were observed as hydronium or Zundel ions, which were trapped by close sulfonate groups. As a result of this trapping, the mobility of the protons was hindered. In pore A, the distance between the sulfur atoms of the hydrophilic groups, which is 5.4 Å, leads to hydronium-sulfonate contact ion pairs. The effect of such contact pairs resembles the effect of the undissociated sulfonate groups, in which bonded protons do not contribute to the proton mobility. For the other pore models (the free, the flexible, and the parallel backbone models), which include more flexible and longer sidechains than the simple model, such hydronium-sulfonate contact ion pairs were also found to be formed and hindering the proton mobility. They cause to decrease the connectivity of the water channel by blocking the pore. Two or three sulfonate groups were found to contribute to the formation of such contact ion pairs. Such contact ion pair formation was also found in the previous computational study of the perfluorinated membranes [43].

As far as the hydrogen bonds are concerned, the onset of the proton mobility depends on the following two conditions. First, a well-connected hydrogen bond network should be established. Second, the hydrogen bond dynamics should be fast. A hydrogen bond network consists of a sufficient number of water molecules connected by hydrogen bonds. As the water content increases, the possibility of a connected hydrogen bond network is also increased. An increased number of available water molecules also leads to a decrease in the energy barrier for breaking and formation of a hydrogen bond [137]. This lowered energy barrier shortens the expected lifetime for a hydrogen bond, which is indeed crucial for a proton jump. The Grotthuss mechanism is only then favored and contributes to the overall proton mobility. Otherwise (when there are too few available water molecules) a proton, which has jumped to neighboring water molecule via a hydrogen bond, will return back to the original place. Hence, not only the first shell of the water molecules around protonated oxygen but also the second shell becomes important for this mechanism. In the narrow pores, the formation of a connected hydrogen bond network is possibly hindered, since it is very likely to have at least one sulfonate group in the first or second shell of a proton complex. In addition to this, sulfonate traps, due to close sulfonate groups, lead to slow hydrogen bond dynamics, which restricts a successful proton transfer. These two conditions were characterized by the number of hydrogen bonds per water molecule and the hydrogen bond lifetime, respectively (see Chap. 6). In the simple pore models for low water content, the number of hydrogen bonds per water molecule was found to be less than for the other pore models. This indicates that the water structure deviates from bulk-like water by showing a lack of well connected water. The hydrogen bond lifetime in these models was observed to be affected by the functional used in the simulations. The simulations with the HCTH functional and dispersion corrections exhibited a shorter lifetime than the ones with the BYLP functional, in which a decrease in the lifetime was observed with increasing water content. In contrast, the other pore models (the free, the flexible, and the parallel backbone models) exhibited high probabilities of having hydrogen bonds. This can be attributed to the fact that the numbers of water molecules in these models were larger than the ones in the simple pore models and the structures of the pore wall were more flexible and had longer side chains than in the simple pore models. Therefore the water molecules have more freedom to rearrange in order to constitute hydrogen bonds. Hence, in these models, a well connected water structure was observed especially for high water content. However, the expected high proton mobility could not be observed. The reason is that the formation of sulfonate ion contact pairs limits the proton transfer through these parts of the pore. The effect of the sulfonate traps was observed to decrease with increasing water content.

Similar to the experimental findings [126, 143, 46], increasing intensities of the vibrational spectra of free water around 3600 cm^{-1} with increasing water content were observed in fixed narrow pores of the ionomer (in the simple pore model). Furthermore, the dangling O-H spectra were found to be closely related to the spectra of water molecules. Even at very low water content, it was possible to observe dangling O-H in the simple pore models. This coincides with the observation made in Chap. 6 that the average number of hydrogen bonds per water molecule in these pores was less than in bulk water. Therefore, it was expect to have dangling O-H bonds. Additionally, the structure of the pores had contributed to the observation of free O-H spectra at very low water content, since the amount of water molecules was not high enough to fill the pores completely, i.e in pore A for $\lambda = 2.5$. Again similar to the experimental findings [126, 143, 46], the spectra belonging to the hydronium were observed to be shifted to lower wavenumbers than the water spectra.

Based on these findings, a possible pore structure, which enhances the proton mobility at low water content, should have the following properties:

- The sulfonate groups spacing should be larger than 7.6 Å.
- A short side chain terminated by a sulfonate group to prevent the formation of the sulfonate contact ion pairs.
- an additional chain (R-X-H_2) should be inserted between the sulfonate groups. It should make hydrogen bonds with sulfonate oxygens, so that the number of water molecules around the sulfonate groups is decreased. These water molecules, then, contribute to form a well connected water structure via hydrogen bonds.

The simulations in this work were based on the AIMD DFT scheme, which provide us to handle the dynamics of the molecular system without predefined potentials. However, the method restricted us to consider a limited number of atoms (smaller than 1000). Therefore, only a limited number of pore models were considered. As a result of periodic boundary conditions, a homogeneous pore distribution in the xy plane and a repeating pore conformation have been assumed in our simulations. It is almost certain that the distribution of pores and the structure of water channels in practice are not homogeneous. Furthermore, here the protons were treated as classical particles. This could also has an effect on the dynamics of the molecular system. Additionally, the long range forces, such as the dispersion correction, are missing in the description of the bare DFT. Their effects on the proton transfer mechanism are important, since, in a proton transfer, one needs to consider the second shell of the water molecules around the protonated water molecule. Therefore, the development and the implementation of more efficient and accurate corrections is required.

Appendix A

Input Files for MD

Force field parameters, MD run parameter for classical MD simulation.

A.1 Force field parameters

Force field parameters which were used for the classical MD simulations are listed below

```
[ atomtypes ]

OE   8 15.9994  0.0000 A 0.327154E-02  0.3196066E-05;Ether Oxy
OS   8 15.9994 -0.7300 A 0.327154E-02  0.3196066E-05;Sulfo Oxy
S   16 32.0600  1.1900 A 0.837855E-02  1.6770247E-05
C    6 12.0110  0.0000 A 0.279435E-02  0.4903538E-05
F    9 18.9984  0.0000 A 0.106291E-02  0.0930631E-05
OW   8 15.9994 -0.8200 A 0.26171E-02   0.26331E-05  ;spc
HW   1  1.0080  0.4100 A 0.00000       0.0000000    ;spc
OD   8 15.9994 -0.4160 A 0.26171E-02   0.26331E-05  ;hydronium
HD   1  1.0080  0.4720 A 0.00000       0.0000000    ;hydronium

[ bondtypes ]

C  F  1   0.13700     292880.0
C  C  1   0.15400     292880.0
C  OE 1   0.15400     292880.0
C  S  1   0.18000     292880.0
S  OS 1   0.14900     292880.0
HD OD 1   0.09700     229280.0

[ angletypes ]

; perfect tetrahydrals angles
C  C  C  2  109.47122 471.45
C  C  F  2  109.47122 472.04
F  C  F  2  109.47122 470.70
S  C  F  2  109.47122 478.15
OS S  C  2  109.47122 456.31
OS S OS  2  109.47122 509.36
S  C  C  2   90.47122 490.91
OE  C  C  2  109.47122 470.70
C  OE  C  2  109.47122 470.70
OE  C  F  2  109.47122 470.70

[ dihedraltypes ]
F C C F  1 0.0  0.46485 3
F C C C  1 0.0  0.46485 3
S C C C  1 0.0  0.46485 3
S C C F  1 0.0  0.46485 3
F C S OS 1 0.0  0.46485 3
C C C C  1 0.0  0.46485 3
C C C S  1 0.0  0.46485 3
C C S OS 1 0.0  0.46485 3
```

A.2 Flexible model

Classisal MD simulation input file: Some of the important parameters for gromacs are listed below

```
dt                        = 0.002                ;(ps)
pbc                       = xyz
periodic_molecules        = no
rlist                     = 0.9
coulombtype               = shift
rcoulomb-switch           = 0.7
rcoulomb                  = 0.85

Tcoupl                    = Berendsen
tau_t                     = 1.0
ref_t                     = 350

Pcoupl                    = berendsen
Pcoupltype                = semiisotropic
tau_p                     = 10.0    10.0
compressibility           = 4.5e-7  4.5e-7
ref_p                     = 1.0     1.0
```

A.3 Parallel backbone model

MD parameters, which were used during the classical MD in order to have a relaxed configuration.

```
dt                        = 0.002                ;(ps)
pbc                       = xyz
periodic_molecules        = no
rlist                     = 0.95
coulombtype               = shift
rcoulomb-switch           = 0.5
rcoulomb                  = 0.8

Tcoupl                    = Berendsen
tau_t                     = 1.0
ref_t                     = 350

Pcoupl                    = berendsen
Pcoupltype                = semiisotropic
tau_p                     = 10.0    10.0
compressibility           = 4.5e-7  4.5e-7
ref_p                     = 1.0     1.0
```

Appendix B

Input Files for AIMD

B.1 Input file for CPMD

Cpmd input file for simple model pore B with λ=2.5

```
&CPMD
  MOLECULAR DYNAMICS
  RESTART COORDINATES WAVEFUNCTION VELOCITIES  ACCUMULATORS  LATEST
  RESTART NOSEP NOSEE
  NOSE IONS
  400 3000
  NOSE ELECTRONS
  0.0160 10000
  EMASS
  400
  TIMESTEP
  4
  MAXCPUTIME
  342600
  MAXSTEP
  250000
  TRAJECTORY XYZ SAMPLE
  10
  MEMORY BIG
  STORE
  100
  VDW CORRECTION ON
&END

&VDW
VDW PARAMETERS
ALL GRIMME
VDW-CELL
4 4 4
&END

&SYSTEM
  ANGSTROM
  SYMMETRY
  6
  CELL
  16.4540494959 1.0  0.39891297 0  0  0
  CUTOFF
  25.0
&END

&DFT
  NEWCODE
  FUNCTIONAL BLYP
  GC-CUTOFF
  5.0d-6
&END

&ATOMS
```

```
CONSTRAINTS
FIX ATOMS
12  1 2 3 4 5 6 7 8 9 10 11 12
END CONSTRAINTS

*C_VDB_BLYP.psp FORMATTED
LMAX=P
 20
0.872062    12.4722    4.63108
0.872062    3.98188    5.72504
12.4722    0.872062    0.802235
12.4722    15.5819    2.99015
15.5819    12.4722    2.44317
15.5819    3.98188    1.34922
3.98188    0.872062    6.27202
3.98188    15.5819    4.0841
8.22703    1.38214    0.255256
8.22703    15.0719    3.53711
1.38214    8.22703    5.17805
15.0719    8.22703    1.8962
11.5525    14.6582    2.05182
12.6245    1.89421    -0.376031
14.5604    12.4485    1.25281
14.6096    4.82534    0.405161
1.78537    11.5422    3.70917
1.90502    3.85913    4.55793
3.82058    14.5606    2.90609
4.87136    1.79591    5.31224

*F_VDB_BLYP.psp FORMATTED
LMAX=P
60
15.7653    8.28219    0.688653
15.2886    7.10485    2.58378
15.4265    9.19736    2.72824
16.7337    12.716    1.86157
14.749    11.4603    0.365747
14.5854    13.5519    0.487449
13.3909    12.2892    1.87894
15.4894    11.3101    3.01597
15.1692    13.3949    3.35165
13.6796    15.6457    2.49299
12.1402    14.1096    0.927681
10.4926    15.2518    1.56034
11.1716    13.6856    2.92716
12.6245    14.9203    4.26207
11.9044    16.6638    3.36346
8.20324    15.9943    2.56238
9.39087    14.9739    4.16041
7.36478    15.2758    4.54558
3.68168    16.727    3.55578
4.59778    14.7158    1.78842
2.59354    14.5682    2.41781
4.13948    13.4112    3.5206
```

```
5.20859    15.4642    4.48163
3.15742    15.1634    5.10738
0.752917    13.6567    4.09302
2.44571    12.1975    2.71723
1.2018    10.6001    2.99164
2.63083    11.026    4.65343
1.58317    12.6913    5.8628
-0.218312    11.956    5.11573
0.554782    8.98624    4.49164
1.64154    8.8057    6.44794
0.800823    7.11228    5.38021
-0.256403    3.65531    5.15016
1.73873    4.69507    3.4981
1.87015    2.65454    4.01152
3.0711    4.10094    5.1576
0.912304    5.18215    6.1887
1.29766    3.14077    6.73512
2.75784    0.760936    5.82162
4.3069    2.30209    4.1508
5.89869    1.13101    4.85936
5.24578    2.77772    6.15002
3.84273    1.49136    7.57084
4.57551    -0.216257    6.6106
8.6487    0.315047    -0.419839
7.0318    1.14646    0.775541
9.00175    1.59192    1.39684
12.7428    -0.287702    0.254126
11.8257    1.73996    -1.45994
13.8404    1.84613    -0.889047
12.3706    3.05614    0.231701
11.2452    0.957611    1.2168
13.3177    1.25446    1.81858
15.7083    2.76207    0.889484
14.1752    4.25113    -0.774785
15.1667    5.94515    0.0131091
13.5777    5.09334    1.21465
14.9432    3.82079    2.64554
16.6536    4.58056    1.7223

*H_VDB_BLYP.psp FORMATTED
LMAX=S
36
12.4017    9.33733    3.57642
12.2269    10.7035    4.90682
11.3511    10.7091    3.41358
8.04439    10.8648    2.72864
7.81486    10.6891    1.10865
7.45441    12.3417    4.70482
6.29424    12.2185    6.73246
6.20506    11.0643    5.64999
7.54467    7.46069    3.39797
7.87153    8.71841    2.47049
4.8953    8.21976    5.91338
5.96134    8.37942    7.36738
```

```
6.51213    7.84369    5.88362
7.88305    6.28918    5.4723
6.48615    6.14388    4.71668
9.45599    4.2577    1.05049
10.9027    4.47174    0.672024
10.1731    5.72592    1.45728
9.1611    7.18027    1.86089
10.0882    7.33657    0.520509
9.89793    10.713    1.857
10.7127    11.9725    1.80989
5.33194    4.02372    1.60605
6.79629    3.7471    1.63667
3.62127    6.13055    1.26277
4.49235    5.5925    0.0654795
10.2776    4.43095    4.78888
11.2472    5.59396    4.69069
4.74613    10.2047    3.71659
5.45047    11.3595    3.02832
4.74381    5.64619    3.82234
5.8397    4.63519    3.58442
9.33627    8.18521    4.8812
10.5592    8.96599    5.19172
12.8587    6.59279    5.47515
12.7422    6.86923    3.88162

*O_VDB_BLYP.psp FORMATTED
LMAX=P
28
11.7575    10.1786    4.2332
8.26558    10.3191    1.92565
6.80658    11.6397    6.14929
7.74958    7.78359    2.4397
5.90117    8.52375    6.34238
7.19357    6.80447    5.06337
10.2963    4.61817    1.44632
10.0174    6.93301    1.46616
12.8432    7.38684    0.689102
13.1945    9.72788    0.807008
12.7731    8.45464    2.98362
8.85029    13.2187    1.63978
6.53826    13.3878    2.23825
8.12928    12.4805    3.93724
3.46028    9.04699    3.4571
2.86951    6.77739    3.41857
3.80554    7.73164    5.59573
7.46291    2.893    -1.99878
9.7344    2.76405    -1.3345
8.20706    3.87954    0.235863
10.7737    11.0586    1.99721
6.02232    3.73105    2.22084
4.4152    5.66762    1.08578
10.3978    5.3289    5.05777
5.56427    10.6751    3.71605
5.50846    5.30039    4.27891
```

```
9.8344    8.54416    5.65398
12.7385    6.17022    4.56226

*S_VDB_BLYP.psp FORMATTED
LMAX=P
4
13.301    8.48563    1.46405
7.86725    13.4546    2.67206
3.03532    7.93157    4.25599
8.4027    2.87568    -0.882529
&END
```

Equilibration During the equilibration the keywords given below were used

```
"QUENCH BO"
"NOSE IONS MASSIVE"
"NOSE ELECTRONS MASSIVE"
```

B.2 Input file for CP2K: BOMD

Input file for CP2K simulations: onyl an example for the free model at λ =2.5 is given below

```
 @SET BXX  22.124
 @SET BXY  22.124
 @SET BXZ  20.000

&FORCE_EVAL
  METHOD QS
@include dft.inc
  &SUBSYS
    &CELL
      ABC  ${BXX} ${BXY} ${BXZ}
      PERIODIC XYZ
    &END CELL
@include subsys.inc
  &END SUBSYS
&END FORCE_EVAL

&GLOBAL
  PROJECT mol
  RUN_TYPE MD
    WALLTIME 340000
&END GLOBAL
@include motions.inc
```

dft.inc:

```
&DFT
 BASIS_SET_FILE_NAME ../GTH_BASIS_SETS
 POTENTIAL_FILE_NAME ../POTENTIAL
 WFN_RESTART_FILE_NAME mol-RESTART.wfn
  &MGRID
    COMMENSURATE
    CUTOFF 360
  &END MGRID

  &POISSON
    &EWALD
      EWALD_TYPE spme
      GMAX 55 55 55
      NS_MAX 50
    &END EWALD
  &END POISSON

  &QS
    METHOD GPW
  &END QS
  &SCF
    SCF_GUESS restart
    MAX_SCF 50
    EPS_SCF 1.E-7
    &OT
       PRECONDITIONER FULL_SINGLE_INVERSE
       MINIMIZER DIIS
       N_DIIS 7
     &END OT
    &OUTER_SCF ON
       EPS_SCF 1.0E-6
       MAX_SCF 20
       OPTIMIZER SD
    &END OUTER_SCF
    &PRINT
      &RESTART
        &EACH
          QS_SCF 10
        &END EACH
        ADD_LAST NUMERIC
      &END RESTART
    &END PRINT
  &END SCF
  &XC
    &XC_FUNCTIONAL BLYP
    &END XC_FUNCTIONAL
    &vdW_POTENTIAL
       DISPERSION_FUNCTIONAL PAIR_POTENTIAL
       &PAIR_POTENTIAL
          TYPE DFTD3
          PARAMETER_FILE_NAME ../dftd3.dat
          REFERENCE_FUNCTIONAL BLYP
       &END PAIR_POTENTIAL
    &END vdW_POTENTIAL
```

```
    &END XC
  &END DFT
```

subsystem.inc:

```
    &TOPOLOGY
      COORD_FILE_NAME MOL.PDB
      COORDINATE pdb
      CONNECTIVITY OFF
    &END TOPOLOGY
    &KIND H
      BASIS_SET DZV-GTH
      POTENTIAL GTH-BLYP-q1
    &END
    &KIND O
      BASIS_SET DZVP-GTH
      POTENTIAL GTH-BLYP-q6
    &END
    &KIND S
      BASIS_SET DZVP-GTH
      POTENTIAL GTH-BLYP-q6
    &END
    &KIND C
      BASIS_SET DZVP-GTH
      POTENTIAL GTH-BLYP-q4
    &END
    &KIND F
      BASIS_SET DZVP-GTH
      POTENTIAL GTH-BLYP-q7
    &END
```

motions.inc:

```
&MOTION
  &MD
    ENSEMBLE NVT
    STEPS 5000
    TIMESTEP 0.25
    TEMPERATURE 350.0
    &THERMOSTAT
      TYPE NOSE
      REGION GLOBAL
      &NOSE
        LENGTH 3
        TIMECON 10.0
      &END NOSE
    &END THERMOSTAT
  &END MD
  &PRINT
    &RESTART
      ADD_LAST NUMERIC
      &EACH
          MD 1
      &END
    &END
```

```
    &TRAJECTORY
    FORMAT DCD
    &END TRAJECTORY
    &VELOCITIES
    &END
  &END PRINT
&END MOTION
&EXT_RESTART
    RESTART_FILE_NAME       mol-1.restart
    RESTART_POS                     T
    RESTART_VEL                     T
    RESTART_CELL                    T
    RESTART_COUNTERS                T
    RESTART_AVERAGES                T
    RESTART_THERMOSTAT              T
    RESTART_DEFAULT                 T
&END EXT_RESTART
```

Appendix C

Figures Related to Results

C.1 Radial Distributions

Radial distribution functions, which were not included in Chap. 5 are shown for S-H and O_S-H (Figs. C.1, C.2, C.3, andC.4).

Radial distribution functions for sulfonate oxygens and mobile oxygens (that do not belong to sulfonate groups) are shown for the other pore models in Figs. C.5, C.6, and C.7. The hydronium oxygen has a tendency to stay close to sulfonate oxygens, as explained in Chap. 5.

Lastly, the radial distribution functions of the mobile oxygens are shown in Figs. C.8, C.9, and C.10.

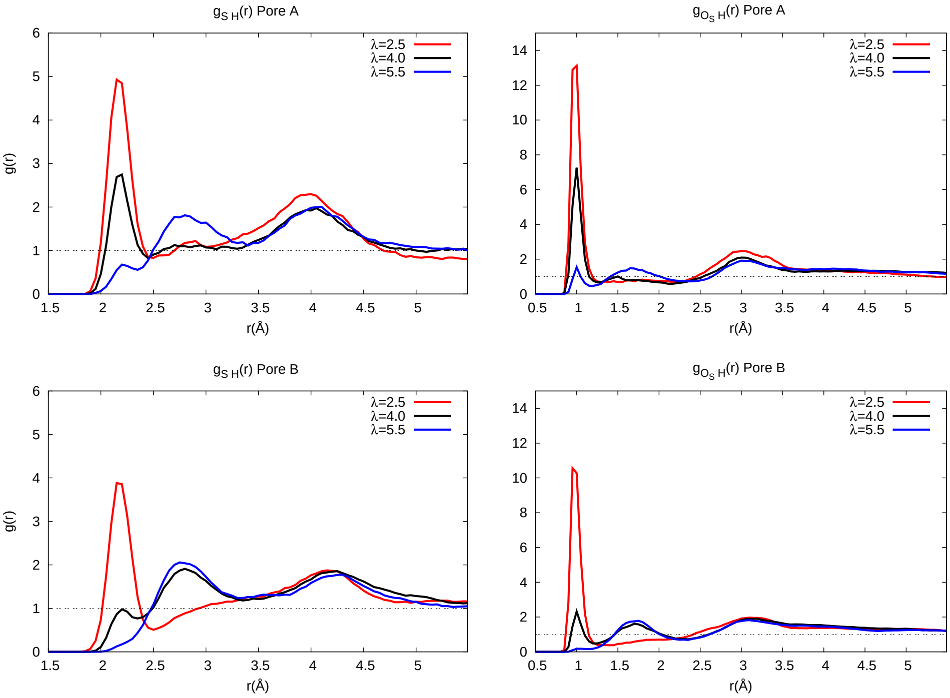

Figure C.1: S-H (left) and O_S-H (right) RDFs for pores A and B in the fixed simple models with the HCTH functional. The first peak is related to the undissociated sulfonate groups. Its intensity decreases with increasing water content. The second peaks become apparent only if the dissociation is achieved.

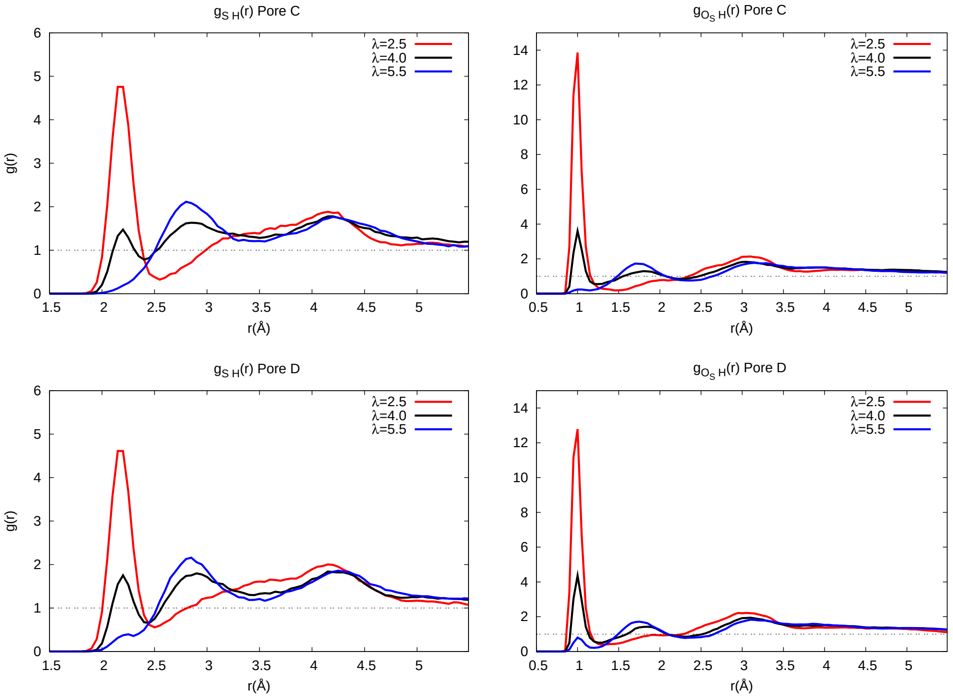

Figure C.2: S-H (left) and O_S-H (right) RDFs pores C (top) and D (bottom) in the fixed simple models with the HCTH functional. Similar to pores A and B with the HCTH functional, the first peak is related to the undissociated sulfonate groups. The area under the first peak is proportional to the acidic proton fractions. It decreases with increasing water content. The second peaks become apparent only if the dissociation is achieved.

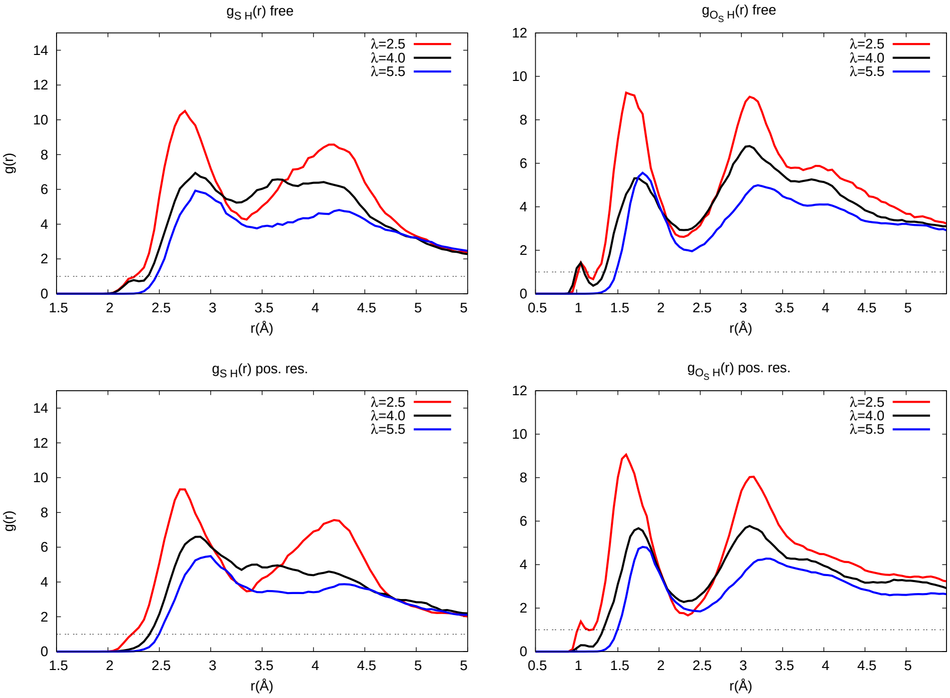

Figure C.3: S-H (left) and O_S-H (right) RDFs for the flexible (below) and the free (top) models. An almost negligible amount of the undissociated sulfonate groups is observed, since the intensity of the first peak (located at 2.3 Å at 1.0 Å for S-H and O_S-H, respectively) is very small or does not appear. The second peak shifts to larger values with increasing water content.

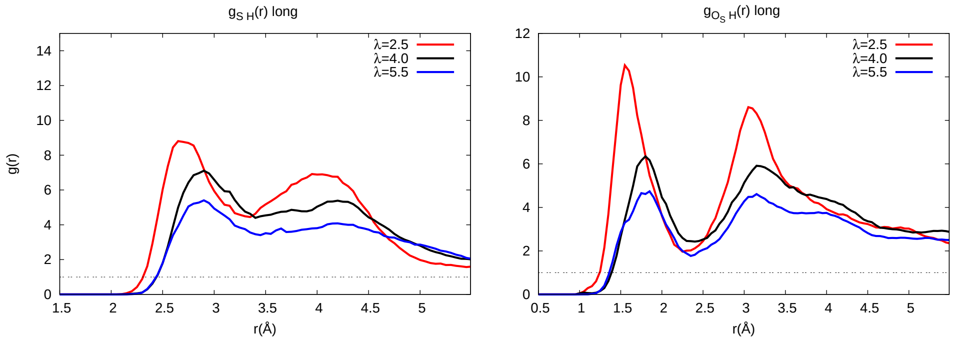

Figure C.4: RDFs of S-H (left) and O_S-H (right) for the parallel backbone model. A peak corresponding to undissociated sulfonate groups is not observed. The intensity of the peak decreases with increasing water content. The peak maximum approaches to 2.8 Å and 1.8 Å, respectively, for S-H and O_S-H with increasing water content. These distances are appropriate for a hydrogen bond between one of the sulfonate oxygens and a water molecule.

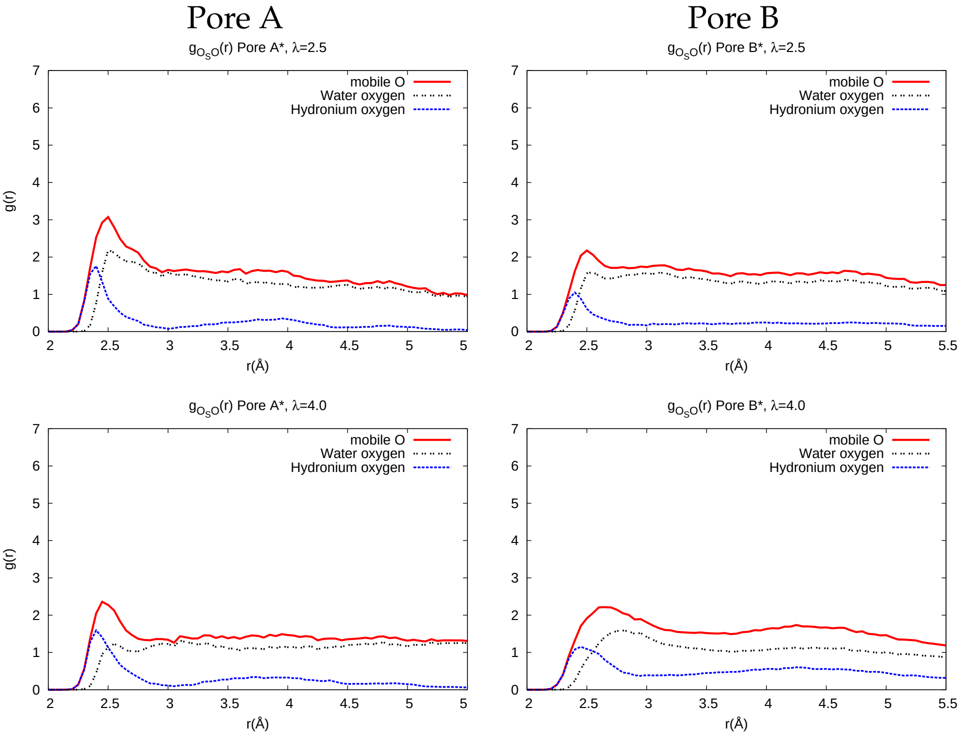

Figure C.5: RDFs of sulfonate oxygen and all mobile oxygen, composed of water and hydronium oxygen for λ=2.5 (left) and 4.0 (right) for the simple helical model with the HCTH functional. The sulfonate oxygens are closer to the hydronium oxygen than to the water oxygen. For both water contents in pore A, the first peak belonging to the hydronium oxygens is located at around 2.4 Å, whereas the one belonging to the water oxygens is located at slightly larger values. The pore B for λ = 2.5 resembles the pore A for λ = 2.5 and 4.0, where a high fraction of the acidic protons exist. In this case, the water molecules are attracted by the undissociated sulfonate groups. However, in pore B for λ = 4.0, where the fraction of the dissociated protons is increased, the water peak shifts to even larger values and it is located at 2.8 Å. When the protons are dissociated, the distance between sulfonate oxygen and water oxygen is determined by the hydrogen bond distance.

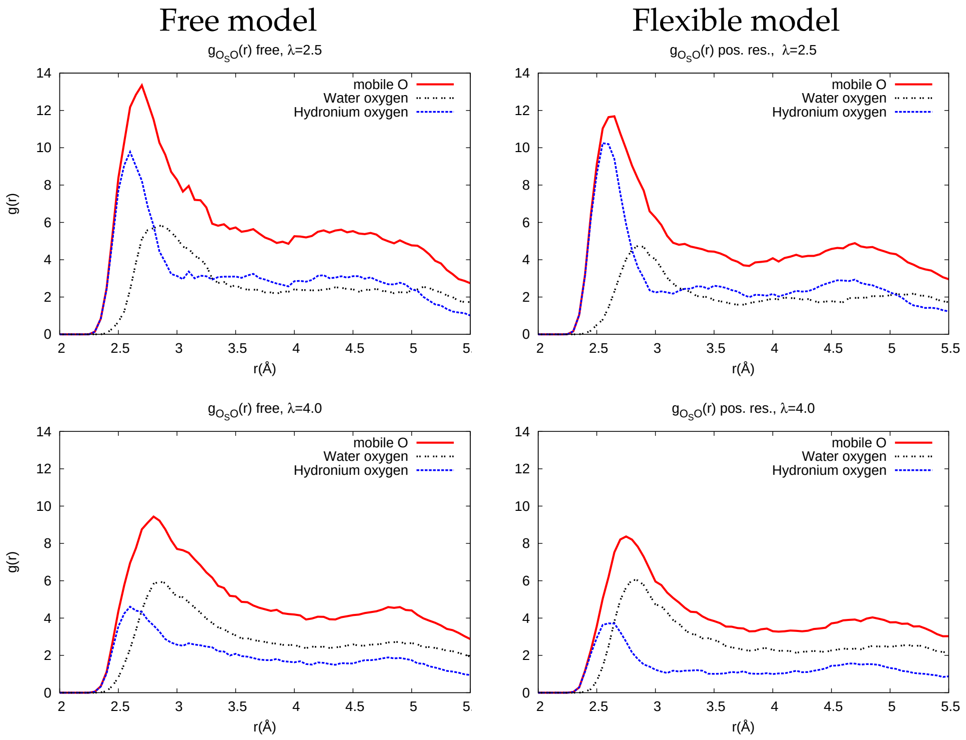

Free model

Flexible model

Figure C.6: RDF of sulfonate oxygen and all mobile oxygens, composed of water and hydronium oxygens for λ=2.5 (left) and 4.0 (right) for the free and the flexible models. Increasing the water content from 2.5 to 4.0 decreases the contribution of the hydronium to the total (mobile oxygen) RDFs. Therefore, the peak belonging to mobile oxygens shifts to larger values with increasing the amount of water.

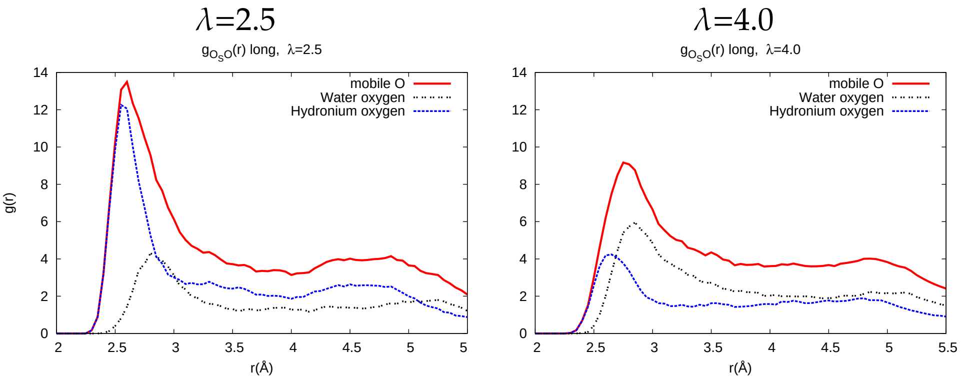

Figure C.7: RDFs of sulfonate oxygen and all mobile oxygens, composed of water and hydronium oxygens for the parallel backbone model. The first peak belonging to hydronium is located at slightly larger values than 2.5 Å. Similar to other pore models, hydronium contributions to total RDFs decrease with increasing water content.

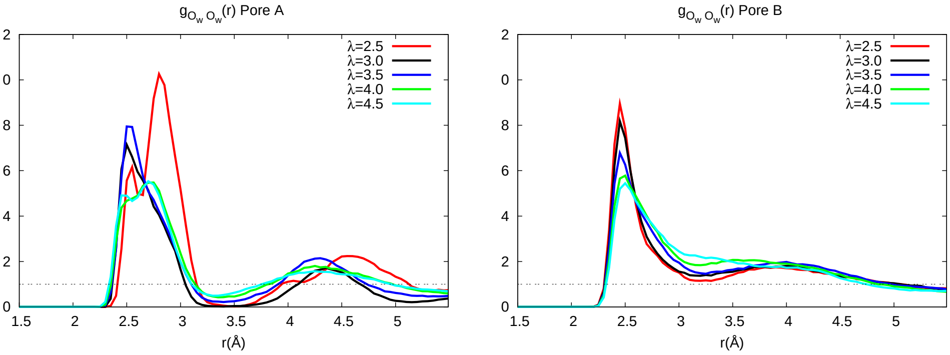

Figure C.8: O_W-O_W RDFs for the fixed simple models with the BLYP functional. The first shell in pore A is composed of two peaks, whose maxima are located at around 2.5 Å and 2.8 Å. These peaks are apparent at low water content. As the water content increases, the peak located at around 2.8 Å appears as a shoulder. The first peak is due to interaction of the water oxygen and the protonated mobile oxygen, which can be hydronium or a Zundel cation. The second peak is due to the hydrogen bonded water molecules. In pore B, this dual peak structure is not observed. In addition, a clear minimum, which is observed at around 3.5 Å in pore A, is not observed in pore B.

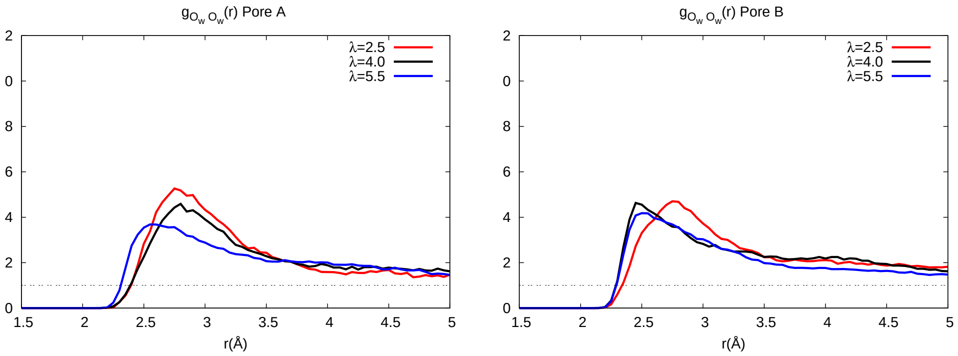

Figure C.9: O_W-O_W RDFs for the fixed simple models with the HCTH functional. In pore A, the maximum of the first peaks belonging to $\lambda = 2.5$ and 4.0, which is located at around 2.8 Å, is shifted to smaller values. It is closely related to the fraction of the dissociated protons. A high fraction of the undissociated protons is observed for $\lambda = 2.5$ and 4.0 in pore A. In pore B, this is valid for $\lambda = 2.5$. Furthermore, a separation between the first and the second shells is not observed in both pores. In this sense, the model resembles to the pore B with the BLYP functional indicating that the water structure is not frozen.

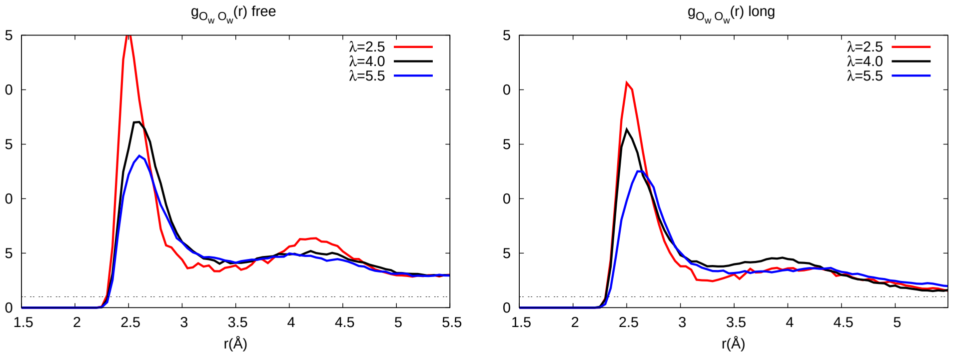

Figure C.10: O_W-O_W RDFs for the free and the parallel backbone models. With increasing water content, the intensity of the first peak decreases and the location of the maxima shifts to larger values. These are related to the fraction of the protonated mobile oxygen, whose effects decrease with increasing numbers of water molecules.

C.2 Density map of protonated oxygens

Density maps of O_P and O_S in pores C and D of the simple pore models are shown in Figs. C.11 and C.12. As the number of water molecules per sulfonate group (λ) increases, delocalization of the protons is expected. This is related to the distribution of the protonated oxygens, which becomes more delocalized with increasing λ. The sulfonate groups spacing also affects the distribution. Hence, the pore structure has an effect on the protonated oxygens distribution.

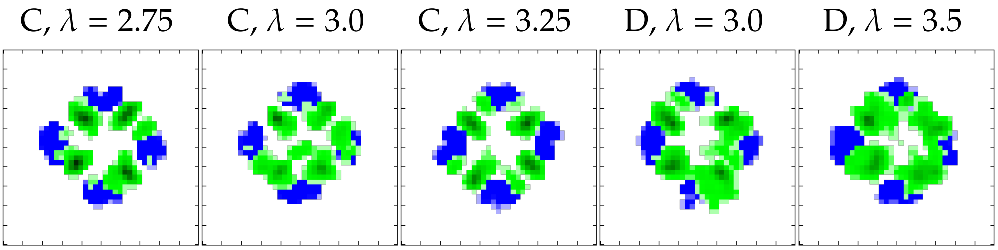

Figure C.11: Density map of the simple helical model with the BLYP functional: Pores C and D

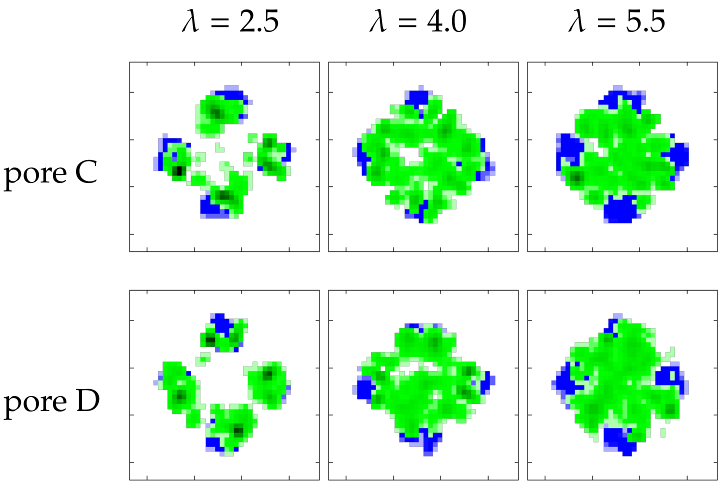

Figure C.12: Density map of pores C and D of the simple helical model with the HCTH functional. Center of proton complex, O_P (green), and sulfonate oxygens, O_S (blue)

References

[1] Agmon, N. (1995). The Grotthuss mechanism. *Chem. Phys. Lett.*, 244:456–462. 11, 19

[2] Alberti, G. and Casciola, M. (2010). Basic aspects in proton-conducting membranes for fuel cells. In Drioli, E. and Giorno, L., editors, *Comprehensive Membrane Science and Engineering*, chapter 2.15, pages 431–465. Elsevier. 25

[3] Alberti, G., Casciola, M., Massinelli, L., and Bauer, B. (2001). Polymeric proton conducting membranes for medium temperature fuel cells (110–160°C). *Journal of Membrane Science*, 185(1):73 – 81. 25

[4] Allen, M. P. and Tildesley, D. J. (1987). *Computer Simulations of Liquids*. Oxford University Press, New York. 31, 83

[5] Andersen, H. C. (1980). Molecular dynamics simulations at constant pressure and/or temperature. *J. Chem. Phys.*, 72:2384–93. 33

[6] Atkins, P. W. and Friedman, R. S. (2004). *Molecular Quantum Mechanics*. Oxford University Press, Oxford, UK, 4. edition. 38

[7] Baer, M., Marx, D., and Mathias, G. (2011). Assigning predissociation infrared spectra of microsolvated hydronium cations $H_3O^+{\cdot}(H_2)_n$ (n=0, 1, 2, 3) by *ab initio* molecular dynamics. *Chem. Phys. Chem.*, 12(10):1906–1915. 20, 180

[8] Bakó, I., Hutter, J., and Pálinkás, G. (2002). Car-Parrinello molecular dynamics simulation of the hydrated calcium ion. *J. Chem. Phys.*, 117:9838. 115

[9] Basnayake, R., Peterson, G. R., Casadonte, D. J., and Korzeniewski, C. (2006). Hydration and interfacial water in nafion membrane probed by transmission infrared spectroscopy. *The Journal of Physical Chemistry B*, 110(47):23938–23943. 180

[10] Beattie, P. D., Orfino, F. P., Basura, V. I., Zychowska, K., Ding, J., Chuy, C., Schmeisser, J., and Holdcroft, S. (2001). Ionic conductivity of proton exchange membranes. *J. Electroanal. Chem.*, 503:45–56. 13

[11] Becke, A. D. (1988). Density-functional exchange-energy approximation with correct asymptotic behavior. *Phys. Rev. A*, 38(6):3098–3100. 43, 60, 210

[12] Berendsen, H., Postma, J., van Gunsteren, W., and Hermans, J. (1981). Interaction models for water in relation to protein hydration. In Pullman, B., editor, *Intermolecular Forces*, volume 14 of *The Jerusalem Symposia on Quantum Chemistry and Biochemistry*, pages 331–342. Springer Netherlands. 67, 72

[13] Berendsen, H. J. C., Postma, J. P. M., van Gunsteren, W. F., DiNola, A., and Haak, J. R. (1984). Molecular dynamics with coupling to an external bath. *J. Chem. Phys.*, 81:3684–3690. 33

[14] Bopp, P. (1987). The determination of vibrational frequencies in H-bonded liquids from molecular dynamics simulations. In Kleeberg, H., editor, *Interactions of Water in Ionic and Nonionic Hydrates*, page 100, Heidelberg. Springer. 193

[15] Bopp, P., Jancsó, G., and Heinzinger, K. (1983). An improved potential for non-rigid water molecules in the liquid phase. *Chem. Phys. Lett.*, 98:129. 115

[16] Botti, A., Bruni, F., Imberti, S., Ricci, M. A., and Soper, A. K. (2004). Ions in water: The microscopic structure of concentrated NaOH solutions. *The Journal of Chemical Physics*, 120(21):10154–10162. 20

[17] Car, R. and Parrinello, M. (1985). Unified approach for molecular dynamics and density-functional theory. *Phys. Rev. Lett.*, 55:2471–2474. 46

[18] Ceperley, D. M. and Alder, B. J. (1980). Ground state of the electron gas by a stochastic method. *Phys. Rev. Lett.*, 45:566–569. 42

[19] Chaiwongwattana, S., Phonyiem, M., Vchirawongkwin, V., Prueksaaroon, S., and Sagarik, K. (2012). Dynamics and mechanism of structural diffusion in linear hydrogen bond. *Journal of Computational Chemistry*, 33(2):175–188. 20, 44, 180

[20] Chakraborty, D. and Chandra, A. (2012). A first principles simulation study of fluctuations of hydrogen bonds and vibrational frequencies of water at liquid–vapor interface. *Chemical Physics*, 392(1):96 – 104. 123

[21] Chen, B., Ivanov, I., Park, J. M., Parrinello, M., and Klein, M. L. (2002). Solvation structure and mobility mechanism of OH^-: A Car-Parrinello molecular dynamics investigation of alkaline solutions. *J. Phys. Chem. B*, 106:12006–12016. 20

[22] Chen, H., Voth, G. A., and Agmon, N. (2010). Kinetics of proton migration in liquid water. *J. Phys. Chem. B*, 114:333–339. 20

[23] Chikvaidze, G., Gabrusenoks, J., Kleperis, J., and Vaivars, G. (2007). Application of micro raman spectroscopy to industrial FC membranes. *Journal of Physics: Conference Series*, 93(1):012026. 189, 190

[24] Choi, P., Jalani, N. H., and Datta, R. (2005a). Thermodynamics and proton transport in nafion. I. membrane swelling, sorption and ion-exchange equilibrium. *J. Electrochem. Soc.*, 152:E84–E89. 15, 163

[25] Choi, P., Jalani, N. H., and Datta, R. (2005b). Thermodynamics and proton transport in nafion. II. proton diffusion mechanisms and conductivity. *J. Electrochem. Soc.*, 152:E123–E130. 21, 163

[26] Clark, J. K. and Paddison, S. J. (2012). Hydration and proton transfer in 3M^{TM} pem ionomers: An *ab initio* study. *MRS Proceedings*, 1384. mrsf11-1384-b06-01. 23

[27] Collette, F. M., Lorentz, C., Gebel, G., and Thominette, F. (2009). Hygrothermal aging of nafion. *J. Membrane Sci.*, 330:21. 25

[28] Commer, P., Cherstvy, A., Spohr, E., and Kornyshev, A. (2002). The effect of water content on proton transport in polymer electrolyte membranes. *Fuel Cells*, 2(3-4):127–136. 12, 26, 67, 72

[29] Cox, M. J., Timmer, R. L. A., Bakker, H. J., Park, S., and Agmon, N. (2009). Distance-dependent proton transfer along water wires connecting acid-base pairs. *J. Phys. Chem. A*, 113:6599–6606. 19

[30] CPMD `http://www.cpmd.org/` Copyright IBM Corp (1990-2008). Copyright MPI für Festkörperforschung Stuttgart (1997-2001). 31, 59, 210

[31] Cramer, C. J. and Truhlar, D. G. (2009). Density functional theory for transition metals and transition metal chemistry. *Phys. Chem. Chem. Phys.*, 11:10757–10816. 31

[32] Cui, S., Liu, J., Selvan, M. E., Paddison, S. J., Keffer, D. J., and Edwards, B. J. (2008). Comparison of the hydration and diffusion of protons in perfluorosulfonic acid membranes with molecular dynamics simulations. *The Journal of Physical Chemistry B*, 112(42):13273–13284. 26

[33] Devanathan, R., Venkatnathan, A., and Dupuis, M. (2007a). Atomistic simulation of nafion membrane: 1. effect of hydration on membrane nanostructure. *J. Phys. Chem. B*, 111:8069–8079. 16, 26

[34] Devanathan, R., Venkatnathan, A., and Dupuis, M. (2007b). Atomistic simulation of nafion membrane. 2. dynamics of water molecules and hydronium ions. *J. Phys. Chem. B*, 111:13006–13013. 16, 26

[35] Devanathan, R., Venkatnathan, A., Rousseau, R.and Dupuis, M., Frigato, T., Gu, W., and Helms, V. (2010). Atomistic simulation of water percolation and proton hopping in nafion fuel cell membrane. *J. Phys. Chem. B*, 114:13681–13690. 15

[36] Dreyfus, B. (1985). Model for the clustering of multiplets in ionomers. *Macromolecules*, 18:284. 13

[37] Eikerling, M. (2006). Water management in cathode catalyst layers of PEM fuel cells. *J. Electrochem. Soc.*, 153:E58–E70. 11

[38] Eikerling, M., Ioselevich, A. S., and Kornyshev, A. A. (2004). How good are the electrodes we use in PEFC. *Fuel Cells*, 3:131–140. 26

[39] Eikerling, M. and Kornyshev, A. (1998). Modelling the performance of the cathode catalyst layer of polymer electrolyte fuel cells. *J. Electroanal. Chem.*, 453:89–106. 11

[40] Eikerling, M., Kornyshev, A. A., Kuznetsov, A. M., Ulstrup, J., and Walbran, S. (2001). Mechanisms of proton conductance in polymer electrolyte membranes. *J. Phys. Chem. B*, 105:3646–3662. 11, 18

[41] Eikerling, M., Kornyshev, A. A., and Stimming, U. (1997). Electrophysical properties of polymer electrolyte membranes: A random network model. *J. Phys. Chem. B*, 101:10807–10820. 14

[42] Eikerling, M., Paddison, S. J., Pratt, L. R., and Zawodzinski Jr, T. A. (2003). Defect structure for proton transport in a triflic acid monohydrate solid. *Chem. Phys. Lett.*, 368:108–114. 16, 21, 53

[43] Elliott, J. A. and Paddison, S. J. (2007). Modelling of morphology and proton transport in PFSA membranes. *Phys. Chem. Chem. Phys.*, 9:2602–2618. 216

[44] Falk, M. (1980). An infrared study of water in perfluorosulfonate (Nafion) membranes. *Canadian Journal of Chemistry*, 58(14):1495–1501. 25, 180

[45] Feng, S. and Voth, G. A. (2011). Proton solvation and transport in hydrated nafion. *The Journal of Physical Chemistry B*, 115(19):5903–5912. 19, 21, 118, 180

[46] Ferrari, M., Catalano, J., Giacinti Baschetti, M., De Angelis, M., and Sarti, G. (2012). FTIR-ATR study of water distribution in a short-side-chain PFSI membrane. *Macromolecules*, 45(4):1901–1912. 180, 218

[47] Fonseca Guerra, C., Bickelhaupt, F. M., Snijders, J. G., and Baerends, E. J. (2000). Hydrogen bonding in DNA base pairs: Reconciliation of theory and experiment. *Journal of the American Chemical Society*, 122(17):4117–4128. 122, 123

[48] Fuhrmann, A., Getfert, S., Fu, Q., Reimann, P., Lindsay, S., and Ros, R. (2012). Long lifetime of hydrogen-bonded DNA basepairs by force spectroscopy. *Biophysical Journal*, 102(10):2381–2390. 123

[49] Fujimura, M., Hashimoto, T., and Kawai, H. (1981). Small-angle X-ray scattering study of perfluorinated ionomer membranes. 1. origin of two scattering maxima. *Macromolecules*, 14:1309–1315. 13

[50] Fulde, P. (1995). Density functional theory. In *Electron Correlations in Molecules and Solids*, volume 100 of *Springer Series in Solid-State Sciences*, chapter Density functional theory, pages 39–59. Springer Berlin Heidelberg. 38, 41

[51] Gasteiger, H., Panels, J., and Yan, S. (2004). Dependence of PEM fuel cell performance on catalyst loading. *J. Power Sources*, 127:162–171. 11

[52] Gebel, G. (2000). Structural evolution of water swollen perfluorosulfonated ionomers from dry membrane to solution. *Polymer 2000, 41, 5829-5838*, 41:5829–5838. 15, 25

[53] Gebel, G. and Lambard, J. (1997). Small-angle scattering study of water-swollen perfluorinated ionomers membranes. *Macromolecules*, 30:7914–7920. 13

[54] Gebel, G. and Moore, R. B. (2000). Small-angle scattering study of short pendant chain perfuorosulfonated ionomer membranes. *Macromolecules*, 33:4850–4855. 25

[55] Gejji, S., Hermansson, K., and Lindgren, J. (1993). *Ab initio* vibrational frequencies of the triflic acid molecule. *J. Phys. Chem.*, 97:6986–6989. 180

[56] Ghielmi, A., Vaccarono, P., Troglia, C., and Arcella, V. (2005). Proton exchange membranes based on the short-side-chain perfluorinated ionomer. *J. Power Sources*, 145:108–115. 25

[57] Gierke, T. D. (1977). 152nd meeting of the electrochemical society. *J. Electrochem. Soc.*, 134:319c. 13, 22

[58] Gierke, T. D., Munn, G. E., and Wilson, F. C. (1981). The morphology in nafion perfluorinated membrane products, as determined by wide- and small-angle X-ray studies. *Journal of Polymer Science: Polymer Physics Edition*, 19(11):1687–1704. 51

[59] Gillan, M. J. and Dixon, M. (1983). The calculation of thermal conductivities by perturbed md simulation. *J. Phys. C*, 16:869–78. 31

[60] Goedecker, S., Teter, M., and Hutter, J. (1996). Separable dual-space gaussian pseudopotentials. *Phys. Rev. B*, 54:1703–1710. 69, 73

[61] Goerigk, L. and Grimme, S. (2011). A thorough benchmark of density functional methods for general main group thermochemistry, kinetics, and noncovalent interactions. *Phys. Chem. Chem. Phys.*, 13:6670–6688. 47, 210, 211

[62] Gottesfeld, S., Halpert, G., and Landgrebe, A. (1995). International symposium on proton conducting membrane fuel cells i. In *Proton Conducting Membrane Fuel Cells I*. 16

[63] Gottesfeld, S. and Zawodzinski, T. A. (2008). Polymer electrolyte fuel cells. In Alkire, R. C., Gerischer, H., Kolb, D. M., and Tobias, C. W., editors, *Advances in Electrochemical Science and Engineering*, volume 5, pages 195–301, Weinheim, Germany. Wiley-VCH Verlag GmbH. 9, 12

[64] Grimme, S. (2006). Semiempirical GGA-type density functional constructed with a long-range dispersion correction. *Journal of Computational Chemistry*, 27:1787–1799. 47, 62, 210, 211

[65] Grimme, S., Antony, J., Ehrlich, S., and Krieg, H. (2010). A consistent and accurate *ab initio* parametrization of density functional dispersion correction (DFT-D) for the 94 elements H-Pu. *J. Chem. Phys.*, 132:154104. 47, 69, 74, 210, 211

[66] Groot, R. D. and Warren, P. B. (1997). Dissipative particle dynamics: Bridging the gap between atomistic and mesoscopic simulation. *J. Chem. Phys.*, 107:4423–4435. 180

[67] Grossman, J. C., Schwegler, E., Draeger, E. W., Gygi, F., and Galli, G. (2004). Towards an assessment of the accuracy of density functional theory for first principles simulations of water. *J. Chem. Phys.*, 120:300–311. 44, 59

[68] Grove, W. R. (1839). On voltaic series and the combination of gases by platinum. *The London and Edinburgh Philosophical Magazine and Journal of Science*, 14(3):127–130. 9

[69] Gruger, A., Regis, A., Schmatko, T., and Colomban, P. (2001). Nanostructure of Nafion membranes at different states of hydration: An IR and raman study. *Vibrational Spectroscopy*, 26(2):215–225. 189

[70] Habenicht, B. F., Paddison, S. J., and Tuckerman, M. E. (2010a). The effects of the hydrophobic environment on proton mobility in perfluorosulfonic acid systems: an *ab initio* molecular dynamics study. *J. Mater. Chem.*, 20:6342–6351. 27, 53, 118, 215

[71] Habenicht, B. F., Paddison, S. J., and Tuckerman, M. E. (2010b). *Ab initio* molecular dynamics simulations investigating proton transfer in perfluorosulfonic acid functionalized carbon nanotubes. *Physical Chemistry Chemical Physics*, 12:8728–8732. 27, 215

[72] Hallinan, D. T. (2009). *Transport in Polymer Electrolyte Membranes Using Time-Resolved FTIR-ATR Spectroscopy*. PhD thesis, Drexel university. 189

[73] Hallinan, D. T. and Elabd, Y. A. (2009). Diffusion of water in nafion using time-resolved fourier transform infrared-attenuated total reflectance spectroscopy. *The Journal of Physical Chemistry B*, 113(13):4257–4266. 123, 180, 187, 190

[74] Hamprecht, F. A., Cohen, A. J., Tozer, D. J., and Handy, N. C. (1998). Development and assessment of new exchange-correlation functionals. *The Journal of Chemical Physics*, 109(15):6264–6271. 43, 61, 210

[75] Harris, F. J. (1978). On the use of windows for harmonic analysis with the discrete fourier transform. *Proceedings of the IEEE*, 66:51–84. 185

[76] Hartwigsen, C., Goedecker, S., and Hutter, J. (1998). Relativistic separable dual-space gaussian pseudopotentials from h to rn. *Phys. Rev. B*, 58:3641–3662. 69, 73

[77] Hayes, R. L., Paddison, S. J., and Tuckerman, M. E. (2009). Proton transport in triflic acid hydrates studied via path integral Car-Parrinello molecular dynamics. *J. Phys. Chem. B*, 113(52):1657416589. 21, 40, 62, 123

[78] Headrick, J. M., Diken, E. G., Walters, R. S., Hammer, N. I., Christie, R. A., Cui, J., Myshakin, E. M., Duncan, M. A., Johnson, M. A., and Jordan, K. D. (2005). Spectral signatures of hydrated proton vibrations in water clusters. *Science*, 308:1765–1769. 20, 180

[79] Heitner-Wirguin, C. (1996). Recent advances in perfluorinated ionomer membranes: structure, properties and applications. *Journal of Membrane Science*, 120(1):1 – 33. 12

[80] Hess, B., Kutzner, C., van der Spoel, D., and Lindahl, E. (2008). Gromacs 4: Algorithms for highly efficient, load-balanced, and scalable molecular simulation. *J. Chem. Theory Comput.*, 4:435–447. 32, 67

[81] Hofmann, D. W. M., Kuleshova, L., D'Aguanno, B., Noto, V. D., Negro, E., Conti, F., and Vittadello, M. (2009). Investigation of water structure in nafion membranes by infrared spectroscopy and molecular dynamics simulation. *J. Phys. Chem.*, 113:632–639. 26, 180

[82] Hohenberg, P. and Kohn, W. (1964). Inhomogeneous electron gas. *Phys. Rev.*, 136:B864–B871. 40

[83] Hristov, J., Paddison, S., and Paul, R. (2008). Molecular modeling of proton diffusion in the short-side-chain perfluorosulfonicacid ionomer. *J. Phys. Chem.*, 112:2937–2949. 16, 25

[84] Humphrey, W., Dalke, A., and Schulten, K. (1996). VMD – Visual Molecular Dynamics. *Journal of Molecular Graphics*, 14:33–38. 113

[85] Idupulapati, N., Devanathan, R., and Dupuis, M. (2010). *Ab initio* study of hydration and proton dissociation in ionomer membranes. *J. Phys. Chem. A*, 114:6904–6912. 25, 44, 123

[86] Ilhan, M. A. and Spohr, E. (2011a). *Ab initio* molecular dynamics of proton networks in narrow polymer electrolyte pores. *Journal of Physics: Condensed Matter*, 23(23):234104. 27, 170

[87] Ilhan, M. A. and Spohr, E. (2011b). Hydrogen bonding in narrow protonated polymer electrolyte pores. *Journal of Electroanalytical Chemistry*, 660(2):347 – 351. Physics and Chemistry of Charge Transfer in Condensed Media - Special issue in Honour of Alexander M. Kuznetsov. 54, 60

[88] Ioselevich, A. S., Kornyshev, A. A., and Steinke, J. H. G. (2004). Fine morphology of proton-conducting ionomers. *J. Phys. Chem. B*, 108:11953–11963. 13

[89] Isaacs, E. D., Shukla, A., Platzman, P. M., Hamann, D. R., Barbiellini, B., and Tulk, C. A. (1999). Covalency of the hydrogen bond in ice: A direct X-ray measurement. *Phys. Rev. Lett.*, 82:600–603. 123

[90] Izvekov, S. and Voth, G. A. (2005). *Ab initio* molecular-dynamics simulation of aqueous proton solvation and transport revisited. *J. Chem. Phys.*, 123:44505. 44, 59, 60, 62, 168, 170, 176, 213

[91] Jacob, T. and Goddard III, W. A. (2004). Adsorption of atomic H and O on the (111) surface of Pt_3Ni alloys. *J. Phys. Chem. B*, 108:8311–8323. 11

[92] Jang, S. S., Blanco, M., Goddard III, W. A., Caldwell, G., and Ross, R. B. (2003). The source of helicity in perfluorinated N-alkanes. *Macromolecules*, 36:5331. 53

[93] Jang, S. S., Molinero, V., Çağın, T., and Goddard III, W. A. (2004). Nanophase-segregation and transport in nafion 117 from molecular dynamics simulations: Effect of monomeric sequence. *The Journal of Physical Chemistry B*, 108(10):3149–3157. 13

[94] Jedlovsky, P., Bako, I., and Palinkas, G. (1994). Reverse monte carlo simulation of liquid water. *Chem. Phys. Lett.*, 221:183. 115

[95] Jonchiere, R., Seitsonen, A. P., Ferlat, G., Saitta, A. M., and Vuilleumier, R. (2011). Van der Waals effects in *ab initio* water at ambient and supercritical conditions. *The Journal of Chemical Physics*, 135(15):154503. 48, 59, 62, 168, 213

[96] Jorgensen, W. L., Chandrasekhar, J., Madura, J. D., Impey, R. W., and Klein, M. L. (1983). Comparison of simple potential functions for simulating liquid water. *J. Chem. Phys.*, 79:926–35. 115

[97] Jorn, R. and Voth, G. A. (2012). Mesoscale simulation of proton transport in proton exchange membranes. *The Journal of Physical Chemistry C*, 116(19):10476–10489. 31

[98] Kamerlin, S. C. L. and Warshel, A. (2010). The EVB as a quantitative tool for formulating simulations and analyzing biological and chemical reactions. *Faraday Discuss.*, 145:71–106. 26

[99] Kirchner, B. (2007). Eigen or Zundel ion: News from calculated and experimental photoelectron spectroscopy. *Chem. Phys. Chem.*, 8:41–43. 20

[100] Knight, C. and Voth, G. A. (2012). The curious case of the hydrated proton. *Accounts of Chemical Research*, 1:101–109. 123

[101] Knox, C. K. and Voth, G. A. (2010). Probing selected morphological models of hydrated nafion using large-scale molecular dynamics simulations. *J. Phys. Chem. B*, 114:3205–3218. 26, 31, 51

[102] Kohn, W. and Sham, L. J. (1965). Self-consistent equations including exchange and correlation effects. *Phys. Rev.*, 140:A1133–A1138. 41

[103] Kolafa, J. (2004). Time-reversible always stable predictor–corrector method for molecular dynamics of polarizable molecules. *Journal of Computational Chemistry*, 25(3):335–342. 69, 73

[104] Koptyug, I. V. (2012). MRI of mass transport in porous media: Drying and sorption processes. *Progress in Nuclear Magnetic Resonance Spectroscopy*, 65(0):1 – 65. 12

[105] Kornyshev, A. A., Kuznetsov, A. M., Spohr, E., and Ulstrup, J. (2003). Kinetics of proton transport in water. *The Journal of Physical Chemistry B*, 107(15):3351–3366. 19, 20

[106] Krack, M. (2005). Pseudopotentials for H to Kr optimized for gradient-corrected exchange-correlation functionals. *Theoretical Chemistry Accounts*, 114:145–152. 69, 73

[107] Kreuer, K., Schuster, M., Obliers, B., Diat, O., Traub, U., Fuchs, A., Klock, U., Paddison, S., and Maier, J. (2008). Short-side-chain proton conducting perfluorosulfonic acid ionomers: Why they perform better in PEM fuel cells. *Journal of Power Sources*, 178(2):499 – 509. 15, 25

[108] Kreuer, K.-D. (1996). Proton conductivity: Materials and applications. *Chem. Mater.*, 8:610–641. 13, 19

[109] Kreuer, K.-D., Paddison, S. J., Spohr, E., and Schuster, M. (2004). Transport in proton conductors for fuel-cell applications: Simulations, elementary reactions, and phenomenology. *Chemical Reviews*, 104(10):4637–4678. PMID: 15669165. 13, 51

[110] Kunimatsu, K., Bae, B., Miyatake, K., Uchida, H., and Watanabe, M. (2011). ATR-FTIR study of water in nafion membrane combined with proton conductivity measurements during hydration/dehydration cycle. *The Journal of Physical Chemistry B*, 115(15):4315–4321. 180

[111] Kuo, I.-F. W. and Mundy, C. J. (2004). An *ab initio* molecular dynamics study of the aqueous liquid-vapor interface. *Science*, 303:658–660. 123

[112] Kusoglu, A., Karlsson, A. M., and Santare, M. H. (2010). Structure-property relationship in ionomer membranes. *Polymer*, 51(6):1457 – 1464. 12, 16

[113] Laasonen, K., Pasquarello, A., Car, R., Lee, C., and Vanderbilt, D. (1993). Car-Parrinello molecular dynamics with Vanderbilt ultrasoft pseudopotentials. *Phys. Rev. B*, 47:10142–10153. 46, 60, 210

[114] Lee, C., Yang, W., and Parr, R. G. (1988). Development of the Colle-Salvetti correlation-energy formula into a functional of the electron density. *Phys. Rev. B*, 37(2):785–789. 43, 60, 210

[115] Lee, H.-S. and Tuckerman, M. E. (2006a). *Ab initio* molecular dynamics with discrete variable representation basis sets: Techniques and application to liquid water. *J. Phys. Chem. A*, 110:5549–5560. 62

[116] Lee, H.-S. and Tuckerman, M. E. (2006b). Structure of liquid water at ambient temperature from *ab initio* molecular dynamics performed in the complete basis set limit. *J. Chem. Phys.*, 125:154507. 62

[117] Lee, S. H. and Rossky, P. J. (1994). A comparison of the structure and dynamics of liquid water at hydrophobic and hydrophilic surfaces - a molecular dynamics simulation study. *J. Chem. Phys.*, 100:3334. 115

[118] Liang, Z., Site, L. D., Chen, M. P. W., Liu, J., Wang, S., Zhou, Z., Li, W., Sun, G., and Xin, Q. (2004). FT-IR study of the microstructure of nafion membrane. *J. Membrane Sci.*, 233:39. 180

[119] Lin, I.-C., Seitsonen, A. P., Coutinho-Neto, M. D., Tavernelli, I., and Rothlisberger, U. (2009). Importance of van der Waals interactions in liquid water. *J. Phys. Chem. B*, 113(4):1127–1131. 48, 62, 168, 213

[120] Lippert, G., Hutter, J., and Parrinello, M. (1999). The gaussian and augmented-plane-wave density functional method for *ab initio* molecular dynamics simulations. *Theoretical Chemistry Accounts*, 103:124–140. 31, 210

[121] Lippert, G., Parrinello, M., and Hutter, J. (1997). A hybrid gaussian and plane wave density functional scheme. *Molecular Physics*, 92(3):477–488. 31, 69, 73, 210

[122] Litt, M. H. (1997). A reevaluation of nafion morphology. *Polymer Preprints*, 38:80–81. 13

[123] Loparo, J. J., Roberts, S. T., and Tokmakoff, A. (2006). Multidimensional infrared spectroscopy of water. ii. hydrogen bond switching dynamics. *The Journal of Chemical Physics*, 125:194522. 123, 180

[124] Luzar, A. (2000). Resolving the hydrogen bond dynamics conundrum. *J. Chem. Phys.*, 113:10664. 123, 139

[125] Lynden-Bell, R. and Debenedetti, P. G. (2005). Computational investigation of order, structure, and dynamics in modified water models. *The Journal of Physical Chemistry B*, 109(14):6527–6534. 115

[126] M. Laporta, M. P. and Zanderighi, L. (1999). Perfluorosulfonated membrane (nafion): FT-IR study of the state of water with increasing humidity. *Phys. Chem. Chem. Phys*, 1:4619–4628. 180, 187, 189, 190, 218

[127] MacMillan, B., Sharp, A. R., and Armstrong, R. L. (1999). N.M.R. relaxation in nafion-the low temperature regime. *Polymer*, 40(10):2481–2485. 23, 25

[128] Marchand, G. (2012). *Advanced Computer Simulations of Nafion / Water Systems*. PhD thesis, Universität Duisburg-Essen. 13, 26, 31, 51

[129] Markovitch, O., Chen, H., Izvekov, S., Paesani, F., Voth, G. A., and Agmon, N. (2008). Special pair dance and partner selection: Elementary steps in proton transport in liquid water. *J. Phys. Chem. B*, 112:9456–9466. 20

[130] Marx, D. (2006). Proton transfer 200 years after von Grotthuss: Insights from *Ab Initio* simulations. *Chem. Phys. Chem.*, 7(9):1848–1870. 11, 19, 20

[131] Marx, D., Chandra, A., and Tuckerman, M. E. (2010). Aqueous basic solutions: Hydroxide solvation, structural diffusion, and comparison to the hydrated proton. *Chem. Rev.*, 110:2174–2216. 123

[132] Marx, D. and Hutter, J. (2000). *Ab initio* molecular dynamics: Theory and implementation. In Grotendorst, J., editor, *Modern Methods and Algorithms of Quantum Chemistry*, volume 1 of *NIC Series*. John von Neumann Institute for Computing. 31, 47

[133] Marx, D. and Hutter, J. (2009). *Ab initio Molecular Dynamics: Basic Theory and Advanced Methods*. Cambridge University Press. 31, 47

[134] Marx, D., Tuckerman, M. E., Hutter, J., and Parrinello, M. (1999). The nature of the hydrated excess proton in water. *Nature*, 397:601–604. 20, 40

[135] Marx, D., Tuckerman, M. E., and Parrinello, M. (2000). Solvated excess protons in water: quantum effects on the hydration structure. *J. Phys.: Cond. Matter.*, 12:A153–A159. 40

[136] Mauritz, K. A. and Moore, R. B. (2004). State of understanding of nafion. *Chem. Rev.*, 104:4535–4585. 13, 23, 25

[137] Moilanen, D. E., Spry, D. B., and Fayer, M. D. (2008). Water dynamics and proton transfer in nafion fuel cell membranes. *Langmuir*, 24(8):3690–3698. PMID: 18220436. 216

[138] Morris, D. R. and Sun, X. (1993). Water-Sorption and Transport Properties of Nafion 117 H. *Journal of Applied Polymer Science*, 50:1445–1452. 13

[139] Mosdale, R., Gebel, G., and Pineri, M. (1996). Water profile determination in a running proton exchange membrane using small-angle neutron scattering. *J. Membrane Sci.*, 118:269–277. 25

[140] Münch, W., Kreuer, K.-D., Silvestri, W., Maier, J., and Seifert, G. (2001). The diffusion mechanism of an excess proton in imidazole molecule chains: first results of an *ab initio* molecular dynamics study. *Solid State Ionics*, 145:437–443. 25

[141] Narasimachary, S. P., Roudgar, A., and Eikerling, M. H. (2008). Ab-initio study of interfacial correlations in proton-conducting polymer electrolyte membranes for fuel cells. *Electrochim. Acta*, 53:6920–6927. 27

[142] Nicolaides, D. B. (1996). Why the Car-Parrinello method is too good to leave to the electronic structure theorists. *CCP5 Newsletter*, (45):52–60. 46

[143] Noguchi, H., Taneda, K., Minowa, H., Naohara, H., and Uosaki, K. (2010). Humidity-dependent structure of surface water on perfluorosulfonated ionomer thin film studied by sum frequency generation spectroscopy. *The Journal of Physical Chemistry C*, 114(9):3958–3961. 180, 218

[144] Nosé, S. (1984). A molecular dynamics method for simulations in the canonical ensemble. *Mol. Phys.*, 52:255–268. 69, 74

[145] Nosé, S. (1984). A unified formulation of the constant temperature molecular dynamics method. *J. Chem. Phys.*, 81:511. 33, 59, 69, 74

[146] Osborn, A. and Moore, R. (2012). 10.37 - morphology of proton exchange membranes. In in Chief: Krzysztof Matyjaszewski, E. and Möller, M., editors, *Polymer Science: A Comprehensive Reference*, pages 721–766, Amsterdam. Elsevier. 12, 13, 14, 15

[147] Paddison, S. J. and Elliott, J. A. (2005). Molecular modeling of the short-side-chain perfluorosulfonic acid membrane. *J. Phys. Chem. A*, 109:7583–7593. 25, 27

[148] Paddison, S. J. and Elliott, J. A. (2006a). The effects of backbone conformation on hydration and proton transfer in the 'short-side-chain' perfluorosulfonic acid membrane. *Solid State Ionics*, 177:2385–2390. 25, 27, 215

[149] Paddison, S. J. and Elliott, J. A. (2006b). On the consequences of side chain flexibility and backbone conformation on hydration and proton dissociation in perfluorosulfonic acid membranes. *Phys. Chem. Chem. Phys.*, 8:2193–2003. 27

[150] Paddison, S. J. and Elliott, J. A. (2007). Selective hydration of the 'short-side-chain' perfluorosulfonic acid membrane. an ONIOM study. *Solid State Ionics*, 178:561–567. 25, 27

[151] Paddison, S. J., Paul, R., and Kreuer, K.-D. (2002). Theoretically computed proton diffusion coefficients in hydrated PEEKK membranes. *Phys. Chem. Chem. Phys.*, 4:1151–1157. 25

[152] Paddison, S. J., Pratt, L. R., Zawodzinski Jr., T., and Reagor, D. W. (1998). Molecular modeling of trifluoromethanesulfonic acid for solvation theory. *Fluid Phase Equil.*, 150-151:235–243. 53

[153] Paddison, S. J., Pratt, L. R., and Zawodzinski, Jr, T. A. (2001). Variation of the dissociation constant of triflic acid with hydration. *J. Phys. Chem. A*, 105:6266–6268. 22

[154] Peighambardoust, S., Rowshanzamir, S., and Amjadichandra, M. (2010). Review of the proton exchange membranes for fuel cell applications. *International Journal of Hydrogen Energy*, 35(17):9349 – 9384. 9

[155] Perdew, J. P., Burke, K., and Ernzerhof, M. (1996). Generalized gradient approximation made simple. *Phys. Rev. Lett.*, 77:3865–3868. 43

[156] Perdew, J. P., Kurth, S., Zupan, A., and Blaha, P. (1999). Accurate density functional with correct formal properties: A step beyond the generalized gradient approximation. *Phys. Rev. Lett.*, 82:2544. 44

[157] Petersen, M. K. and Voth, G. A. (2006). Characterization of the solvation and transport of the hydrated proton in the perfluorosulfonic acid membrane nafion. *J. Phys. Chem. B*, 110:18594–18600. 26

[158] Petersen, M. K., Wang, F., Blake, N. P., Metiu, H., and Voth, G. A. (2005). Excess proton solvation and delocalization in a hydrophilic pocket of the proton conducting polymer membrane nafion. *J. Phys. Chem. B Letters*, 109:3727–3730. 26

[159] Pratt, L. R. and Haan, S. W. (1981a). Effects of periodic boundary conditions on equilibrium properties of computer simulated fluids. i. theory. *J. Chem. Phys.*, 74:1864–72. 33

[160] Pratt, L. R. and Haan, S. W. (1981b). Effects of periodic boundary conditions on equilibrium properties of computer simulated fluids. ii. application to simple liquids. *J. Chem. Phys.*, 74:1873–6. 33

[161] Remler, D. K. and Madden, P. A. (1990). Molecular dynamics without effective potentials via the Car-Parrinello approach. *Molecular Physics*, 70:921. 31, 46

[162] Rollet, A.-L., Gebel, G., Simonin, J.-P., and Turq, P. (2001). A sans determination of the influence of external conditions on the nanostructure of nafion membrane. *Journal of Polymer Science Part B: Polymer Physics*, 39:548–558. 25

[163] Rollet, L. R. A.-L., Gebel, G., and Diat, O. (2002). Evidence of elongated polymeric aggregates in nafion. *Macromolecules*, 35:4050–4055. 21

[164] Rossky, P. J. and Lee, S. H. (1989). Structure and dynamics of water at interfaces. *Chemica Scripta*, 29a:1. 115

[165] Roudgar, A., Narasimachary, S., and Eikerling, M. (2008). *Ab initio* study of surface-mediated proton transfer in polymer electrolyte membranes. *Chem. Phys. Lett.*, 457:337–341. 27

[166] Roudgar, A., Narasimachary, S. P., and Eikerling, M. (2006). Hydrated arrays of acidic surface groups as model systems for interfacial structure and mechanisms in pems. *J. Phys. Chem. B*, 110:20469–20477. 27

[167] Sagnella, D. E., Laasonen, K., and Klein, M. L. (1996). Ab-initio molecular dynamics study of proton transfet in a polyglysine analog of the ion channel gramicidin A. *Biophys. J.*, 71:1172–1178. 53, 67, 72

[168] Schlegel, H. B. (2003). *Ab initio* molecular dynamics with Born-Oppenheimer and extended Lagrangian methods using atom centered basis functions. *Bull. Korean Chem. Soc.*, 24(6):1–6. 45

[169] Schmidt-Rohr, K. and Chen, Q. (2008). Parallel cylindrical water nanochannels in nafion fuel-cell membranes. *Nature Materials*, 7:75–83. 13, 14, 22, 26, 51

[170] Schuster, M., Rager, T., Noda, A., Kreuer, K. D., and Maier, J. (2005). About the choice of the protogenic group in pem separator materials for intermediate temperature, low humidity operation: A critical comparison of sulfonic acid, phosphonic acid and imidazole functionalized model compounds. *Fuel Cells*, 5:355. 25

[171] Seeliger, D., Hartnig, C., and Spohr, E. (2005). Aqueous pore structure and proton dynamics in solvated nafion membranes. *Electrochim. Acta*, 50:4234. 26, 31, 39, 40, 42, 47

[172] Selvan, M. E., Keffer, D. J., and Cui, S. (2011). Reactive molecular dynamics study of proton transport in polymer electrolyte membranes. *The Journal of Physical Chemistry C*, 115(38):18835–18846. 26

[173] Selvan, M. E., Keffer, D. J., Cui, S., and Paddison, S. J. (2010). A reactive molecular dynamics algorithm for proton transport in aqueous systems. *The Journal of Physical Chemistry C*, 114(27):11965–11976. 26

[174] Smit, B. and Frenkel, D. (1996). *Understanding Molecular Simulations. From Algorithms to Applications*. Academic Press, San Diego. 163

[175] Spohr, E. (2004). Molecular dynamics simulations of proton transfer in a model nafion pore. *Molecular Simulation*, 30(2-3):107–115. 26

[176] Spohr, E., Commer, P., and Kornyshev, A. A. (2002). Enhancing proton mobility in polymer electrolyte membranes: Lessons from molecular dynamics simulations. *J. Phys. Chem. B*, 106(41):10560–10569. 26, 32, 33

[177] Sprik, M., Hutter, J., and Parrinello, M. (1996). *Ab initio* molecular dynamics simulation of liquid water: Comparison of three gradient-corrected density functionals. *J. Chem. Phys.*, 105:1142. 44

[178] Stich, D., Marx, D., Parrinello, M., and Terakura, K. (1997). Protonated hydrogen clusters. *J. Chem. Phys.*, 107:9482. 40

[179] Stone, J. (1998). An efficient library for parallel ray tracing and animation. Master's thesis, Computer Science Department, University of Missouri-Rolla. 113

[180] Sun, J., Haunschild, R., Xiao, B., Bulik, I. W., Scuseria, G. E., and Perdew, J. P. (2013). Semilocal and hybrid meta-generalized gradient approximations based on the understanding of the kinetic-energy-density dependence. *Journal of Chemical Physics*, 138(4):044113. 44

[181] Sun, J., Xiao, B., and Ruzsinszky, A. (2012). Communication: Effect of the orbital-overlap dependence in the meta generalized gradient approximation. *The Journal of Chemical Physics*, 137(5):051101. 44

[182] Sunda, A. P. and Venkatnathan, A. (2011). Molecular dynamics simulations of triflic acid and triflate ion/water mixtures: A proton conducting electrolytic component in fuel cells. *Journal of Computational Chemistry*, 32(15):3319–3328. 23, 28

[183] Tangney, P. (2006). On the theory underlying the Car-Parrinello method and the role of the fictitious mass parameter. *J. Chem. Phys.*, 124:044111. 44, 46

[184] Taniguchi, A., Akita, T., Yasuda, K., and Miyazaki, Y. (2004). Analysis of electrocatalyst degradation in PEMFC caused by cell reversal during fuel starvation. *J. Power Sources*, 130:42–49. 11

[185] Tanimura, S. and Matsuoka, T. (2004). Proton transfer in nafion membrane by quantum chemistry calculation. *J. Polymer Sci. B*, 42:1905–1914. 23

[186] Tkatchenko, A. and Scheffler, M. (2009). Accurate molecular van der Waals interactions from ground-state electron density and free-atom reference data. *Phys. Rev. Lett.*, 102:073005. 47

[187] Troullier, N. and Martins, J. L. (1991). Efficient pseudopotentials for plane-wave calculations. *Phys. Rev. B*, 43:1993–2006. 61, 210

[188] Tse, J. S. (2002). *ab inito* molecular dynamics with density functional theory. *Annual Review of Physical Chemistry*, 53(1):249–290. PMID: 11972009. 31, 47

[189] Tuckerman, M., Laasonen, K., Sprik, M., and Parrinello, M. (1995a). *Ab initio* molecular dynamics simualtion of the solvation and transport of H_3O^+ and OH^- ions in water. *J. Phys. Chem.*, 99:5749. 40

[190] Tuckerman, M., Laasonen, K., Sprik, M., and Parrinello, M. (1995b). *Ab initio* molecular dynamics simulation of the solvation and transport of hydronium and hydroxyl ions in water. *J. Chem. Phys.*, 103:150. 20, 40

[191] Tuckerman, M., Marx, D., Klein, M., and Parrinello, M. (1997). On the quantum nature of the shared proton in hydrogen bonds. *Science*, 275:817–820. 40

[192] Tuckerman, M., Marx, D., and Parrinello, M. (2002). The nature and transport mechanism of hydrated hydroxide ions in aqueous solution. *Nature*, 417:925–929. 40

[193] Tuckerman, M. E., Chandra, A., and Marx, D. (2010). A statistical mechanical theory of proton transport kinetics in hydrogen-bonded networks based on population correlation functions with applications to acids and bases. *J. Chem. Phys.*, 133(12):124108. 44, 60, 62, 123

[194] Tuckerman, M. E. and Parrinello, M. (1994a). Integrating the Car-Parrinello equations. I. basic integration techniques. *J. Chem. Phys.*, 101:1302. 31

[195] Tuckerman, M. E. and Parrinello, M. (1994b). Integrating the Car-Parrinello equations. II. multiple time scale techniques. *J. Chem. Phys.*, 101:1316. 31

[196] Tulub, A. A. (2004). DFT:B3LYP *ab initio* molecular dynamics study of the Zundel and Eigen complexes, $H_5O_2{}^+$ and $H_9O_4{}^+$, in the triplet state in gas phase and solution. *J. Chem. Phys.*, 120:1217–1222. 20, 44, 180

[197] van Duin, A. C. T., Dasgupta, S., Lorant, F., and Goddard III, W. A. (2001). ReaxFF: A reactive force field for hydrocarbons. *J. Phys. Chem. A*, 105:9396–9409. 26

[198] Vanderbilt, D. (1990). Soft self-consistent pseudopotentials in a generalized eigenvalue formalism. *Phys. Rev. B*, 41:7892–7895. 60, 210

[199] VandeVondele, J. and Hutter, J. (2003). An efficient orbital transformation method for electronic structure calculations. *The Journal of Chemical Physics*, 118(10):4365–4369. 69, 73

[200] VandeVondele, J., Krack, M., Mohamed, F., Parrinello, M., Chassaing, T., and Hutter, J. (2005). Quickstep: Fast and accurate density functional calculations using a mixed gaussian and plane waves approach. *Computer Physics Communications*, 167(2):103 – 128. 69, 73

[201] Vassilev, P., Hartnig, C., Koper, M. T. M., Frechard, F., and van Santen, R. A. (2001). *Ab initio* molecular dynamics simulation of liquid water and water-vapor interface. *J. Chem. Phys.*, 115:9815. 213

[202] Verlet, L. (1967). Computer 'experiments' on classical fluids. I. thermodynamical properties of Lennard-Jones molecules. *Phys. Rev.*, 159:98–103. 33

[203] Vishynakov, A. and Neimark, A. V. (2001). Molecular dynamics simulation of microstructure and molecular mobilities in swollen nafion membranes. *J. Phys. Chem. B*, 105:9586–9594. 26

[204] von Grotthus, C. J. D. (1806). Mémoire sur la décomposition de l'eau et des corps qu'elle tien en dissolution à l'aide de l'électricité galvanique. *Ann. Chim.*, LVIII:54. 19

[205] Walbran, S. and Kornyshev, A. A. (2001). Proton transport in polarizable water. *J. Chem. Phys.*, 114:10039–10048. 170

[206] Wang, C., Clark II, J. K., Kumar, M., and Paddison, S. J. (2011). An *ab initio* study of the primary hydration and proton transfer of CF_3SO_3H and $CF_3O(CF_2)_2SO_3H$: Effects of the hybrid functional and inclusion of diffuse functions. *Solid State Ionics*, 199–200(0):6 – 13. 23, 27, 180

[207] Wang, Y., Kawano, Y., Aubuchon, S. R., and Palmer, R. A. (2003). TGA and time-dependent FTIR study of dehydrating Nafion-Na membrane. *Macromolecules*, 36(4):1138–1146. 180

[208] Wigner, E. (1934). On the interaction of electrons in metals. *Phys. Rev.*, 46:1002–1011. 42

[209] Williams, T., Kelley, C., and many others (2010). Gnuplot 4.4: an interactive plotting program. url=http://gnuplot.sourceforge.net/. 86

[210] Xu, G. and Pak, Y. (1992). Proton and deutron NMR study of PTFE ionomer membranes. *Solid State Ionics*, 50(3-4):339–343. 21

[211] Xu, H., Stern, H. A., and Berne, B. J. (2002). Can water polarizability be ignored in hydrogen bond kinetics? *J. Phys. Chem. B*, 106:2054–2060. 122

[212] Yandrasits, M. and Hamrock, S. (2012). 10.33 - poly(perfluorosulfonic acid) membranes. In in Chief: Krzysztof Matyjaszewski, E. and Möller, M., editors, *Polymer Science: A Comprehensive Reference*, pages 601 – 619. Elsevier. 12

[213] Zhang, H. and Shen, P. K. (2012). Recent development of polymer electrolyte membranes for fuel cells. *Chemical Reviews*, 112(5):2780–2832. 9, 17

List of Publications

1. Ilhan, M. A. and Spohr, E. (2011). Hydrogen bonding in narrow protonated polymer electrolyte pores. *Journal of Electroanalytical Chemistry*, 660:347-351.
2. Ilhan, M. A. and Spohr, E. (2011). *Ab initio* molecular dynamics of proton networks in narrow polymer electrolyte pores. *Journal of Physics: Condensed Matter*, 23:234104.

Curriculum Vitae

Der Lebenslauf ist in der Online-Version aus Gründen des Datenschutzes nicht enthalten.

Declaration

I herewith declare that I have produced this paper without the prohibited assistance of third parties and without making use of aids other than those specified; notions taken over directly or indirectly from other sources have been identified as such. This paper has not previously been presented in identical or similar form to any other German or foreign examination board.

The thesis work was conducted from November 2008 to May 2014 under the supervision of Prof. Eckhard Spohr at the University of Duisburg-Essen.

Hiermit versichere ich, dass ich die vorliegende Arbeit mit dem Titel "*Ab Initio* Molecular Dynamics Simulation of Proton Transfer in Narrow Ionomer Pores" selbst verfasst und keine außer den angegebenen Hilfsmitteln und Quellen benutzt habe, und dass die Arbeit in dieser oder ähnlicher Form noch bei keiner anderen Universität eingereicht wurde.

Essen, im Mai 2014

Acknowledgements

I would like to express my special appreciation and gratitude to my advisor Professor Dr. Eckhard Spohr. I would like to thank you for encouraging my research and for providing me with a scientific perspective. I would also like to thank Professor Dr. Philippe Bopp, Professor Dr. Georg Jansen, PD Dr. Holger Somnitz, and Dr. Mira Todorova for their comments and suggestions. I would especially like to thank my colleagues, members of the theoretical chemistry, and members of the theoretical organic chemistry at University of Duisburg-Essen for adorable time in Essen.

A special thanks to my family. It is difficult to find appropriate words to express how grateful I am to them for all that they have made on my behalf. I would also like to thank all of my friends who supported me in writing.

The calculations in this work were performed at the CRAY XT6m computer of University of Duisburg-Essen and at the LIDO cluster at Technical University Dortmund.